

Damage and Repair Identification in Reinforced Concrete Beams Modelled with Various Damage Scenarios using Vibration Data

ALI ABDULHUSSEIN AL-GHALIB

A thesis submitted in partial fulfilment of the requirements of

Nottingham Trent University for the degree of

Doctor of Philosophy

March 2013

This work is dedicated to my late mother for her sacrifices to the family.

Mum, this is for you... Thank you so much.

Acknowledgments

I would like to thank my friend and the director of study, Dr Fouad Mohammad, for his unending support and experienced advice throughout some very tough times of my study. Thanks are also expressed to the rest members of the supervisory team, Dr Mujib Rahman and Prof John Chilton.

I would also like to thank the laboratory technicians, Mr Jez Keeling and Ms Judith Kippling, for their help with practical issues during the experimental tests.

I wholeheartedly recognise the very important concepts suggested by Prof Paul Reynolds from the Department of Civil and Structural Engineering at the University of Sheffield. He was always willing to help with many experimental and theoretical problems arose during the project.

I must also thank Dr Martin Bencsik from the School of Science and Technology at the Nottingham Trent University. In this research, talks with him have helped to solve several problems in signal processing and promoted some ideas on damage identifications that are now reflected in this thesis.

Of course, there are no words can fairly describe the vital role of my dear family. I here pay homage to my late parents who had trust in my future that all sound conceivable. Without the inherited values and inspiration, my life would have been different. My dear wife, Sawsan, my lovely angels, Sarah and Sarra, and their relentless love and joy have brought incredible strength that any troubles slip away. My sister swapped the responsibility with me to look after our sick mother, allowing the onset of this project, for that I show her heartfelt thanks. I also must say thanks to my sister in law and her husband, Batoul and Salah, for looking after my paperwork over Iraq in the last three and a half years.

Finally, profound gratitude is dedicated to the guarantor, solicitor Suaad Salman, for guaranteeing me with a severe contract in front of the sponsor. This attitude is unique, and for that I am indebted to her.

Ali Al-Ghalib/ August 2012

Abstract

This research aims at developing a novel vibration-based damage identification technique that can efficiently be applied to real-time large data for detection, classification, localisation and quantification of the potential structural damage.

A complete testing procedure of the Experimental Modal Analysis (EMA) in freely supported beam based on impact hammer, as a relevant excitation source for field measurements, was established and the quality of its measurements was ensured. The experimental data in this research was collected from five laboratory-scale reinforced concrete beams modelled with various ranges of common defects.

Reliable finite element beam models for the five beams in their normal conditions were developed correlated and updated using the results of the experimental tests.

As a first round of investigation of the damage identification methods, the results of the modal parameters along with a number of their formulations and combinations were evaluated as model-based damage characterisation systems. Different ways for the representation and visualisation of the measurements in the time- or frequency-domain in a format pertinent for pattern identification were assessed.

A two-stage combination between principal component analysis and Karhunen-Loève transformation (also known as canonical correlation analysis) was proposed as a statistical-based damage identification technique. The suggested technique attempts to detect features regarding outliers or variation in the structural dynamic behaviour. In addition, it is used to serve as an unsupervised classification tool for data representing different structural conditions. Vibration measurements from time- and frequency-domain were tested as possible damage-sensitive features in an effort to avoid the expensive prolonged calculations of the modal parameters.

In the first stage of the algorithm, principal component analysis is conducted on data from frequency response functions or response power spectral density functions in order to reduce the size of the data. The first prominent principal components that account for a reasonable percentage of the variance in the original data are preserved.

In the second stage, the important principal components are provided as inputs to Karhunen-Loève transformation to constitute the new transformed space. Within-class and between-class covariance matrices are exploited for maximising the discriminant capacity between subgroups. The new generated sets of data are analysed as a typical mathematical eigenproblem to account for the first two or three principal components that retain the major part of the variance. These components are next being employed for significant visualisation of the original data.

The proposed system would provide unsupervised means that is capable to process, compare and discriminate between different periodically-collected immense data without considerable unnecessary effort for computations and modelling. The results of this statistical system help in distinguishing between normal and damaged patterns in structural vibration data. Most importantly, the system further dissects reasonably each main group into subgroups according to the levels of damage.

The performance of this technique was credibly tested and verified on real measurements collected from the five beams with various detailed damage states. Its efficiency was conclusively proved on data from both frequency response functions and response-only functions. The outcomes of this two-stage system show realistic detection and classification and outperform results from the rival principal component analysis-only.

Publications

The following papers have been published as a direct outcome of this thesis:

Refereed Journal Papers

Ali A. Al-Ghalib, Fouad A. Mohammad, Mujib Rahman and John Chilton (2011). Damage Identification in a Concrete Beam Using Curvature Difference Ratio, *Journal of Physics: Conference Series*, Volume 305.

Refereed Conference Papers

Ali A. Al-Ghalib, Fouad A. Mohammad, Mujib Rahman and John Chilton (2010). Dynamic Parameters of Incrementally Loaded Reinforced Concrete Beams, *Proceedings of the 10th International Conference on Recent Advances in Structural Dynamics RASD 2010, July 2010*, Southampton, UK.

Ali A. Al-Ghalib, Fouad A. Mohammad, Mujib Rahman and John Chilton (2011). Damage Identification in a Concrete Beam Using Curvature Difference Ratio, *Proceedings of the 9th International Conference on Damage Assessment of Structures DAMAS 2011, July 2011, St Anne's College, University of Oxford*, Oxford, UK.

Ali A. Al-Ghalib, Fouad A. Mohammad, Mujib Rahman and John Chilton (2011). Non-destructive Assessment of Damaged and Repaired Concrete Beams, *Proceedings of the 35th International Symposium on Bridge and Structural Engineering, IABSE-IASS, September 2011*, London, UK.

Ali Al-Ghalib, Dr Fouad Mohammad, Dr Mujib Rahman and Prof John Chilton (2011). Damage and Repair Quantification in Reinforced Concrete Beams Using Vibration Data, *Proceedings of the 4th International Conference on Concrete Solutions, September 2011*, Dresden, Germany.

Mohammed Usman, Dr Mujib Rahman and Ali Al-Ghalib (2011). The Use of NDT in Evaluation of Rubber Modified Self Compacting Concrete, *Proceedings of the 4th International Conference on Concrete Solutions, September 2011*, Dresden, Germany.

Ali Al-Ghalib, Dr Fouad Mohammad, Dr Mujib Rahman, Prof John Chilton (2011). Experimental Modal Analysis: A complete worked test on RC Beam, *Proceedings of the 3rd International scientific conference of Salahaddin University-Erbil (SU-ERBIL2011), October 2011, Erbil, Kurdistan, IRAQ.*

Mujib Rahman, Ali Al-Ghalib and Fouad Mohammad (2011). Vibration And Flexural Properties of Rubberised Concrete Beams, *Proceedings of the 7th Central European Congress on Concrete Engineering, September, 2011, Balatonfüred, Hungary.*

Table of Contents

| | |
|--|--------------|
| Acknowledgments | iii |
| Abstract | iv |
| Publications | vi |
| Refereed Journal Papers..... | vi |
| Refereed Conference Papers | vi |
| Table of Contents | viii |
| List of Figures | xiv |
| List of Tables | xvii |
| Nomenclature | xviii |
| Matrix and Vector Notation | xviii |
| Parameter Symbols | xix |
| Acronyms | xx |
| 1. Introduction | 1 |
| 1.1 Rationale | 1 |
| 1.2 Problem Definition | 2 |
| 1.3 Scope of the Research..... | 3 |
| 1.4 Outline of the Thesis | 5 |
| 2. Background on Structural Health Monitoring | 7 |
| 2.1 Introduction..... | 7 |
| 2.2 Structural Health Monitoring..... | 7 |
| 2.2.1 Overview | 7 |
| 2.2.2 Concept of Structural Health Monitoring | 9 |
| 2.2.3 Motivations for Structural Health Monitoring..... | 10 |
| 2.3 Damage Identification Strategy | 13 |
| 2.3.1 Damage Identification Algorithms | 13 |
| 2.3.2 Data Collection Systems | 15 |
| 2.3.2.1 Wire-based SHM System..... | 16 |

| | | |
|-----------|--|-----------|
| 2.3.2.2 | Wireless SHM System | 17 |
| 2.3.2.3 | Network-based Sensing System..... | 18 |
| 2.4 | Timeline of SHM: the Past, Present and Future | 19 |
| 2.4.1 | The Past Legacy | 19 |
| 2.4.1.1 | Pioneered Technical Research on Vibration-based Monitoring | 19 |
| 2.4.2 | The Present Assets in Structural Health Monitoring | 22 |
| 2.4.2.1 | Overview | 22 |
| 2.4.2.2 | Assessment and Monitoring Standards and Guidelines..... | 23 |
| 2.4.2.3 | Supplement Software Related to Structural Health monitoring | 24 |
| 2.4.3 | The Future of Structural Health Monitoring..... | 25 |
| 2.5 | Summary | 27 |
| 3. | Technical Literature Review..... | 29 |
| 3.1 | Introduction..... | 29 |
| 3.2 | Damage Identification using Basic Modal Parameters..... | 29 |
| 3.3 | Development of Damage Identification Paradigms..... | 30 |
| 3.4 | Model-based Damage Identification Methods (Inverse Problem)..... | 33 |
| 3.4.1 | Mode Shape Curvature/Strain Mode Shape Changes..... | 33 |
| 3.4.2 | Damage Detection using Non-iterative Modal Flexibility Methods | 34 |
| 3.4.3 | Strain-energy-based Damage Indicator Method | 37 |
| 3.4.4 | Model Updating Methods | 40 |
| 3.4.4.1 | General..... | 40 |
| 3.4.4.2 | Direct Finite Element Model Updating Methods | 41 |
| 3.4.4.3 | Iterative FE Model Updating Methods (Inverse Eigensensitivity Method)..... | 43 |
| 3.5 | Parameter-based Damage Identification Methods | 46 |
| 3.5.1 | Statistical Pattern Recognition Methods (Forward Problem) | 46 |
| 3.5.1.1 | Principal Component Analysis and Singular Value Decomposition..... | 48 |
| 3.5.1.2 | Coefficients ARMA Family Models..... | 51 |
| 3.5.1.3 | Statistical Outlier Detection..... | 54 |
| 3.5.2 | Neural Networks in Structural Damage Identification | 56 |
| 3.5.3 | Wavelet Analysis of Vibration Signals..... | 59 |
| 3.6 | Summary | 61 |
| 4. | Theory of Analytical and Experimental Modal Analysis..... | 63 |
| 4.1 | Experimental and Analytical Modal Analysis Methods | 63 |
| 4.2 | Vibration Analysis Models | 64 |

| | |
|--|-----------|
| 4.3 Theory of Analytical Modal Analysis | 69 |
| 4.3.1 Finite Element Analysis | 70 |
| 4.3.2 The Fundamentals of Structural Finite Element Analysis | 70 |
| 4.3.3 The Stiffness and Mass Matrices of Beam Element | 70 |
| 4.3.4 The Damping Matrix | 71 |
| 4.3.5 Dynamic Modulus of Elasticity | 74 |
| 4.3.6 Freely Supported Beam under Modal Testing | 74 |
| 4.3.7 Practical Implementation of FE Modelling | 77 |
| 4.4 Theory of Experimental Modal Analysis..... | 78 |
| 4.4.1 Theoretical Background..... | 78 |
| 4.4.2 Fundamental Components of Experimental Modal Analysis | 79 |
| 4.4.3 Derivation of Frequency Response Function..... | 81 |
| 4.4.4 Sampling and Quantisation of Continuous Time Signals..... | 85 |
| 4.5 Transducers and Data Acquisition Devices | 85 |
| 4.5.1 Force Transducers..... | 85 |
| 4.5.1.1 Instrumented Impact Hammer Excitation..... | 86 |
| 4.5.2 Response Transducers (Accelerometers)..... | 88 |
| 4.5.3 Data Acquisition Devices | 88 |
| 4.6 Experimental Modal Analysis Procedure | 89 |
| 4.6.1 Phase I: The Preparatory Phase | 90 |
| 4.6.2 Phase II: The Exploratory Phase..... | 90 |
| 4.6.2.1 Excitation/Response Check | 91 |
| 4.6.2.2 Immediate Repeatability Check..... | 91 |
| 4.6.2.3 Homogeneity Check | 92 |
| 4.6.2.4 Reciprocity Check..... | 92 |
| 4.6.2.5 FRF Shape Check | 92 |
| 4.6.2.6 Coherence Function Check..... | 93 |
| 4.6.3 Phase III: The Measurements Phase | 94 |
| 4.6.4 Phase IV: The Post-Test Analysis Phase | 94 |
| 4.7 Summary | 95 |
| 5. Research Methodology | 97 |
| 5.1 Introduction..... | 97 |
| 5.2 Damage State Scenarios..... | 99 |
| 5.3 Experimental Modal Analysis | 100 |

| | |
|--|------------|
| 5.4 Prediction and Correlation of Analytical Model..... | 100 |
| 5.5 Damage Classification Level in Identification Problem..... | 101 |
| 5.5.1 Statistical Models of Damage Classification..... | 102 |
| 5.5.1.1 Principal Component Analysis | 102 |
| 5.5.1.2 Karhunen-Loève Transformation | 104 |
| 5.5.1.3 Integration between PCA and KLT as Classification Tool | 106 |
| 5.6 Summary..... | 109 |
| 6. Experimental Work and Finite Element Model Updating..... | 110 |
| 6.1 Introduction..... | 110 |
| 6.2 Description of the Induced Damage | 113 |
| 6.2.1 Test Beam A | 113 |
| 6.2.2 Test Beam B..... | 115 |
| 6.2.3 Test Beam C..... | 116 |
| 6.2.4 Test Beam D | 117 |
| 6.2.5 Test Beam E..... | 117 |
| 6.3 Pre-Test Finite Element Modelling..... | 118 |
| 6.4 Testing Plan | 120 |
| 6.4.1 Experimental Modal Analysis: Preparatory Phase | 121 |
| 6.4.2 Experimental Modal Analysis: Exploratory Phase..... | 122 |
| 6.4.2.1 Excitation/Response Check | 122 |
| 6.4.2.2 Immediate Repeatability Check..... | 124 |
| 6.4.2.3 Reliability (Homogeneity) Check..... | 126 |
| 6.4.2.4 Reciprocity Check..... | 127 |
| 6.4.2.5 Coherence Check | 128 |
| 6.4.2.6 FRF Shape Check | 130 |
| 6.4.3 Experimental Modal Analysis: Measurements Phase..... | 132 |
| 6.4.4 Experimental Modal Analysis: Post-Test Analysis Phase..... | 133 |
| 6.5 Correlation of Analytical Model..... | 133 |
| 6.5.1 Effect of Damping on Predicted Data..... | 139 |
| 6.5.2 Effect of Shear Deformation on Predicted Data | 139 |
| 6.5.3 Effect of Modulus of Elasticity on Predicted Data | 142 |
| 6.6 Summary..... | 144 |
| 7. Damage Identification using Modal Parameters and their Formulations..... | 146 |
| 7.1 Introduction..... | 146 |

| | |
|---|------------|
| 7.2 Post-test Analysis and Estimation of Modal Parameters | 147 |
| 7.2.1 Overview | 147 |
| 7.2.2 Resonance Frequency Extraction..... | 148 |
| 7.2.3 Damping Estimation | 148 |
| 7.2.4 Mode Shape Estimation | 150 |
| 7.3 Damage Identification using Modal Parameters..... | 154 |
| 7.3.1 Effect of Damage on Natural Frequencies..... | 154 |
| 7.3.1.1 Natural Frequencies of Beam A..... | 154 |
| 7.3.1.2 Natural Frequencies of Beam B..... | 156 |
| 7.3.1.3 Natural Frequencies of Beam C..... | 158 |
| 7.3.1.4 Natural Frequencies of Beam D..... | 159 |
| 7.3.1.5 Natural Frequencies of Beam E..... | 160 |
| 7.3.2 Effect of Damage on Modal Damping | 161 |
| 7.3.2.1 General..... | 161 |
| 7.3.2.2 Modal Damping of Beam A..... | 162 |
| 7.3.2.3 Modal Damping of Beam B..... | 163 |
| 7.3.2.4 Modal Damping of Beam C..... | 164 |
| 7.3.2.5 Modal Damping of Beam E..... | 164 |
| 7.3.3 Effect of Damage on Frequency Response Functions..... | 165 |
| 7.3.4 Effect of Damage on Mode shapes..... | 168 |
| 7.3.4.1 General..... | 168 |
| 7.3.4.2 Mode Shapes of Beams A, B and C..... | 169 |
| 7.3.4.3 Mode Shapes of Beams D and E | 172 |
| 7.3.5 Effect of Damage on Modal Assurance Criterion | 173 |
| 7.3.6 Effect of Damage on Coordinate Modal Assurance Criterion | 174 |
| 7.3.7 Effect of Damage on Curvature Mode Shapes | 177 |
| 7.4 Damage Quantification using Moment-Curvature Relationship | 179 |
| 7.4.1 Theoretical Background..... | 179 |
| 7.4.2 Damage Quantification in Beam A..... | 181 |
| 7.4.3 Damage Quantification in Beam B..... | 185 |
| 7.4.4 Damage Quantification in Beam C..... | 187 |
| 7.5 Damage Identification using Curvature Difference Ratio | 189 |
| 7.6 Summary..... | 192 |
| 8. Implementation of Statistical Pattern Recognition Models to Vibration Data. | 194 |

| | |
|--|------------|
| 8.1 Introduction..... | 194 |
| 8.2 Statistical Pattern Recognition Paradigm | 195 |
| 8.3 Data Analysis using Time Domain Records..... | 199 |
| 8.3.1 The Raw Time Signals..... | 199 |
| 8.3.2 Statistical Moments of Acceleration-time Histories | 201 |
| 8.3.3 Probability Density Functions | 208 |
| 8.3.4 Normal Probability Plots | 210 |
| 8.3.5 Correlation Coefficients of Raw Time-histories..... | 212 |
| 8.3.6 Application of Principal Component Analysis on Various Data Sets | 216 |
| 8.3.6.1 PCA of Statistical Moments | 216 |
| 8.3.6.2 Principal Component Analysis on Response Time-histories..... | 217 |
| 8.4 Frequency Domain Analysis..... | 219 |
| 8.4.1 Power Spectra of Response Time Histories..... | 220 |
| 8.4.2 Frequency Response Functions | 222 |
| 8.4.3 Principal Component Analysis on Data Sets from FRFs..... | 223 |
| 8.4.4 Principal Component Analysis on Data Sets from RPS | 226 |
| 8.5 Karhunen-Loéve Transformation | 228 |
| 8.5.1 Two-stage PCA-KLT on Data Sets from FRFs | 228 |
| 8.5.2 Two stage PCA-KLT on Data Sets from Response Power Spectra | 230 |
| 8.6 Performance of Novelty Detection Approach on Data from FRFs | 231 |
| 8.7 Discussion and Summary..... | 235 |
| 9. Conclusions and Recommendations for Future Research | 238 |
| 9.1 Conclusions..... | 238 |
| 9.2 Recommendations for Future Research | 241 |
| Appendix A: Stiffness and Mass Matrices of the Beam Element | 244 |
| Appendix B: Sampling and Quantisation of Continuous Time Signals..... | 247 |
| References..... | 250 |

List of Figures

| | |
|---|-----|
| Figure 2.1: Classification of damage identification methods | 10 |
| Figure 2.2: Basic steps in damage diagnosis algorithms. | 15 |
| Figure 2.3: Typical configuration of a wire-based SHM system (after Wenzel, 2009). 16 | |
| Figure 2.4: Typical configuration of a wireless SHM system (after Wenzel, 2009)..... | 17 |
| Figure 2.5: Typical configuration of a Smartsync SHM system (after Dae Kun Kwon et al., 2011). | 18 |
| | |
| Figure 3.1: Flow chart for structural damage identification methods..... | 32 |
| | |
| Figure 4.1: Configuration of test beam under free-free support condition. | 76 |
| Figure 4.2: Test beam under free-free support condition- photograph..... | 77 |
| Figure 4.3: Generic impact hammer modal testing set-up..... | 80 |
| Figure 4.4: Three fundamental steps of EMA. | 80 |
| Figure 4.5: DeltaTron [®] version 8208 instrumented impact hammer- photograph. | 87 |
| Figure 4.6: Impact time histories and frequency spectra from different hammer tips.... | 87 |
| Figure 4.7: DeltaTron [®] model 4514 accelerometer–photograph..... | 88 |
| | |
| Figure 5.1: Flow chart of the damage identification methodology of the research. | 99 |
| Figure 5.2: Flow chart of the proposed classification paradigm..... | 108 |
| | |
| Figure 6.1: Beam A - configuration for static loading..... | 114 |
| Figure 6.2: Beam A - one of the static loading stages- photograph..... | 114 |
| Figure 6.3: Beam A - strengthening with CFRP layers-photograph..... | 115 |
| Figure 6.4: Beam B - mid span zone at the final damage state– photograph. | 115 |
| Figure 6.5: Beam C- configuration of static loading. | 116 |
| Figure 6.6: Beam C - under one of the static loading stages- photograph..... | 116 |
| Figure 6.7: Beam C - mid span zone at the final damage state-photograph. | 117 |
| Figure 6.8: Beam E- Preparation to cast the beam with two polystyrene blocks. | 118 |
| Figure 6.9: Configuration of the test grid points. | 120 |
| Figure 6.10: Presentation of AutoMAC data for reduced 11 selected DOFs. | 120 |
| Figure 6.11: Beam A - excitation/response check (time domain). | 123 |
| Figure 6.12: Beam A - excitation/response check (frequency domain). | 124 |
| Figure 6.13: Beam E - immediate repeatability check for drive mobility at point 1.... | 126 |
| Figure 6.14: Beam E - homogeneity check using two different level excitations..... | 127 |
| Figure 6.15: Beam E - homogeneity check using four different level excitations. | 127 |
| Figure 6.16: Beam E - reciprocity check for transfer mobility A_{13} | 128 |

| | |
|---|-----|
| Figure 6.17: Beam E - coherence function check for drive mobility at point 1 (A_{11}).. | 129 |
| Figure 6.18: Beam E - coherence function check for transfer mobility A_{61} | 130 |
| Figure 6.19: Beam E- FRF shape check for drive mobility function at points 1..... | 131 |
| Figure 6.20: Beam A- numerical and experimental mode shapes (intact condition). .. | 135 |
| Figure 6.21: Beam B- numerical and experimental mode shapes (intact condition).... | 136 |
| Figure 6.22: Beam C- numerical and experimental mode shapes (intact condition).... | 136 |
| Figure 6.23: Beam D- numerical and experimental mode shapes (intact condition). .. | 137 |
| Figure 6.24: Beam E- numerical and experimental mode shapes (intact condition).... | 137 |
| Figure 6.25: Beam B- FRF overlap check for effect of damping. | 138 |
| Figure 6.26: Beam B- FRF overlap check for effect of shear deformation. | 142 |
| Figure 6.27: Beam B- FRF overlaps check for effect of modulus of elasticity..... | 144 |
| | |
| Figure 7.1: Deviation in resonances of beam A with different loading levels. | 156 |
| Figure 7.2: Deviation in resonances of beam B with different loading levels..... | 157 |
| Figure 7.3: Deviation of frequency in beam C under different damage levels..... | 159 |
| Figure 7.4: Comparison of frequencies in beam D..... | 160 |
| Figure 7.5: Comparison of frequencies in beam E. | 161 |
| Figure 7.6: Deviation in damping ratios from the intact condition for beam A. | 163 |
| Figure 7.7: Deviation in damping ratios from the intact condition for beam B. | 164 |
| Figure 7.8: Normalised change in modal damping for beam C..... | 165 |
| Figure 7.9: Drive point FRFs for beams A, B and C under different load levels..... | 167 |
| Figure 7.10: Experimental mode shapes for intact and damaged steps of beam A. | 170 |
| Figure 7.11: Experimental mode shapes for intact and damaged steps of beam B. | 171 |
| Figure 7.12: Experimental mode shapes for intact and damaged steps of beam C. | 171 |
| Figure 7.13: Comparison of the first five flexural mode shapes of beam D..... | 172 |
| Figure 7.14: Comparison of the first five flexural mode shapes of beam E. | 173 |
| Figure 7.15: Comparison of curvature of the first bending mode for the five beams. . | 178 |
| Figure 7.16: Internal pseudo static force system of a beam element. | 180 |
| Figure 7.17: Inertia shear force distribution for beam A based on first mode..... | 182 |
| Figure 7.18: Inertia bending moment distribution for beam A based on first mode. ... | 182 |
| Figure 7.19: Flexural stiffness variation for beam A based on first mode. | 184 |
| Figure 7.20: Flexural stiffness variation for the entire length of beam B based on first mode..... | 186 |
| Figure 7.21: Flexural stiffness variation between support points for beam B based on first mode. | 186 |
| Figure 7.22: Flexural stiffness variation for beam C based on first mode..... | 188 |
| Figure 7.23: Curvature Difference Ratios for first curvature mode shape of beam B.. | 191 |
| | |
| Figure 8.1: Flow chart for implementation of SHM programme (after Farrar et al., 2001a). | 198 |

| | |
|---|-----|
| Figure 8.2: Raw response time signals of beam A at point #1, when force is at #1..... | 200 |
| Figure 8.3: Raw response signals of beam A at point #6, when force is at #1..... | 200 |
| Figure 8.4: Raw response signals of beam B at point #3, when force is at #1..... | 201 |
| Figure 8.5: The first four statistic moments from position #1 (end span) of beam A. . | 204 |
| Figure 8.6: The first four statistic moments from channel #6 (mid span) of beam A. . | 204 |
| Figure 8.7: First four statistical moments of beam A (raw time histories)..... | 207 |
| Figure 8.8: First four statistical moments of beam A (normalised data)..... | 207 |
| Figure 8.9: First four statistical moments of beam B (raw time histories)..... | 208 |
| Figure 8.10: PDFs using time histories from point #1 and point #2 of beam A..... | 210 |
| Figure 8.11: Normal probability plots of time signals from channel #1 of beam A..... | 212 |
| Figure 8.12: Normal probability plots of time signals from channel #2 of beam A..... | 212 |
| Figure 8.13: Correlation coefficients from beam A for different states and locations. | 215 |
| Figure 8.14: Correlation coefficients from beam B for different states and locations. | 215 |
| Figure 8.15: Statistical moments of time histories of beam A projected on the first two PCs..... | 217 |
| Figure 8.16(a): Percentage variance given by each PC of beam A; (b): Variance values given by the first PC of each state for beam A. | 217 |
| Figure 8.17: Condition discriminant using response time signals with respect to the first two PCs..... | 219 |
| Figure 8.18: Cumulated percentage variance using output time signals. | 219 |
| Figure 8.19: The RPS of beam A at position #1 (end point). | 221 |
| Figure 8.20: The RPS of beam A at position #6 (mid span)..... | 222 |
| Figure 8.21: The FRFs of beam B at position #4..... | 223 |
| Figure 8.22: First and second PCs based on data sets of FRFs, all five beams..... | 226 |
| Figure 8.23: First and second PCs based on data sets of RPS, beams A, B and C..... | 228 |
| Figure 8.24: First and second PCs of PCA-KLT based on data from FRFs..... | 230 |
| Figure 8.25: First and second PCs of PCA-KLT based on data from RPS. | 231 |
| Figure 8.26: Variation of COSH distance with record number. | 234 |
| Figure 8.27: Summation of COSH distance over all DOFs with respect to the states. | 234 |
| Figure B.1: Sampling of analogue signal using various sampling rates. | 248 |
| Figure B.2: Quantisation of analogue signal using different vertical resolutions. | 249 |

List of Tables

| | |
|---|-----|
| Table 4.1: Definition of common FRFs (after Ewins, 2000; McConnell and Varoto, 2008)..... | 66 |
| Table 4.2: Relationship between the three models of an undamped dynamic system (after Maia and Silva, 1997). | 68 |
| | |
| Table 6.1: Specifications of the five test RC beams. | 112 |
| Table 6.2: Data acquisition parameters and associated setting values. | 125 |
| Table 6.3: Comparison between experimental (Exp) and numerical (Num) natural frequencies. | 134 |
| Table 6.4: Comparison between numerical natural frequencies using Timoshenko (Timo) and Euler-Bernoulli (Euler) models alongside the experimental (Exp) results. | 141 |
| Table 6.5: Comparison between numerical natural frequencies based upon dynamic (E_d) and static (E_s) modulus of elasticity along with the experimental (Exp) results. | 143 |
| | |
| Table 7.1: Comparison of identified frequencies and damping ratios for test beams. . | 149 |
| Table 7.2: Artificial damage influence on MAC values for the RC beams..... | 175 |
| Table 7.3: Artificial damage influence on COMAC values for the RC beams. | 176 |
| Table 7.4: Successive mid span stiffness decrease of beam A based on the moment-curvature ratio. | 185 |
| Table 7.5: Successive mid span stiffness decrease of beam B based on the moment-curvature ratio. | 187 |
| Table 7.6: Successive mid span stiffness decrease of beam C based on the moment-curvature ratio. | 189 |
| Table 7.7: Summary of damage identification results tested on measurement from the five beams. | 193 |
| | |
| Table 8.1: Cumulative percentage of total variation carried by the first 10 PCs, based on data sets from FRFs. | 226 |
| Table 8.2: Cumulative percentage of total variation carried by the first 10 PCs, based on data sets from RPS densities. | 228 |
| Table 8.3: Cumulative percentage of total variation carried by the first 10 KLT-PCA, based on data sets from FRFs. | 229 |
| Table 8.4: Cumulative percentage of total variation carried by the first 10 KL-PCs, based on data sets from RPS. | 231 |
| Table 8.5: Summary of statistical-based identification methods tested on measurement from the five beams | 237 |

Nomenclature

The following list represents the symbols that are common in the Chapters of this thesis. Other symbols are used in individual Chapters. All symbols are defined in the context when they first appear.

Matrix and Vector Notation

| | |
|-------------------------------------|--|
| $[\]$ | Matrix |
| $\{ \}$ | Vector |
| $[\]^T, \{ \}^T$ | Transpose of a matrix; transpose of a vector |
| $[I]$ | Identity matrix |
| $[\]^{-1}$ | Inverse of a matrix |
| $[B]$ | Between-class covariance matrix |
| $[C]$ | System viscous damping matrix |
| $[D]$ | System structural (hysteretic) damping matrix |
| $[f], [F]$ | System flexibility matrix |
| $[K]$ | System stiffness matrix |
| $[M]$ | System mass matrix |
| $[S]$ | Within-class covariance matrix |
| $[X]$ | Original data matrix |
| $[Z]$ | Component scores matrix |
| $\{ f(t) \}$ | Time-varying nodal forces vector |
| $\{ x(t) \}$ | Time-varying nodal displacements vector |
| $\{ \dot{x}(t) \}$ | Time-varying nodal velocities vector |
| $\{ \ddot{x}(t) \}$ | Time-varying nodal accelerations vector |
| $[\psi], [y]$ | Mode shapes (Eigenvector) matrix |
| $[\phi], [V]$ | Mass-normalised mode shape matrix |
| $\{ \phi \}^r, \{ \psi \}^r$ | r^{th} mode shape vector, Eigenvector |
| $[H(\omega)], [\alpha(\omega)]$ | Frequency response function matrix |
| $[\omega^2], [\lambda]$ | Diagonal eigenvalue (natural frequencies) matrix |

| | |
|--------------|--------------------------------------|
| $[\Sigma]$ | Covariance matrix |
| $[\Sigma]_i$ | Covariance matrix of class group (i) |

Parameter Symbols

| | |
|--------------------|--|
| $\gamma^2(\omega)$ | Coherence function |
| A_{jk}^r | Modal constant for r^{th} mode of vibration |
| c | Number of classes (groups) in a data matrix |
| f_{max} | Working (Nyquist) frequency |
| f_s | Sampling (digitising) frequency |
| $G_{ff}(\omega)$ | Single-sided auto-spectrum of the input signal |
| $G_{fx}(\omega)$ | Single-sided cross-spectrum between input and output signals |
| $G_{xx}(\omega)$ | Single-sided auto-spectrum of the output signal |
| $H_{jk}(\omega)$ | Individual FRF element between coordinates j and k (response at j due to excitation at k) |
| i | Imaginary unit ($\sqrt{-1}$) |
| N | Total number of degrees of freedom |
| n | Number of observations (rows in a data matrix) |
| p | Number of features (columns in a data matrix) |
| r | Mode number |
| $S_{ff}(\omega)$ | Dual-sided auto-spectrum of the input signal |
| $S_{fx}(\omega)$ | Dual-sided cross-spectrum between input and output signals |
| $S_{xx}(\omega)$ | Dual-sided auto-spectrum of the output signal |
| t | time variable |
| T | Repeat period / data acquisition period |
| $x(t)$ | Time-varying displacement degrees of freedom |
| ζ_r | Viscous damping ratio of r^{th} mode of vibration |
| η_r | Structural damping loss factor of r^{th} mode of vibration |
| \bar{x} | Mean of feature vector in original data |
| σ_x | Standard deviation of data sample |

| | |
|-----------------|--|
| φ_{jr} | j^{th} element of the r^{th} mode of vibration |
| ω | Frequency of vibration |
| ω_r, f_r | Natural frequency of r^{th} mode of vibration |

Acronyms

| | |
|---------|---|
| AASHTO | American Association of State Highway and Transportation Office |
| ADC | Analogue-to-Digital Converter |
| AMADEUS | Accurate Modelling and Damage Detection in the High Safety |
| ANN | Artificial Neural Network |
| AR | Auto-Regressive |
| ARMA | Auto-Regressive Moving Average |
| ARNN | Auto-Regressive Neural Network |
| BRIME | Bridge Management in Europe |
| BRIMOS | Bridge Monitoring system |
| CFRP | Carbon Fibre Reinforced Polymer |
| COMAC | Coordinate Modal Assurance Criterion |
| DAQ | Data Acquisition |
| DOF | Degree-Of-Freedom |
| DSF | Damage-Sensitive Feature |
| DTA | Dynamic Testing Agency (UK) |
| EMA | Experimental Modal Analysis (also known as Modal Testing) |
| FE | Finite Element |
| FEM | Finite Element Method |
| FFT | Fast Fourier Transform |
| FHWA | Federal Highway Administration |
| FRF | Frequency Response Function |
| KLT | Karhunen-Loève Transformation |
| LAN | Local Area Network |
| LRFD | Load and Resistance Factor Design |
| LTBP | Long-Term Bridge Performance |

| | |
|-------|--|
| MA | Moving Average |
| MAC | Modal Assurance Criterion |
| MDLAC | Multi Damage Location Assurance Criterion |
| MDOF | Multi-Degree-Of-Freedom |
| MF | Modal Flexibility |
| MLP | Multi-Layer Perceptron |
| NASA | National Aeronautical and space Administration |
| NBI | National Bridge Inventory |
| NDE | Non-Destructive Evaluation |
| NDT | Non-Destructive Test |
| ONS | Office of National Statistics |
| PC | Principal Component |
| PCA | Principal Component Analysis |
| PDF | Probability Density Function |
| PR | Pattern Recognition |
| PSD | Power Spectral Density |
| QA | Quality Assurance |
| RBF | Radial Basis Function |
| RC | Reinforced Concrete |
| RPS | Response Power Spectrum |
| RRF | Relative Response Function |
| SAMCO | Structural Assessment Monitoring and Control |
| SDOF | Single-Degree-Of-Freedom |
| SHM | Structural Health Monitoring |
| SPR | Statistical Pattern Recognition |
| SVD | Singular Value Decomposition |
| ULS | Uniform Load Surface |
| WT | Wavelet Transform |

1. Introduction

1.1 Rationale

There is a big increase in the stock of civil engineering infrastructure that encountered problems of ageing and deterioration, and therefore there is an urgent need for continuous monitoring of the health of structures. Civil engineering authorities are of growing concern of the limited reliability of current visual and other local Non-Destructive Testing (NDT) systems. Repeated failure incidents in bridges happened newly despite the fact that the collapsed structures were under monitoring scheme. Unlike other similar areas, owners and operators of civil engineering infrastructure never tolerate collapses and save no effort to ensure the safety of the structures. The unexpected collapse of such structures has a notorious symbolic impact on the economy and stability of any country.

Providing the rise in the number of the infrastructure experienced problems coupled with the recurrent failures of some major structures, the visual and other local NDT monitoring systems are evidently inefficient. The inefficiency manifested in their limited and prolonged procedure and inability to quantify unexpected and wide range of structural defects. These reasons consequently have dedicated to study the application of the vibration-based damage detection methods for structures (Farrar and Jauregui, 1998; Mazurek and DeWolf, 1990).

Conversely, the permanent vibration-based monitoring systems are widely accepted in the past few decades, and they are resounding successes in various disciplines, namely mechanical engineering, automotive and aeronautic systems. Besides their global and automated performance, data from these systems provides quantitative results about any type of structure. Given that these only methods can present a mathematical model for the actual structure (Zhengsheng et al., 2005), the available integration between the experimental measurements and analytical model makes these methods even more attractive. Furthermore, the growth of these monitoring systems has recently been galvanised by the evolution and cost reduction of digital computing hardware and sensing technologies (Farrar and Worden, 2007). As a result, it becomes more feasible

and practical with the witnessed advances of software and measurement utilities to generalise the success of these monitoring systems in other disciplines in the civil engineering area.

1.2 Problem Definition

A large number of technical articles were published over the past three decades on the use of vibration data in damage identification methods to detect, locate and quantify the damage. Many of the papers achieved some correlation, but the cases were either numerical simulations, laboratory samples or simulated damage in field structures scheduled for demolition (Carden and Fanning, 2004; Friswell and Penny, 1997). The most satisfactory methods in damage identification seem to be based on modal parameters and use the inverse type (model-based) methods (Friswell and Penny, 1997). However, it is widely accepted that there is no yet a perfect method to be used for damage detection, localisation and quantification by exploiting the vibration data. No algorithm has yet been suggested to apply universally to identify any type of damage in any type of structure (Carden and Brownjohn, 2008; Carden and Fanning, 2004; Wenzel, 2009). The development of vigorous damage detection and location algorithms based on response monitoring data of an in-use structure is still a challenge, even though the availability of such model will open the door to more accurate estimation of the remaining life of a structure (Friswell, 2007).

Having utilised low frequency vibration data by the model-based methods, a number of shortcomings emerge in damage identification resulting in a limited accuracy because of the global nature of the lower modes (Friswell and Penny, 1997). In addition, the model-based methods are computationally expensive and they are impossible to apply in embedded nature as online real-time monitoring systems (Wenzel, 2009). The programme of permanent monitoring for suspected structure will end in too many unmanageable amounts of data. The human capacity to assess large amounts of data is very limited, so Statistical Pattern Recognition (SPR) methods need to be introduced into the procedure (Wenzel, 2009). Indeed, many researchers thought with the damage identification as Pattern Recognition (PR) forward problem. The alternative algorithm

would overcome difficulties associated with the inverse problem, and in the meantime could be pertinent to evaluate immense real-time data.

A pattern classification paradigm for Structural Health Monitoring (SHM) of civil engineering structures was first proposed by Sohn and Farrar in 2001 (Wenzel, 2009). Small amount of the given references in the literature exploited statistical approaches to quantify the observed changes in the damage-sensitive features. The majority of the small effort of these references is assigned for extracting damage-sensitive features from vibration measurements (Fugate et al., 2001).

The fact that a wide range of civil engineering structures are of unknown history is another problematic obstacle confronts the use of the vibration-based monitoring systems in civil engineering. Bridges or other individual structures have very little in common with each other and almost any structure is a unique model (Wenzel, 2009). In general, data from a real-life as-built model of the structure is commonly unavailable. Consequently, a prediction of analytical model for the original intact condition will serve as a basic guide to which the deviation of present measurements is eventually compared with it.

1.3 Scope of the Research

In spite of the prospective benefit of the automated permanent monitoring systems where a large number of sensors generate massive vibration data, they also produce a severe difficulty later in processing and interpreting of this data (Friswell and Penny, 1997). Therefore, statistical pattern classification methods would be relevant to perform a reliable site-location diagnosis technique. It would be inevitable for a successful technique to rely only on individual signals to perform damage diagnosis process. Only in this situation, the conventional modal models with their intensive computations, corrections and inherent inaccuracies can be avoided.

At the risk of repetition, the gap in the knowledge body of damage identification methods is recognised in the following main points:

- Inadequacy of the model-based methods to timely handle immense data from present monitoring systems.

- Little effort in the literature has been recently started on using the rival methods, namely Statistical Pattern Recognition (SPR) methods. The majority of the little effort has been particularly devoted to the selection of features those are sensitive to damage.

For these reasons, this research will be principally interested in developing a statistical classification algorithm performs a well-timed identification for data collected at site without further need for daunting modelling. To make such algorithm even simpler and credible, signal-only-based vibration data will be investigated as damage-sensitive features. A classification of data from various state conditions is important, if not vital, for effective identification at the quantification and prediction levels (Worden and Duijck, 2004). Damage detection is also distinguished by making use of the classification step, as damage can be identified without previous knowledge on the behaviour of the system when it is damaged (Worden and Duijck, 2004).

Using the vibration data collected from five laboratory-scale Reinforced Concrete (RC) beams modelled with different damage conditions together with the practical knowledge and theory, the research presented in this thesis will satisfy the following primary objectives:

1. A good deal of this research will be assigned to develop an unsupervised statistical method to classify damage according to its different class levels. The method will attempt different damage-sensitive features, namely: temporal features such as raw time-signals and statistical moments of the time signals; and spectral features such as Response Power Spectral (RPS) density and Frequency Response Functions (FRFs). Data of both features will be acquired and processed from the five RC beams modelled with a wide range of defects. The data of experiments will be used to question the performance of the proposed method. The final outcome of this method can be envisaged in various disciplines of SHM. The contribution is unique to the area of damage identification, overcomes the difficulties of modelling and provides a substantial progress towards the objective of fast and reliable damage assessment methodology.

2. Experimental Modal Analysis (EMA) will be used to investigate the effects of different purpose-made defects on the modal parameters (natural frequencies, mode shapes and modal damping ratios) of the five RC beams. The investigations will be extended to apply some formulations of the modal parameters such as the curvatures and Direct Stiffness Calculation (DSC) to locate and quantify the damage. The vibration data of two repaired beams will be exploited to assess the improved strength in externally strengthened beams using Carbon Fibre Reinforced Polymer (CFRP) sheets.
3. A comprehensive correlation between the predicted data from the Finite Element (FE) beam models of the tested beams and from EMA will be implemented. The measured data will be utilised as a reference model to study the effect of some physical parameters such as the boundary conditions, modulus of elasticity, damping model and shear deformation on the accuracy of the numerical model.
4. Data sets from RPS density will be examined as damage-sensitive features as oppose to sets from FRFs. The success of this feature to be conclusive will be feasible in damage identification of civil engineering structures where the ambient loadings are difficult to estimate.
5. The vibration measurements in the time or frequency domain will be explored with various statistical models such as Probability Density Functions (PDFs), normal probability plots, Principal Component Analysis (PCA) and correlation coefficients as possible competitive damage identification models.
6. The COSH distance measure and mean COSH distance will be examined as a quantity to detect the outlier in frequency spectrum sets from various state conditions. Such measure will serve as a means for identification of the severity of damage according to their significance.

1.4 Outline of the Thesis

The research work presented in this thesis is organised in nine Chapters. Chapter 1 presents a brief description of the motives in the research topic, research aims, objectives and the methodology used to satisfy the objectives. Chapter 2 is dedicated to explain in detail the background of SHM methods and their attributes. The Chapter

reviews the main developments occurred in this area over the past three decades. Chapter 3 provides a comprehensive literature review on the prominent methods used in the damage identification area. The Chapter explains in more detail the limitations of current methods, and the critical points noted are used to justify the potential benefit of this research. Chapter 4 introduces the theoretical and experimental background of both analytical and experimental modal analysis. In addition, the main parameters affect predicting correlated analytical models are discussed. In the meantime, the characteristics of each individual piece of the new designated equipment associated with the procedure used to perform the experimental work are explained. Chapter 5 addresses the methodology and the theoretical background of a new statistical-based damage identification method developed in the research. Chapter 6 submits a complete description of the five RC beams with their subsequent damage state conditions. The description is followed by the test procedure supplemented by the necessary quality assurance checks. The validation of the predicted models with an extensive investigation of the corresponding updating parameters is also provided. Chapter 7 utilises the Single Degree Of Freedom (SDOF) peak-picking method to perform modal parameter analysis. The estimated data is subsequently used as damage identification parameters. Formulations and combinations of the modal parameters are also assessed as model-based damage identification techniques. Chapter 8 investigates the significance of using vibration data from time or frequency domain, as damage-sensitive parameters, with various statistical-based damage identification methods. It is in this Chapter the new damage identification method is applied. The proposed method is tested and verified with numerous experimental examples from data of this work. Eventually, the main observations, contributions and limitations are concluded in Chapter 9. Pertinent subjects for further future research are also recommended in this Chapter.

2. Background on Structural Health Monitoring

2.1 Introduction

This Chapter presents a basic definition to the subject of Structural Health Monitoring (SHM) and structural damage identification in civil engineering infrastructure. Then, a historical review on the themes pertinent to the work and the motives played role in the evolution of this area are discussed. Next, the Chapter goes over the invaluable quality knowledge brought together by researchers, companies and construction authorities. After that, the Chapter highlights promising future extent of monitoring business besides the motives that will develop the technology in the area of research. Finally, the most notable verdicts in the literature of SHM and vibration-based monitoring methods are summarised at the end of the Chapter.

2.2 Structural Health Monitoring

2.2.1 Overview

Nowadays, much civil engineering RC infrastructure is experiencing problems of ageing and deterioration after decades of use and abuse by humans and the environment (Zhengsheng et al., 2005). These structures are now raising challenging problems of safety and suitability, and therefore, the demand is increased to assess their performance. After several collapses, civil engineering authorities in the United States and other industrious countries mandated periodic safety inspection regulations for these structures (Hunt, 2000).

The Office of National Statistics (ONS) data indicate that the budget spent on UK infrastructure repairs and maintenance for 2009-2010 is estimated at £1.8 billion. However, for the purposes of the investigation a conservative estimate for infrastructure renewals and capacity enhancement a budget of £15 billion per annum has been assumed (HM Treasury, 2010). Similar surveys have estimated costs of retrofitting of

infrastructure in the United States by US\$ 2.2 trillion, and about US\$ 930 billion of the amount for bridges (Report Card for America's Infrastructure, 2009). Even for developing a third world country such as Iraq, after decades of carelessness to the sector of maintenance, statistics estimate that costs of rehabilitation or reconstruction of the ruined and neglected infrastructure at US\$ 400 billion (Iraqi Planning Minister, 2009). Notwithstanding that for existing structures, a reliable inspection and condition assessment system has the potential to extend the periodic maintenance scheme (Farrar and Worden, 2007; Zhengsheng et al., 2005).

Inspection is typically carried out to decide if the tested structure is in need of repair or demolition, estimate the amount of needed repair or whether further testing is required. The integrity and robustness of structural components are needed to be improved before series damages accumulate, requiring more expensive repairs (Gassman and Tawhed, 2004). Damage diagnosis, adequacy and integrity assessment for a structure are conventionally conducted through a wide range of traditional Non-Destructive Evaluation (NDE) techniques such as tap testing, visual inspection, liquid penetrate, ultrasonic, rebound hammer, impact echo, thermography, acoustic emission, X-ray inspection, and so forth. Some of these techniques are carried out during constant scheduled periods or after a drastic event such as earthquake, flood disaster or accidental collision. In addition, NDE procedures may take place during construction and during the whole life cycle of a structure (Balageas et al., 2006). However, civil engineering authorities are of increasing concern of the limited extent of the current NDE methods. Practically, to most NDE methods require a reliable knowledge of the damaging process of the material prior to the detection and characterisation of concealed defects. Moreover, such methods are qualitative, subjective and expensive. Therefore, the development of an efficient procedure that overcomes the limitations of these techniques, as well as be able to evaluate the health of a structure or its components early will have significant economical management and maintenance impact. Through achieving safe and functional intelligent systems, structures will be designed to work with the safety margin without need to extended period of inspection (Worden and Duijue, 2004).

To this end, as an effective replacement or supplement to the traditional inspection methods, vibration-based condition assessment methods have become popular as they are easy to conduct, inexpensive, global and quantitative. In these methods, complete measurements for 200m long bridge can be collected by two engineers within one day (Wenzel, 2009). These methods have been studied widely and developed for the last 20 years as a SHM tool for bridges (Owen et al., 2004). Even with the presence of their experimental errors, measurements from these methods give a more reliable representation for the tested structure than the simulated analytical model (Hwang and Kim, 2004). Stiffness coefficients of a structure could be directly determined by vibration measurements without any need to analytical support provided the test and processing of data are well planned and implemented. No other testing method could provide such comprehensive information for actual structures (Zhengsheng et al., 2005).

2.2.2 Concept of Structural Health Monitoring

In short, SHM in civil engineering infrastructure is the process of applying a damage diagnosis and prognosis algorithm for a structure. The practice is aimed to track different facets of the performance and robustness of a structure to reach a sound decision on its safety and serviceability (Farrar and Worden, 2007). The process entails the monitoring of a structure over time using periodically spaced measurements. The extraction of damage-sensitive features from these measurements and the structural or statistical modelling of these features will help to determine the current state of the system health. For long-term SHM, the output of this process is periodically updated considering the ability of the structure to continue to perform its intended function in light of the inevitable aging and damage accumulation resulting from the operational environments. Additionally, in severe unusual event, such as an earthquake, hurricane or object collision, SHM is used as a quick test to check the condition of a structure. This test is intended to provide, in an immediate time, dependable information about a structure performance during such extreme events and the subsequent integrity of its components (Farrar and Worden, 2007). In general, damage identification of civil structures is recognised in two manners, manual inspection and automatic continuous monitoring. The direct methods identify the damage directly, while the global methods identify the damage indirectly through collected set of measurements, which are utilised

later on to identify the damage (Ettouney and Alampalli, 2012). Figure 2.1 shows the main features of SHM damage assessment methods, and their difference from NDE methods.

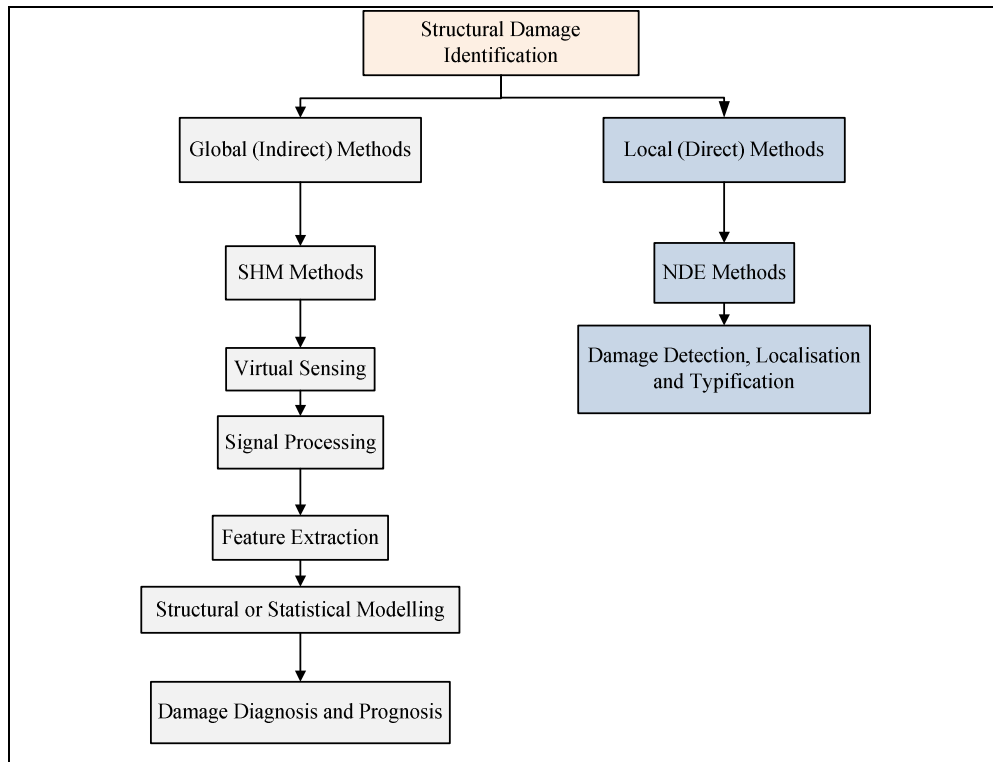


Figure 2.1: Classification of damage identification methods

(Adaptation after Ettouney and Alampalli, 2012).

2.2.3 Motivations for Structural Health Monitoring

The monitoring programmes have historically been implemented for the purpose of understanding and eventually calibrating models of the load-structure-response chain. One of the earliest known documents on the systematic bridge monitoring was conducted by Carder in 1937 during the construction of the Golden Gate Bridge of San Francisco bay. The programme involved measuring periods of various components to understand the dynamic behaviour and likely results of an earthquake (Brownjohn, 2007). However, the monitoring practice is widely used thereafter to assess the integrity and ensure the adequacy of suspected structures.

Factually, the earliest civil engineering infrastructure where the SHM was first recognised is the dams. A legislation permitting regular inspection of dams initiated in

the UK because of the failure of the 30m Dale Dyke embankment dam, which caused death of 254 people near Sheffield, UK in 1864 (Brownjohn, 2007). The most recent form of legislation in the UK is the Reservoir Act of 1975 that gives a supervising engineer the responsibility for conditional surveillance of a reservoir and dam, including keeping and interpretation of operational data. Thus, dams are historically the first class of civil infrastructure for the mandated application of SHM (Brownjohn, 2007). So much recent attention in the civil engineering SHM community has been concentrated on bridges that it overshadowed the official application of SHM technology to other infrastructure such as dams for several decades (Brownjohn, 2007).

Nonetheless, the subject of SHM in bridges was only recognised after the collapse of Silver Point Bridge, a 680m-long bridge over the Ohio River, in the USA in 1967 (Wenzel, 2009). After the collapse of this bridge, the United States federal government mandated biennial inspection schemes for all highway bridges. The National Bridge Inventory (NBI) program began in 1971 and represents the establishment of a national bridge inspection program. In this context, a rating is made through biennial inspections routine to the 597000 bridges of the Federal Highway Administration (FHWA) as assessment effort to remove the deficient highway bridges from service (Wenzel, 2009). The bridges are generally rated and monitored at least once every two years largely using visual inspection techniques. However, due to its prolonged process, in 1987 the FHWA began to consider increasing the intervals of the inspection programme beyond two years for some bridges (Mazurek and DeWolf, 1990).

The calamities continue. One example, a single span of the Sung-Su Bridge over the Han River in Seoul fell into the river, killing 20 people and injuring about 30 people in 1994. The pin connections of the bridge between the cantilever spans and the middle suspension span broke down unexpectedly during a heavy-traffic day without previous warning (Sohn, et al., 2004). The collapse of this bridge caused enormous shock to the Korean society, and stimulated safety awareness of civil structures nationwide (Sung-Pil Chang, 2006).

Another example is the collapse of I-35W Mississippi River Bridge in 2007. The primary cause for the failure was the under-sized gusset plates. In addition to the design error, an accumulation of 2 inches of concrete were added to the road surface over the years, increasing the dead load by 20%.

In the past, many owners were unsatisfied totally with the traditional defects mapping process, using binoculars or rope access. The main disadvantage is the difficulty to produce a scaled defects map allowing an accurate and reproducible monitoring, crack evolution, opening measurement, etc. (Lançon et al., 2011). Despite the fast developed technology in the area of instrumentations of detailed numeric defects mapping, such as (SCANSITES[®]) and high density 3D coordinate geometric scanning (LIDAR), these technologies are still unable to provide information on concealed defects.

The significant problems resulting from the traditional visual inspection and other manual NDT methods have undermined the use of these methods, and in the meantime revolutionised the automatic SHM systems. The increased age of the infrastructure stock, the escalated demand on the maintenance of this stock in addition to several catastrophic collapses have galvanised imposing safer and functional monitoring programmes to the existing structures. Furthermore, the horizontal and vertical expansion in recent projects has encouraged the authorities to enforce parallel monitoring schemes on the construction companies.

Unlike other comparable areas, owners and operators of civil engineering infrastructure in the developed countries never tolerate failure of a structure because of its symbolic and detrimental effects on the economy and stability of the country. The accessibility of the structure, subjectivity and qualitative nature of visual inspection, unanticipated obscure damage along with the unpredictable response of the large slender structure to the operational loadings have unleashed the development and use of dynamic-based monitoring systems. More recently, the development of this quantifiable monitoring approach has been closely coupled with the evolution, miniaturisation and cost reduction of digital computing hardware and sensing instrumentations (Farrar and Worden, 2007).

Collectively, the collapse events and the need for an effective continuous automated damage monitoring system have devoted to study the application of global, vibration-based damage detection methods to bridge structures (Farrar and Jauregui, 1998; Mazurek and DeWolf, 1990).

2.3 Damage Identification Strategy

2.3.1 Damage Identification Algorithms

The essence of global damage identification by looking at changes in the dynamic properties is that dynamic properties (natural frequencies, mode shapes and modal damping ratios) are functions of physical properties (mass, stiffness and damping) of a structure. Therefore, changes in physical properties manifested as drop in stiffness as a consequent of cracks, spalling, delamination, foundation settlement or loosing of a connection will induce measurable changes in dynamic properties (Doebling et al., 1998; Farrar et al., 2001a; Zhengsheng et al., 2005).

Dynamic testing of structures is nowadays a well-established methodology for SHM systems. Dynamic data collection and processing are significantly developed, thus the limitations of traditional visual monitoring method can be overcome. In the context of damage identification, the obtained structural response can be used in conjunction with several numerical methods, which can be grouped into two complementary main problems, namely inverse problem and forward problem. The first group methods rely on a reference structural model, e.g. FE model, where the changes in measurement results linked to the changes in the structural model. In a totally different direction, the second group methods use the changes in raw or processed vibration measurements to specify damage-sensitive characteristics. Thereafter, the characteristics are further utilised to detect different damage conditions by using proper Pattern Recognition (PR) algorithm.

The idea of a concatenated hierarchical structural damage identification problem was started in 1993 by Rytter in his PhD thesis when the damage status is clearly defined in four levels (Carden and Fanning, 2004; Farrar and Worden, 2007):

- Detection: is the damage present in the system (existence)?
- Localisation: where is the damage (location)?
- Quantification: what is the size of the damage (severity)?
- Prediction: what is the estimated residual safe-life of the system (prognosis)?

Similarly, the first three levels are summed under a general term referred to as diagnosis, while the last level of the damage identification is known as prognosis. Although the above-mentioned order addresses the main questions of a damage identification problem, further fifth level, classification level, was later inserted before the quantification level. Classification is important, if not vital, for effective identification at the quantification and prediction levels (Worden and Duijck, 2004). In addition, prediction level is distinguished from other levels in that it cannot be accomplished without an understanding of the physics of the damage, i.e. categorisation. Level 1, detection, is also distinguished making use of classification level, as the damage can be identified without previous knowledge on the behaviour of the system when it is damaged. In order to achieve this, a small divergence towards PR methods or machine learning is needed (Worden and Duijck, 2004).

The inverse problem or model-based methods address the first three levels of damage identification problem. This problem needs a reference structural model and the observed change in measured data is accounted to the physical system parameters. The numerical model is set such that it provides sensible agreement with the experimental results, hence the predicted updated model can be utilised to obtain the new physical changes.

The forward problem or non-model-based methods, on the other hand, satisfy the first level of damage identification task. This problem adopts a general statistical model of particular response signature, e.g. time-series analysis, and a relevant statistical algorithm on the extracted damage-sensitive features is applied to improve detection of damage. When data is available from both undamaged and damaged structures, the SPR algorithms will fall into the general title referred to as supervised learning.

Unsupervised learning refers to statistical algorithms that are applied to data where examples from the damaged structure are unavailable.

In the damage level respective, if statistical algorithms are applied in an unsupervised mode, they will typically be used to answer questions regarding the existence and location of damage. Yet, when they are applied in a supervised learning mode and coupled with analytical models, the statistical algorithms can further be used to determine the type and severity of damage (Figueiredo et al., 2009).

The human capacity to assess flooding real-time amounts of data is very limited, so Pattern Recognition (PR) methodologies need to be introduced into the procedure. The procedure scrutinises the incoming data and informs the operator of unusual events, but it will only be as good as the specification of what is meant by unusual (Wenzel, 2009). In a comparison form, Model-based damage identification scheme shares common steps with its counterpart, parameter-based identification scheme. These steps are illustrated in Figure 2.4.

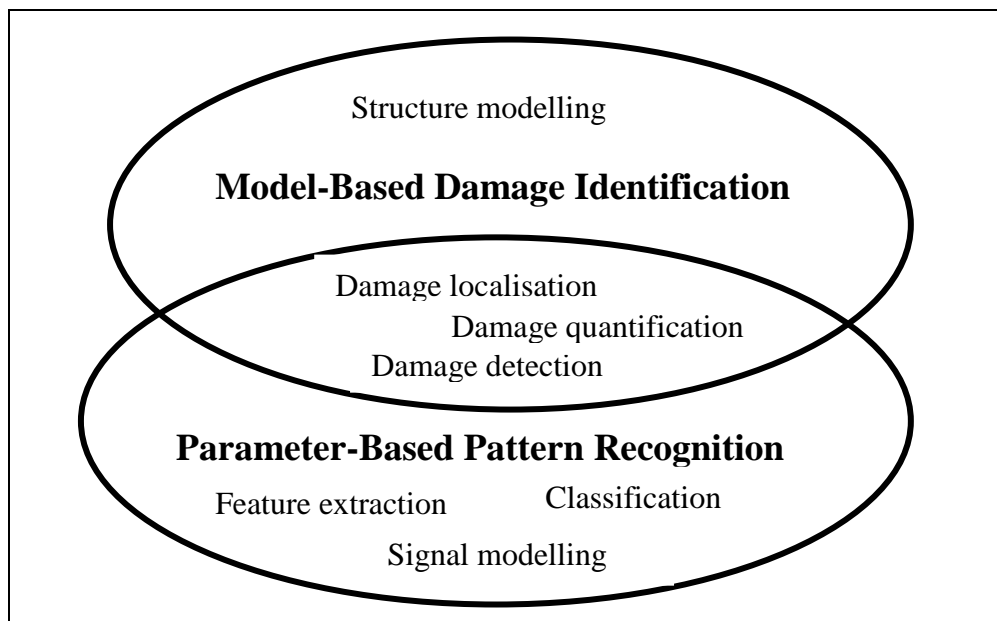


Figure 2.2: Basic steps in damage diagnosis algorithms.

2.3.2 Data Collection Systems

The data collection part of the SHM process entails selecting the quantities to be measured; the types of sensors to be used; the positions where the sensors to be placed;

the number, resolution and range of sensors; and the proper data acquisition, storage, and sampling hardware (Sohn et al., 2004).

In SHM systems, one of the major differences from NDE is that the sensors and actuators are embedded or surface mounted on the monitored structure (Balageas et al., 2006). Typically, SHM configuration is associated with online global damage identification, whereas NDE is usually carried out off-line in a local manner after damage has been located (Farrar and Worden, 2007). The ultimate intent of the SHM technology is to provide an unattended, automatic and reliable monitoring system that subjective human elements can be eliminated.

2.3.2.1 Wire-based SHM System

A conventional configuration of SHM system is to generally locate sensors throughout the structure and then wired to a central data acquisition device such as data logger. Figure 2.5 shows schematically the layout for such systems. The wired system has proved to be exceptionally reliable and practical; however, it experiences serious problems of its cables. This manifests in their cost, difficulty in deployment and noise infusion (Dae Kun Kwon et al., 2011).

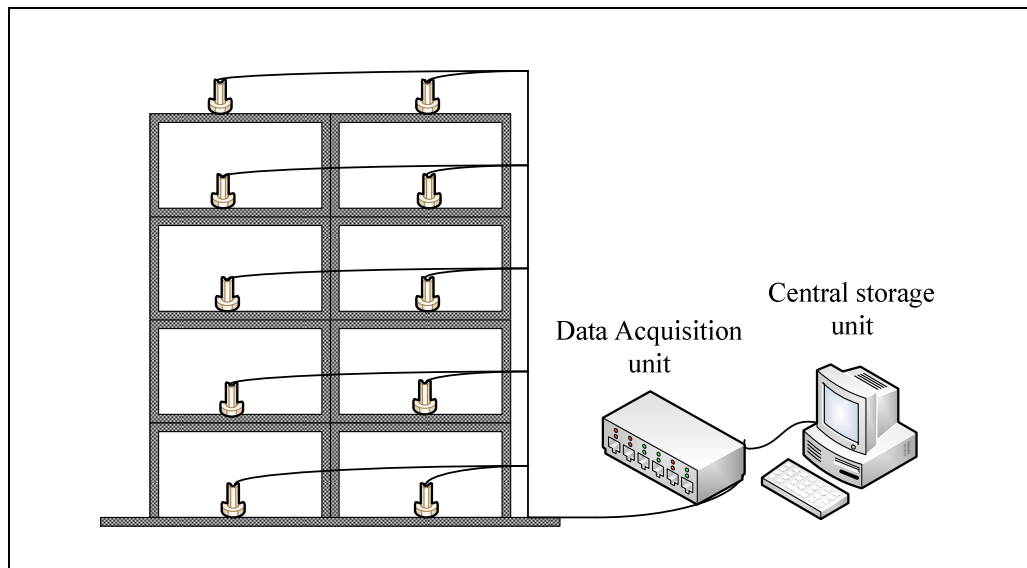


Figure 2.3: Typical configuration of a wire-based SHM system (after Wenzel, 2009).

2.3.2.2 Wireless SHM System

As a result of wire system shortcomings, recent developments invest in wireless sensing field. Dense sensor networks with computational and monitoring abilities at sensing venue can now be achieved. Figure 2.6 shows the architectural design for a wireless sensor network. A key aspect of such a network is its capacity to provide a finer sensing mesh, because the network is independent of multiple cables and is not limited by the number of channels existing in a data acquisition system (Wenzel, 2009).

In the wireless sensing units, each unit is accountable for three objectives: response data collection, storing and processing of the measurements, e.g. Fast Fourier Transformation (FFT), and eventually data transformation and communication within a specific open space range (Lynch, 2007). In the recent years, wireless sensor technology has quickly grown and been applied to a number of different engineering applications. In the context of structural monitoring systems, wireless communications joined with traditional sensors can considerably cut down the monitoring costs, whilst provided the functionality that does not exist in present conventional structural monitoring systems (Lynch, 2007).

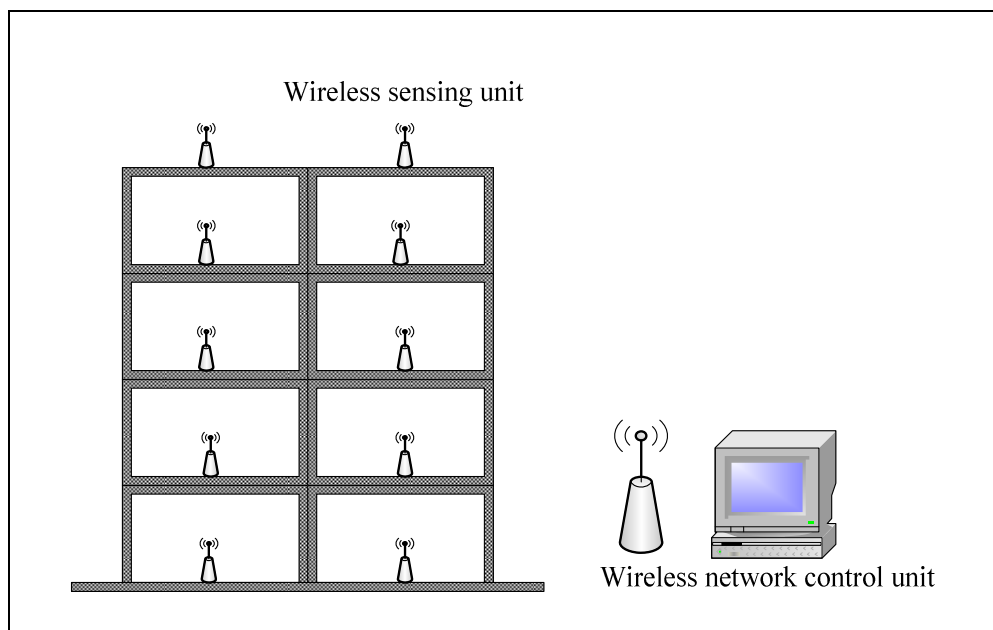


Figure 2.4: Typical configuration of a wireless SHM system (after Wenzel, 2009).

2.3.2.3 Network-based Sensing System

Having experienced limitation of radio band range, sensing technology has been taken further using modern networks installation of the building, e.g. Local Area Networks (LAN) and Internet. In this technology, the system is more reliable and sustainable than wireless systems, drawing both its power and communication paths from the existing infrastructure of the building (Dae Kun Kwon et al., 2011).

Most recent technology exploiting exist networks of a building provides optimal functionality of the wireless system, and implements data processing/extracting for permanent SHM. A centralised server conducts fundamental data acquisition and database management processes, whereas it also offers visualisation for the captured data that can be confidentially accessed through a web browser (Dae Kun Kwon et al., 2011). Conceptual configuration of the new smart sensing system is shown in Figure 2.7. This cutting edge technology, the Smartsync, has been installed in the world-tallest building, Burj Khalifa, and its performance has efficiently been confirmed in practical application (Dae Kun Kwon et al., 2011).

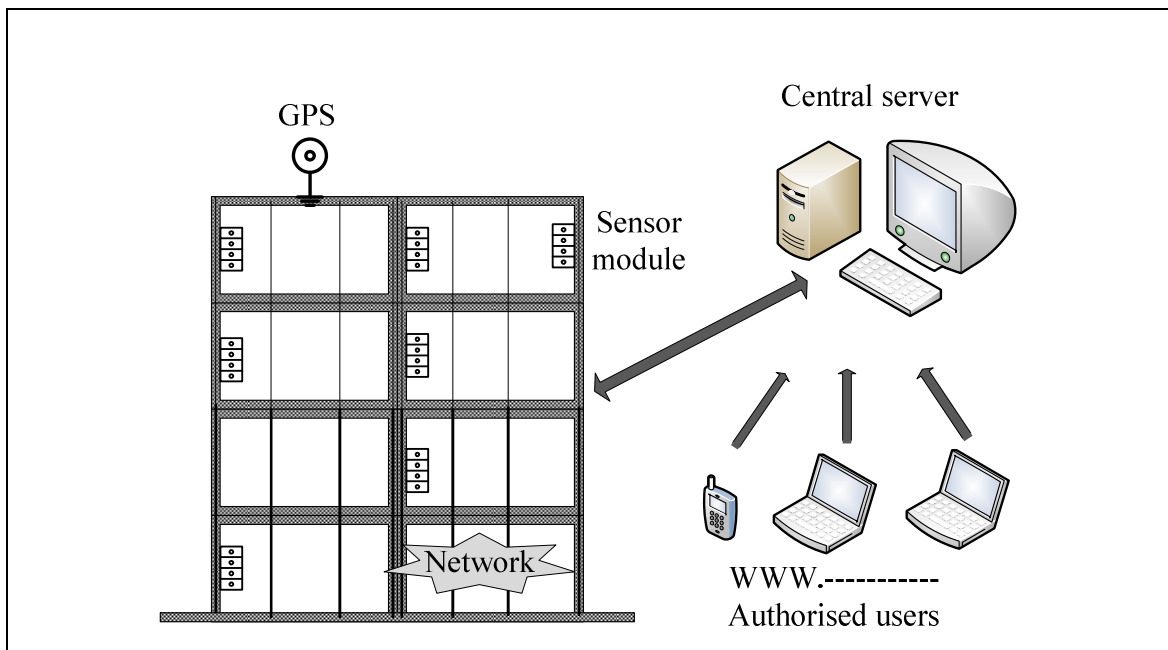


Figure 2.5: Typical configuration of a Smartsync SHM system (after Dae Kun Kwon et al., 2011).

2.4 Timeline of SHM: the Past, Present and Future

2.4.1 The Past Legacy

Primitive techniques of structural appraisal using vibration monitoring belong to thousands of years ago. Ringing sound of clay pots can reveal cracks, and tapping along the surface of an object can expose voids presence (Hearn and Testa, 1991).

In a methodical way, throughout the 1970s and 1980s, the oil industry stimulated the efforts to develop vibration-based damage identification methods so as to monitor offshore platforms. In order to circumvent the difficulties of the structure accessibility and mysterious damage location, a common methodology employed by this industry was to simulate various possible damage patterns with numerical models, determine the changes in resonant frequencies and correlate these changes with those measured on the top of a platform surface. Owing to the aggressive environmental effects coupled with a number of very practical operational difficulties, this technology was abandoned for offshore platforms in the early 1980s (Farrar and Worden, 2007).

In conjunction with the development of the space shuttle, the aerospace industries began to study the use of vibration-based damage identification during the late 1970s and early 1980s. This work was continued with current applications being investigated for the National Aeronautical and Space Administration (NASA) space station and further for design of reusable launch vehicles (Farrar and Worden, 2007). Currently, vibration testing of prototype structures is an essential model-based design tool used in everyday design in the automotive and aerospace industries (Pavic et al., 1997).

2.4.1.1 Pioneered Technical Research on Vibration-based Monitoring

The subject of vibration-based damage identification was started in the offshore industry as a forward problem. However, enormous amount of research was shortly endeavoured to generalise this technology to other applications suffer similar problems as those in the offshore structures. In the early investigations of the problem, only changes in the basic modal properties, which are resonant frequencies, modal damping ratios and mode shapes, were considered in damage diagnosis.

SHM has received considerable consideration in the technical literature, where there has been an intensive effort to develop a reliable mathematical and physical foundation for this technology. Comprehensive literature reviews on methods that have been proposed for civil, aerospace and mechanical structures were cited by Doebling et al., 1996; Doebling et al., 1998; Sohn et al., 2004; Carden and Fanning, 2004.

According to Doebling et al. review (1996), the first journal article on damage detection using vibration data dates back to 1969, when Lifshitz and Rotem detected the onset of unbonding in composite materials. They looked at the changes in the dynamic moduli and damping, which can be related to the frequency shift, as indicating damage in particle filled elastomers (Lifshitz and Rotem, 1969).

Vandiver pioneered the era of damage detection using vibration data in 1975 and 1977 by examining the change in the frequencies associated with the first two bending modes and first torsional mode of an offshore light station tower to identify damage (Doebling et al., 1996; Vandiver, 1977).

The use of changes in modal frequencies to detect damage, as an inverse problem, was started by Cawley and Adams in 1979. They proposed a method for locating the site of damage in a composite materials by correlating the changes in measured frequency of pairs of modes with the changes in calculated frequency of the same modes (Cawley and Adams, 1979).

In RC research practice, Chowdhry and Ramirez used in 1992 the impact modal test to identify damage in reinforced and plain concrete beam samples. The damage was simulated as delaminations and cracks, and changes in resonance frequencies as well as power spectra were used to detect the damage (Doebling et al., 1996).

The dynamic response methods have been recognised by British Standards since 1986 as a Non-Destructive Testing (NDT) method for assessment of structural integrity and remaining service life, fault finding, assessment of the need for repairs and identification of defects (BS 1881, 1986). According to British Standards, the dynamic response might be used to predict stiffness and other structural properties whereby the approach is most fully developed for integrity testing of piles.

In an early study on damping for damage detection, Salane and Baldwin conducted vibration tests on a laboratory-scale bridge model as well as a full-scale highway bridge in 1990. They concluded that changes in damping ratios can detect occurrence of damage. In the laboratory model, damping ratios decreased when the damage was produced, but initially damping increased and subsequently decreased in the full-scale bridge (Williams and Salawu 1997).

Mode shape measurements for the location of structural damage without the use of a prior FE model was possibly first presented by West in 1984 (Doebbling et al., 1996). The author used the Modal Assurance Criterion (MAC) to determine the degree of correlation between modes from the test of an undamaged Space Shuttle body flap and the modes from the test of the flap after it has been subjected to acoustic loading. The mode shapes were partitioned using various schemes and the change in MAC across the different partitioning techniques was used to localise the structural damage (Doebbling et al., 1996).

To the knowledge of Samman and Biswas (1994), the first field application of vibration testing as an NDE method for structures was done by Anifantis et al. (1983). In this work, the damage in an industrial building induced by an earthquake was assessed.

In full-scale RC structure context, Kato and Shimada performed vibration measurements on an existing prestressed concrete bridge during a failure test in 1986. The change of vibration characteristics due to deterioration of the bridge during the failure test was obtained. Moreover, a measured mechanism on the change of vibration characteristics is compared with a numerical analysis. Reductions in natural frequencies were detected as the statically applied load approached the ultimate load; however, damping values were largely unaffected. The ambient vibration method of system identification was used (Kato and Shimada, 1986).

During the last two decades, enormous amount of research was done utilising derivations and formulations of the basic modal parameters in order to suggest a comprehensive damage identification model. Elaborated review for the distinctive methods is presented in the next Chapter of this thesis (Chapter 3).

Inasmuch as all vibration-based damage diagnosis processes rely on experimental measurements with basic uncertainties, many researchers have opted to statistical analysis procedures. These methods depend on the signatures obtained from vibration response data recorded at sensing points in order to obtain features that are sensitive to the presence of damage. A statistical pattern classification algorithm for SHM of civil structures was first proposed by Sohn and Farrar in 2001 (Wenzel, 2009).

2.4.2 The Present Assets in Structural Health Monitoring

2.4.2.1 Overview

Present-day SHM, in general, along with vibration-based monitoring, in particular, are well-established practice in civil engineering with a significant accumulated knowledge in both technical literature and applications. In conjunction with all deficiencies of other manual inspections, and over 30 years on the birth of adaptation vibration monitoring, the technology is increasingly used in condition monitoring industry, mainly since the early 1990s. In the last two decades, a great deal of research and publication has been done in the area of SHM. Also, the area has witnessed a great increase of SHM methods, with long-term monitoring systems applied on bridges in United States, Europe and Asia. This provides a sound level of theoretical knowledge and practical experience that will take SHM for further level of development (Carden and Brownjohn, 2008).

Transportation infrastructure, because of its importance as a key utility of the society, is the subject of several SHM initiatives in many countries. Several major research programmes are dedicated to this subject in the European Union. As an example, Sustainable Bridges is a project that assesses the railway bridges to satisfy the needs of the 2020 situation and provides the means for up-grading them if they are inappropriate (Casas, 2006). In Japan, the attention has moved from new construction to the maintenance and management programme. The programme involves huge activities, tests and proposals to improve the management of bridges. In Korea, subsequent to the collapse of the Sung-Su Bridge in 1994, the government carried out safety inspections covering most major bridges constructed until that time in an effort to assess their capacity and estimate the required repair or supplement (Sung-Pil Chang,

2006). In China, latest collapses have activated a national bridge programme dedicated to improve the safety and performance level of the bridges nationwide (Wenzel, 2009). In Eastern Asian countries, predominant requirements have mandated the companies that construct the bridges to periodically monitor and persistently confirm their structural health (Farrar et al., 2001a; Worden and Farrar, 2007).

2.4.2.2 Assessment and Monitoring Standards and Guidelines

In the context of condition assessment, many European countries (such as France, Germany, Italy, Poland and Spain) have no specific guidance for condition and safety assessment of highway bridges. In their assessment practice, design requirements of new bridges are commonly applicable for this purpose (Casas, 2006). Reduction is disallowed in the individual assessment safety levels compared with design in Germany. Such regulations and standards do not exist in Asian and South American countries. Few countries such as UK, Denmark, USA and Canada are using specific guidelines or standards for structural safety assessment of highway bridges (Casas, 2006).

There is an agreement that the most efficient assessment process is based on the application of different and gradually sophisticated assessment levels. A five-level model is presented in Bridge Management in Europe (BRIME) as a preparation to set guidelines for the assessment of structures. The lowest level of the scheme, Level 1, is the simplest and uses Load and Resistance Factor Design (LRFD) analysis, load combinations and partial factors as in design code. However, the most complicated level, Level 5, entails strength model including probability distribution for all variables (Casas, 2006).

In the context of the SHM, the implementation of new automated technologies needs a clear requirement and motivation to be accepted by owners and operators. Before a breakthrough in the implementation of new technologies can happen, the requirements and motivation have to be clearly understood and argued with the potential clients. One of the motivations to accept and apply these services is that the new technologies should be liable by the means of standard applications supported by codes, standards and guidelines (Wenzel, 2009). A most useful standard on SHM, particularly for bridges,

has been elaborated in the European-based Structural Assessment Monitoring and Control (SAMCO) network (Wenzel, 2009).

Another research project devoted to the same task is AMADEUS (Accurate Modelling and Damage Detection in the High Safety and Cost Structures) project funded by the Commission of the European Union. The ultimate engineering objective of AMADEUS is to develop methods, guidelines and procedures for routine, non-destructive, in-service maintenance, health monitoring, and damage detection in structures (Sohn et al., 2004).

2.4.2.3 Supplement Software Related to Structural Health monitoring

One of the widely used monitoring software is BRIMOS[®] (Bridge Monitoring System), which is a rating assessment system using vibration data. In BRIMOS[®], full scale experimental vibration measurements are merged with numerical model updating to provide a comprehensive understanding of a structural integrity. The classification output result is a factor out of five different rating risk levels based on various parameters such as measurement of eigenfrequencies; mode shapes; damping ratios; dynamic displacement; visual inspection information; FE model update; and reference data (Wenzel, 2009). After an experimental investigation consisting of data acquisition through the BRIMOS[®] Recorder and modal information extraction through the BRIMOS[®] software, the structural indicators obtained are used as input for the updating procedures.

As a numerical framework, the updating procedures are performed by using VCUPDATE[®] software, a structural assessment through FE Model Updating. In this analysis, the FE approximation of the real structure is brought closer to the real measured model by using the experimental measurements so as to produce a more reliable model and a shift in properties, related to damage, can be captured (Wenzel, 2009).

The knowledge of AMADEUS project is integrated into an independent PC-based expert system to help conducting in place structural assessment. In the development of the system three main advances will be made in various technical fields. For example,

advances is made in fatigue life prediction of structures as well as a computer program called MODPLAN is implemented to determine the best measurement, suspension, and excitation points to be used during the modal testing of structures. Finally, various damage detection criteria are considered (Sohn et al., 2004).

The previous software exemplifies identification systems that used the vibration measurements as basis for damage characterisation. On the other hand, other software such as PONTIS, commercial bridge management system represents the conventional assessment of the structure starting with a visual field inspection that provides a subjective impression of the condition of the structure. Some preliminary analytical investigations are performed in order to provide a rating as a basis for decisions. It is one of the popular tools for bridge managements that developed by American Association of State Highway and Transportation Office (AASHTO) since 1989. The PONTIS system assists in achieving information of inspection databases about bridge networks. Additionally, PONTIS comprises several modelling techniques that quantify decision making process and address knowledge gaps in many bridge management procedures (Ettouney and Alampalli, 2012).

2.4.3 The Future of Structural Health Monitoring

Despite the shortcomings of the manual inspection systems, the current available automatic monitoring technologies are not widely being accepted. Obstacles such as uniqueness of each civil engineering structure; the systems are still unverified, expensive and non-compulsory by law; and the unavailability of the guide standards make the methods impractical (Wenzel, 2009). There is an increasing gap between the theory and practice that must be bridged before the implementation of these techniques becomes broader (Catbas et al., 2006). However, the need for replacing the manual inspection systems by an automatic monitoring seems vibrant. In order to address the challenges deter popularisation of the new systems, effective initiatives have been taking place around the world.

Federal Highway Agency (FHWA) commenced in 2005 the Long-Term Bridge Performance (LTBP) program of research and development to address these needs. The LTBP program is an aspirant 20 year (2005–2025) research effort, which is planned to

achieve specific short- and long-term objectives (Wenzel, 2009). The programme will encompass detailed inspection; periodic testing and assessment; continuous monitoring and forensic investigation of representative case studies of bridges all over the USA in order to monitor and document their performance. An overall of 2000 bridges ought to be monitored and partially searched by forensic engineering after they are decommissioned (Wenzel, 2009).

Some European countries have developed standards, guidelines and codes for the evaluation of existing civil structures, Structural Assessment, Monitoring and Control (SAMCO). The SAMCO network spans the whole of Europe and covers various communities of interests. The network joins construction companies, bridge-owners and managers, railway consultants, road authorities, equipment suppliers, monitoring experts, research institutions, housing authorities, universities, and so on. Programmes like this and the SAMCO guideline on bridge monitoring and assessment will provide the bases needed for the increasing future application of reliable methods in bridge assessment (Wenzel, 2009).

The Republic of Korea has begun a 10-year bridge SHM, which methodically addresses major field activities including a real track test for three bridges. The programme organised at the Seoul National University, where invaluable data and methodologies are generated. In Japan, the maintenance and management programmes of current structures have drawn the interest rather than construction of new projects. Immense programmes, tests and initiatives are included to develop the management of bridges (Wenzel, 2009).

The best known pioneer monitoring programme has been set in Hong Kong. This programme has been established for more than 10 years with a number of major monitoring systems in place. The programme with its special size produces important data that can be employed in the development of codes and guidelines for the design of major structures (Wenzel, 2009).

A vivid future can be expected for the monitoring industry, although it is not easy to estimate the time the development will take. The monitoring subject is now taken to completely digital database solutions, and real-time measurements in automatic

updating information will be available for every structure. Furthermore, any data set of monitoring process or other operation programmes will be available and accessible through the internet. In this respect, monitoring processes would be generally automated and the structural condition will constantly be scrutinised. At this stage, there is no longer needed to disagree about the importance of SHM industry of bridges. The first integrated SHM systems possibly will be conducted and operated by 2020 (Wenzel, 2009).

2.5 Summary

The failure or close to failure events of civil engineering infrastructure and the need for more reliable automated monitoring system have dedicated to study the application of global vibration-based monitoring methods. The replacement of current manual NDT techniques by an effective universal system is ahead of the curve of civil engineering communities. By developing such reliable intelligent systems, structures will be designed to work within the safety margin without a need to extended period of inspection.

SHM systems have been developed over many years and are now ingrained and distinctive area of theoretical and applied research on damage identification and structural monitoring. Many techniques, methodologies and approaches have been developed over the past 30 years as a wide diversity of damage identification methods (Staszewski and Robertson, 2007). Nonetheless, there is an increasing gap between the theory and the practice that must be bridged before the implementation of these techniques becomes wider. The delay in the implementation of the technology is accounted partially to the insufficient evaluation and validation of these techniques in real civil engineering applications (Catbas et al., 2006). Accordingly, it is sensible for civil engineering practitioners to become more familiar with the vibration of structures, including the use of Experimental Modal Analysis (EMA) as an indispensable testing tool for assessing the vibration performance of existing structures.

It is expected that the structural condition monitoring will witness integrated SHM systems to be possibly implemented and operated by 2020 (Wenzel, 2009). By that

time, systems will offer automated online monitoring thereby problems will be diagnosed, operator informed and action taken as part of the SHM system.

3. Technical Literature Review

3.1 Introduction

In the early studies of the subject of damage characterisation, only changes in basic modal data, which are resonant frequencies, modal damping ratios and mode shapes, have been considered. Then, the last two decades have witnessed considerable efforts on research and publications that a large number of monitoring paradigms have been put forward (Carden and Brownjohn, 2008).

Extensive literature surveys on damage identification methodologies were presented by Carden and Fanning (2004), Doebling et al. (1996) and Sohn et al. (2004). Most of the covered literature explored detection, localisation, classification and quantification of damage in laboratory samples or simulated damage in field structures scheduled for demolition (Carden and Fanning, 2004). Estimation of the remaining life of the structures has not received enough focus in the literature studies, although it is the final target in any identification process. In this Chapter, the researcher focused on the ingrained methods in both types of damage identification practice: the model-based type and the parameter-based type. More attention in this presentation was allocated to the method and its merits, rather than mentioning publications utilised that method. Notwithstanding this respect, the up-to-date as well as salient publications linked with each approach were referred to in the context of each method.

3.2 Damage Identification using Basic Modal Parameters

Basically, the reduction in modal frequencies and the increase in modal damping ratios as global vibration parameters only detect the occurrence of damage. Even though major limitations are associated with their use for advanced investigations, they may be utilised as appropriate thresholds to generate more detailed analysis. However, the rather low sensitivity of frequency shifts to small levels of damage besides inaccurate experimental measurements of modal damping have weakened using the modal parameters for damage identification (Williams and Salawu, 1997).

As a result, mode shape information is included to individually locate the damage (Teughels and De Roeck, 2004; Wang et al., 2007). From vibration theory, reduction in stiffness is associated with modification of the modes of vibration of a structure. Vibration mode shapes can be influenced by local damage and offer a better means for location of damage (Salawu and Williams, 1994). Mode shapes are spatially distributed quantities and, hence, provide information that can be used to locate the damage (Farrar et al., 2001a). Therefore, mode shapes along with their formulations such as the difference between scaled mode shapes and the relative difference methods are included in damage location process. However, modal displacements are somewhat insensitive to slight local changes in the stiffness of a section (Maeck and De Roeck, 1999; Pandey et al., 1991). Moreover, displacement of multiple damage sites usually is difficult, if not impossible, to be efficiently used for most damage location techniques (Salawu and Williams, 1994). Furthermore, the sensitivity of the Modal Assurance Criterion (MAC) together with a number of its formulations as other expressions for mode shapes depends very much on the nature of the damage. If the damage is distributed, such as widespread distributed cracking in concrete members, the mode shape may change slightly, although the frequency will considerably decrease. On the other hand, localised damage may result in large reductions in the MAC values (Yeung and Smith, 2005). Additionally, any differences in MAC and Coordinate Modal Assurance Criterion (COMAC) calculations are averaged and spread over all measurement points in the case of MAC or over all mode shapes in the case of COMAC (Pandey et al., 1991). In brief, the modal parameters are found to be inconsistent in providing credible condition assessment of a structure (Bayissa, 2007).

3.3 Development of Damage Identification Paradigms

Owing to the limitations associated with using the fundamental modal parameters in damage identification, many researchers have switched to alternative sensitive parameters, including combinations of modal parameters and/or FRFs, and their derived adaptations as possible successful damage identification formulae.

Numerical methods based on the FE model updating for iterative methods or non-iterative methods are both used along with damaged or possibly damaged structures in

the linear stage. These methods, which are based on changes in experimentally measured and/or predicted flexibility and stiffness, are capable of determining the presence of damage, locate that damage and quantify its severity. However, the problem with these methods is that they are all linear models (Doebbling et al., 1996). In addition, there are some inherent difficulties in the application of model-based methods in the damage identification problem. For example, uncertainties, measurements of noise and lack of sensitivity of damage are all common problems produce singular ill-conditioning problem, which can lead to large discrepancies in the model parameters (Vanik et al., 2000). Meanwhile, the incomplete set of measured data requires extra information from the FE model in order to identify damage location. As a result, there will definitely be errors even in the model of the undamaged structure (Friswell and Penny, 1997).

Conversely, the development of the methods that enhance the ability to include the nonlinear structural effects has the potential to significantly expand the subject of damage identification (Doebbling et al., 1996). This need evokes more use of Statistical Pattern Recognition (SPR) methods together with the experimentally measured dynamic data to account for the occurrence of damage and estimate its impact.

Figure 3.1 shows both types of methods reviewed in this Chapter: inverse (model-based) methods and forward (parameter-based) methods, together with the main aspects associated with each class.

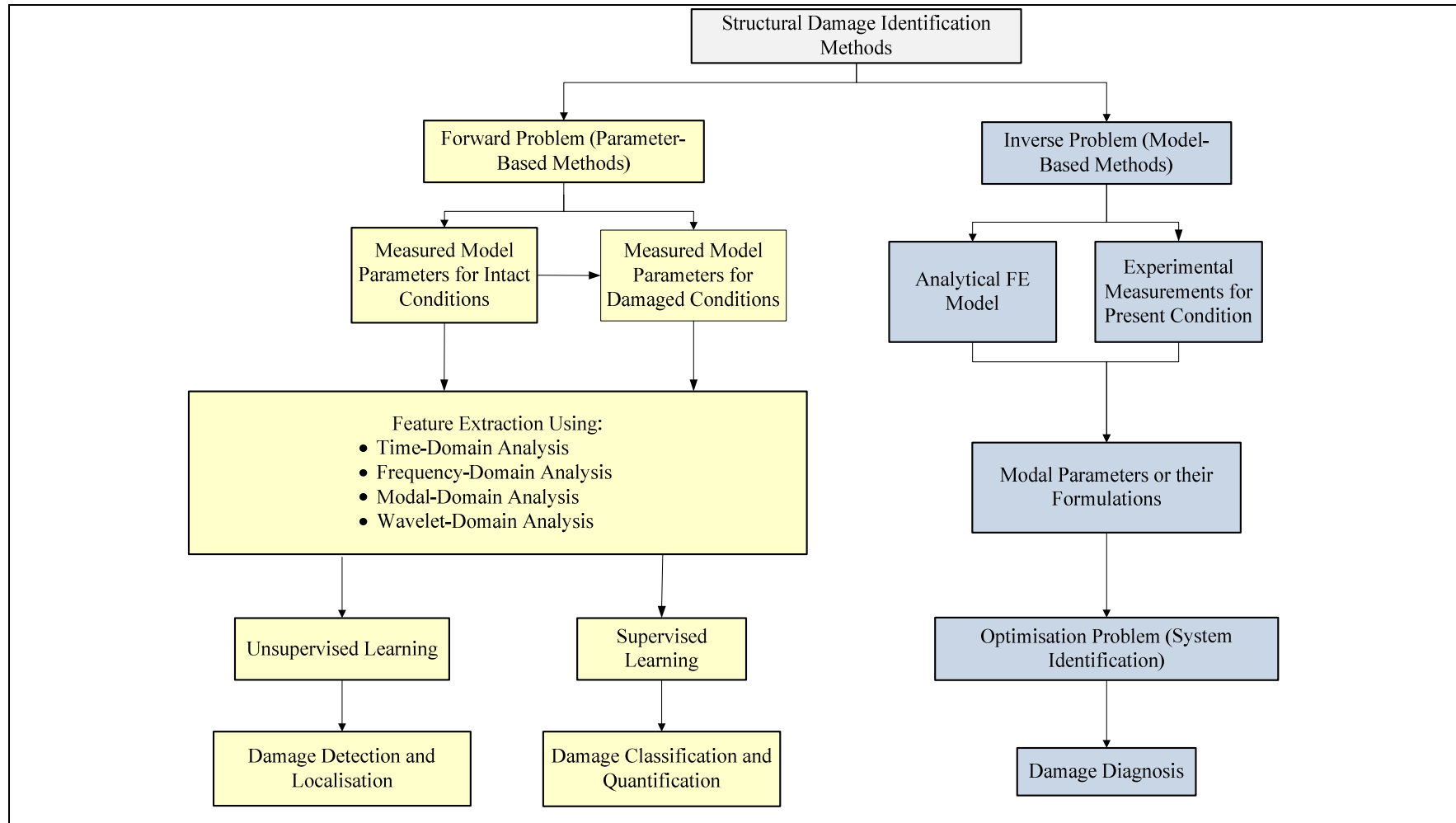


Figure 3.1: Flow chart for structural damage identification methods.

3.4 Model-based Damage Identification Methods (Inverse Problem)

This first group of methods treats the subject of damage identification as an inverse problem. In this respect, the availability of a mathematical reference model for the structure is at the heart of the system in that way the perturbation in measured vibration data can be compared and accounted to the changes in this model.

3.4.1 Mode Shape Curvature/Strain Mode Shape Changes

As an alternative of using mode shapes to obtain spatial information about damage, mode shape derivatives such as the curvature is applied. The use of changes in curvatures to locate damage relies on the fact that the maximum change in a mode shape arises in the region of the defect. Only curvature mode shape can give an indication of multiple damage locations (Salawu and Williams, 1994). This idea is driven by the fact that the second derivative of a mode shape is considerably more sensitive to small defects in the structure than is the mode shape itself (Farrar et al., 2001a).

Pandey et al. (1991) initiated that concept of using absolute changes in mode shape curvature as a good indicator of reduction in the value of flexural stiffness (EI) of beam cross-sections. The curvature at any point of a beam element (y'') is given as:

$$y'' = \frac{M}{EI} \quad (3.1)$$

Where:

M is the bending moment at the point

Additionally, the curvature of continuous deflection mode shape is approximately computed using the central difference, which can be written as:

$$y'' = \frac{y_{i+1} - 2y_i + y_{i-1}}{(\Delta x)^2} \quad (3.2)$$

Where:

Δx is the length of the element

y'' is the displacement mode shape at a specific position (i)

It is generally experienced that the numerical computation of the second-order derivative curves involves problems when the data is noisy. In order to alleviate rough curvatures, Maeck in his PhD thesis in 2003 used Lagrange interpolation polynomial to calculate the second-order derivatives. This methodology helps to avoid spiky and noisy curvatures, and the curvature is smoothed by a means of regularisation methods (Balageas et al., 2006).

3.4.2 Damage Detection using Non-iterative Modal Flexibility Methods

Pandey and Biswas (1994) used the complete mode shapes and natural frequencies for the damaged and undamaged cases to identify both the location and amount of damage by approximating the flexibility matrices before and after occurrence of damage, $[f]$ and $[f^*]$, respectively. This method is known as Modal Flexibility (MF), in which the flexibility matrices can be approximated from the modal data as defined in Equations 3.3 and 3.4 below:

$$[f] \approx \sum_{r=1}^m \frac{\{\varphi_r\}\{\varphi_r\}^T}{\omega_r^2} \quad (3.3)$$

$$[f^*] \approx \sum_{r=1}^m \frac{\{\varphi_r^*\}\{\varphi_r^*\}^T}{\omega_r^{*2}} \quad (3.4)$$

Where:

ω_r is the natural frequency of r^{th} mode of vibration

$\{\varphi_r\}$ is the r^{th} mode shape vector

m is the number of measured modes; and the asterisks signify properties of the damaged structure

From the pre-damage and post-damage flexibility matrices, a measure of the flexibility change caused by the damage can be obtained from the difference of the respective matrices as defined in Equation 3.5:

$$[\Delta f] = [f] - [f^*] \quad (3.5)$$

Where:

$[\Delta f]$ is the change in the flexibility matrix

Each column of this matrix is processed to obtain the absolute maximum value (δ_j) of the elements in that column, which can be written as (Pandey and Biswas, 1994):

$$\delta_j = \max |\delta_{ij}| \quad (3.6)$$

Where:

δ_{ij} are the elements of the matrix $[\Delta f]$, and δ_j is taken to be a measure of the flexibility change at each measurement position, j

The column of the flexibility matrix corresponding to the largest change is indicative of the Degree Of Freedom (DOF) where the damage is located.

This method requires that the experimental modal properties to be complete and consistent with the analytical modal model. Therefore, the expansion analytical procedures would be applied to the incomplete measured mode shape vectors (m), and defined at (n) DOFs. Flexibility matrix outperforms its counterpart stiffness matrix as it converges quickly with limited number of modes and, hence, can sensibly be obtained from relatively a small number of low modes of vibration (Pandey and Biswas, 1994).

In 1998, the method was used by Farrar and Jauregui in an extensive comparative study to assess simulated fatigue cracks in steel girders of the decommissioned I-40 Bridge over the Rio Grande in Albuquerque, New Mexico (Farrar and Jauregui, 1998).

Moreover, the MF approach is further developed to what is known as the Uniform Load Surface (ULS) and its curvature. The coefficients of the i^{th} column of the modal flexibility matrix represent the deformation at i^{th} DOF of a structure due to a unit load

vector. The multiplication of the flexibility matrix by a virtual unit load vector, applied at all DOFs, represents the deflected shape of the structure, and referred to as the uniform load surface (ULS) as given in Equation 3.7.

$$ULS_i = \sum_{j=1}^n f_{ij} = \sum_{j=1}^n \left[\sum_{r=1}^m \frac{\varphi_r^j \varphi_r^i}{\omega_r^2} \right] \quad (3.7)$$

Where:

ULS_i is the uniform load surface at point i due to a virtual uniform load at (n) DOFs

f_{ij} is the MF at DOF (i) due to an excitation force at DOF (j)

φ_r^i, φ_r^j are the mass-normalised modal elements for mode (r) at DOFs (i) and (j)

Zhang and Aktan (1995) used the changes in the curvatures of ULS before and after damage to locate that damage (Doebbling et al., 1996).

Zhang and Aktan (1995) suggested the use of deflections due to a virtual unit load vector as a way to study the modal convergence criteria based on MF of the structure. This method was utilised later to calibrate FE model. In their proposal, the deflected shape vector $\{\delta\}$ of a structure under a unit load vector $\{F\}$ was given in Equation 3.8:

$$\{\delta\} = [f]\{F\} \quad (3.8)$$

Wu and Law (2004) extended the ULS curvature approach further for two dimensional plate structures. In their proposal, a new approach to compute the ULS curvature is suggested based on the Chebyshev polynomial approximation, instead of the central difference method.

Zhengsheng et al. (2005) used the MF concept to study a quantitative measure of the contribution of different modes to the general dynamic response of steel bridges in the state of Ohio. A series of contribution coefficients are proposed to identify which modes are most proper in the process of modal testing and FE model calibration.

Catbas et al. (2006) discussed the use of pseudo-flexibility where it is unfeasible to excite very large structures such as long-span bridges. In their proposal, only output response tests, known as ambient vibration tests, are exploited as practical and common investigation in the real-life. The structure is excited by ambient excitations due to traffic, wind, etc. and the concept of the pseudo-flexibility matrix is implemented on data sets collected from the full-size Z24 benchmark Bridge in Switzerland. The MF matrix obtained from the measurements is incomplete when the test grid is spatially truncated. In order to eliminate the contribution of the unmeasured parts in the modal flexibility, these parts are to be multiplied by zero load vectors as there is no load on these locations. As a result, displacement profiles obtained from this computation do not require the contribution of the flexibility coefficients, which are not measured. The authors suggested practical approaches for common problems in damage detection and condition assessment of real structures. For example, problems such as environmental effects on vibration measurements, incomplete vibration measurements and condensed spatial measurement grid are addressed. Finally, the proposed approaches were applied to two real-life decommissioned highway bridges, which are Seymour Steel Stringer Bridge, Cincinnati, Ohio and Z24 Posttensioned Concrete Bridge, Switzerland.

3.4.3 Strain-energy-based Damage Indicator Method

In their statistical-based algorithm, Stubbs et al. (1995) utilised the modal strain energy as a feature-sensitive indicator to locate the damage in beam-like structures. In this method, the total strain energy in Euler-Bernoulli beam (U_L) can be determined by integrating the strain energy over the entire beam length as:

$$U_L = \frac{1}{2} \int_0^L EI[y''(x)]^2 dx \quad (3.9)$$

The shear deformation in this model is neglected, and the strain energy of an infinitesimal element (Δl) of the beam is given by:

$$U_{\Delta l} = \frac{1}{2} \int_0^{\Delta l} EI [y''(x)]^2 dx \quad (3.10)$$

However, to determine the modal strain energy, the general static deflection shape (y) is to be replaced by the continuous mode shape $\varphi_i(x)$. Therefore, the modal strain energy of the entire beam ($U_{L,i}$) and of an element of that beam ($U_{\Delta l,i}$) are written as:

$$U_{L,i} = \frac{1}{2} \int_0^L EI \varphi_i''(x)^2 dx \quad (3.11)$$

$$U_{\Delta l,i} = \frac{1}{2} \int_0^{\Delta l} EI \varphi_i''(x)^2 dx \quad (3.12)$$

Defining the ratios of the element strain energy to the total beam strain energy for the undamaged (u) and damaged (d) states, and are described as (Stubbs et al., 1995):

$$F_{i,\Delta l}^u = U_{i,\Delta l}^u / U_{i,L}^u \quad (3.13)$$

$$F_{i,\Delta l}^d = U_{i,\Delta l}^d / U_{i,L}^d \quad (3.14)$$

Obviously, the summation of strain energy ratios over all elements can be obtained as (Stubbs et al., 1995):

$$\sum_{\Delta l} F_{i,\Delta l}^u = 1 \quad (3.15)$$

and

$$\sum_{\Delta l} F_{i,\Delta l}^d = 1 \quad (3.16)$$

If the ratios of the element strain energy are assumed to be very small ($F_{i,\Delta l}^u \ll 1$ and $F_{i,\Delta l}^d \ll 1$), the following condition can approximately be established (Stubbs et al., 1995):

$$F_{i,\Delta l}^u + 1 \cong F_{i,\Delta l}^d + 1 \quad (3.17)$$

Substituting Equations 3.13 and 3.14 into Equation 3.17 yields:

$$\left(\frac{U_{i,L}^d + U_{i,\Delta l}^d}{U_{i,L}^u + U_{i,\Delta l}^u} \right) \frac{U_{i,L}^u}{U_{i,L}^d} = 1 \quad (3.18)$$

By making some further assumptions, Stubbs et al. (1995) developed the following formula for damage location indicator ($\beta_{i,\Delta l}$):

$$\begin{aligned} \beta_{i,\Delta l} &= \frac{EI_{\Delta l}^u}{EI_{\Delta l}^d} = \frac{\int_0^{\Delta l} [\varphi^{d''}(x)]^2 dx + \int_0^L [\varphi^{d''}(x)]^2 dx}{\int_0^{\Delta l} [\varphi^{u''}(x)]^2 dx + \int_0^L [\varphi^{u''}(x)]^2 dx} \frac{\int_0^L [\varphi^{u''}(x)]^2 dx}{\int_0^L [\varphi^{d''}(x)]^2 dx} \\ &= \frac{Numerator_{i,\Delta l}}{Denominator_{i,\Delta l}} \end{aligned} \quad (3.19)$$

To account for all measured modes, a single indicator for an element at particular location (β_j) is given as:

$$\beta_j = \frac{\sum_i Numerator}{\sum_i Denominator} \quad (3.20)$$

The damage indicator values are then to be standardised, by subtracting the mean value (μ) and dividing the result on the standard deviation (σ) as:

$$Z_j = \frac{\beta_j - \mu}{\sigma} \quad (3.21)$$

In the next step, a statistical algorithm was developed to classify the Z_j indicators into damaged and undamaged locations (Stubbs et al., 1995).

The use of modal strain energy has some remarkable advantages, which include using only a small number of mode shapes, and damping and frequency information are not needed. Additionally, multiple damage sites can be localised without solving a system of equations. Although the theory of damage localisation is started in beam structures, the approach is further generalised to plate structures by Cornwell et al. in 1999. In their methodology, plate-like structures are modelled by a two dimensional curvature, and the model is verified by using data from simulated FE plate model and experimental laboratory-scale aluminium plate (Cornwell et al., 1999).

Once again, however, it is commonly recognised that the numerical formulation of the second-order curvatures from the measured mode shapes involves problems of noise and lack of smoothness. This approach needs a dense measurement grid points with a high level of control, where it is unlikely to be practical in real structures.

3.4.4 Model Updating Methods

3.4.4.1 General

Model updating method is a process by which an incomplete modal model from test measurements is described in term of meaningful physical quantities. The objective of model updating is to adjust the stiffness, mass and damping matrices of a numerical model so as to bring the system to a better agreement with the test results.

Since the damage in a system is an intentional or unintentional change to the material and geometric properties, which affects the system performance, parameter distributions obtained as outcomes of updating process can provide useful information about the possible structural damage (Mordini et al., 2007). Basically, FE model updating in an inverse problem used to identify and correct uncertain parameters of FE predicted model, and it is usually treated as an optimisation problem. In a model updating process, not only a satisfactory correlation is required between analytical and experimental results, but also the updated parameters should preserve the physical significance (Jaishi and Ren, 2007).

In general, the FE model updating methods may be divided into two groups: the non-iterative (direct) methods and iterative (sensitivity) methods. In the non-iterative methods, the elements of stiffness and mass matrices are directly updated using one-step procedures (Jaishi and Ren, 2007). The resulting updated matrices reproduce the measured structural modal properties exactly but do not generally maintain structural connectivity, and the corrections suggested are not always physically meaningful (Jaishi and Ren, 2005).

On the other hand, methods in the sensitivity group are generally iterative and, per se, need more computational effort. However, to balance this disadvantage, they operate with incomplete mode shape vectors (Ewins, 2000).

3.4.4.2 Direct Finite Element Model Updating Methods

FE model updating, which belongs to the class of inverse problem in structural damage identification, is used to detect, locate and quantify damage. Primarily, the model updating techniques intend to minimise the differences between the eigenfrequencies and eigenmodes residuals (Bakir et al., 2007).

One of the earliest efforts in the model updating was suggested by Baruch, and dated back to 1978 (Maia and Silva, 1997). In his proposal, Baruch presumed that the mass matrix is correct and the objective function (distance) between the original and updated FE models defined by the Euclidean norm (ε) given by Equation 3.22 is minimised.

$$\varepsilon = \left\| [M_a]^{-\frac{1}{2}} [K_x] - [K_a] [M_a]^{-\frac{1}{2}} \right\| \quad (3.22)$$

Where:

$[M_a]$ is the analytical mass matrix

$[K_a]$ is the analytical stiffness matrix

$[K_x]$ is the experimental stiffness matrix

The objective function is minimised using Lagrange multipliers to give the following expression for the stiffness error matrix $[\Delta K]$ (Ewins, 2000; Maia and Silva, 1997):

$$\begin{aligned} & [\Delta K] \\ &= -[K_a][\varphi_x][\varphi_x]^T[M_a] - [M_a][\varphi_x][\varphi_x]^T[K_a] + [M_a][\varphi_x][\varphi_x]^T[K_a][\varphi_x][\varphi_x]^T[M_a] \\ &+ [M_a][\varphi_x][\omega_x^2][\varphi_x]^T[M_a] \end{aligned} \quad (3.23)$$

Where:

$[\varphi_x]$ is the measured mode shape matrix

$[\omega_x^2]$ is the measured resonant frequency matrix

Similar approach was later adopted by Berman and Nagy in 1983 to update the mass matrix (Maia and Silva, 1997). The Error Matrix Method (EMM), adopted by Sidhu and Ewins in 1984, used pseudo flexibility matrices generated from the truncated m -dimensional modal space (Balageas et al., 2006; Ewins, 2000).

The stiffness error matrix is given by:

$$[\Delta K] = [K_a^*]([K_a]^{-1} - [K_x]^{-1})[K_a^*] \quad (3.24)$$

Where:

$$[K_a]^{-1} = [\varphi_a][\omega_a^2]^{-1}[\varphi_a]^T \quad (3.25)$$

$$[K_x]^{-1} = [\varphi_x][\omega_x^2]^{-1}[\varphi_x]^T \quad (3.26)$$

$[K_a^*]$ represents the analytical condensed stiffness matrix that reduced from the original stiffness matrix $[K_a]$ to the measured DOFs

However, these non-iterative updating methods are convergent for small $[\Delta K]$ and, as a result; the updated matrices are often physically unachievable from which no real eigen-solution can be found. Besides that, they have been shown very sensitive to measurement noise, and disregard the connectivity of the original FE model (Maia and Silva, 1997).

A number of direct model updating methods in structural dynamics have been proposed by Mottershead and Friswell (1993); Friswell and Mottershead (1995); Maia and Silva (1997).

Regarding the performance of Baruch algorithm, it was already stated that the incomplete measured modal sets are closely reproduced. However, there is nothing to prevent the updated model from generating spurious modes in the frequency range of interest. In addition, the FE mass and stiffness matrices may endure a loss of positive-definiteness in the updating process (Mottershead and Friswell, 1993).

For further critical evaluation of non-iterative model updating methods Mottershead and Friswell (1993) can be consulted.

3.4.4.3 Iterative FE Model Updating Methods (Inverse Eigensensitivity Method)

The basic idea of the FE model updating is to use the differences between the predicted and the measured structural response to update the structural parameters of the numerical model (such as stiffness and internal forces) as well as some boundary conditions (Mordini et al., 2007). The iterative updating methods use the sensitivity of the parameters to update the FE model. In these methods, the model updating procedure is based on a mathematical optimisation problem where the errors between numerical and experimental eigenfrequencies and mode shapes are set as an objective function. In this respect, the objective function is to be minimised by making changes to the pre-selected set of physical parameters of the FE model, and the optimum solution is obtained subsequently using sensitivity-based optimisation methods. Owing to the nonlinear relationship between the vibration data and the physical parameters, an iterative optimisation process is performed. This approach is able to update the relevant physical parameters and to locate erroneous regions of the model (Jaishi and Ren, 2007).

A main difference between the various sensitivity-based update schemes is the method used to estimate the sensitivity matrix. Basically, either the experimental or the analytical quantities can be used in the differentiation (Doebbling et al., 1998).

The Eigensensitivity method is based on the use of the truncated Tylor expansion of the eigenfrequencies and eigenvectors as a function of the unknown updating parameters. The changes in modal data are assumed to be linear relationship of the sensitivities, and can be defined as (Ewins, 2000):

$$\Delta\omega_r^2 = \frac{\partial\omega_r^2}{\partial a_1} \Delta a_1 + \frac{\partial\omega_r^2}{\partial a_2} \Delta a_2 + \dots + \frac{\partial\omega_r^2}{\partial a_n} \Delta a_n \quad (3.27)$$

$$\{\varphi\}_r = \frac{\partial\{\varphi\}_r^2}{\partial b_1} \Delta b_1 + \frac{\partial\{\varphi\}_r^2}{\partial b_2} \Delta b_2 + \dots + \frac{\partial\{\varphi\}_r^2}{\partial b_n} \Delta b_n \quad (3.28)$$

The corresponding modal sensitivities are obtained by differentiating the stiffness matrix as:

$$\frac{\partial \omega_r^2}{\partial a_i} = \{\varphi\}_r^T \frac{\partial [K]}{\partial a_i} \{\varphi\}_r \quad (3.29)$$

Where:

$\frac{\partial \omega_r^2}{\partial a_i}, \frac{\partial \{\varphi\}_r^2}{\partial b_i}$ represent the rate of change of r^{th} natural frequency and r^{th} mode shape with respect to the change in stiffness and/ or mass of the element (i)

a_i, b_i are the correction parameters of the stiffness and/or mass elements in the model

This can be explained into a sensitivity matrix as:

$$[S] = \begin{bmatrix} \frac{\partial \omega_1^2}{\partial a_1} & \dots & \frac{\partial \omega_1^2}{\partial a_n} \\ \dots & \dots & \dots \\ \frac{\partial \omega_m^2}{\partial a_1} & \dots & \frac{\partial \omega_m^2}{\partial a_n} \\ \frac{\partial \{\varphi_1\}}{\partial b_1} & \dots & \frac{\partial \{\varphi_1\}}{\partial b_n} \\ \dots & \dots & \dots \\ \frac{\partial \{\varphi_m\}}{\partial b_1} & \dots & \frac{\partial \{\varphi_m\}}{\partial b_n} \end{bmatrix} \quad (3.30)$$

Also, the correction parameter vector as a function of the sensitivities can be defined as:

$$\{\Delta p\} = [S]^* \{\delta\} \quad (3.31)$$

Where:

$[S]^*$ is the pseudo-inverse matrix of the sensitivity matrix $[S]$

$\{\delta\}$ is the change between the predicted and measured modal parameters

The sensitivity matrix should be computed for each iteration; the correction parameters vector $\{\Delta p\}$ is updated until a satisfactory minimum for the objective function is reached. In other words, the iterative system obtained above is repeated until a minimum least-square is achieved. This process can lead to an extreme computational effort. However, in order to minimise the computation time, the resolution of

differences in frequency and mode shape at which the sensitivity matrix to be updated and processed can be optionally chosen.

The criterion of convergence can be built either based on the frequency deviation between the experimental and numerical frequency corresponding to the iteration and/or on the correlation between experimental and numerical mode shapes (Mordini et al., 2007). In view of tuning as well as damage detection, the objective function considering frequency residual, MAC related function, and flexibility residual is the best for FE updating (Jaishi and Ren, 2005).

Messina et al. (1998) circumvented the sensitivity iterative updating by obtaining the correlated damage state through searching for parameters vector which maximises the statistical Multi Damage Location Assurance Criterion (MDLAC) that derived on the same basis as MAC. The parameters vector in Messina's approach represents the stiffness reduction factor introduced to any arbitrary pattern of damage such that $\Delta p = 1$ for no damage and $\Delta p = 0$ for complete loss of the element. Accordingly, the resulted analytical prediction of the frequency changes thereby to be correlated with the measured frequency vector.

More significant FE model updating works on real-size civil structures were done by Teughels and De Roeck (2004), Bakir et al. (2007), Bakir et al. (2008) and Zárata and Caicedo (2008).

Unfortunately one of the major drawbacks in the FE model updating methods is that solving the new set of equations using pseudo-inverse technique and introducing the extra set of equations destroy the natural banding in the mass and stiffness matrices, and hence lose computational efficiency (Mottershead and Friswell 1993). The FE model updating methods provide information on the occurrence, location and extent of damage as reductions in the stiffness of elements. These methods are generally limited to situations where the pre-damage and post-damage structure can be modelled as a linear system. In addition, the practices are typically unable to identify the type of observed damage, yet in place damage is presented in terms of local drop of stiffness at the level of elements (Worden et al., 2007).

3.5 Parameter-based Damage Identification Methods

3.5.1 Statistical Pattern Recognition Methods (Forward Problem)

The heavy involvement of the wireless sensing technology in many civil engineering applications has led to a proliferation of site-location monitoring paradigms. Damage diagnosis performed at the sensing node requires that only the results of the assessment need to be transmitted to the central decision support system. Although the huge potential benefit of the SHM of smart structures where the large number of sensors and actuators generates data, it also produces a severe difficulty later in processing and interpretation of this data (Friswell and Penny, 1997). Nonetheless, statistical signal processing and pattern classification methods particularly suit analysis at sensing nodes because these methods need just individual signals to apply damage diagnosis and prognosis process.

Statistical Pattern Recognition (SPR) methods have been developed over the last two decades for applications in finance, engineering and biology. In the last decade, developments in the engineering field have been motivated by the need for image processing for medical and computer visualisation implementations, fingerprint pattern detection, speech recognition and many other applications (Duda et al., 2001).

SPR methodologies have successfully been used to characterise faults in machinery systems or to discriminate vibration data from different rotating parts. The rotating machinery damage diagnosis problems have nearly obtained an exclusive non-model based paradigm (Farrar and Duffey 1999; Farrar and Worden, 2007). However, there are many difficulties appear in extending this paradigm to civil engineering structures. Civil engineering structures do not enjoy the benefits existing in machinery such as minimum operational and environmental changeability, large databases for different damage pattern and clear damage type (Farrar and Worden, 2007). Civil structures commonly have complicated geometry; are built with different materials such as steel, RC and composites, whose performance are not completely anticipated. These structures are heavily influenced by local environmental conditions that push them well further than their design limits (Wenzel, 2009). Diagnosis and prognosis of civil engineering structures are more problematical because these systems are formed out of

substructures or components, where damage to these subsystems imposes force redistribution. These components will not necessarily fail, whereas their defective position increases stresses in the remaining elements of a structure. Further analyses of the subsystems and the global system are required to identify failure mechanisms, which can cause partial or complete failure of the structure (Wenzel, 2009).

In damage identification context, due to some inherent difficulties in the model-based monitoring systems, many researchers thought with damage identification as a pattern recognition forward problem. The alternative algorithm would overcome difficulties associated with the inverse problem; in the meantime it can be relevant to deal with flooding real-time huge data.

The damage identification problem as dealt by SPR paradigm represents a four-level procedure (Farrar et al., 2001a; Sohn et al., 2001); they are:

- operational evaluation;
- data acquisition and cleansing;
- feature extraction and data compression; and
- statistical model development for feature analysis.

The first two steps are also included in the damage identification when approached as model-based problem. Feature extraction step entails identifying damage-sensitive properties, obtained from the measured vibration response, which allows detectable damage event. Statistical model development is concerned with the implementation of algorithms that analyse the distribution of extracted features in an effort to determine the damage state of a structure. The algorithms used in statistical model development fall into one of the three following general categories (Farrar et al., 2001a; Sohn et al., 2001):

1. Group Classification.
2. Regression Analysis.
3. Outlier detection.

The suitability of using an appropriate classification scheme depends so much on the available data and information. General pattern recognition (PR) algorithms are broadly

divided into supervised learning and unsupervised learning, Figure 3.1. In supervised learning schemes, the algorithm is learnt on a dataset whose outcome variables are observed, and predictions are made with respect to the training model. On the other hand, unsupervised learning schemes are algorithms where no outcome variables are observed, therefore the main aim is to classify or cluster the data (Wenzel, 2009). In this context, Damage presence and location in a system can be accomplished in an unsupervised learning means. Nonetheless, the type and size of damage can only be accomplished in a supervised learning means and coupled with analytical models or data from different known conditions (Worden et al., 2007).

Many modern approaches of damage identification are based on the idea of PR. In the general aspect, PR algorithm is simply one that allocates a class label to a sampling measured data that share same feature, usually from a finite set. In the case of damage identification, the measured data can be vibration mode shapes, scattered wave profiles and so on. Damage type, location, size, etc will be encoded the proper group class. With the intention of conducting higher levels of identification using PR, it will almost be essential to construct examples of data corresponding to each class (Worden and Dulieu, 2004).

3.5.1.1 Principal Component Analysis and Singular Value Decomposition

The fundamental objective of Principal Component Analysis (PCA) method is to reduce the dimension of data sets in which there are a large number of interrelated (correlated) variables, whilst preserving as much as possible of the variation present in the original data sets. This reduction is accomplished by transforming to a new set of variables, the principal components (PCs), which are uncorrelated and are ordered so that the first few PCs retain most of the variation (Jolliffe, 2002). For instance, a vector $\{x\}$ can be transformed to another linear orthogonal plane according to its i^{th} largest variance as in Equation 3.31:

$$\{z\} = [V]^T \{x\} \quad (3.32)$$

Where:

$[V]$ is the orthogonal matrix whose i^{th} column is the i^{th} eigenvector of the covariance matrix

The covariance matrix $[\Sigma]$ for a data set $X = \{x_1, x_2, \dots, x_n\}$ can be described as:

$$[\Sigma] = \sum_{i=1}^n (x_i - \bar{x})(x_i - \bar{x})^T \quad (3.33)$$

Where:

\bar{x} is the mean of the data set

Furthermore, the covariance (or correlation) matrix of the original data set can directly be written as:

$$[\Sigma] = [V][\lambda][V]^T \quad (3.34)$$

The $[\lambda]$ denotes a diagonal matrix whose i^{th} diagonal element is λ_i , the i^{th} eigenvalue of $[\Sigma]$.

Similarly, within the same context, Singular Value Decomposition (SVD) is used to decompose a non-square matrix $[A]$ into the following products:

$$[A] = [U][\lambda][V]^T \quad (3.35)$$

Where:

$[U]$ and $[V]$ are orthogonal matrices such that $[U][U]^{-1} = [I]$ and $[V][V]^{-1} = [I]$

This main aspect of PCA is particularly beneficial if a set of data with many variables lies, in effect, close to a two-dimensional subspace plane. In this case, the data can be visualised with respect to these two dimensions, thus giving an easy graphical representation of what the data is look-alike, in place of presenting as a large bunch of numbers to hardly be assimilated (Jolliffe, 2002). If a good representation of the data exists in a small number of dimensions, the PCA will find it, as long as the first (r) PCs give the best-fitting- dimensional subspace. Therefore, if the values for each observation of the first two PCs are plotted, the best possible two-dimensional representation of the

data (similarly for three or more dimensions) will be achieved. To this end, a meaningful interpretation would be valid for the variables as soon as the PCs are obtained (Jolliffe, 2002).

An early application of PCA in civil engineering was carried out by Sohn and Farrar in 2000 (Sohn et al., 2004). In this study, measurements from a real-size RC pier model was analysed by subjecting static/dynamic loadings in a laboratory environment. The ultimate goal in using PCA was to reduce the size of data collected from different sensors in this test. Time series data from 39 measurement points on the bridge pier is transformed into a single time series by implementing PCA. In fact, Sohn and Farrar find that simply the first PC contains about 30% of the total information of the 39 time series. The 39 time series is projected onto the first principal component and the projected time series is later used for successive feature extraction and statistical process control (Sohn et al., 2004).

Having used as a technique for dimension reduction, PCA allows discarding those linear combinations of the records that contribute the least to the general variance. Basically, there are two main applications of PCA. First, the approach is being able to provide an effective means of visualising the data. If the reduced space contains a three dimension or less, the reduced data can be plotted in a form that displays relationships between the variables. Second, the technique can offer an efficient means of feature extraction, i.e. the significant information in the data will be reserved while processing a demonstration for the data in a reduced dimension space. In the reduced dimensional space, structure such as clusters may be visualised reflecting the distribution of data in the original higher dimensions (Sohn et al., 2001).

In their report of applying the SPR paradigm to data from a patrol boat, Sohn et al. (2001) used the PCA method for the discrimination purposes. Three strain time-histories were measured with the same sensor when the boat exhibit two different structural conditions. The first four statistical moments and AR parameters were calculated as damage-sensitive features of the time signals. Then, the PCA method was applied at data sets of the first four moments also at AR parameters in order to get graphical discrimination between features from different signals. The observation was

not conclusive for the situation of using the moment data. Nonetheless, data points from different strain signals represented by AR parameters were successfully separated using the PCA method (Sohn et al., 2001).

Despite its reliability and efficiency as an unsupervised classification and feature extraction tool, PCA has not been widely tested in the area of the damage identification and feature extraction particularly in civil engineering area. In their important and extensive review of this subject, which covered the literature up to 1996, Doebling et al. have not mentioned this method as damage identification tool. Likewise, in the similar successive review, which considered the literature of the subject for the period 1996-2001, Sohn et al. (2004) recognised PCA twice, as a data reduction tool. In this review, PCA was firstly exploited by Sohn and Farrar in 2000 as a data reduction for 39 time histories collected from RC pier model.

3.5.1.2 Coefficients ARMA Family Models

The analyses of time-series functions rely on the fact that time-series collected over time possibly have particular structure, such as auto-correlation, trend or typical seasonal variation (Figueiredo et al., 2009). Regression models are widely applied to time-series in an effort to extract some damage sensitive features from undamaged and damaged structures (Nair et al., 2006).

The Auto-Regressive (AR) model for a time signal can be given as:

$$y(t) = \sum_{i=1}^m \varphi_i y(t-i) + \varepsilon(t) \quad (3.36)$$

Also, the Auto-Regressive Moving Average (ARMA) model for a time signal is given by Equation 3.36:

$$y(t) = \sum_{i=1}^m \varphi_i y(t-i) - \sum_{i=1}^n C_i \varepsilon(t-i) + \varepsilon(t) \quad (3.37)$$

Where:

$y(t)$ is the measured response time signal at time t

$y(t-i)$ is the response at previous time

φ_i is the AR coefficient to be estimated

C_i is the moving average coefficient

$\varepsilon(t-i)$ is the previous predicted error

$\varepsilon(t)$ is the present error

The AR and Moving Average (MA) coefficients are obtained by minimising an error function based on the measured response and predicted response using Equations 3.36 and 3.37. Additionally, roots of the characteristic polynomial containing the AR parameters can be correlated to the modal frequencies and damping of the system and the ARMA model can be used to examine the time variation of these parameters (Nair et al., 2006). The coefficients of the AR or ARMA models are also chosen as damage-sensitive features for the successive control analysis. Then, the coefficients obtained from successive new data set are relatively scrutinised with the baseline reference coefficients. Any significant deviation from the baseline of the coefficients would indicate either a change in environmental conditions or damage (Sohn et al., 2004).

The mean and variance of the residuals of the AR model are used by Worden et al. (2000) as a means for unsupervised damage detection. The resulting residuals outside the bounds of control limits are considered outliers and used to indicate a change in the condition of the system (Carden and Fanning, 2004).

Nair et al. (2006) suggested a new Damage-Sensitive Feature (DSF) parameter to locate the damage in the ASCE four-storey frame benchmark model. The new damage-sensitive parameter is defined as a function of the first three AR components, and given in Equation 3.38:

$$DSF = \frac{\varphi_1}{\sqrt{\varphi_1^2 + \varphi_2^2 + \varphi_3^2}} \quad (3.38)$$

Where:

ϕ_1 , ϕ_2 and ϕ_3 are the first three coefficients in AR analysis

The results show that the damage detection algorithm is able to detect the occurrence of all simulated damage patterns in the ASCE benchmark structure. In this study, the defects are modelled as slight, moderate and severe corresponds to removal of single brace, removal of all braces in a story and removal of all braces in two stories, respectively (Nair et al., 2006).

The study also proposed two indices to locate the damage, LI_1 and LI_2 , which are defined in Equations 3.39 and 3.40, respectively:

$$LI_1 = \frac{d_{mean}}{d_{undam\ cloud}} \quad (3.39)$$

$$LI_2 = \frac{d_{dam\ cloud}}{d_{undam\ cloud}} \quad (3.40)$$

Where:

d_{mean} represents the distance between the centres of the damaged and undamaged DSF cloud indices

$d_{dam\ cloud}$ represents the distance from the origin to the centre of the damaged cloud of DSF indices

$d_{undam\ cloud}$ represents the distance from the origin to the undamaged cloud of DSF indices

Likewise, the results of the damage localisation algorithm indicated that the index LI_1 is able to localise minor damage patterns. However, the second localisation index, LI_2 , appeared to be non-sensitive to the minor damage in the structure.

Cheung et al. (2008) applied the AR coefficients to identify damage in the Z24 Bridge when subjected to a number of progressive damage tests. Three different damage scenarios: settlement of one bridge pier, removal of post tensioning anchor heads and breaking of tendons were investigated in this study. The damage was identified and potentially quantified through two measures based on: (1) the distance between the

mean values of the AR coefficients normalised to the square root of the sum of the variances of the baseline (undamaged) and damaged cases, designated as γ ; and (2) the Mahalanobis distance between the baseline and damaged structure designated as DM (Damage Measure). It was found that γ will change sign depending on the type of damage, while DM as defined was positive for all damage states, and no correlation can be found between the damaged and undamaged measures.

In a research by Carden and Brownjohn (2008), the time-series responses were modelled by Autoregressive Moving Average (ARMA) models, and the ARMA coefficients were then used as inputs of a classifier. The classifier was capable of learning in an unsupervised manner and of tagging new classes whenever the structural response displayed change. The approach was demonstrated with experimental data from the ASCE benchmark structure, the Z24 Bridge and the Malaysia–Singapore Second Link Bridge. The classifier was found conclusive of identifying structural change in all cases and of forming distinctive classes corresponding to different structural status in most cases.

3.5.1.3 Statistical Outlier Detection

Outliers are commonly investigated as observations that are a long distance from, or disproportionate with, the remainder of the records (Worden et al., 2000). Normally, a number of algorithms for outlier analysis can be performed as damage detections in an unsupervised environment, which implies the data from damaged state is unavailable (Sohn et al., 2004; Wenzel, 2009).

The field of outlier statistics has a very substantial body of theoretical knowledge that supports the methodology, and is proved to be a rich source of algorithms for subject of damage detection (Worden et al., 2000). The outlier detection technique is well-established field of statistics; thus it is systematically used in the area of damage detection of civil engineering structures in the last decade.

As an early attempt, Ruotolo and Surace (1997) use changes in the rank of a matrix as a measure of outlier detection. In their methodology, a matrix is first assembled where each column represents the feature vector measured through a range of environmental

and operational conditions of a structure. The SVD approach is first used to estimate the rank of this matrix. Second, this matrix is enlarged by adding an additional column containing a new feature vector from a potential damage case of the system. The new added vector will be flagged as independent from the initial measured vectors, and the rank of the matrix will increase, if the new feature vector corresponds to a damaged structure (Sohn et al., 2004).

Similarly, the Mahalanobis distance is a popular distance measure for multivariate statistics that can be used to identify and quantify outliers. The Mahalanobis distance outmatches the Euclidean distance because it considers the correlation between the variables, and it is independent of the size of the record points (Figueiredo et al., 2009). The Mahalanobis distance (D) between that group and a new potential outlier pattern is described as:

$$D = \sqrt{(x - \bar{x})^T \Sigma^{-1} (x - \bar{x})} \quad (3.41)$$

Where:

\bar{x} is the mean vector of the normal data set

Σ is the sample covariance matrix

x is the new suspected outlier pattern

In the unsupervised level, the tuning of threshold values for outlier detection is a vital objective to statically distinguish between damaged and undamaged cases. Worden et al., 2000; Sohn et al., 2001 employed the Monte Carlo method to obtain these values (Figueiredo et al., 2009).

Worden et al. (2000) tested a laboratory-scale aluminium plate strengthened by two channels under free-free boundary conditions. The sample was utilised to detect nine different damage scenarios simulated by cuts through plate thickness. In this study, Mahalanobis distance (D) was used as a damage sensitive feature for outlier analysis. The analysis was applied to the transmissibility functions of different paths, and D was described as a successful means in identifying damage to specific size.

Figueiredo et al. (2009) used AutoRegressive (AR) model along with Mahalanobis squared distance (D^2) to detect damage in a three story aluminium frame prototype modelled with 16 different defect and operation conditions along with its baseline state. The undamaged state of the structure was defined by using the AR model of four time-series measured at specific channel for the first nine state conditions. The mean vector and the covariance matrix were formed using five AR parameters AR(5) and 30 AR parameters AR(30). The study concluded that D^2 provides robust damage indicator for AR(30) compared to AR(5), which is always unchanging under the operational and environmental effects related to the undamaged states. However, the magnitude of the outliers from the undamaged training set is much bigger than from damaged states. Moreover, the outliers from D^2 calculated based on the residuals errors from AR(5) and AR(30) models, as damage-sensitive features, offered consistent indicator to damage states (Figueiredo et al., 2009).

3.5.2 Neural Networks in Structural Damage Identification

As forward problem, Artificial Neural Networks (ANNs) methods are used with vibration parameters to relate the dynamic changes to their corresponding underlying structural changes. In these methods, a neural network is trained with appropriate sets of input data, obtained by numerical simulation, real measurements or a combination from both sources. This process allows the network to learn different damage pattern, adjust the weights (w) accordingly and assign label for each individual different case.

As a result, the network suggests the expected output vector (y) through an optimisation procedure by minimising the objective function $E(w)$ between the predefined target vectors $\{t_i\}$ and the predicted input vectors $\{x_i\}$, as defined in Equation 3.42 (Bishop, 2006):

$$E(w) = \sum_{i=1}^{i_{max}} \|y(x_i - w) - t_i\|^2 \quad (3.42)$$

A detailed discussion on the properties and algorithms of ANNs can be followed in the reference (Bishop, 2006).

There are many damage detection algorithms that utilise ANNs to detect, localise and quantify the damage in structures. One of the earliest attempts, Rytter and Kirkegaard (1997) evaluated two neural networks for damage assessment purpose, namely the Multi-Layer Perceptron (MLP) network with back propagation and the Radial Basis Function (RBF) network. The results of a full-scale four-storey RC building under earthquake loadings were used in the investigations. FE models were utilised to simulate the random reductions in the stiffness of the members at each floor, and the outcomes were used as input training sets (Rytter and Kirkegaard, 1997). The related relative deviations in the first four resonant frequencies and two lower mode shapes were exploited as inputs, and the relative bending stiffness of the frame elements were used as outputs. Overall of 4900 sets of frequencies and mode shapes were randomly produced for different damage scenarios. The prospects of localising the damage and estimating its size by using the two ANNs were addressed. The results show that MLP network can be used as a vibration-based damage identification tool, but RBF network is unsuccessful completely in this aspect (Rytter and Kirkegaard, 1997; Sohn et al., 2004).

Important progress has followed the initial work by Rytter and Kirkegaard, thereby moving forwards the practice of neural networks methods in SHM. For instance, Levin and Lieven (1998) used the RBF network to update the FE model of a cantilever beam. The noise resistant capability of the updating technique was then tested by adding Gaussian noise to the original experimental data. It has been concluded that this updating technique is advantageously able to withstand the presence of noise in experimental data as well as it is capable of working with a limited number of experimentally measured DOFs and modes (Levin and Lieven, 1998).

Zang and Mregun (2001) exploited the PCA method as a data reduction technique to assign the most significant Principal Components (PCs) of measured FRFs. Three different neural networks, each corresponding to a coordinate direction, were trained and verified using 80 PCA-reduced FRFs collected from railway wheels. The output of this procedure was to allocate the condition of the specimen, whether it was healthy or damaged (Zang and Mregun, 2001).

Furthermore, ANNs were used by Owen and Haritos (2004) as a classifier tool to distinguish between measurements of vibration collected from three scale-model RC bridge decks with different load-imposed damage levels. Classification data showed that the ANNs were very successful at classifying the data into damaged and undamaged states only without further classification about other features, i.e. repaired and final damaged state, which are real cases of the test (Owen and Haritos, 2004).

In a research carried out by Yeung and Smith (2005), a method for detecting the onset of damage in bridges is developed using the dynamic response spectra evaluated from continuously monitored instruments, together with ANNs for pattern recognition. The method is tested analytically using an FE model of the historical Clifton Suspension Bridge in Bristol, England. Simulated damage on the real bridge, in the form of loss of continuity of riveted connections in the main girders, is simulated in the numerical FE model. The study concluded that a reliable damage identification rate of about 70% can be achieved even though a moderate amount of noise was added to the dynamic response signals (Yeung and Smith, 2005).

Figueiredo et al. (2009) used AutoRegressive Neural Network (ARNN) to detect damage in a three-story aluminium frame model inflicted with 16 state conditions besides its intact reference state. The training data matrix is composed of undamaged autoregressive model parameters from two time histories of an accelerometer (Channel 5) mounted at the third floor of the test model. The undamaged state conditions include the baseline condition state and eight other states with simulated operational and environmental variations. It is noted that the residual errors of the ARNN grew when the features of damaged states were fed to the network. However, one of the damaged states was misclassified as undamaged through this process.

Neural networks are able to treat damage mechanisms indirectly, in a way that it is unnecessary to model the structure in so much detail. The method can also deal with non-linear damage mechanisms easily. For success, ANNs require that the essential features in the damaged structure are embodied in the training data sets. However, the robustness of networks to these errors is not sufficiently tested. Of course, the other major problem with ANNs algorithms is that they require a huge amount of

computation for structures of practical complexity, although these methods are well convenient to parallel computation (Friswell and Penny, 1997).

Most of the reviewed neural-network-based approaches yet experience from one general obstacle that the training is performed in a supervised mode and that the successful ANNs demand large training data sets from both the undamaged and damaged systems (Friswell and Penny, 1997; Sohn et al., 2004). Many active studies endeavour to generate the training data sets related with diverse damage cases from numerical simulations because the acquisition of data sets from the damaged structure is impossible for most applications. Therefore, the success of these ANN approaches over again depends upon the reliability of the analytical models used to generate the data sets (Sohn et al., 2004).

3.5.3 Wavelet Analysis of Vibration Signals

Wavelet Transform (WT) is a mathematical method by which a time signal is decomposed into consecutive windowed time-domain functions of different frequency resolutions. This real-time time-frequency breakdown gives the WT an advantage over the Fourier transform in investigating non-stationary signals (Sun and Chang, 2002). The constructed small waves (wavelets) are very much related to the required sensitivity of the records, and they display imperative structure of the signal. Nonetheless, wavelet analysis enjoys a key benefit compared with Fourier transform method that the data is represented in both time and frequency domains (Mallat, 1999). Fourier transform is improper for specifying non-stationary aspects of the signal as the transformation is unable to designate the time of the signal when a specific frequency occurred (Wenzel, 2009).

WT methods do not have only one set of fundamental functions as in the Fourier transform, which basically exploits no more than the cosine and sine functions. As an alternative, wavelet transform has unlimited possibility of choosing fundamental functions. Therefore, the wavelet analysis has the privilege to provide direct access to information that can be hidden by other time-frequency methods like Fourier analysis. On the whole, WT is an expanded application of a windowing technique with changeable-sized windows. It permits using short time intervals for high-frequency

information and longer time intervals wherever low-frequency information is needed (Wenzel, 2009).

In the context of SHM, WT methods and their results could recognise damage occurrence, location, or even its size, but not exactly, when the damage happened (Wenzel, 2009). Wavelet transforms are insightful to signatures in the signal such as a step. Therefore, they may be used to locate a sudden change in a mode shape, often indicative of damage, or find an abrupt change in response from an acceleration time function (Carden and Fanning, 2004). When applied to the space domain, an important issue in the use of wavelet analysis is the number of DOFs measured. The denser the mesh of the measurements in the spatial domain, the more information can be provided by the wavelet analysis (Carden and Fanning, 2004).

An early work was conducted in wavelet-based system identification of nonlinear structures by Staszewski in 2000 (Wenzel, 2009). The proposed characteristics are illustrated using two simple simulated models. Sun and Chang (2002) used the wavelet packet transform for decomposition of the signals in an effort for the assessment of damage in structures. The component energies are determined and then used to detect damage as inputs to ANN models for damage identification purpose. The methodology is demonstrated on numerical simulations of a three-span continuous bridge under impact excitation. The results prove that the wavelet packet transform-based element energies are rational candidate parameters because they are sensitive to structural damage (Sun and Chang, 2002).

Staszewski and Robertson (2007) presented a study of recent advances and applications of wavelet analysis for damage detection. This includes two main approaches of signal processing, which are the time-frequency analysis and time-scale analysis. Additionally, continuous or discrete wavelet decomposition, wavelet-based data compression, denoising and feature extraction, linear and nonlinear system identification are discussed. The paper demonstrated a number of examples on the wavelet analysis that forms a set of successful signal processing tools that not only complement, but also significantly outperform damage detection outcomes based on Fourier analysis. However, due to the complexity of the mathematical knowledge and algorithms associated with the analysis,

the applications are mostly limited to academic research (Staszewski and Robertson, 2007).

Despite the good deal of research, the method is still now in its infancy stage and its applications are very much limited to the small scale case-studies because the method requires a profound mathematical knowledge. The toolboxes of wavelet analysis from different techniques of fields that unrelated to the monitoring process are required to exhibit further progress in SHM practice (Staszewski and Robertson, 2007). Another drawback is that WT resolution is rather poor in the high-frequency region. As structural damage is normally a local event captured most likely by high frequency modes, this likely limit can affect the use of the wavelet-based damage assessment techniques (Sun and Chang, 2002).

3.6 Summary

The main features, advantages and limitations of each individual damage identification method mentioned in this Chapter were stated within the text of that method per se. Nevertheless, some important points from this survey can generally be summarised as they are found unequivocally critical to the advances of SHM and vibration-based monitoring methods.

In the damage identification context, a great number of technical literatures were reviewed and discussed. Many of the resulting papers achieved some correlation, but usually the cases were either simulation, very controlled experiments or the researchers had some idea of what to expect (Friswell and Penny, 1997). To date, there is no superior perfect method to be used for damage detection, localisation and quantification by exploiting vibration data. No algorithm has yet been suggested that can be applied universally to identify any type of damage in any type of structure. In addition to the application of dynamic procedures, extensive experience is required in this area (Carden and Brownjohn, 2008; Carden and Fanning, 2004; Wenzel, 2009).

Model-based analysis methods (inverse type methods) are computationally expensive and they are impossible to apply in embedded nature as online real-time monitoring (Wenzel, 2009). The process of permanent monitoring of suspected elements will end

up in too many unmanageable amounts of data. The human capacity to assess immense amount of data is very limited; therefore, SPR methodologies need to be introduced into the procedure (Wenzel, 2009).

The most dazzling methods in damage diagnosis seem to be based on modal data and use the forward type methods. Having employed low frequency vibration data, a number of shortcomings emerge in damage identification resulting in a limited accuracy because of the global nature of the lower modes (Friswell and Penny, 1997).

In brief, the development of vigorous damage detection and location algorithms based on response monitoring data of an in-use structure is still a challenge, even though the availability of such model will open the door for more accurate estimation of the remaining life of a structure (Friswell, 2007).

4. Theory of Analytical and Experimental Modal Analysis

4.1 Experimental and Analytical Modal Analysis Methods

Modal testing or also known as Experimental Modal Analysis (EMA) is the only one of the vibration analysis methods that provides understanding of the dynamic properties of structures, operation conditions and performance quality (Maia and Silva, 1997). Modal analysis is mainly implemented to derive a mathematical model to the dynamics of structures, but the differences occur later in the way of using this model for further analyses (Ewins, 2000). Modal analysis covers nowadays a wide range of applications in vibration field, such as: estimations of vibration behaviours; correlations and updating of analytical models; development of experimentally based models; assessment of the robustness of structures; detection and identification of structural damage; development of specifications for the design and test practice; and modifications and corrections for design models (Maia and Silva, 1997).

The problem of the dynamics of structures can be approached primarily by two ways, namely: experimental analysis and analytical analysis. When approached as analytical analysis only, the model poses difficulties of verification and validation. Conversely, there appears incomplete information in considering the experiments without analysis because this makes the outcomes difficult to understand and explain (Reynolds, 2000). In the meantime, embarking on the problem of modal analysis through the analytical model is important for two reasons. First, a preliminary analytical model would help to carry out reliable measurements. Second, experiment results can be used later to correct and update the analytical model.

This is to say, the work done in this project has adopted both analytical and experimental modal models, and therefore, reviews on both models are outlined in this Chapter. In the respective of analytical models, a concise description to the concepts ensuring an accurate model is highlighted. The fundamental concepts resulting in a truer FE modelling, namely: simulation of boundary conditions; distributed physical properties; and approximation of damping are investigated. In addition, the Chapter is

concerned with giving a theoretical background to the necessary experimental formulations of the modal testing. In the test practice, the selected measurement devices and their merits coupled with the individual settings are discussed. Finally, the Chapter explains briefly the procedure, set-up and necessary checks entail accomplishing a reliable EMA for civil engineering structures.

4.2 Vibration Analysis Models

In general, the dynamic properties of an N Degrees Of Freedoms (DOFs) system could be defined in terms of its mass $[M]$, damping $[C]$ and stiffness $[K]$ matrices, each matrix is of a dimension $N \times N$. This phase of analytical modelling is referred to as the spatial model. The spatial model explained by the $[M]$, $[C]$ and $[K]$ matrices produces a system of eigen-equations producing a set of vibration modes, designated as the modal model. The solution of the system eigenproblem leads to the modal model, which comprises a set of modal parameters of N natural frequencies (ω_r) with associated N modal damping ratios (ζ_r) and N vibration mode shape vectors $\{\phi_r\}$. The modal model describes various natural vibration parameters when a structure oscillates naturally, without any excitation. It is usual that the results of the analytical analysis and EMA to be compared through the parameters from the modal model.

Furthermore, the third model in vibration analysis is when the characteristics of a structure are extracted based on how the structure will respond under an excitation. This is to say that the structural properties depend not only on the natural physical phenomena, but also on the magnitude of the induced force. However, the general test for this task is run under standard excitation and is described as the response model (Ewins, 2000).

From the analytical point of view, the essential stage of the response model representation starts by solving a system of the forced vibration motion equations of the spatial form, which can be given as:

$$[M]\{\ddot{x}(t)\} + [C]\{\dot{x}(t)\} + [K]\{x(t)\} = \{f(t)\} \quad (4.1)$$

Where:

$\{\ddot{x}(t)\}$ is the acceleration vector

$\{\dot{x}(t)\}$ is the velocity vector

$\{x(t)\}$ is the displacement vector

When a harmonic vibration does exist, the displacement vector $\{x(t)\}$ can be expressed as:

$$\{x(t)\} = \{X\}e^{i\omega t} \quad (4.2)$$

Similarly, the excitation force vector $\{f(t)\}$ can be expressed as:

$$\{f(t)\} = \{F\}e^{i\omega t} \quad (4.3)$$

Where:

$\{X\}$ is the complex amplitude of the response; i.e. $\{X\} = \{x_0 e^{i\phi}\}$

$\{F\}$ is the complex amplitude of the force, i.e. $\{F\} = \{f_0 e^{i\phi}\}$

Both $\{X\}$ and $\{F\}$ are independent of time containing information on the Magnitude and Phase.

The solution of the system of motion equations given in Equation 4.1 in the frequency domain constitutes the following form:

$$[[K] - \omega^2[M] + i\omega[C]]\{X\}e^{i\omega t} = \{F\}e^{i\omega t} \quad (4.4)$$

In this form, the complete system motion equations can be replaced by a single matrix. This matrix is designated as FRF matrix $[H(\omega)]$ in which the elements of this matrix are not constant, but frequency dependent. That is, each element in this matrix $H_{ij}(\omega)$ represents the ratio of a response X_i , caused by a harmonic force F_j , as given below:

$$\{X\} = [H(\omega)]\{F\} \quad (4.5)$$

Where:

$$[H(\omega)] = [[K] - \omega^2[M] + i\omega[C]]^{-1} \quad (4.6)$$

$[H(\omega)]$ is an $N \times N$ receptance matrix encompassing all system dynamic characteristics

The receptance matrix form of Equation 4.6 is the third procedure of modelling the dynamic system and is referred to as the response model as opposed to the spatial or modal model. When the response displacement is replaced by velocity or acceleration, this function is referred to as mobility or accelerance, respectively. The three common definitions of FRF, which are easily attainable from each other, are presented in Table 4.1.

Table 4.1: Definition of common FRFs (after Ewins, 2000; McConnell and Varoto, 2008).

| Response | Definition of FRF | Name | Inverse FRF |
|--------------|--|-------------|----------------------|
| Displacement | $H(\omega) = \alpha(\omega) = \frac{\text{displacement}}{\text{force}}$ | Receptance | Dynamic stiffness |
| Velocity | $Y(\omega) = \frac{\text{velocity}}{\text{force}} = i\omega H(\omega)$ | Mobility | Mechanical Impedence |
| Acceleration | $A(\omega) = \frac{\text{acceleration}}{\text{force}} = -\omega^2 H(\omega)$ | Accelerance | Apparent Mass |

Based on the modal analysis theory, FRFs of Equation 4.6 can be rewritten in different ways. For example, by pre-multiplying both sides by $[\varphi]^T$ and post-multiplying both sides by $[\varphi]$, Equation 4.6 yields the following form:

$$[\Phi]^T [[K] - \omega^2[M] + i\omega[C]][\Phi] = [\Phi]^T [[H(\omega)]]^{-1}[\Phi] \tag{4.7}$$

Using the orthogonally property of the mode shapes, the new form of Equation 4.7 can be written as:

$$[\omega_r^2 - \omega^2 + 2i\zeta\omega_r^2] = [\Phi]^T [[H(\omega)]]^{-1}[\Phi] \tag{4.8}$$

Where:

[K], [M] and [C] matrices are taken as given in the following Equations 4.9, 4.10 and 4.11, respectively:

$$[K] = \sum_{r=1}^N \{\phi\}_r^{-T} [\omega_r^2] \{\phi\}_r^{-1} \quad (4.9)$$

$$[M] = \sum_{r=1}^N \{\phi\}_r^{-T} [I] \{\phi\}_r^{-1} \quad (4.10)$$

$$[C] = \sum_{r=1}^N \{\phi\}_r^{-T} [2\zeta_r \omega_r] \{\phi\}_r^{-1} \quad (4.11)$$

Conversely, the modal static flexibility matrix can be determined from a system stiffness matrix [K] as:

$$[F] = [K]^{-1} = \sum_{r=1}^N \frac{\{\phi\}_r \{\phi\}_r^{-1}}{\omega_r^2} \quad (4.12)$$

Using Equation 4.8, the system receptance matrix [H(ω)], which is defined in terms of the physical properties and given by Equation 4.6, can be equally defined in terms of the modal properties as:

$$[H] = \sum_{r=1}^N \frac{\{\phi\}_r \{\phi\}_r^{-1}}{\omega_r^2 - \omega^2 + 2i\zeta_r \omega_r^2} \quad (4.13)$$

In this representation, each individual element in [H] matrix represents an FRF of specific input-output DOF locations. These frequency functions are usually described with subscripts to denote the input and output locations as $H_{j,k}$. The notation refers to the ratio of the dynamic response at DOF (j) due to an exciting force at DOF (k), which can be defined for the damped system as:

$$H_{jk}(\omega) = \sum_{r=1}^N \frac{\phi_{jr} \phi_{kr}^T}{\omega_r^2 - \omega^2 + 2i\zeta_r \omega_r^2} \quad (4.14)$$

In the common theoretical route it is possible to embark on the problem from its spatial model building up the complete response model. However, it is also possible to embark on the task in reverse direction as it is the case in the EMA. That is, from the measured response properties, such as FRFs, the modal parameters and the spatial properties can be obtained. This is the experimental route of the vibration analysis of a system (Ewins, 2000). Table 4.2 summarises the relationships between the three undamped dynamic models and their interdependence as they constitute the fundamentals of modal testing procedures.

Table 4.2: Relationship between the three models of an undamped dynamic system (after Maia and Silva, 1997).

| Derived from | To obtain | | |
|----------------|--|---|---|
| | Spatial model | Modal model | Response model |
| Spatial model | ----- | $[[K] - \omega^2[M]]\{\phi\} = \{0\}$ | $[H(\omega)] = [[K] - \omega^2[M]]^{-1}$ |
| Modal model | $[M] = ([\phi][\phi]^T)^{-1}$ $[K] = [M][\phi][\omega_r^2][\phi]^T[M]$ | ----- | $H_{ij}(\omega) = \sum_{r=1}^N \frac{\phi_{ir} \phi_{jr}}{\omega_r^2 - \omega^2}$ $[H(\omega)] = [\phi][\omega_r^2 - \omega^2]^{-1}[\phi]^T$ |
| Response model | $[F] = [K]^{-1} = [H(\omega)]_{\omega=0}$ $[M] = \frac{[H(\omega_1)]^{-1} - [H(\omega_2)]^{-1}}{\omega_2^2 - \omega_1^2}$ | $H_{ij}(\omega) = \sum_{r=1}^N \frac{\phi_{ir} \phi_{jr}}{\omega_r^2 - \omega^2}$ | ----- |

4.3 Theory of Analytical Modal Analysis

The central idea of analytical modal analysis is to obtain the modal properties of a structure (natural frequencies, mode shapes and modal mass) from its assumed geometrical and material properties. The analytical modal properties could then be used qualitatively and quantitatively to verify the modal properties obtained from the EMA.

Besides providing a good level of confidence to the measurements, the merits of establishing an accurate analytical model can be outlined in the following points (Maia and Silva, 1997):

- the model will be capable to regenerate all of the measured modal parameters;
- the model will be capable to regenerate all of the unmeasured modal parameters; and
- the model will provide all of the accurate distributed mass, damping and stiffness elements with the correct boundary conditions and connectivity.

For the modal model of undamped system, the natural frequencies and their corresponding mode shapes and modal masses can be obtained directly from $[K]$ and $[M]$ matrices by solving the mathematical standard eigenproblem of the following form for a non-trivial solution:

$$[[K] - \omega^2[M]]\{\phi\} = \{0\} \quad (4.15)$$

The non-trivial solution of Equation 4.15 for which not all mode vectors of $\{\phi\} = 0$ requires that the determinant coupled with the eigenvector $\{\phi\}$ be equal to zero, as:

$$|[K] - \omega^2[M]| = 0 \quad (4.16)$$

There are many numerical methods available for the calculation of eigenvalues and eigenvectors of a standard eigenproblem (i.e. $[M]$ is being the identity matrix and $[K]$ is the diagonal eigenvalues matrix). For the purpose of this work, the subspace iterative method of eigenproblem as performed by MATLAB software was chosen.

4.3.1 Finite Element Analysis

The Finite Element (FE) analysis is a widely used structural analysis method, which relies on the application of displacement method. With the heavy involvement of computers in the engineering life, the theory of FE analysis became ingrained subject in the structural analysis body. Therefore, the presentation of this method will be limited to the fundamental aspects and assumptions that are relevant and might affect the dynamics of one-dimensional beam element, which considered as the model to the RC beams in this research.

4.3.2 The Fundamentals of Structural Finite Element Analysis

The FE method is an approximate analysis technique where a structure is divided into a number of elements connected to each other at their nodes. Each node may have one or more DOF, which are defined as independent displacements (translations and rotations), and are used to express the movement of each node (Reynolds, 2000). However, attention to the following problematical points of the FE modelling will provide a better representation of the dynamics of structures (Maia and Silva, 1997):

- estimation of distributed material properties of structural elements;
- discretisation of real geometrical shape;
- simulation of boundary conditions;
- estimation of proportional damping; and
- reduction of FE model to obtain a compatibility with the test model.

4.3.3 The Stiffness and Mass Matrices of Beam Element

Shear deformation in RC beams could be significant and thus could be of practical importance in the verification of the measured vibration data. When shear deformations exist significantly, beam sections that are originally considered perpendicular to the neutral axis are no longer perpendicular after deformation. The set of shape functions that describes the deformation of beam nodes along the neutral axis is different. For bending mode of Euler-Bernoulli beam sections remain perpendicular to the neutral axis. However, for deep Timoshenko beam model, these sections are no longer remaining perpendicular to the neutral axis after deformation. Timoshenko beam theory

is higher order than the Euler-Bernoulli theory; it is known to be superior in predicting the transient response of the beam. The superiority of the Timoshenko model is more pronounced for beams with a low span/depth ratio. The exclusion of shear deformation effect may result in a considerable error of analytical model validation; hence additional source of uncertainty in the measured data is unjustifiably added.

The shear deformation tends to significantly affect the higher natural frequencies rather than the fundamental natural frequency. This observable fact is very influential as truncated sets of modal parameters are less sensitive to local damages, and as a matter of fact high order modal data should therefore be taken to provide better results in damage detection area.

In addition, the results of a consistent mass matrix assume continuous distribution of mass throughout the elements by using their shape functions. For a prismatic beam element including shear deformation the consistent mass coefficients corresponding to the nodal coordinates are determined by a procedure similar to the determination of the stiffness coefficients. In this case, the mass coefficient (m_{ij}) is described as the force at DOF (i) due to unit acceleration at DOF (j) while all other DOFs are maintained at zero acceleration.

The final forms of the stiffness and mass matrices of the beam element are presented in Appendix A; also the derivation of these two matrices is explained in more details.

4.3.4 The Damping Matrix

As in any experiment-based modelling method, EMA methods require richness in the theoretical preparations that will subsequently improve the corresponding analytical simulation. This is simply because that in the experimental field sound arguments must be prepared to explain the most general circumstances, such as uncertain damping type, inevitable randomness of damping distribution and the possibility to encounter non-linear behaviour. Therefore, it is important to consider the effect of various distributions of damping on the vibration of the structure in order to obtain more realistic analytical modelling.

Although damping of systems is highly changeable parameter, and likely to remain unpredictable for the projected future (Ewins, 2000), it is convenient to embark on the effect of damping from a special type of damping, which is easy to represent in the free vibration analysis.

This particular type of damping is designated as proportional damping for the reason that the damping matrix $[C]$ is directly proportional to the stiffness matrix $[K]$ as defined below (Ewins, 2000):

$$[C] = a_0[K] \quad (4.17)$$

Where:

a_0 is an arbitrary proportion factor

The advantage of using this type of damping in the dynamic analysis is that the natural frequencies are very close to those of the undamped system, and the mode shapes are the same. Analysis results have shown that the damped system will have eigenvalues and eigenvectors as described in Equations 4.18 and 4.19 (Ewins, 2000):

$$\bar{\omega}_r = \omega_r \sqrt{1 - \zeta_r^2} \quad (4.18)$$

Where:

$\bar{\omega}_r$ is the damped eigenvalue of the mode r

ω_r is the undamped eigenvalue of the mode r

ζ_r is the viscous damping ratio of the mode r

$$[\phi]_{damp} = [\phi]_{undamp} \quad (4.19)$$

Where:

$[\phi]$ is the eigenvectors matrix

However, the distribution of damping described above is not always found to be reasonable, because the actual damping mechanisms are usually dependable in parallel with stiffness elements (hysteretic or internal damping) and with mass elements (friction damping). The most common form of viscous damping is Rayleigh damping in which

the damping matrix is given by the distribution of structural (hysteretic) damping matrix $[D]$, and is defined proportionally as (Ewins, 2000):

$$[D] = a_0[K] + a_1[M] \quad (4.20)$$

Where:

a_0 and a_1 are arbitrary proportion factors

For the latter individual damping distribution case, the mathematical eigenproblem model should be described as:

$$|[K + iD] - \omega^2[M]| = 0 \quad (4.21)$$

And in this case, the corresponding general FRF matrix is written as (Ewins, 2000):

$$[H(\omega)] = [[K] + i[D] - \omega^2[M]]^{-1} \quad (4.22)$$

In order to simplify the solution of the equations of motion by mode-superposition method, the conditions upon which the uncoupling inertial and elastic forces exist are still applied to the damping matrix. The orthogonality condition of the damping is only satisfied when the damping matrix is considered proportional to the stiffness and/or mass matrices, Equation 4.23. Therefore, the damping coefficient related to each mode (r) can be written as (Clough and Penzien, 2003; Paz, 1991):

$$C_r = 2\zeta_r\omega_r \quad (4.23)$$

It is also useful to employ the measured modal damping instead of the assumed Rayleigh values in the motion equations so as to increase the accuracy of response analysis (Reynolds, 2000).

Including the effect of damping through the proportional damping will improve the overall analytical behaviour, because it removes the sharp peaks of the resonances, widens the peaks of resonance and anti-resonance troughs. In the meantime, the

included damping effect arises as diminished FRF amplitude in the predicted response models.

As a parting comment, the assembled stiffness, mass and damping matrices are used, in this work, within the context of the eigenproblem analysis and also to reproduce analytical FRFs.

4.3.5 Dynamic Modulus of Elasticity

The dynamic modulus of elasticity represents the purely elastic property of concrete and is being utilised in estimating the stiffness matrix of the analytical modal model. The property is measured before the development of the micro cracks in the specimen and when the concrete is unaffected by creep. In fact, the stresses in the structural members are very small under the condition of impact vibration test. As a result, dynamic modulus is almost similar to the initial tangent modulus (Kato and Shimada, 1986; Neville, 1995), and its value is considerably greater than the secant (static) modulus.

For the analytical modal analysis, the following simple empirical formula proposed by Lydon and Balendran (1986) was adopted:

$$E_d = 1.205 E_c \quad (4.24)$$

Where:

E_d is the dynamic (tangent) elastic modulus

E_c is the static (secant) elastic modulus

4.3.6 Freely Supported Beam under Modal Testing

In order to avoid the influence of poorly defined boundary conditions on the modal parameters, a completely free-free test set-up can be adopted as a model for this reason. The procedure can remove significantly the intervention of support rigidity from the test model (Ren and De Roeck, 2002).

In the laboratory testing environment, free boundary condition is one of the extremes that is most frequently employed. For a structure to be really free, it should be suspended (floating) in the air, free in space with no holding points whatsoever. Such

situation is commonly designated as free-free. In the real life, freely supported or ungrounded structure is clearly impossible. However, simulation of free-free conditions is very easy to achieve in laboratory environments. It suffices to suspend or support a structure using very flexible (also designates as soft) springs so that the resonance frequencies of the mass of the structure on the stiffness of the supports or suspension devices are very low and far away from the frequency range of interest. Figures 4.1 and 4.2 exemplify the use of the flexible elastic ropes (bungee cords) for the simulation of free-free conditions of a beam assembly, tested in the horizontal direction (Maia and Silva, 1997).

For the free-free test, the rigid body modes, which are no longer having zero natural frequencies, have values which are very low in relation to those of the bending modes (very low in this context means that the highest rigid body mode frequency is less than 10-20% of that for the lowest bending mode) (Ewins, 2000). If this suspension criterion is satisfied, the rigid body inertia properties can still be derived from the very low frequency behaviour of the structure without having any significant influence on the flexural modes of the tested object.

One added precaution which can be taken to ensure minimum interference by the suspension on the lowest bending mode of the structure is to attach the suspension as close as possible to nodal points of the mode in question. At the same time, particular attention should be paid to the possibility of the suspension adding significant damping to otherwise lightly damped test pieces (Ewins, 2000).

In addition, the primary direction of excitations should generally be perpendicular to the plane that contains the suspension cords, as given in Figure 4.1 (Ewins, 2000).

Dynamic testing experience revealed the difficulty of creating ideal boundary conditions particularly for small structures. The finite rigidity of the supports can significantly influence the mode shapes and eigenfrequencies. Therefore, it is necessary to exclude any spurious contribution from the supporting elements, even for the higher modes. In real-life structures, the resonant frequencies are much smaller compared with the laboratory-size beams because of the longer dimensions. As a result, interfering with

the stiffness of the supports is not of significant effect, at least for the lower modes which are mainly controlling the response (Unger et al., 2006).

As a parting conclusion, when measuring dynamic characteristics of a structure for computer model verification, the free-free boundary condition is preferred over the pinned boundary condition. Similarly, the latter is preferred over the fixed boundary condition (McConnell and Varoto, 2008).

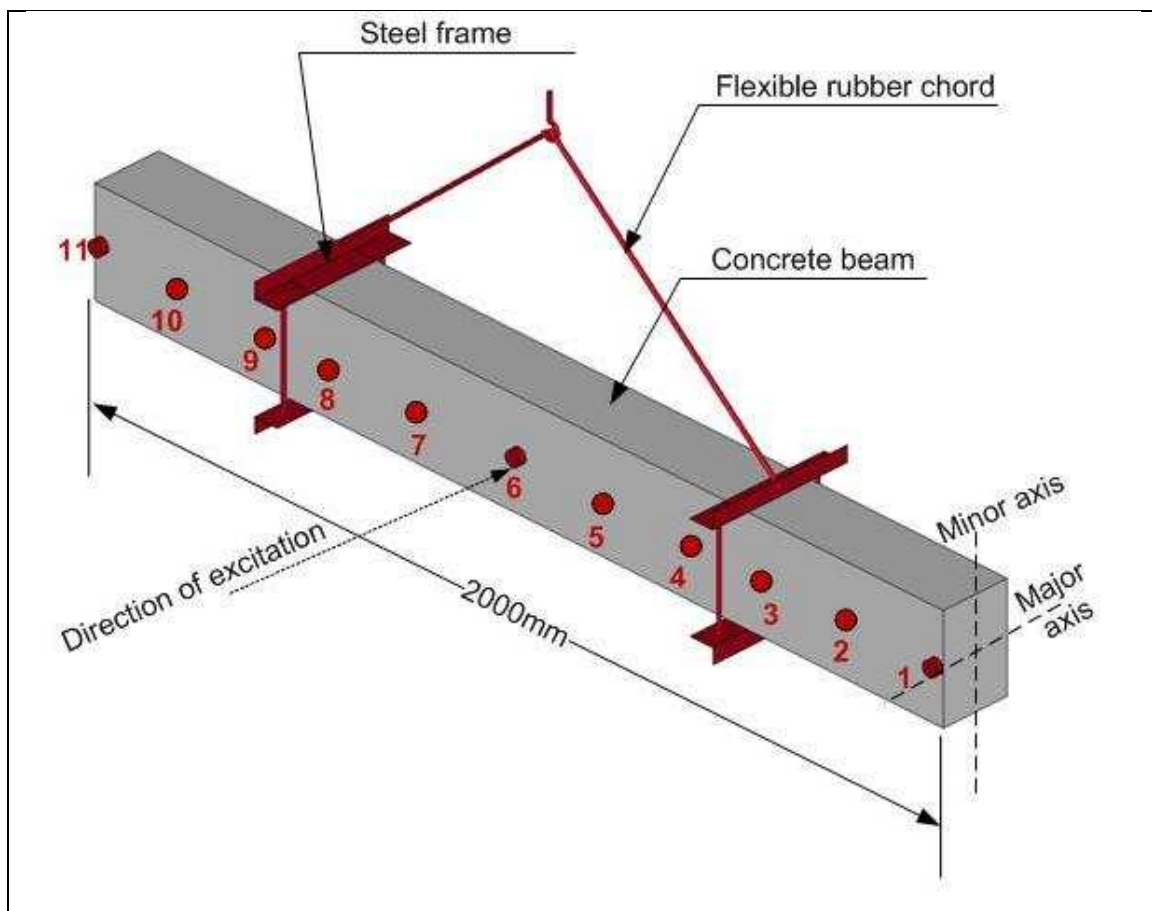


Figure 4.1: Configuration of test beam under free-free support condition.

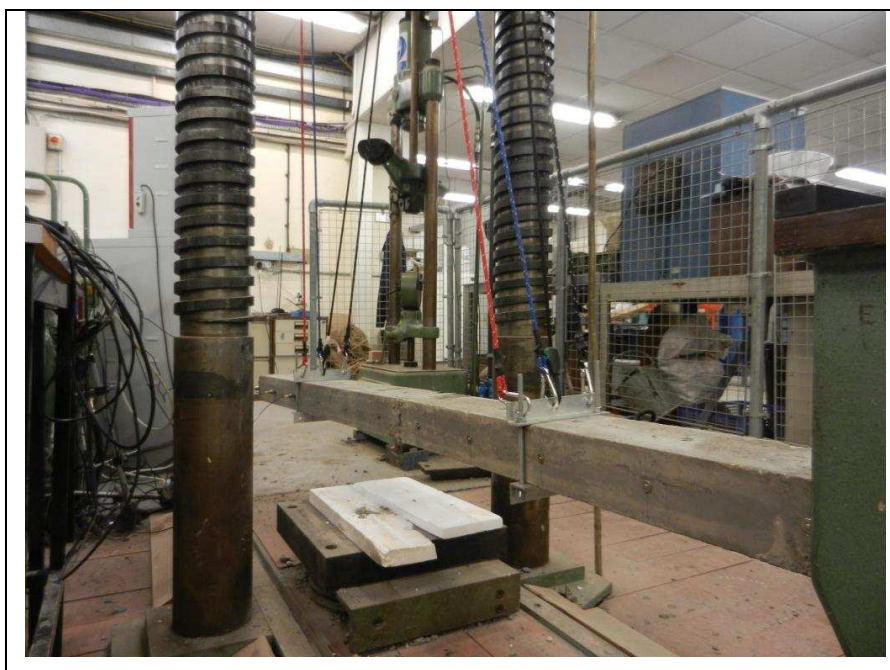


Figure 4.2: Test beam under free-free support condition- photograph.

4.3.7 Practical Implementation of FE Modelling

Prior to the EMA, a preliminary analytical modal analysis should be carried out to explore the frequency range of interest and check the adequacy of the test grid to avoid any spatial aliasing between different mode shapes (Reynolds and Pavic, 2000). Then, the model is further utilised to correlate the analytical model with the EMA results. A successfully correlated analytical model has the potential to predict a baseline model for a structure in its normal condition, as a means to balance the shortage of information for the intact condition, which is critical in any damage identification process.

In this work, the effect of different physical parameters was studied for the spatial undamaged beam in order to predict and update the analytical model. The beam was simulated using linear elastic one-dimensional prismatic beam elements. For this purpose, FE dynamic analysis codes were developed in the MATLAB[®] based environment. Each of the 2.0m beam samples was modelled by 22 beam elements. In order to simulate the ideal free-free boundary condition, yet at the same time, to ensure a stable analysis condition, very small suspension stiffness (1.0N/m) was added at points of suspension. In addition, the effect of shear deformation (Timoshenko beam)

was included in the assembled stiffness and mass matrices of the beam elements. Contrarily to the static analysis, vibration characteristics are highly influenced by the effect of shear deformation as the shear deformation tends to affect the higher modes significantly. Furthermore, the effect of proportional viscous damping was considered in the work in order to achieve more realistic analytical model. Finally, the dynamic modulus of elasticity (tangent) estimated using the empirical formula given in Equation 4.27 was used in predicting the analytical model.

4.4 Theory of Experimental Modal Analysis

4.4.1 Theoretical Background

It is generally believed that more confidence can be put on experimental data since measurements are taken on a true structure. Therefore, the physical parameters, which are obtained as results of the modal testing, can be used credibly in various ways to avoid or to cure the problems encountered in structural dynamics. In the experimental route, vibration measurements are directly collected from a physical structure, without any assumptions about the constructed model, and that is the reason why modal testing models are considered to be more reliable than other theoretical or numerical models.

On the whole, the experimental approach that describes the vibration behaviour of the structures is referred to as modal testing, or EMA, on which the vibration characteristics of a structure is studied from the collected measurements. It is evidence that neither the spatial model as explained by Equation 4.1 nor the modal model as explained by Equations 4.15 and 4.16 are capable of providing measured physical parameters for the structure. Therefore, the basic constitution law defined by Equation 4.25 is recalled to set up the relationship between the excitation force and response (Ewins, 2000):

$$Properties = \frac{Response (output)}{Force (input)} \quad (4.25)$$

For a system of known properties, any additional measured parameter in Equation 4.25 is sufficient to describe the entire event of a system completely. Conversely, when the properties of the tested structure are unknown, both parameters, the response and the force, must be measured simultaneously in order to define the features of the system.

Modal testing lies in the last type of testing, where the output response along with the input excitation are simultaneously collected to construct the FRF measurements, which are necessary for subsequent modal analysis and modelling stage (Ewins, 2000). The experimental measurement of the ratio between the responses of the structure to the excitation forces resulting in $N \times N$ frequency response matrix $[H(\omega)]$ constitutes the response model. The mathematical description of the response model was previously given in Equations 4.5 and 4.6 where only this model is able to give a physical estimate to the properties of a structure.

4.4.2 Fundamental Components of Experimental Modal Analysis

The EMA scheme includes various instrumentation components such as the one adopted in the current research and illustrated in Figure 4.3, which shows a generic layout of the modal test set-up.

However, there are three basic components that are considered essential in any modal testing, which are:

- an excitation tool to induce the exciting force;
- a transduction sensing system to measure the response; and
- an analyser, to capture, process and analyse the data.

In general, the procedure of EMA consists of three fundamental steps, these steps as given in Figure 4.4 are:

1. Acquiring the analogue excitation and response time signals
2. Processing the signals, this includes filtering, sampling, windowing and transforming the signals into frequency domain
3. Extracting the modal parameters from the constructed FRFs

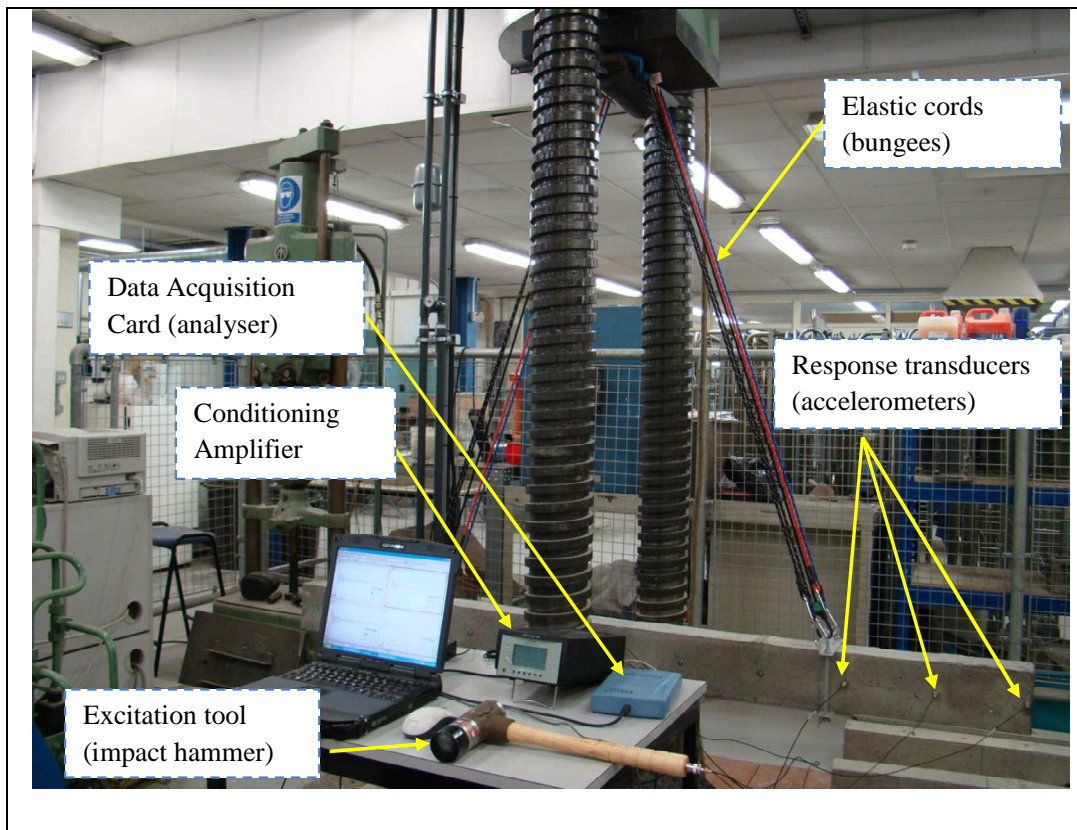


Figure 4.3: Generic impact hammer modal testing set-up.

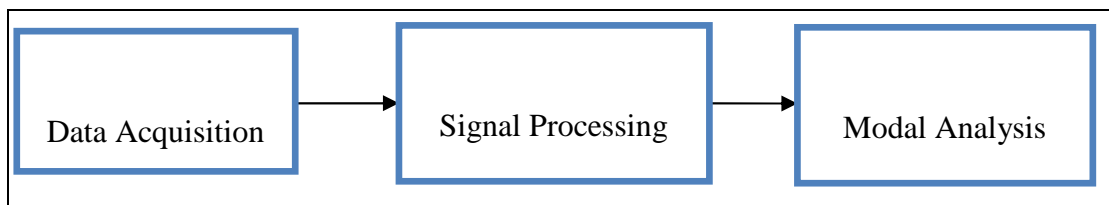


Figure 4.4: Three fundamental steps of EMA.

Furthermore, in order to obtain a complete mathematical definition to a test structure, a proper set of modal parameters should be determined resulting in full measurements of the natural frequencies (ω_n), damping ratios (ζ_n) and mode shape vectors $\{\phi_n\}$. The procedure of determining these parameters consists of three major steps:

- Measuring an appropriate set of FRFs
- Analysing these functions using an appropriate curve-fitting procedure
- Combining the results of the curve-fits to construct the required model

Using the knowledge of the theoretical relationship between FRFs and modal properties, it is possible to show that an appropriate set of FRFs, including either one row or one column of the FRFs matrix $[H(\omega)]$, is sufficient to construct a complete mathematical model. In practice, this either means exciting the structure at one point and measuring the responses at the (n) points or measuring the response at one point, while the excitation force is roved at each of the (n) points, in turn. The last option is most conveniently achieved using a hammer or other non-attaching excitation device (Ewins, 2000).

4.4.3 Derivation of Frequency Response Function

As FRF relates the response of a structure to an applied force, it is considered the fundamental relationship for defining the characteristics of a linear system. The simplest FRF form requires a process using input-output channel frequency analyser. These dual channels are basic to process the ratio of an output to input signals. For a linear system in time history, the input signal $f(t)$, output signal $x(t)$ and the property response function $h(t)$ are all related in the time domain by the so-called Duhamel integral, which can be described as (McConnell and Varoto, 2008):

$$x(t) = \int_{-\infty}^t f(\tau)h(t - \tau)d\tau \quad (4.26)$$

Then, the sampled digital signals are transferred to the frequency components using Fourier transform (Fourier series) in order to calculate the complex Fourier components of the signals. These equations are defined as:

$$\begin{aligned} X(\omega) &= \mathcal{F}[x(t)] \\ F(\omega) &= \mathcal{F}[f(t)] \\ H(\omega) &= \mathcal{F}[h(t)] \end{aligned} \quad (4.27)$$

Where:

\mathcal{F} is used to represent the Fourier transform of the corresponding time signal

Subsequently, FRF relationship for a linear structure in the frequency domain can be expressed as (McConnell and Varoto, 2008):

$$X(\omega) = H(\omega) F(\omega) \quad (4.28)$$

However, Fourier Transform requires a complete periodic representation content of the sampled data. For a periodic or transient input or output signals, an FRF can be directly estimated from the basic form given in Equation 4.28. Nonetheless, when these signals are stationary random this is not the case; hence, a relevant methodology is needed to cover such type of signals. This is achieved through a method for computation of FRFs that is appropriate to all types of signals often referred to as FRF estimator (Reynolds, 2000).

The most frequent FRF estimator is called $H_1(\omega)$ and is calculated by multiplying Equation 4.28 by the conjugate of the input frequency spectrum $F^*(\omega)$, which can be written as:

$$F^*(\omega) X(\omega) = H(\omega) F^*(\omega) F(\omega) \quad (4.29)$$

The computed auto-spectra of the input signals (S_{ff}) and the cross-spectra between the output and input signals (S_{fx}) are used to estimate the corresponding FRF. Thus, Equation 4.29 can be rewritten as:

$$H(\omega) = H_1(\omega) = \frac{S_{fx}(\omega)}{S_{ff}(\omega)} \quad (4.30)$$

Where:

$S_{fx}(\omega)$ is the dual-sided cross-spectrum between input and output

$S_{ff}(\omega)$ is the dual-sided auto-spectrum of the input excitation signal

Only single-sided auto-spectrum $G_{ff}(\omega)$ and single-sided cross-spectrum $G_{fx}(\omega)$ defined for positive ω are commonly utilised to obtain FRF measurements. As a result, the FRF formula can be rewritten as (McConnell and Varoto, 2008):

$$H_1(\omega) = \frac{G_{fx}(\omega)}{G_{ff}(\omega)} \quad 0 < \omega < +\infty \quad (4.31)$$

The second estimate of $H(\omega)$ is known as $H_2(\omega)$, and derived by multiplying each side of Equation 4.28 by the conjugate of the output response frequency spectrum $X^*(\omega)$; hence $H(\omega)$ can be defined as:

$$X^*(\omega) X(\omega) = H(\omega) X^*(\omega) F(\omega) \quad (4.32)$$

$$H(\omega) = H_2(\omega) = \frac{S_{xx}(\omega)}{S_{xf}(\omega)} \quad (4.33)$$

For single-sided frequency spectra, Equation 4.33 can be written as:

$$H_2(\omega) = \frac{G_{xx}(\omega)}{G_{xf}(\omega)} \quad 0 < \omega < +\infty \quad (4.34)$$

The values obtained by $H_1(\omega)$ and $H_2(\omega)$ are different and depending on the measurement situation, particularly signal noise. Theoretically, the phase in both equations is the same (Ewins, 2000). In this research, $H_1(\omega)$ was used to process the calculation of FRFs from the time histories. H_1 estimator is advantageous compared with H_2 , when the noise is present in the response signal and uncorrelated with the force noise. The noise is likely to decrease with the averaging (McConnell and Varoto, 2008).

Furthermore, the third estimate is called $H_a(\omega)$ and calculated by using only the magnitude (modulus) of both sides of basic FRF relationship (Equation 4.28) so as to obtain a general estimate to the FRF magnitude. This magnitude can be derived as:

$$X^*(\omega) X(\omega) = H^*(\omega) H(\omega) F^*(\omega) F(\omega) \quad (4.35)$$

$$|H(\omega)|^2 = |H_a(\omega)|^2 = \frac{S_{xx}(\omega)}{S_{ff}(\omega)} \quad (4.36)$$

Once again, for single-sided frequency spectra, Equation 4.36 can be written as:

$$|H(\omega)|^2 = \frac{G_{xx}(\omega)}{G_{ff}(\omega)} \quad 0 < \omega < +\infty \quad (4.37)$$

As a verification check, the degree of linear relationship between the output and the input at each frequency, referred to as the coherence function $\gamma^2(\omega)$, is used as a measure of accuracy. The coherence function is a useful means of specifying the degree of correlation between two functions, $H_1(\omega)$ and $H_2(\omega)$, at each frequency point, and can be described as:

$$\gamma^2(\omega) = \frac{H_1(\omega)}{H_2(\omega)} \quad (4.38)$$

$$\gamma^2(\omega) = \frac{|S_{fx}(\omega)|^2}{S_{ff}(\omega) \cdot S_{xx}(\omega)} = \frac{|G_{fx}(\omega)|^2}{G_{ff}(\omega) \cdot G_{xx}(\omega)} \quad (4.39)$$

The coherence function is used as a data quality assessment tool which identifies how much the linearity of the output signal is related to the linearity of the measured input signal and is rated on a scale of 0 to 1 (Ewins, 2000). It is worth saying that this estimate is based on statistical averages of the quantities $G_{ff}(\omega)$, $G_{xx}(\omega)$ and $G_{fx}(\omega)$. If this quantity is calculated for single measurements, the coherence will be unity, even in the presence of noise, since there is no information available to indicate that the output is not due to the input. However, it is only for several measurements are averaged that the coherence concept can detect the lack of relationship (McConnell and Varoto, 2008).

The instant frequency spectra, which are the resulting Fourier transform for each channel, are used to create the averaged auto-spectra $G_{ff}(\omega)$, $G_{xx}(\omega)$ and averaged cross-spectra $G_{fx}(\omega)$. The averaged auto-spectra and cross-spectra are then utilised to generate the FRF and the coherence function. The important averaged FRF and coherence measurements can be mathematically defined as in Equations 4.40 and 4.41, respectively:

$$H(\omega) = \frac{\sum_{i=1}^n [G_{fx}(\omega)]_i}{\sum_{i=1}^n [G_{ff}(\omega)]_i} \quad (4.40)$$

$$\gamma^2(\omega) = \frac{|\sum_{i=1}^n [G_{fx}(\omega)]_i|^2}{\sum_{i=1}^n [G_{ff}(\omega) * G_{xx}(\omega)]_i} \quad (4.41)$$

Where:

n is the number of specified averages carried out on the measurements

As a principle for impact tests, five averages are usually accepted as an adequate number to reduce the statistical variance of a measurement due to the random noise and also due to the effects of nonlinearities (Agilent Technologies, 2000; Catbas et al., 2008).

4.4.4 Sampling and Quantisation of Continuous Time Signals

In fact, one of the fundamental steps in signal processing analysis is to convert the original analogue signals into digital signals. In this step, an analogue signal is converted at equal time steps (Δt) over a specific time period (T), and referred to as sampling of the signal. Conversely, apart from the horizontal sampling of the analogue signal, the process of describing the amplitude of the discrete time signal is referred to as quantisation. The main aspects of these two steps are illustrated and explained in details in Appendix B.

4.5 Transducers and Data Acquisition Devices

4.5.1 Force Transducers

Practically, the input dynamic forces can be applied through ambient excitation loading such as traffic loading in bridges. Specifically, in EMA the input force is applied through contacting or non-contacting devices (Ewins, 2000). In the first type, an exciter remains in direct contact to the structure during the test providing either continuous (periodic, random) or transient (pulse, chirp) excitation signals. The second type represents devices provided force either without direct contact, such as an electromagnet, or in contact for a short period, such as a hammer (Ewins, 2000). Conversely, it is most convenient for modal testing of structures with straight, linear components to induce such force through impact excitation. The excitation is produced by hitting a structure with an impact hammer which is easily to move along the tested elements, and the responses are collected from fixed accelerometers. As a result, large number of FRFs is generated within relatively short time (McConnell and Varoto,

2008). The hammer does not need a connecting device, and has no mass-load effect on the test structure. It provides a small, light, cheap excitation technique (Maia and Silva, 1997) and relevant for field measurements. However, the impact pulse of this equipment is difficult to control in shape, amplitude, position and direction for several consecutive excitations. In addition, the challenges arise in test structures contain nonlinearities (Maia and Silva, 1997). Inasmuch as the favourable advantages of hammer excitation and in the same time to explore the effect of the above mentioned disadvantages on RC beams afflicted with various nonlinearities, the excitation in this work was provided by the means of the impact hammer.

4.5.1.1 Instrumented Impact Hammer Excitation

The DeltaTron[®] impact hammer version 8208 used for all measurements collected in this work is shown in Figure 4.5. The hammer is supplied with a set of four interchangeable impact tips controlling the frequency content and the impulse. The mass of the hammer head is 1.4kg (3lb) and the nominal force range is 22.1kN (5000lb) for full scale of $\pm 5V$, and its reference sensitivity is 0.22mV/N (1.00mV/lb). The force signal is measured using a piezoelectric force transducer located inside the hammer head. The force transducer contains an integrated amplifier which permits the hammer to be connected to the conditioning amplifier unit using a 5.0m (16.4ft) PVC insulating cable by a means of BNC connector without significant degradation in the signal.

As the hammer hits a structure, the induced input time signal is typically of a very short half-sine or a delta function resulting in a flat spectrum over the excited range of frequency, as shown in Figure 4.6. This signal is embodied by its peak value and duration time, where the frequency bandwidth is inversely proportional to the impulse duration. The excitation force is controlled by the hammer mass and resilience of the tip. The tip resilience needs to select such that all the modes of interest are excited by the impact force over the frequency range being considered. The harder is the tip, the wider the frequency range that is covered by the force. In this work, the impact force was generated from a hammer with the hard tip which manages to excite frequency range of up to 1000Hz, as shown in the frequency spectra of Figure 4.6. Beyond the

assigned frequency range, the force induced by the hardest tip does not excite higher modes; therefore, higher frequencies are not expected to show in the frequency spectra.

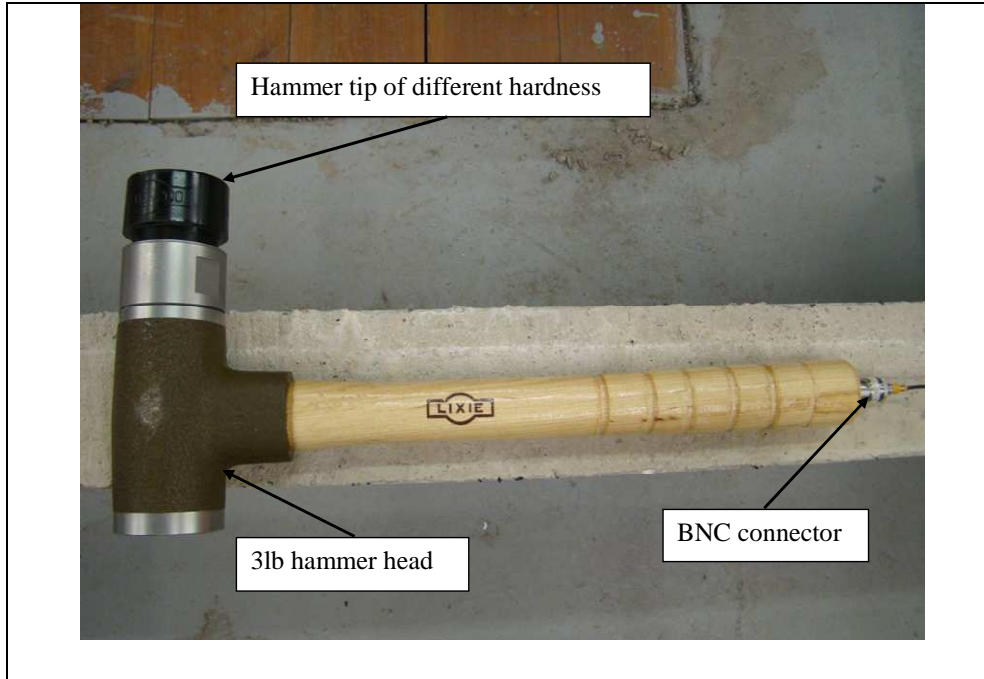


Figure 4.5: DeltaTron[®] version 8208 instrumented impact hammer- photograph.

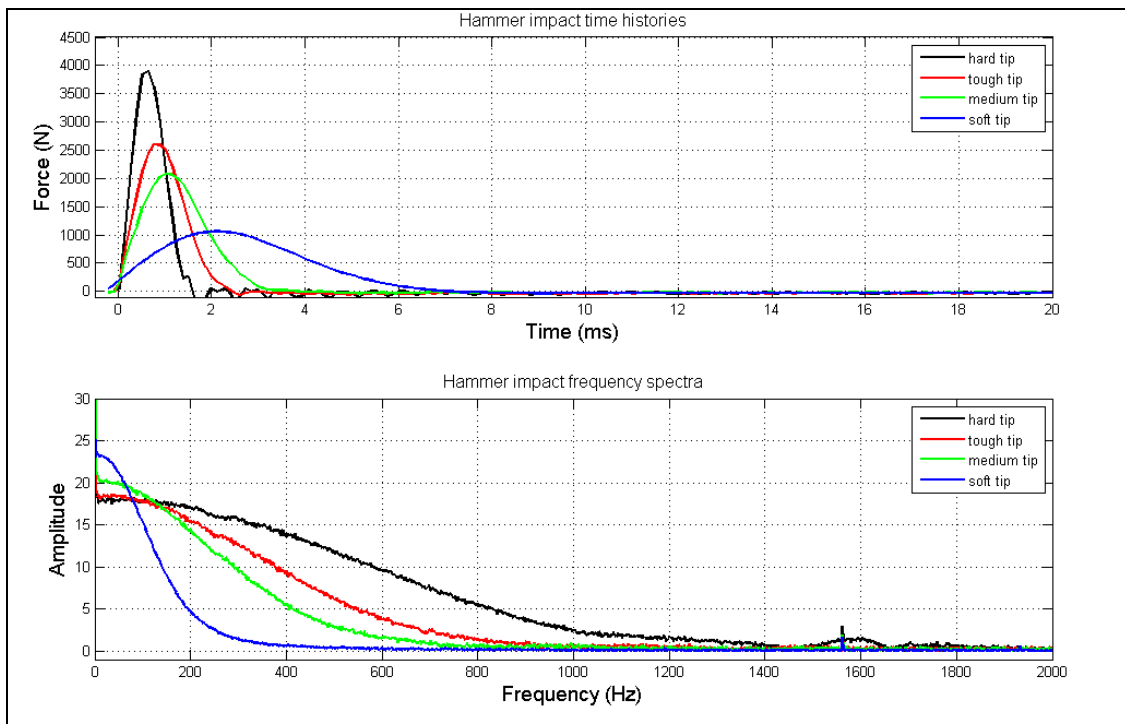


Figure 4.6: Impact time histories and frequency spectra from different hammer tips.

4.5.2 Response Transducers (Accelerometers)

The vibration responses of the RC beams were collected using DeltaTron[®] model 4514 accelerometers with a sensitivity of 1.005mV/ms^{-2} (9.86mV/g) and frequency range of 1Hz-10kHz. A sample of the accelerometer used in the measurements is shown in Figure 4.7. The accelerometer includes integrated amplifier that converts the movement of the seismic mass into acceleration signal in the form of voltage. In order to measure the acceleration response of the RC beams, steel studs were glued first on the measuring grid of each beam (Figures 4.2 and 4.3). Then, the accelerometers were attached to the studs by which the studs and the screwed accelerometers were affixed normal to the structure surface. This arrangement permits to attach and rove the accelerometers over the test sample as well as the accelerometers to capture the responses in the direction of excitation without big problem of transverse sensitivity.

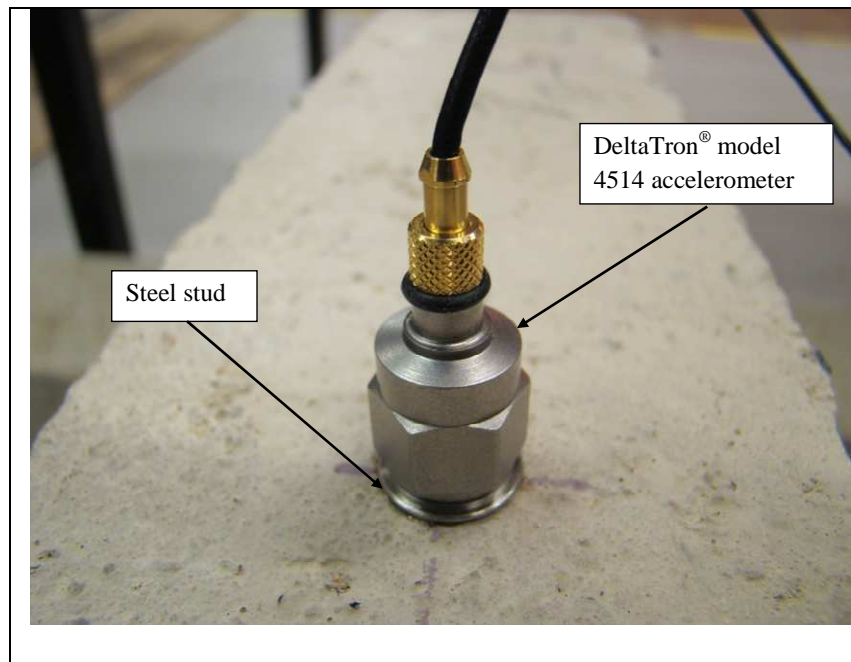


Figure 4.7: DeltaTron[®] model 4514 accelerometer–photograph.

4.5.3 Data Acquisition Devices

The desired gains are set for amplification the input signal in order to generate optimal measurement resolution and noise reduction provided the resulting output signal plus any overshoot voltage will not exceed the limit of the output range of the amplifiers (i.e. $\pm 5\text{V}$). The Data Acquisition (DAQ) system used for the measurements consists of 4

channels simultaneously sampling differential amplifier modules for signal conditioning, NEXUS™ type 2690 conditioning amplifier, Figure 4.3. After the analogue time signals were captured and before any digitisation is performed, the signals should be filtered to remove the interfering of higher frequencies into the analysis frequency range. This is usually done through the use of a set of analogue filters on the front-end of the sampling system called anti-aliasing filters (Avitabile, 2001). The NEXUS™ 2690 module comprising a low-pass, sharp roll off 8th order Bessel filter was used to take out any high frequency signals that might occur in the identified range. The NEXUS™ 2690 module has a cut-off frequency that ranges from 0.1Hz to 22.4kHz.

Next, the captured time signals were sampled to the N digital data points to represent the original continuous signals. All the signals were sampled on a four-channel 12-bit high-resolution PicoScope 4424 DAQ. The DAQ oscilloscope is controlled using its own software that can be used for signal acquisition where four input signals are digitally sampled and transformed into frequency domain; however, the system is unable to perform immediate calculation of FRFs. In this respect, the raw digital time signals were stored directly on a PC, and a signal processing analysis code was devised in the MATLAB® environment for subsequent modal analysis including the FRF and coherence function computations. It is worth pointing out that the sampling parameters selected to digitise the analogue signals captured the signals in the assigned finite time window ($T=500\text{ms}$). Therefore, this characteristic skips the need for applying window function at the time signals (Avitabile, 2007).

4.6 Experimental Modal Analysis Procedure

Reynolds (2000) and Reynolds and Pavic (2000) reported that the UK Dynamic Testing Agency (DTA) divided the EMA procedure into four phases, as follows:

1. The preparatory phase
2. The exploratory phase
3. The measurement phase
4. The post-test analysis and modal parameter estimation phase

The structure of EMA was followed completely during the course of this project in order to satisfy the predetermined requirements and to acquire high quality measurements. The theoretical description of these four phases as well as the procedure and benefit of each necessary check will be explained in this section. However, the experimental results of each phase and related checks are left for Chapter 6.

4.6.1 Phase I: The Preparatory Phase

This is the first step in any modal testing process where an estimate to the natural frequencies of a system is determined. The maximum observable frequency is inversely proportional to the time step (Δt) chosen, which was defined in Equation B.3 (Appendix B). In this study, 4096 samples were taken at a sampling rate of 8.2ksample/s ($\Delta t = 0.000122\text{s}$, $f_s = 8192\text{Hz}$, $\Delta f = 2\text{Hz}$).

Based on this estimate along with the number of modes needs to collect, an appropriate measuring kit and its proper range were chosen. Equally important, numerical models are also used for selection of the test grid, reference accelerometer locations, and check the adequacy of the test grid to avoid any spatial aliasing between different mode shapes (Reynold and Pavic, 2000). For instance, in the free-free beam test of Figure 4.1, if accelerometers were only attached at positions 1, 3, 6, 9, and 11, there would have been symmetry between the second and the fourth mode due to the spatial aliasing of different mode shapes.

4.6.2 Phase II: The Exploratory Phase

This phase includes conducting a number of preliminary measurement checks to determine the suitability of the structure for modal testing; to help in the selection of data acquisition setting parameters; and exploring the stability and consistency of the measured data. These first round measurements are the key element of the quality assurance (QA) system applicable at all EMA (Reynolds and Pavic, 2000). They comprise a series of successive measurements that are described in the rest of this section.

4.6.2.1 Excitation/Response Check

This check requires inducing an input excitation to the structure, and at the same time capturing this signal and the corresponding response of the structure with a sampling rate that describes reasonably both signals. Both the time domain signals and the associated frequency spectra are visually examined. The shape, clarity, and strength of each measured signal together with other main characteristics, such as the duration of the impact signal, must be satisfied. In the context of impact time histories, there should be a half-sine shape function when the force is applied using a soft hammer tip on the concrete surface. Sharper peak with shorter duration of a delta shape function is expected when a hammer of harder tip is used, Figure (4.6). In the frequency domain respective, the shape of the time signal results in a flat spectrum over the excited range of frequency where a good idea about the frequency bandwidth can be drawn. In the context of response time signals, for a driving point function ($H_{1,1}$) Figure 4.1, the response should start immediately, while there is a small delay for the remote transfer function ($H_{11,1}$), because of the speed of wave propagation through the structure (Reynolds, 2000). Through the visual observation of time domain input/output signals, any potential jump of the accelerometer due to the blow of the hammer will be revealed. In addition, indications of loose connection of transducer cables will be soon observed, specifically when motivated by the movement of the test object or the hammer (Reynolds and Pavic, 2000).

4.6.2.2 Immediate Repeatability Check

The immediate repeatability as an essential check in any EMA is carried out to ensure the repeatability of definite measurements. For this check, two successive identical driving point FRF measurements are made. Then, the FRFs are to be compared and should have an almost similar shape. In theory, they should be identical, whereas, in practice, small differences between the two FRFs, caused by unmeasured noise, will appear and are acceptable (Reynolds and Pavic, 2000). In this check is the first time where the FRF calculations are performed and visualised. Therefore, it is quite convenient, at this stage, to examine the quality of FRF data, such as the shape, duration, and frequency content. In addition, measured FRFs can be utilised to perform some Single Degree Of Freedom (SDOF) curve fitting or peak amplitude analysis in

order to explore the reliability of the measurements compared with the preliminary analytical results.

4.6.2.3 Homogeneity Check

This test is the first of the two linearity checks conducted on the test structure. The check is slightly different from the repeatability check, where non-identical measurements are made. The FRF is measured using slightly different set-up, such as different excitation signals, to the original signal. In this check, measurement data is endeavoured to prove independent of the tested structure, aiming at checking the linearity of the structural behaviour (Ewins, 2000; Reynolds and Pavic, 2000). In the impact excitation test, a reliability check is carried out using different hammer tips to induce different excitation levels. In order to ensure the linearity of a structure, the low and high excitation levels should not highlight any significant variation between the FRF measurements.

4.6.2.4 Reciprocity Check

The reciprocity check is the second of the two linearity checks organised to the test structure, which is based on Maxwell's Reciprocity Theorem. This theorem states that, for a linear elastic structure, transfer mobility FRF measured by the excitation force at a point (i) and the response at a point (j) is identical to a transfer mobility measured by the response at a point (i) and the excitation force at a point (j) (Ghali et al., 2009). Once again, the current check aims at implying the linearity of the structure when two different transfer measurements display very good correlation and the plots of the functions overlay well.

4.6.2.5 FRF Shape Check

In this check, one of the necessary properties in FRF measurements is to ensure the occurrence of relatively clear anti-resonance troughs. For a driving point FRF, there must be a clear anti-resonance existing between each two adjacent resonances. However, for transfer point FRF; it is most likely to expect a valley between two adjacent resonances rather than trough. The second property, which gives a rational decision about the accuracy of the measured FRFs, is the resonance and anti-resonance

peaks should display the same sharpness on a semi-log plot. The success to achieve so indicates a good measurement quality, both in the context of frequency resolution and adequate excitation level resulting in a reasonable definition of the resonance region. Other useful observation can be drawn from transfer function at nodal points where it displays only some natural modes. For example, the mid span FRF in a symmetrical beam will show only the odd modes (1st, 3rd, 5th, etc). Therefore, the even modes (2nd and 4th, etc modes) will not be seen in the FRF measurement. Results of this check confirm the fact that a limited set of measured transfer functions and/or poor selection for these measurements will allow some resonances not being appeared, even when they are excited, as the accelerometer is placed at a node point. Another visual check aids to assess qualitatively the FRF measurements is that a negative phase loss through resonance frequencies and a positive phase gain through anti-resonances can be observed. For point mobility FRF, the value of phase is always between 0° and 180° (Maia and Silva, 1997).

4.6.2.6 Coherence Function Check

The verification of the degree of linear relationship between the output and the input at each frequency, referred to as the coherence function γ^2 , is used as a check for the accuracy of measurements. The coherence function was derived and given in Equation 4.39. The function is used as a data-quality assessment tool by identifying how much the linearity of the output signal is related to the linearity of the input signal and is rated on a scale of 0 to 1. It is worth saying that this estimate is based on statistical averages of the quantities $G_{ff}(\omega)$, $G_{xx}(\omega)$ and $G_{fx}(\omega)$, as given in Equation 4.41. If this quantity is calculated for single measurements, the coherence will be unity, even in the presence of noise, since there is no information available to indicate that the output is not due to the input. However, it is only for several successive averaged measurements the coherence function can detect the lack of relationship (McConnell and Varoto, 2008).

Generally, it is necessary to average several individual time signals before confident results are obtained. The two major reasons behind the need for averaging are: to get statistical authentic measurements; and to remove the false random noise from the acquired signals (Ewins, 2000). The value of the coherence function at frequencies

close to the modes of vibration of the structure should be close to unity. Reynolds (2000) reported that the UK Dynamic Testing Agency (DTA, 1993) suggest a minimum value of 0.9. However, for measurements made on civil engineering structures, a low value of the coherence function is accounted for a level of background noise. There could be point in the coherence check where their values dip off lower than 0.9 at all resonances close to modes of vibration (Reynolds, 2000). This suggests a high level of extraneous unmeasured noise, when other reasons for low coherence values can be dropped through the linearity and other checks. As a parting comment, low values of coherence can be eliminated, when a random noise contributes majorly to the poor coherence results (Ewins, 2000).

4.6.3 Phase III: The Measurements Phase

This phase represents the main data acquisition stage, where all required and necessary FRF data is collected. Single-input excitation method is the most straightforward implemented method. Theoretically, one measured row or column of the FRF matrix is enough to describe all modal parameters for a structure, as given in Equations 4.13 and 4.14. The driving point FRF gives information on the modal frequencies and damping ratios of the system, while a complete set of FRFs contains information regarding the mode shapes at the measured locations. However, in practice, the information from a single row or a single column could be insufficient to describe the vibration mode shapes accurately, and several successive measurements of single-input may be implemented (Maia and Silva, 1997). The simplest form of single-input method is the impact test where the excitation is induced through an instrumented hammer and responses are captured through only one fixed accelerometer. In this situation, one row in the FRF matrix is measured.

4.6.4 Phase IV: The Post-Test Analysis Phase

This phase is normally carried out after field measurements are recorded and their quality is assured. In this stage, FRF measurements are analysed to determine the modal parameters of the test structure. In the context of modal parameter extraction, various methods are available to perform a convenient analysis and obtain the mathematical model. As very suitable to the measurements of this research, the simplest modal

analysis model between the SDOF methods designated as peak picking or peak amplitude is used. The method functions satisfactorily in structures that their FRFs show well-defined separated modes at resonance frequencies (Ewins, 2000).

Other alternative methods are classified as Multi Degree Of Freedom (MDOF) modal analysis methods. These general global methods are used in particular cases where more detailed curing is necessary for closely spaced coupled modes of FRF measurements or for heavily damped structures by which the resonance is not dominated by one mode only (Ewins, 2000). The mathematical background of the peak amplitude method and its application on the measurements from this work is given in Chapter 6.

4.7 Summary

First, this Chapter embarks on the theoretical relationships among the three models of the dynamics of structures, namely: the spatial, modal and response models. The fundamental criteria and their related derivations needed to define each model are made.

Second, the Chapter provides a brief theoretical background to the analytical and experimental modal analysis. The distributed material and geometric parameters that affect predicting a reliable analytical model for beam-like RC structures are discussed. In this context, FE beam elements with particular consideration to the modelling of support condition; dynamic modulus of elasticity; shear deformation effect; and assumption of proportional damping are found accountable to generate correlated modal data. One of the important benefits of predicting analytical model is to derive with confidence vibration parameters of quantities such as rotational DOFs which are difficult to measure experimentally (Ewins, 2000; Maia and Silva, 1997).

Third, complete derivations for the formulae related to the computation of modal data such as FRF and coherence function are given. The knowledge gained from the mathematical formulations is used to develop the codes of utility software for both the numerical FE model and experimental modal measurements.

Fourth, the Chapter describes the specifications, details and proper set-up for the equipments commissioned for this work. Also, general facts on the signal processing analysis and the concepts influence the quality of the measurements are reviewed.

Finally, the paradigm for the procedure of EMA technique is explained comprehensively along with the necessary phases and corresponding checks involved in the procedure. The four phases for a typical modal testing, as given in the UK DTA (1993), are reviewed for implementing in civil engineering structures. Through following rigorous testing procedures with all necessary checks, one can ensure that the vibration measurements whether in the time, modal or frequency domain- represent a realistic experimental model of the dynamics of structure.

5. Research Methodology

5.1 Introduction

As concluded from the literature review covered in Chapter 3, one can underline vigorously the following basic difficulties in using the modal parameters alongside the model-based diagnosis techniques:

1. FE models and other conventional modal parameters models often require intensive labour processing, computations, corrections and turn out with unavoidable inaccuracies caused by the user intervention and modelling inaccuracy (Sohn and Farrar, 2001).
2. All vibration-based damage detection processes depend on experimental measurements with inherent uncertainties, particularly when acquired from civil engineering infrastructure, which is always subjected to severe operational and/or environmental conditions (Fugate et al., 2001).
3. The modal parameters (resonances, damping ratios and mode shapes) as damage-sensitive features are incapable to distinguish between changes from structural damage or from operational and environmental effects (Figuerido et al., 2009).
4. Boundary conditions in a structure may cause changes in the vibration data, if these boundary conditions are prone to changes with age. In the term of data recognition, complex mathematical techniques, including nonlinear modelling, need to be set in order to obtain the most probable solution (Wenzel, 2009).
5. The demerit of dealing with the modal parameters instead of the FRF is that the curve fitting process might remove information that would assist to identify the damage. In fact, in FRF the data is closer to the raw state condition of the system (Friswell, 2007).

On the other hand, Statistical Pattern Recognition (SPR) paradigm, as opposed to its counterparts FE and other model-based models, has the following merits:

1. A successful smart recognition algorithm should perform a real-time analysis and implements online identification for data collected at site. The process requires a simple and credible routine that can supply decisive diagnosis in a well-timed way. Signal-only-based approach makes the statistical evaluation approach vibrant for the development of an automated health monitoring system.
2. Statistical analysis procedures are crucial if the changes in vibration response need to be indicative of damage than to be related to the operational and/or environmental variability (Fugate et al., 2001; Sohn et al., 2000). The central idea of a successful investigation is to determine features that are sensitive to damage, and not sensitive to the operational and environmental conditions (Worden et al., 2007).
3. In the problem of damage identification when approached through SPR paradigm, modelling errors, design parameters' assumptions, human contribution and computational errors are to be avoided as much as possible (Sohn and Farrar, 2001). In addition, uncertainties in measurements can be swallowed without affecting the damage diagnosis effort.

Having considered the limitations of the modal parameters in the model-based methods and the advantages of SPR methods, this research focuses mainly on developing a new statistical-based damage identification technique that functions with data collected at site without a need for overwhelming curve fitting and modelling. In order to make the technique more capable to handle real-time immense data, different data sets from time and frequency domain measurements are tested as prospective damage sensitive features. The outcome of the proposed damage identification algorithm can subsequently be supplemented by any suitable model-based method for further inspection of the condition of structure. Therefore, the main effort of this research mobilises on the objective of testing wide range of damage sensitive features in the suggested non-model-based statistical damage identification method. Nonetheless, in Chapter 7, one of the prominent model-based methods, Direct Stiffness Calculation (DSC), is explored as a supplemental tool to ultimately locate the damage and quantify

its scale. The flow chart for the methodology of the identification procedure adopted in this research is shown if Figure 5.1.

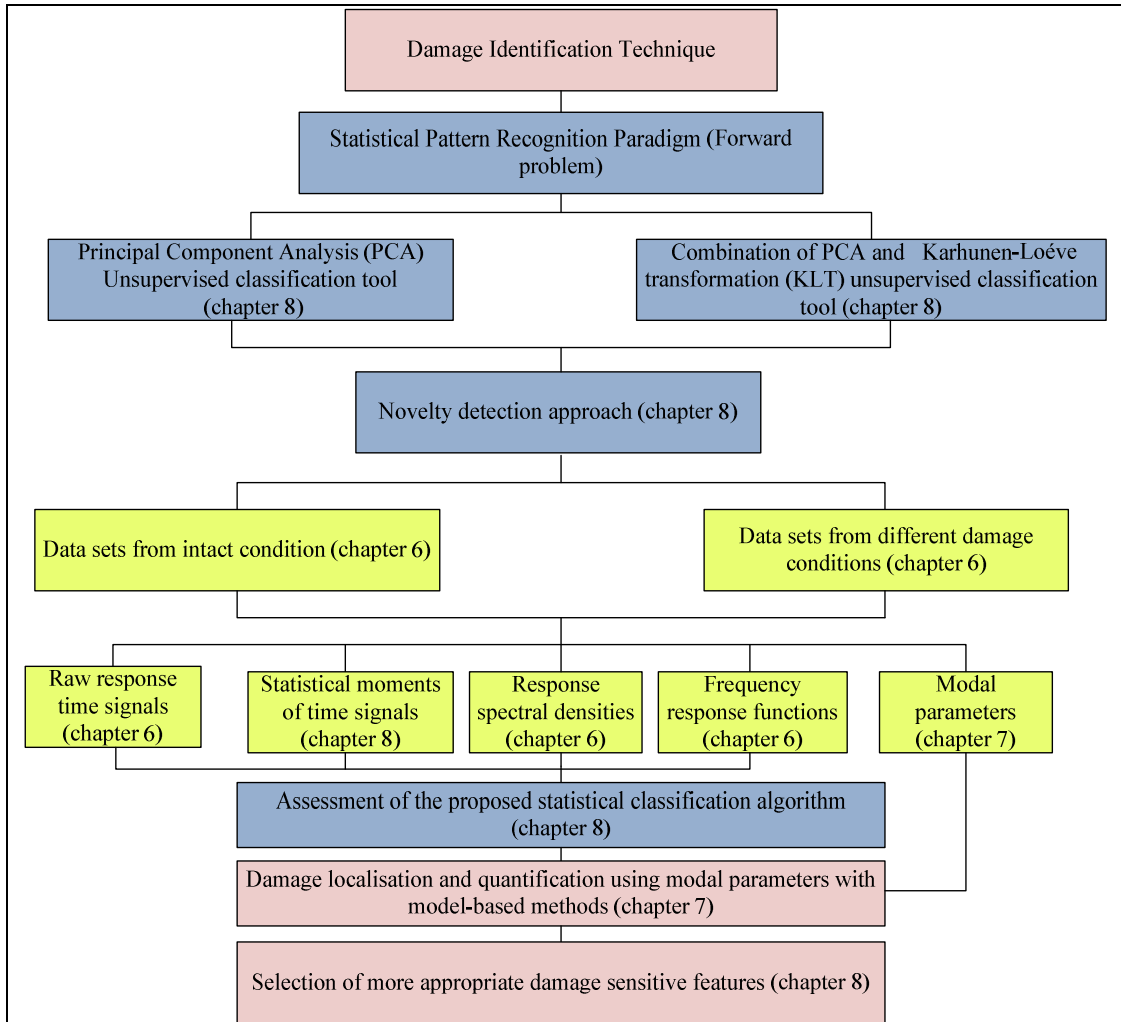


Figure 5.1: Flow chart of the damage identification methodology of the research.

5.2 Damage State Scenarios

The major aim of the research is assigned to apply a new damage identification technique to different damage sensitive features in an effort to obtain those carry notable physical properties of structural changes. In this context, various scenarios of structural damage are created in five RC beams to represent common problems in real-life SHM. The damage in the first group beams is represented by incremental levels of flexural cracking produced by successive four-point bending loadings. The load cycles are designed to produce close level of damage so as to explore the extent of the classification algorithm to discriminate between close levels. Equally, the damage in the

second group beams is accomplished through purpose-made void(s) near the end of the beams. The defects induced in the second group is meant to model familiar practical problems in civil engineering structures manifested as delamination, unfilled joints and non-homogeneous casting of concrete elements. The cavities are deliberately produced close to the ends of each beam in order to place the localised damage at a low curvature area of the flexural element where it is less likely to capture compared with anomalies in a high curvature area. The measurements are carried out on the five RC beams using instrumented impact hammer as a suitable excitation tool for field measurements. In this respect, the effect of operational condition due to non-similar repetitions of impact excitation in the direction, position and magnitude are also included in conjunction with the sensitivity of the damage features. Then, the vibration measurements of EMA whether in the time, frequency or modal domain are utilised for rigorous examination, validation and verification of the proposed technique.

5.3 Experimental Modal Analysis

In the perspective of EMA, a complete testing procedure in freely supported beam is established and the quality of its measurements is ensured through a series of essential QA checks. In order to consider the variability in the data due to using the impact excitation, measurements from the two alternatives, roving hammer and roving accelerometer, are collected and compared in this research. Owing to the use of transient excitation, the research interrogates the effect of high input force level on provoking the non-linearity of the beams. Furthermore, a notable real problem in bridges is that the ambient excitation forces are difficult to measure, and the conventional modal parameters are unable to find. Therefore, data sets from RPS density are investigated as damage sensitive features as oppose to data sets from FRFs. The success of this feature to be conclusive will be of a practical value in damage identification of civil engineering bridges where the ambient loadings are complicated.

5.4 Prediction and Correlation of Analytical Model

The fact that a wide range of civil engineering structures are of unknown history is another problematic obstacle hinders the progress of the vibration-based monitoring beyond the research area. Bridges or other individual structures have very little in

common with each other and almost any structure is a unique model (Wenzel, 2009). In general, data from a real-life as-built model of the structure is commonly unavailable. Consequently, it is much difficult in this area to establish data bases; thus any supervised learning system is unlikely to be immediately trained. To this end, prediction of analytical model for the original intact condition serves as a basic guide is invaluable that the deviation of present measurements eventually compared with it. A good effort of this research is attributed to build a preliminary analytical model, and the influence of different physical properties is discussed. In this respective, the effect of the boundary conditions, modulus of elasticity, damping system model and shear deformation on the accuracy of the analytical model are studied.

5.5 Damage Classification Level in Identification Problem

Although the first three levels of damage diagnosis (detection, localisation and quantification) address the main questions of the problem, fourth level referred to as classification is later added to the identification scheme.

Classification of data from various state conditions is indispensable for effective identification in higher levels of the structural condition identification (Worden K, Dulieu-Barton, 2004). Damage detection is also distinguished by making use of the classification step because damage can be identified without previous knowledge on the behaviour of the system when it is damaged (Worden K, Dulieu-Barton, 2004). Therefore, for these reasons, this research is specially concerned in developing a statistical classification algorithm provides a well-timed discrimination for data collected at the site without further need for additional processing. To make such algorithm functional and reliable, signal-only-based vibration data are investigated at first as possible damage sensitive features. It is significant to review the shortcomings of the conventional classification techniques in dealing with vibration data in this Chapter. In the mean time, the main attributes of the proposed technique to overcome the difficulties are also given in this Chapter. However, the complete application of the classification paradigm on data from time and frequency domains is elaborately explained in Chapter 8.

5.5.1 Statistical Models of Damage Classification

5.5.1.1 Principal Component Analysis

Principal Component Analysis (PCA) is a classical technique of multivariate statistics for reduction the dimensionality of a data set into a lower dimension with an insignificant loss of information (Jolliffe, 2002). It is quite often that there are a large number of interrelated variables in the original data sample, however the reduction is accomplished through transforming to a new set of uncorrelated (orthogonal) variables designated as the Principal Components (PCs) (Jolliffe, 2002).

Statistically, the variance in a data matrix $[X]$ of (n) observations can be expressed as:

$$[\Sigma] = \frac{1}{n-1} \sum_{i=1}^n (x_i - \bar{x})(x_i - \bar{x})^T \quad (5.1)$$

The covariance matrix $[\Sigma]$, which holds the variance of the original data, can linearly be decomposed into a set of orthogonal vectors by using the Singular Value Decomposition (SVD) algorithm, which can be given as:

$$[\Sigma] = [V][\lambda][V]^T \quad (5.2)$$

Where:

$[\lambda]$ is a diagonal matrix containing the ranked eigenvalues of $[\Sigma]$

$[V]$ is the orthogonal matrix containing the corresponding eigenvectors, which are also known as Principal Components (PCs) or loadings

The eigenvalues provide information about the variance of the PCs. The eigenvectors with higher magnitude of eigenvalues are the PCs of the original data.

Therefore, the transformation of the original data into new p -dimensional uncorrelated PCs can be written as:

$$[Z] = [V]^T [X] \quad (5.3)$$

Where:

[Z] is a matrix whose its i^{th} vector is the projection of the original data vector $\{x\}_i$ onto the eigenvector (i) of the covariance matrix $[\Sigma]$, and so on. These transformed vectors are called the component scores.

The covariance matrix of the new coordinates is a diagonal matrix, and for the first value on the diagonal is to retain the maximum variance. It should be noted that if the p-coordinate data set is completely a linear combination of $r < p$ variables, the projections onto the first (r) PCs will entirely describe the data, and the remaining (p-r) projections or scores will be approximately zero. In practice, the scores are all of specific values due to inherent non-linearity, however the values are insignificant, and a proper number of components should be selected to preserve the important features of the original sample.

In the SHM context, PCA method is used for two primary applications. First, the technique can be employed as a means of evaluation of patterns in the data. The evaluation is achieved through a linear mapping of data from the original feature space into a transformed feature space. Transformation of the data into a new plane permits a useful means of feature extraction and the prominent characteristics in the actual data to be preserved explicitly, while presented in a representation of the new reduced dimension.

Second, the technique can be used as a tool of reducing the dimensionality of the data. Data reduction can be achieved by reversing the projection back to the original feature space using only the PCs with higher eigenvalues, Equation 5.3 (Figueiredo, 2009). If the most characteristics in the actual data are contained in the first two or three PCs, the reduced data can be plotted in a way that shows the relationships between the data points.

A general assumption in many forms of PCA as discriminant analysis method is that the covariance matrix $[\Sigma]$ is alike for all groups (the centralisation of data matrix $[X]$ is based on the means of all groups), and the PCA may therefore be done on an estimate of this common within-group covariance. Unfortunately, this procedure probably is not always acceptable for two reasons. First, the within-group covariance matrix may be different between different groups. The performance of the PCA method, when equal

within-group covariance matrix is not assumed, will be discussed later in the following section. Second, more serious problem encountered in using PCs based on a unique within-group covariance matrix to discriminate between groups is that there is no agreement that the separation between groups will be in the direction of the high-variance PCs (Jolliffe, 2002). Thus, the first few PCs will only be useful for discriminating between groups in the case where within- and between-group variation have the same dominant directions.

5.5.1.2 Karhunen-Loève Transformation

If the between-group variation is much larger than within-group variation, then the first few PCs for the overall covariance matrix will define directions in which there are large between-group differences. Therefore, such PCs seem more useful than those based on within-group covariance matrices. However, the technique should be used with some caution, as it will work well only if between-group variation dominates within-group variation (Jolliffe, 2002). If this is not the case in original data sets, the between-group and within-group variation matrices together are simultaneously used to maximise the features of the original data sets.

To that end, Karhunen-Loève Transformation (KLT) is another statistical multivariate technique related to the PCA family, which is devised to investigate relationships between populations of data sets. In general, the KLT in its basic form is similar to the PCA. However, the main discrepancy between the two transformations appears in pattern recognition applications because the class information is incorporated in KLT as a supervised learning mode, while it is discarded in PCA (Webb, 2001).

In this technique, the new feature space is constructed from eigenvectors of the within-class sample covariance matrix $[S]$, which is defined as:

$$[S] = \frac{1}{N-c} \sum_{i=1}^c \Sigma_i \quad (5.4)$$

Where:

c is the number of classes (groups) in data

N is the number of measurement points (observations)

Σ_i is the sample covariance matrix of class (i) group that can be described as:

$$\Sigma_i = \sum_{j=1}^N (x_j - \bar{x})(x_j - \bar{x})^T \quad (5.5)$$

Devijver and Kittler (1982) suggest using the discriminatory information contained in the class means to rank the PCs and select the subset features that are used in further classification analysis (Jolliffe, 2002; Webb, 2002). The procedure is implemented in two stages. In the first stage, a transformation of data samples to a new space displays the averaged within-class covariance matrix [S] as a diagonal matrix. In this respective, the transformation vectors that de-correlate the data samples based on the within-class covariance matrix is:

$$[Y] = [V]^T [X] \quad (5.6)$$

Where:

[V] is the eigenvectors matrix of [S] and the average within-class covariance matrix in the new transformed space is:

$$[\Lambda]_p = [V]_p^T [S] [V]_p \quad (5.7)$$

Where:

$[\Lambda]_p$ is a diagonal matrix of the variances of transformed features (eigenvalues of [S])

The first stage of transformation results in a significant reduction of the original data into a new uncorrelated r-dimension space, such that:

$$[\Lambda]_r = [V]_r^T [S] [V]_r \quad (5.8)$$

In the second stage of the transformation, the between-class covariance matrix [B] of the original data sets can first be defined as:

$$[B] = \frac{c}{(c-1) * N} \sum_{i=1}^c (x_i - \bar{x})(x_i - \bar{x})^T \quad (5.9)$$

Where:

\bar{x} are means of features of original data

x_i are means of the features within the group itself

The between-class covariance matrix [B] is further transformed in a new data space given by:

$$[\bar{B}] = [\Lambda]_r^{-\frac{1}{2}} [V]_r^T [B] [V] [\Lambda]_r^{-\frac{1}{2}} \quad (5.10)$$

This stage is to compress the class mean information by finding the orthogonal transformation that transforms the class mean vectors into a reduced dimension.

That is, the new definition of data sets in terms of their within-class [S] and between-class [B] covariance matrices leads up to a typical mathematical eigenproblem, where its eigenvalues and eigenvectors can be found by many numerical methods. The generalised eigenproblem of data sets in accordance with their two covariance matrices, [S] and [B], will also take the standard eigenproblem from as:

$$[B - \lambda^2 S][V] = [0] \quad (5.11)$$

Where:

[B] and [S] are between-class and within-class covariance matrices,

$[\lambda_i]$ and [V] are the eigenvalues and eigenvectors of the system, respectively

To this end, the KLT helps to obtain a linear discriminant analysis by maximising the discriminant capacity between subgroups without involving distribution assumptions, but only a nearest class mean type rule is assumed as an optimal distribution of the classes (Webb, 2002).

5.5.1.3 Integration between PCA and KLT as Classification Tool

Mainly, the noticeable means of using PCA in a discriminant analysis is to compress the size of original data by replacing (p) features of data sample [X] by the first r-high variance PCs. If the first two or three PCs explain a high part of the variance, they tend

to provide a meaningful visualisation for the data, in an unsupervised way, presenting an illustrative prospect of the separation between the groups (Jolliffe, 2002). If this is not the case, any additional orthonormal transformation using PCA will produce same uncorrelated features for which the vectors are de-correlated. Therefore, another transformation system that performs with different aspects of variation in the data will be able to insert higher percentage of variation in the first few PCs, and hence will give better representation to the original data.

In a proposed two-stage transformation technique, it is possible not to suffice with the first few PCs and go further up to the number of PCs that preserves most of the variation of original data. This represents first stage transformation, and is accomplished through PCA as given in the upper part of the flow chart of Figure 5.2, and specified as unsupervised learning mode. This part is commonly implemented on an individual covariance matrix computed from the normalised data samples. In order to establish more sensitive classification means, KLT technique is suggested to be additionally applied at the outcome of the first transformation stage. The technique integrates the first stage of the PCA, and uses the output data from its transformation as input data set for a second transformation stage. The lower part of the flow chart given in Figure 5.2 presents the main steps of the second transformation stage.

This is to say, the proposed classification technique can be outlined in the following steps:

- A number (r) of the first loading vectors (eigenvectors) from the first transformation stage (PCA) that accounts for almost 100% of the total variation are set to be the data matrix for KLT.
- The rows of the new feature vectors (p) must be labelled according to their respective classes.
- The within-class covariance matrix ($[S]$, Equation 5.4) and between-class covariance matrix ($[B]$, Equation 5.9) are computed using the new set of data.
- Both covariance matrices are decomposed into new uncorrelated space, as given by the eigenproblem of Equation 5.11.

- The plot of the first two PCs, from the new transformation, will offer insight to the visualisation of the data. Great and valuable amount of the information in data is maximised and inserted in the first two or three PCs. The first few PCs account for higher percentage of the total variation, and no significant loss in information is experienced.

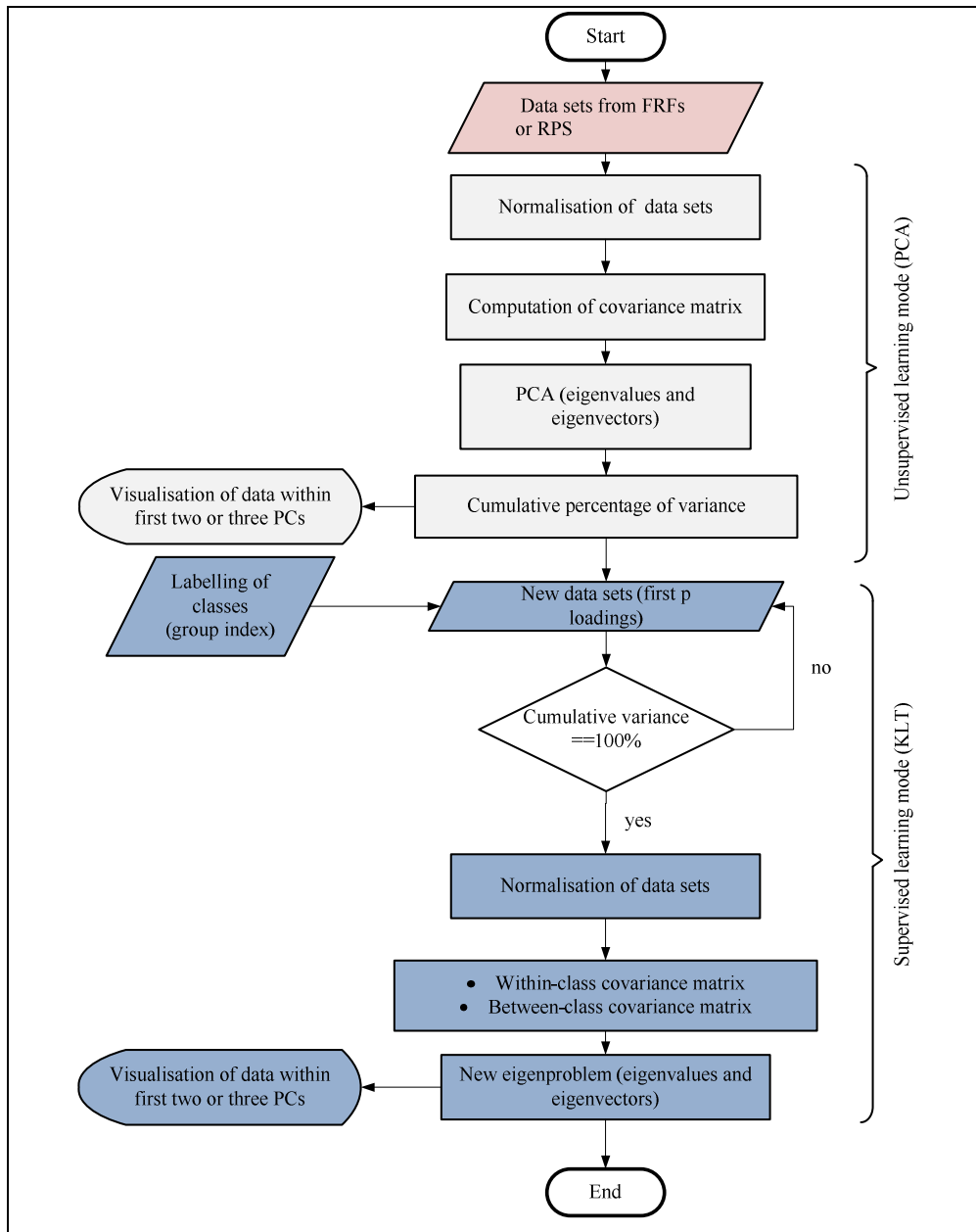


Figure 5.2: Flow chart of the proposed classification paradigm.

5.6 Summary

This Chapter is devoted to introduce the main aspects of the methodology adopted throughout this research. It embarks on the problem by mentioning the shortcomings and limitations of model-based damage identification methods. In the meantime, the need for using statistical-based damage identification methods is unambiguously underlined. Then, the damage patterns implemented in the five RC test beams with a brief description to the specifications of each damage state group are outlined. Next, the vibration testing procedure including the essential excitation type alongside the main quality assurance checks are summed up. Prediction of analytical model for the original intact condition provides a basic reference will be very useful that the variation in the measurements can be compared with it. Therefore, the Chapter approached the importance of predicting a correlated analytical model. The effect of some physical parameters on the prediction is discussed. Most importantly, a complete description to the statistical classification model developed, checked and verified in this research is presented in final part of this Chapter. The insufficiency of PCA as a classification model at providing detailed dissection for data sets of diverse subgroups, and the capability of the proposed PCA-KLT to give more comprehensive classification are explained.

6. Experimental Work and Finite Element Model Updating

6.1 Introduction

In order to investigate different models of damage identification methods into RC beams, five laboratory-scale beams were constructed and modelled with various damage scenarios. Each beam in its specific state condition was tested under freely supported condition using Experimental Modal Analysis (EMA). The five beams were all similar in length and cross-sectional dimensions, but they were different in concrete strength, steel reinforcement and type of damage presented.

These beams were testing chronologically in the following order:

1. Beam A: A 2.0m long RC beam was tested under seven different state conditions, namely: intact, 3kN load, 6kN load, 10kN load, 13kN load, 16kN load and repaired conditions.
2. Beam B: A 2.0m long RC beam was tested under seven different state conditions, namely: intact, 3kN load, 6kN load, 10kN load, 13kN load, 15.5kN load and repaired conditions. NB Beam B has different characteristic strength from beam A.
3. Beam C: A 2.0m long RC beam was tested under three different state conditions, namely: intact, 10kN load 14.5kN load conditions.

For the three beams A, B and C, the tests were implemented when the static loadings and the corresponding modal tests resulting in vibration bending modes about the major bending axis.

4. Beam D: A 2.0m long RC beam was tested in two different state conditions; its intact (solid) state condition and with a purpose-made single void at the end.
5. Beam E: A 2.0m long RC beam was tested in two different state conditions; its intact (solid) state condition and with two symmetrical purpose-made voids at its ends.

For the last two beams D and E, the measurements were implemented when the modal tests resulting in vibration bending modes about the minor bending axis.

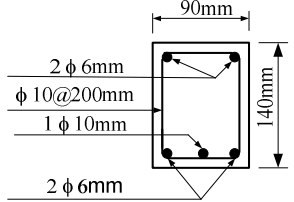
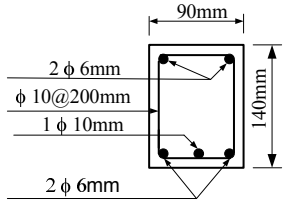
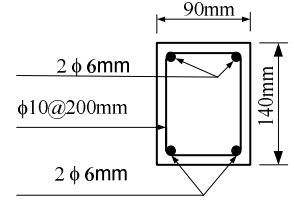
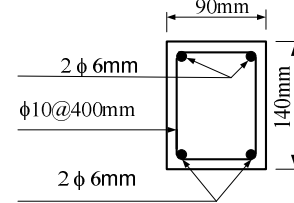
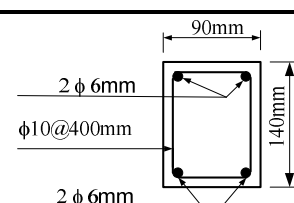
Table 6.1 shows the dimensions, physical parameters and reinforcement details of the five RC beams.

The five RC beams were cast and tested in the concrete laboratory at Nottingham Trent University, School of Architecture, Design and the Built Environment for the period between October 2010 and October 2011.

It was found necessary to design the state conditions of each beam to represent practical cases from the field of SHM in civil engineering structures. In addition, the configurations of the test in conjunction with the type of damage were selected carefully to represent the underlying damage excluding any unfavourable operational and environmental conditions, which is purely the main focus of this research. Furthermore, the test samples were set also to make the measurements possible to model and correlate with the FE method discarding any approximations.

It is worth pointing out that it could have been better to test bigger size structures representing a real-life case studies. However, the availability of resources and the convenience of the devices dictated severely the size of test beams.

Table 6.1: Specifications of the five test RC beams.

| Test Beam | Cube strength N/mm ² | Mass kg/m ³ | E _d MPa [*] | G _d MPa [†] | Reinforcement |
|-----------|------------------------------------|------------------------|---------------------------------|---------------------------------|---|
| Beam A | 20.4 | 2240 | 19.1x10 ³ | 8.13x10 ³ |  |
| Beam B | 29.0 | 2270 | 27.5x10 ³ | 11.5x10 ³ |  |
| Beam C | 27.3 | 2320 | 25.0x10 ³ | 10.4x10 ³ |  |
| Beam D | 26.0 | 2310 | 24.0x10 ³ | 10.0x10 ³ |  |
| Beam E | 27.3 | 2320 | 27.5x10 ³ | 11.7x10 ³ |  |

^{*}E_d: Dynamic (tangent) modulus of elasticity.

[†]G_d: Dynamic (tangent) shear modulus of elasticity.

6.2 Description of the Induced Damage

The structural state conditions conducted on the five test beams can be divided into four main groups. The first group was the baseline state condition and referred to as intact for the beams A, B and C, but referred to as solid for beams D and E. The second group was concerned only with beams A, B and C; this is represented by different levels of flexural cracking resulting from successive four-point bending loadings. The third group was interested with studying the effect of repair work conducting on beams A and B only. Finally, the fourth group included defective beams (D and E) where artificial voids were induced at the end of the beams.

6.2.1 Test Beam A

Test beam A was subjected to two symmetrical static point loads at a separation of 0.3m in order to create a four-point bending loading, as shown in Figure 6.1. A photograph representing the static loading process is shown in Figure 6.2. This loading arrangement produced a middle zone of evenly distributed defects due to the constant bending moment over this zone. As the overall supporting width of the testing machine was smaller than the length of the beam, the span of the test beam was taken as 1.2m and an overhanging distance of 0.4m was left from each side. Then, the beam was subjected to five incremental load steps in order to produce controlled levels of damage. At the end of each load step, the beam was unloaded, and the simple supports were replaced by free-free supports to carry out the EMA on a completely freely supported beam. At the final loading step corresponding to 16kN load when the beam became too frail, and just before the formation of the plastic hinge, the loading process was stopped, the cracking pattern thoroughly surveyed and the beam was dynamically tested then repaired.

To repair the damage, the defective zone was strengthened by bonding a single layer of external Carbon Fibre Reinforced Polymer (CFRP) type TORAYCA-FT 300B to cover 500mm long and 90mm width of the beam. The tensile modulus of elasticity of this type is 220kN/mm^2 resulting in tensile strength of 3340N/mm^2 . The CFRP has become a well-known refurbishment material used in civil engineering over the past decade. Whereas using CFRP as a post-strengthening material in rehabilitation of concrete improves the strength, it does not have much effect on the stiffness. In the current repair

work, the particular use of CFRP sheets is based on bending moment, where the maximum bending moment zone was strengthened with these sheets. High strength and moisture resistant epoxy (West System Epoxy) that is made out of two separate parts, resin and hardener, was used to glue the CFRP sheets to the beam. The mixing ratio of 1.0g of hardener for every 5.0g of resin was used to guarantee a good cure. The combination should commonly be mixed for around 120s, and there is only less than 20min before it turns into solid. Figure 6.3 shows the test beam A after the repair work was conducted.

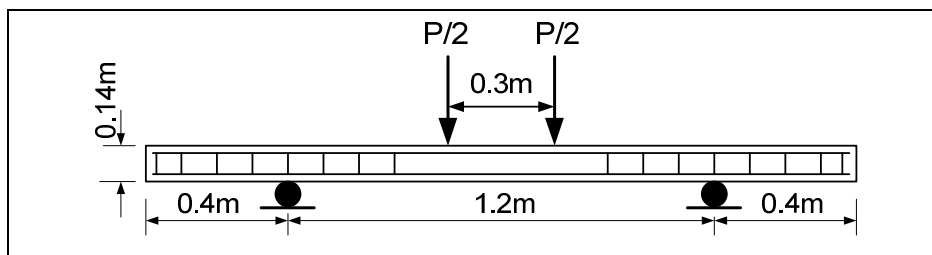


Figure 6.1: Beam A - configuration for static loading.



Figure 6.2: Beam A - one of the static loading stages- photograph.



Figure 6.3: Beam A - strengthening with CFRP layers-photograph.

6.2.2 Test Beam B

Beam B was subjected to the similar damage and repair conditions conducting on beam A. Thus, this section suffices with mentioning the only discrepancy, where the final static loading step was terminated earlier at 15.5kN as the beam went through heavy cracks, as shown if Figure 6.4.



Figure 6.4: Beam B - mid span zone at the final damage state-
photograph.

6.2.3 Test Beam C

The test beam (Beam C) was subjected to two symmetrical static point loads at a separation of 0.3m as a four-point bending loading. The width of the testing machine was sufficient to permit the span of the test beam to be as 1.8m, and with an overhanging distance of 0.1m from each side, as shown in Figure 6.5. Also, a photograph presenting the four-point bending load procedure is shown in Figure 6.6. Aside from the reference state condition, the beam was subjected to two incremental load steps: namely 10kN load and 14.5kN load steps. At the final load step, the beam was completely damaged and wide flexural cracks were observed over the mid span zone. A photograph showing the severe damage of Beam C after it was loaded by 14.5kN is presented in Figure 6.7.

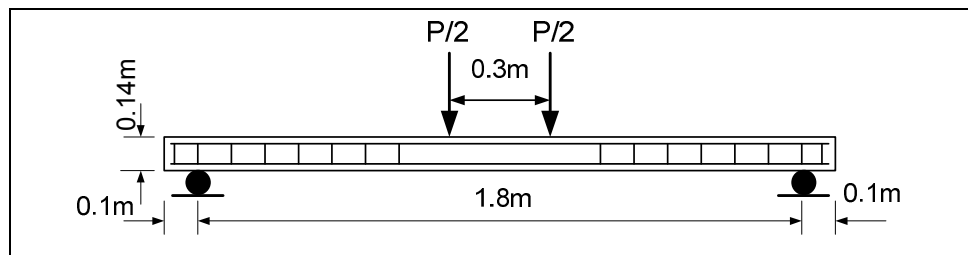


Figure 6.5: Beam C- configuration of static loading.



Figure 6.6: Beam C - under one of the static loading stages- photograph.



Figure 6.7: Beam C - mid span zone at the final damage state-photograph.

6.2.4 Test Beam D

In this beam, a void of $5 \times 6 \times 40\text{cm}^3$ size made of a block of polystyrene was concealed inside one end of the beam. The drop in the cross-sectional area at the region of this void was approximately 25%, while the drop in the moment of inertia was 4.8%.

6.2.5 Test Beam E

Two identical voids each of $6 \times 10 \times 20\text{cm}^3$ size were made by blocks of polystyrene and concealed inside the right and left ends of the beam as shown in Figure 6.8. Each individual void caused an approximate drop in the cross-sectional area of 50% and drop in the moment of inertia of about 21%. These voids were then closed by filling with concrete, left for 28 days to get the concrete matured and the beam after that was tested under a solid beam condition.

The defects induced in beams D and E served as models for familiar practical problems in civil engineering structures manifested as voids, delaminations, unfilled joints and any non-homogeneity in concrete elements.



Figure 6.8: Beam E- Preparation to cast the beam with two polystyrene blocks.

6.3 Pre-Test Finite Element Modelling

In any EMA, the testing strategy implies commencing with development of a pre-test FE (analytical) model in order to satisfy the following necessary points:

- An initial estimate to the range of first group of natural frequencies is obtained. Therefore, an appropriate measurement kit and data acquisition parameters can be selected.
- An approximate test grid can be chosen reasonably to avoid the potential spatial aliasing problem.
- From the initial estimate of FRF measurements and the associated shape of modes, a convenient method for modal parameters estimation can be decided.
- A verified pre-test FE model could be utilised as a reference model for further updating procedure based upon experimental modal data.

The FE model developed primarily according to normal dynamics of structures modelling is shown in Figure 6.9. The beam was modelled using 10 one-dimensional beam elements. The effect of supporting cords was assumed as trivial linear suspension

stiffness of 1.0N/m so as to ensure stable condition problem. The added stiffness has no significant influence on the bending frequency parameters because its value is very small compared with the mass of the beam. Shear deformation effect was included in the assembled mass and stiffness matrices. The modulus of elasticity taken constant for all elements was the tangent modulus, in accordance with (Abeele and De Visscher, 2000; Kato and Shimada, 1986; Neville, 1995). The value of the modulus of elasticity was changed according to the compressive strength of each corresponding beam. Finally, bending modes of vibration and vibration data on the major or minor bending axis were obtained in accordance with the actual test configuration of each particular case.

Based on several testing trials with different configurations, and after many numerical FE modelling on the beam, the 11 point test grid illustrated in Figure 6.9 was selected. Auto Modal Assurance Criterion (AutoMAC) is commonly used to check whether or not a selection of DOFs is sufficient (Ewins, 2000). The AutoMAC matrix calculated for this test grid is presented in Figure 6.10. The presence of off-diagonal non-zero terms in this figure was normal due to the fact that the perfect orthogonality condition is only applicable when all the DOFs are included in the analysis (Ewins, 2000). Nevertheless, Ewins (2000) considers that MAC values of less than 10% (or 0.1) should be achieved for uncorrelated modes. The highest off-diagonal value observed in the current grid was 13% (0.13) which served to consider the test grid sufficient without spatial aliasing problem.

As a parting comment, it was necessary to select the location of a reference accelerometer location to be used for the EMA with roving excitation. The drive point measurement of this point should display all modes of vibration of the beam. Making use of a priori knowledge of the vibration modes in freely supported beam provided with the assistance of the analytical analysis, the reference test point was chosen at the end of the test beam (point 1) (see Figure 4.1).

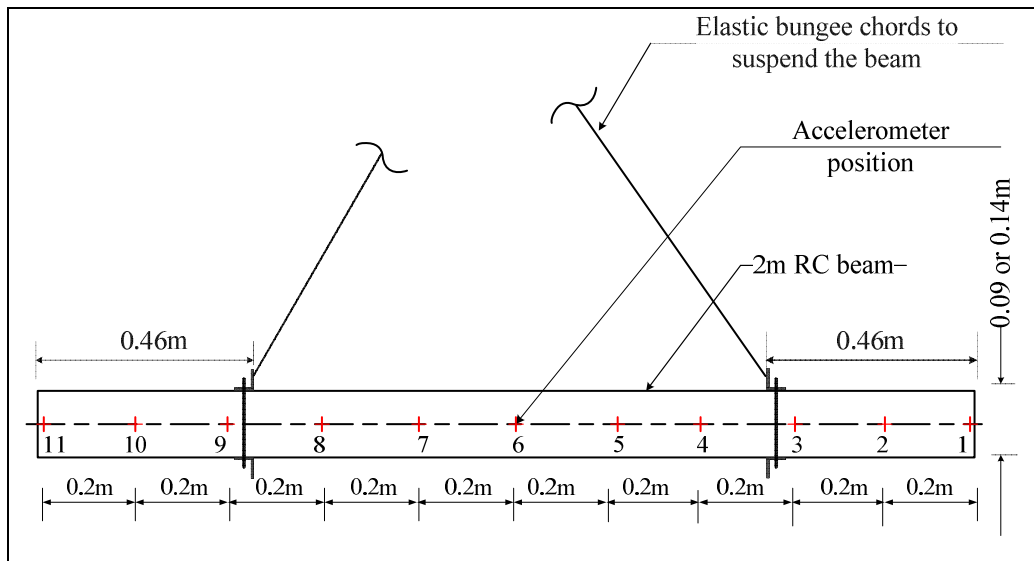


Figure 6.9: Configuration of the test grid points.

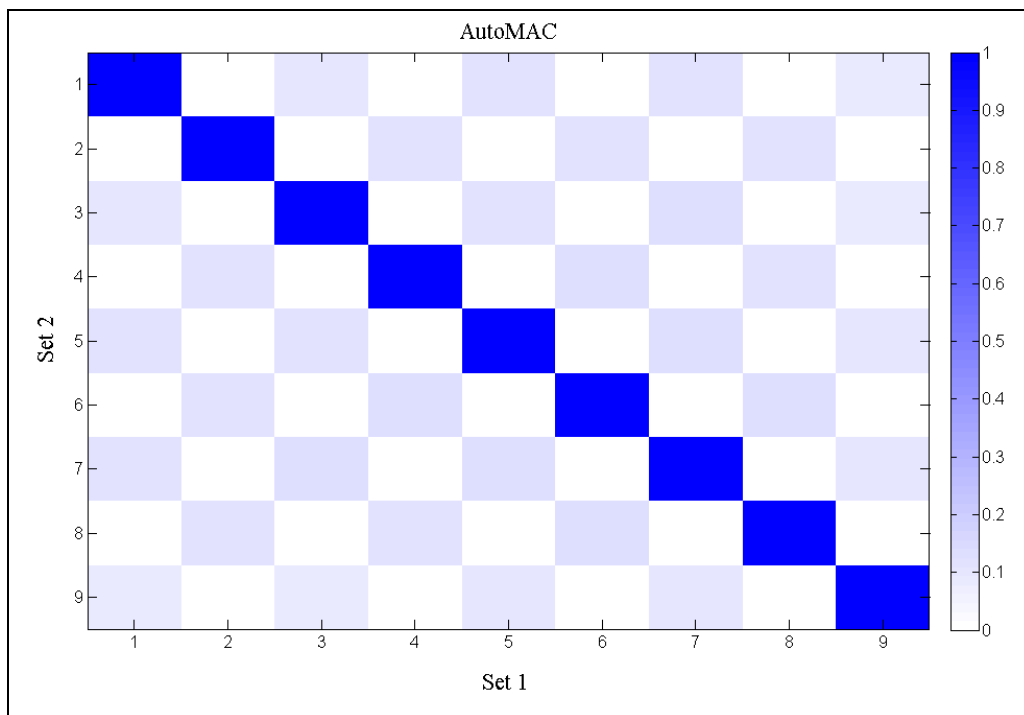


Figure 6.10: Presentation of AutoMAC data for reduced 11 selected DOFs.

6.4 Testing Plan

In general, two main objectives were planned for the test results collected from the five beams, these were:

- Use of the vibration measurements whether in time, frequency or modal domain to validate SHM methods utilising different models; and
- Use of the modal data in the following updating of the FE model of each beam.

Therefore, the size of acquired vibration measurements and the quality of modal results were decided in light of the following considerations:

- The author initiated the modal analysis test in the School of Architecture, Design and the Built Environment utilising a newly-purchased measuring kit. Thus, an important effort went to perform sufficient trials for the sake of the comparison and correlation of results using different excitations.
- High quality modal data was indispensable as it was intended to use for identification of small defects in relatively small samples by which accurate results were necessary. In general, small size samples are sensitive to the operational and environmental conditions, and every account needed to be deemed to avoid the effect of these conditions.
- The measurements were not only acquired for appropriate set of FRFs (either one row or one column), but enough rounds of measurements per each state condition were implemented as they were proposed to use with Statistical Pattern Recognition (SPR) methods.

6.4.1 Experimental Modal Analysis: Preparatory Phase

After the beam and the equipment had been provided for the test, series of arrangements was taken before start acquiring the first round of measurements for QA checks. In the context of the beam, a rigid and mobile place to suspend the test beam was selected at the upper cross head of the 1000kN universal testing machine. This head is rigidly fixed by two screwed columns and driven by a motor, Figure 4.3. This arrangement allowed lowering the head closer to the test beam to fasten the cords, then lifting it to float the beam.

Following the results of the pre-test FE analysis, the steel studs were attached at the corresponding marked test grid points. Also, purpose-made two supporting frames were

positioned at the nodal points of the first mode of the beam to be used later to fasten the suspension cords.

In the context of the equipments, proper location for the data acquisition hub was chosen close to the beam allowing adequate freedom to the movement of hammer instructed by the length of the wires. The relevant setting parameters of the acquisition devices were chosen in accordance with the estimated analytical results and acquisition system specifications.

6.4.2 Experimental Modal Analysis: Exploratory Phase

As soon as the test beam and equipment had been prepared for the first EMA measurements, a full set of data Quality Assurance (QA) checks were performed as it is stated by the UK DTA procedure outlined in section 4.6.2.

6.4.2.1 Excitation/Response Check

This first check was satisfied through applying an input excitation at test point (1) and the resulting responses were captured simultaneously at two test points (points 1 and 11). Results of the excitation/response checks of Beam A are shown in Figure 6.11. In addition, the auto spectrum densities resulting from the excitation and response time histories are shown in Figure 6.12. From the results of this check the following observations can be drawn:

- The impact force resembled a regular half-sine shaped signal when applied using the hard tip on the concrete beam. The signal took duration up to 1.2ms, as shown in Figure 6.11 (lower trace).
- The corresponding response looked like what was expected without indicating any odd behaviour. No signs of loose connection of the transducer cables and no indications for jumping of the accelerometer were arisen. The acceleration response had a peak of 94g, and then it diminished to the ambient vibration in approximately 50ms, as shown in Figure 6.11 (upper trace).
- In drive point measurement (the excitation was at point 1 and the response was at the same point), the response started immediately. However, there was a delay for the remote transfer measurement, when the response was measured at point

11. In the last case, the signal wave needed more time to travel through the beam to arrive at point 11 (Reynolds, 2000).

- Plots of the frequency spectra for the excitation and response signals representing by the magnitude (complex modulus) are displayed on ordinary scale in Figure 6.12. The shape and frequency content (0-1000)Hz seemed consistent and compatible with the objectives of the work. The signal to noise ratio of the response spectrum was high and the environment noise seemed without significant effect. The first four resonances of the possible modes of vibration of the beam were clear in the response spectrum.
- The excitation frequency spectrum resulted in a reasonably flat shape was as expected, and the frequency content was as required. No significant drop off, zeros or distortion were observed by which it was considered reasonably flat over the frequency range of interest. Extremely flat excitation spectrum is not desirable in modal measurement resulting in poor measurement as too much excitation makes all modes of vibration respond (Avitabile, 2007).

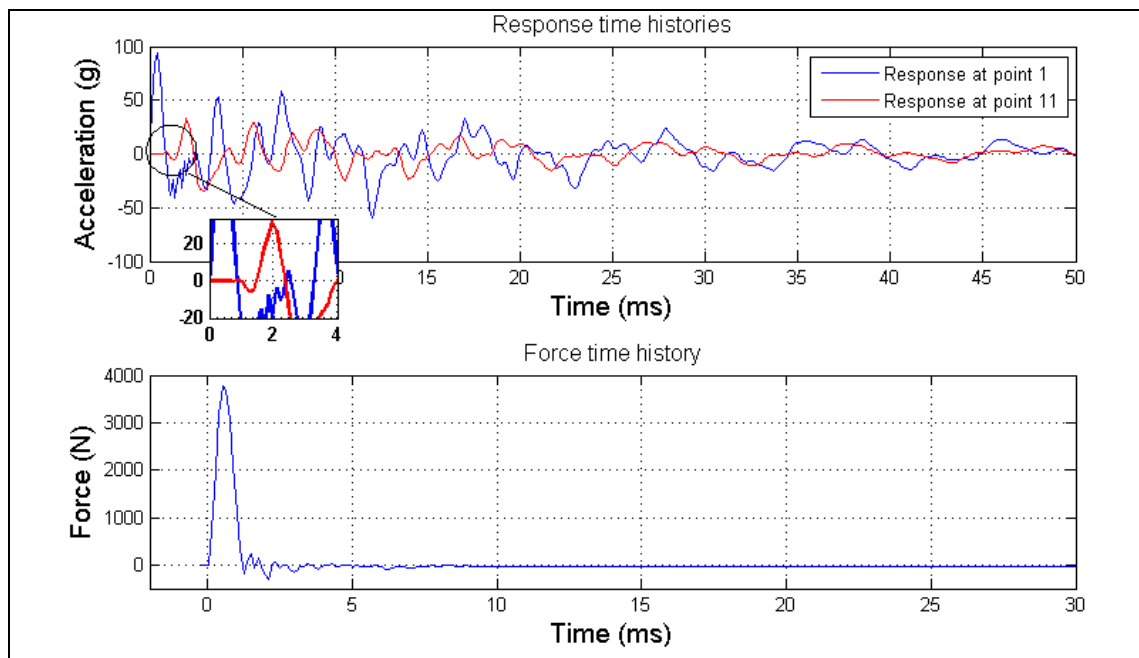


Figure 6.11: Beam A - excitation/response check (time domain).

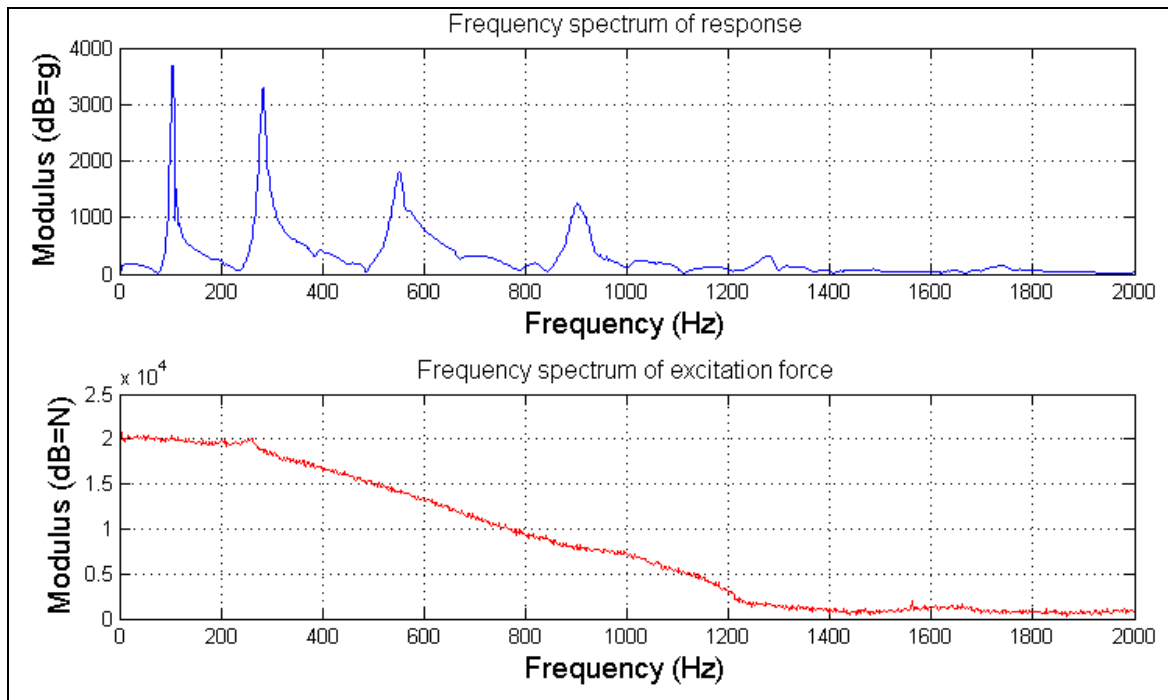


Figure 6.12: Beam A - excitation/response check (frequency domain).

6.4.2.2 Immediate Repeatability Check

As described in section 4.6.2.2, the immediate repeatability check was carried out to ensure the repeatability of a particular measurement. As it was the first attempt to display an FRF measurement, therefore, it was a prospect to explore different data acquisition parameters and different excitation levels. The selected data acquisition parameters and the corresponding excitation characteristics are given in Table 6.2.

Although some of the selected setting values were dictated by the maximum limit of the acquisition system, the values did not have any negative effects on the modal results. For instance, the author managed to deal with the relatively low frequency resolution by completing the trail of zeros in the response and excitation time history for an extra duration period beyond the nominal acquisition period resulting in higher resolution of frequency domain.

Figure 6.13 shows the results of the immediate repeatability check conducted on drive point FRF of Beam E using impact excitation. The FRF is predominantly plotted in logarithmic scale so as to compress the large signal magnitude and expand the small ones, allowing easier visualisation of all frequencies in the signal (Figueiredo et

al., 2009). It is evident from the visual inspection of the two functions that they overlaid reasonably well up to the frequency below 800Hz as this range was sufficiently excited by the hammer. Any trivial discrepancies observed can be accounted to the effect of variable damping produced by the supporting cords and also due to the non-precise repetitions of the excitation. In addition, it is likely that this was caused by the presence of an extra short term environmental noise which can be normalised over several numbers of averages. Although several attempts were made to get perfect overlay, the outcome remained with the same quality. Most importantly, Figure 6.13 emphasises that the frequency and approximate magnitude of the peaks corresponding to the modes of vibration of the structure are the same for both measurements suggesting there was no significant nonlinearity in the test beam (Reynolds, 2000). Beyond this range, the response became noisier as the modes of vibration in this region did not respond well to the excitation. In short, the immediate repeatability check highlights that any substantial problems with the data acquisition parameters or with the test set-up were less likely to be important.

Table 6.2: Data acquisition parameters and associated setting values.

| Parameter | Setting values |
|-------------------------------------|----------------|
| Acquisition time duration | 500ms |
| Acquisition frequency bandwidth | 10-1200Hz |
| Frequency resolution | 2Hz |
| Number of frequency domain averages | 4 |
| Response time window | Non |
| Excitation time window | Non |
| Excitation hammer tip | Hard (black) |
| Excitation duration (hard tip) | 1.3ms |
| Excitation frequency bandwidth | 800Hz |

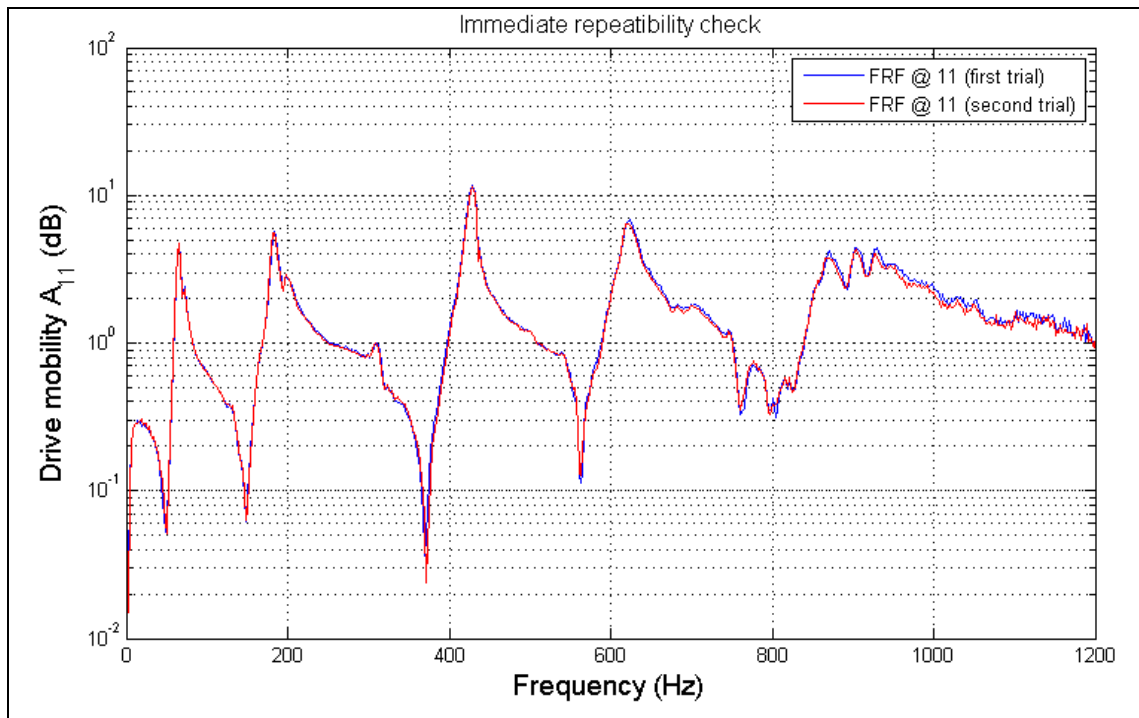


Figure 6.13: Beam E - immediate repeatability check for drive mobility at point 1.

6.4.2.3 Reliability (Homogeneity) Check

This check is concerned with the linearity of the test structure where non-identical excitations are applied. The reliability check of this work was conducted using all hammer tips resulting in four different force levels. Results showing the reliability check performed on drive mobility function of point 5 generated using only the hard and tough hammer tips are shown in Figure 6.14. Also, same drive mobility function generated using all four hammer tips are shown in Figure 6.15, but for clarity they were shown for shorter frequency range (0-500)Hz. It is clear that the measurement made using the tough tip (low-level) excitation is noisier than the measurement made using the hard tip (high-level) excitation. This observation was also experienced by Reynolds (2000) and reported as an anticipated and common for civil engineering structures.

It was clear from the characteristics of the excitation the hard hammer tip must be used for the course of this work in order to excite the desired frequency range.

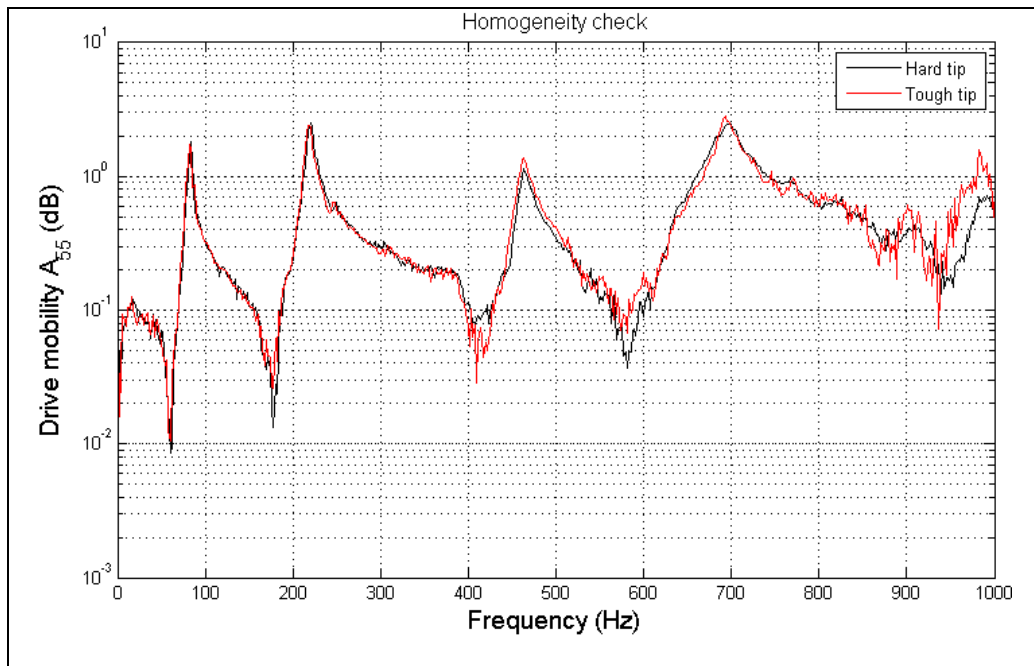


Figure 6.14: Beam E - homogeneity check using two different level excitations.

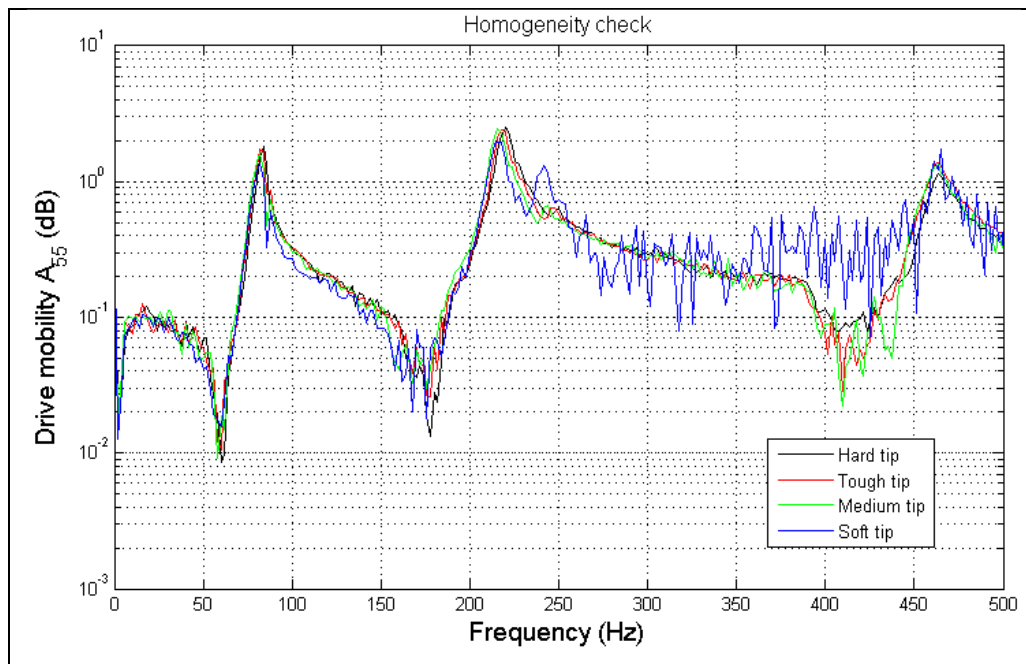


Figure 6.15: Beam E - homogeneity check using four different level excitations.

6.4.2.4 Reciprocity Check

The procedure to do the reciprocity check is explained in section 4.6.2.3. For the context of this work, results showing reciprocity check performed on transfer mobility function between points 1 and 3 is illustrated in Figure 6.16. Considering the excitation

force was swapped between two locations (points 1 and 3) provided non-identical magnitudes, both functions showed very good agreement. It is clear that the second measurement looked noisier than the first measurement, suggesting that the second one was influenced by significant noise which is influential in such structures. The bottom line of this check is the two FRFs can be considered to be sufficiently similar so as not to be a cause for concern with respect to the testing procedure and acquisition setting values.

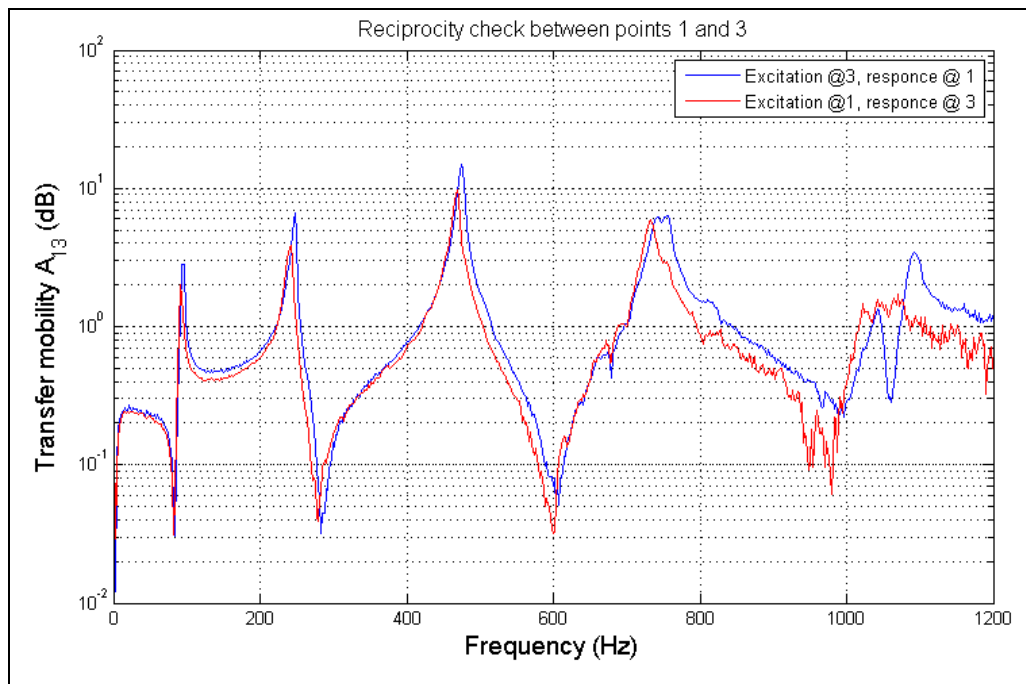


Figure 6.16: Beam E - reciprocity check for transfer mobility A_{13} .

6.4.2.5 Coherence Check

Figures 6.17 and 6.18 show the drive mobility at point 1 and transfer mobility (between points 1 and 6) checks of coherence function for Beam E, respectively. These checks were accomplished for averaged functions obtained for four sets of measurements. It can be seen from these figures that the coherence functions were very good for the measurements. The coherence function values for the most of the frequency range were close to one. Also, the values at all FRF peaks corresponding to the resonances of the beam were very close to one. However, the coherence values slightly dropped off in anti-resonance regions, but it is not problem for such measurement. Low coherence in

immediate anti-resonance regions is anticipated due to the fact that the beam has no response at these frequencies, and therefore, the response of the system is not coherently related to the excitation force (Avitabile, 2007). Anti-resonant frequencies unlike resonance frequencies are local characteristics and in the case of impact excitation they tend to change in accordance with each input force. Therefore, one particular measurement is not perfectly consistent with the next measurement and this will be shown in the coherence function. Another important means to improve the coherence function and get rid of the spiky drops is by increase the number of averages performed on the data sets. Higher number of data sets will normalise the extraneous noise occurred. The bottom line of that is the low coherence is fairly acceptable in the immediate region of the peaks, but it is not acceptable at the vicinity of each peak (Avitabile, 2007). As can be seen in Figures 6.17 and 6.18, the coherence for the most of the frequency range was close to one and, in the meantime, no significant wide dip off was noted in the vicinity of the peaks. Therefore, the results of the coherence check were considered to be satisfactory for the benefit of this check.

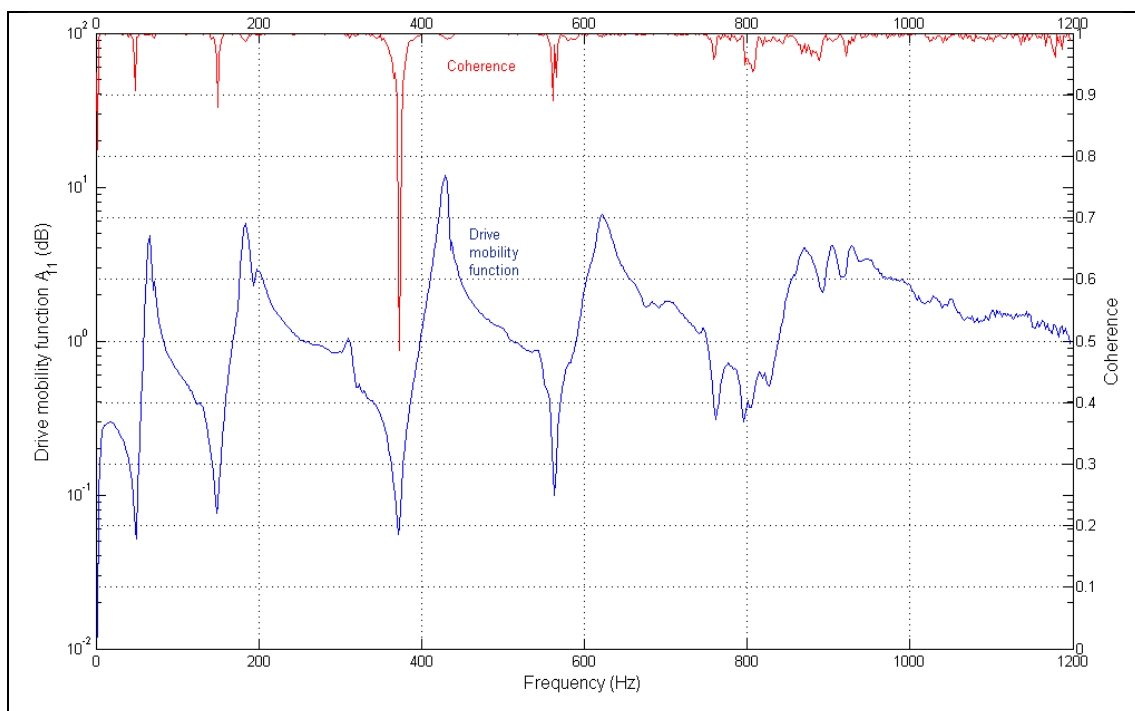


Figure 6.17: Beam E - coherence function check for drive mobility at point 1 (A_{11}).

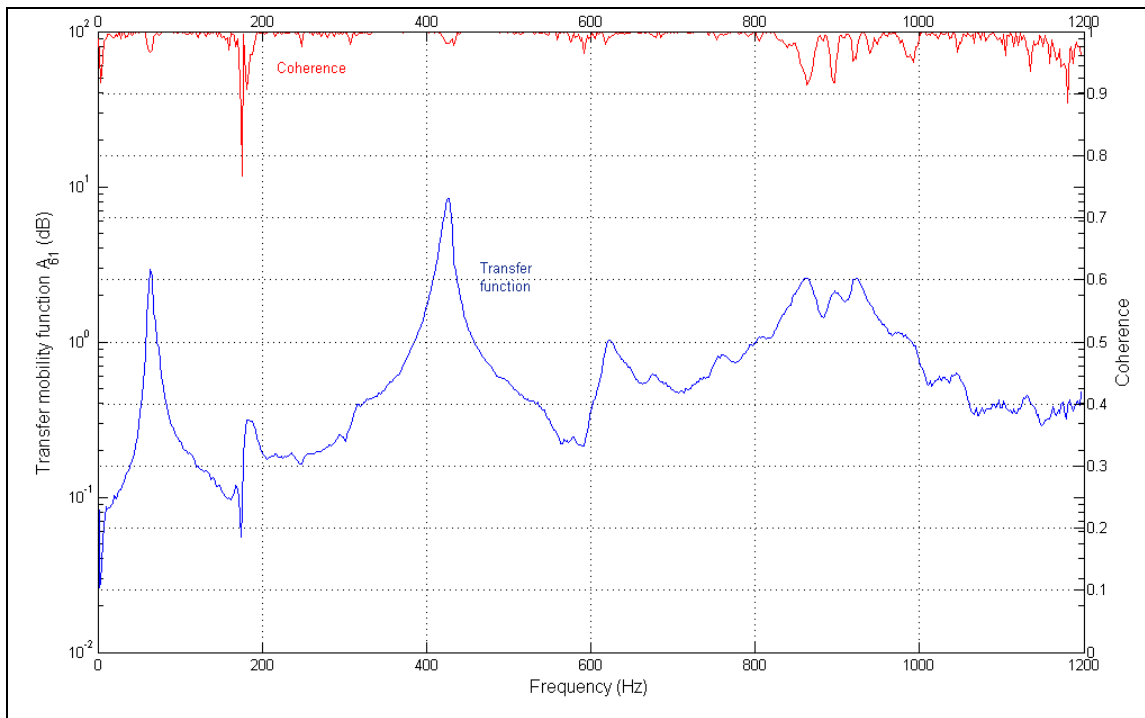


Figure 6.18: Beam E - coherence function check for transfer mobility A_{61} .

6.4.2.6 FRF Shape Check

In the FRF shape check, one of the prime checks of FRF data is to assure the occurrence of relatively clear anti-resonance troughs with their sharp peaks when drawn on logarithmic-scale plot. A drive point mobility measurement was made and illustrated in Figure 6.19. The property of existence of the anti-resonance between each two adjacent resonances was clearly satisfied in the check. However, for transfer point mobility FRF, it is most likely to expect a valley between the two adjacent resonances rather than trough, as shown in Figure 6.19. The second check, which gives a rational decision about the accuracy of the measured FRFs, is that the resonance peaks and the anti-resonance should display the same sharpness on a semi-logarithmic plot. Success to achieve so indicates a good measurement quality, both in sense of the frequency resolution and excitation level resulting in a reasonable definition of the anti-resonance region. However, the transfer point mobility showed only the odd natural modes (1st, 3rd, 5th), as the mid span point (point 6) is a node for all even natural mode shapes (Figure 6.18). Therefore, the even modes (2nd and 4th modes) did not appear in the FRF where the reference output location was chosen at that node point of these particular modes. Results shown confirmed the fact that a limited set of measured transfer

functions and/or poor selection for these measurements allow some resonances not being appeared, even when they are excited, as the accelerometer is mounted at a node point. Another visual check aided to validate the quality of FRF measurements was that a phase loss through resonance frequencies and a positive phase gain through anti-resonances were observed. For drive point mobility, the value of phase was always between 0° and 180° , as shown in Figure 6.19 (lower-left trace). In common, when Bode plots (the FRF modulus and phase as functions of the frequency) are considered for a drive point measurement, the phase loses 180° as the function crosses resonance frequency and gains 180° as it crosses anti-resonance frequency (Avitabile, 2001). Nonetheless, in a hysteretic damping model it is expected the phase angle is not exactly starts at 180° (Maia and Silva, 1997).

The real part of FRF against frequency and imaginary part against frequency are also shown in Figure 6.19. It is important to note that the real part of a drive point function crosses the frequency axis at the resonances, whereas at the same point the imaginary part is at its maximum value. One another important feature of the drive point function serves as a check is that all peaks of the imaginary part for the drive point measurement must point to the same direction (Avitabile, 2001), Figure 6.19 (upper-right trace).

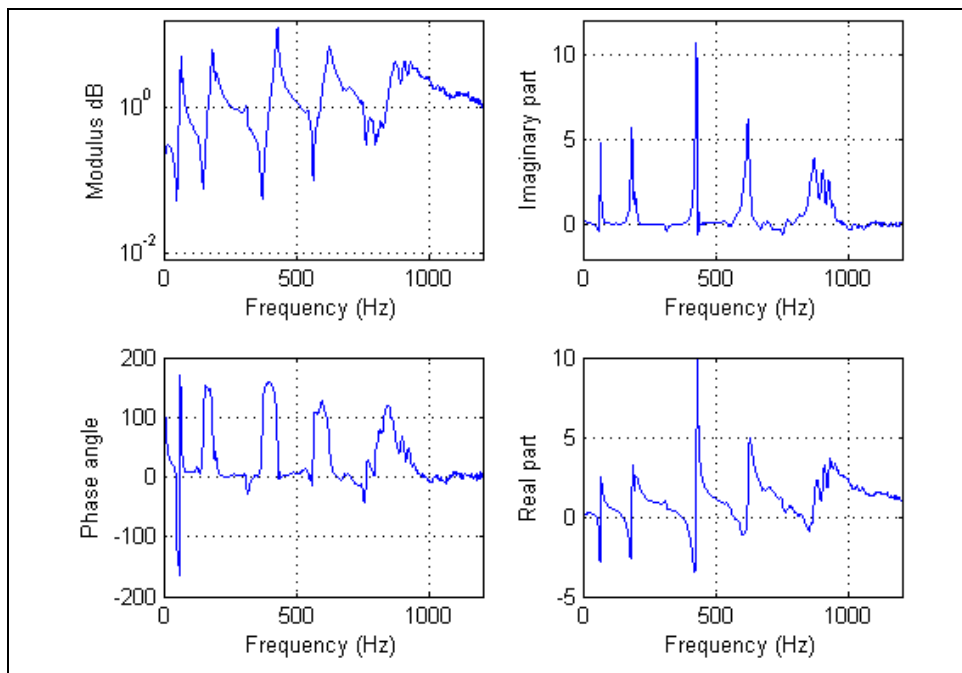


Figure 6.19: Beam E- FRF shape check for drive mobility function at points 1.

In brief, QA checks carried out throughout the exploratory phase were to ensure two main objectives: the suitability of the data acquisition setting parameters and modal extraction method; and the suitability of the test structure for EMA.

All QA checks performed for the beam indicated that there were no significant disagreements in each particular check with the expected results of a satisfactory check. In addition, any minor inconsistent observations were less likely to be deemed significant in the meantime; they were unlikely to attribute to the set-up procedure or data acquisition parameters. Conversely, the slight discrepancies experienced throughout the check survey can be related to two reasons: the inconsistency of the impact location and strike angle between one and next blow; and extraneous noise occurred in the background of the test arrangement.

6.4.3 Experimental Modal Analysis: Measurements Phase

Making uses of the characteristics offered by the acquisition equipments, for each of the five RC beams and in particular for each state condition, three rows and a single column in the FRF matrix were collected. The simplest form of single-input method, the impact excitation test, was used through the instrumented impact hammer. Three accelerometers were mounted starting from the right-hand end (point 1) at stations 0.2m apart. These three accelerometers were subsequently repositioned at new three locations in order to cover the entire beam length with a total of 11 measurement points (see Figures 4.1 and 6.9). The beam was impacted and accelerations measured normal to the direction of the soft cords. In the case of roving accelerometers, the beam was impacted at a single location at the right-hand end (point 1) resulting in a single column in FRF matrix. Additionally, three accelerometers were mounted at points 1, 2 and 3 and kept at the same positions while the impact excitation was roved over the whole beam to test the beam thoroughly. Processing of the data from the last procedure resulted in associated first three FRF rows in the frequency response matrix. The fact that the author would not have sufficed with a single row or a single column of FRF measurements is to use the vibration measurements whether in time, frequency or modal domain to validate different damage identification models where immense data in several methods is critical. Also, in order to take into account the variability in the data

due to the two alternatives, roving accelerometer and roving hammer. Moreover, for each of the three available accelerometers, four time histories were measured for each structural state condition. These four averages were used to reduce the influence of random noise in the FRF estimates. As a final note, the first four or five modes of vibration, depending upon whether the flexural modes about the major or minor neutral axis, can clearly be extracted from the analysis of beam measurements calculated in this work.

6.4.4 Experimental Modal Analysis: Post-Test Analysis Phase

This section suffices with the main aspects of this phase, while the application of the pertinent analysis method on the real measurements of this work will be explained and displayed in details in the next Chapter. This phase is normally carried out after field measurements are fulfilled and their quality is ensured. In this stage, measured FRF data is analysed to determine the modal parameters of the tested structure. Three modal parameters describe the inherent dynamic properties of a system, these generally are: resonance frequencies, mode shapes and damping coefficients. In this respect, various methods are available to perform a convenient analysis and obtain the mathematical model. The simplest post-test analysis method so-called peak-picking is normally used in conjunction with SDOF systems to obtain modal parameters. This method works effectively with structures whose FRFs show well-defined sufficiently separated modes at resonance frequencies that the FRF data at the vicinity of a resonance frequency is treated as SDOF (Ewins, 2000; He and Fu, 2001). The existence of widely spaced modes served to bring to light the suitability of using SDOF estimation in EMA to ensure that such modes are correctly estimated (Reynolds, 2000). The analysis method and the results of this phase are presented in section 6.2 of this thesis.

6.5 Correlation of Analytical Model

The prime objective of this section is to develop an adaptable spatial-based analytical model for the test structure in order to use the accurate predicted model for further useful applications. The experimental modal data for each particular beam was used to validate the corresponding FE model, and the accuracy of the predicted

parameters was checked with their counterpart measurements. Making use of all experimental data of the five intact beams, this study used the FE method to regenerate the synthesis dynamic characteristics of the associated beams. For this purpose, one-dimensional FEM dynamic analysis routine was established in the MATLAB[®] programming environment. The RC beam was divided into 22 one-dimensional elements. The beam density and Young's modulus of elasticity were taken in accordance with the beam characteristics given in Table 6.1. Results showing the comparison between the numerical and experimental natural frequencies for the intact state condition are summarised in Table 6.3. The numerical model assumed an adjusted dynamic (tangent) modulus of elasticity. Also, the results of beams D and E represented data from the defective (voided) state condition. For the majority of the listed results, the predicted frequencies were agreed strongly with the first four (or five) bending frequencies operated by the modal testing. The percentage of deviation was less than 1% for all the observed frequencies in beams A and B. For beam E, the only observed difference was in the third resonance and was of 3%. However, maximum deviation of 6.8% was observed in the third mode of beam D and of 14% in second mode of beam C. In these two cases, the difference was fairly big and could be accounted to some obscure material non-homogeneity by which it was difficult to recognise and model accurately.

Table 6.3: Comparison between experimental (Exp) and numerical (Num) natural frequencies.

| Test Beam | Mode 1 | | Mode 2 | | Mode 3 | | Mode 4 | | Mode 5 | |
|--------------|-------------|-------------|-------------|-------------|-------------|-------------|-------------|-------------|-------------|-------------|
| | Num | Exp | Num | Exp | Num | Exp | Num | Exp | Num | Exp |
| | ω Hz | ω Hz | ω Hz | ω Hz | ω Hz | ω Hz | ω Hz | ω Hz | ω Hz | ω Hz |
| Beam A | 104.5 | 104.4 | 284.6 | 282.1 | 549.5 | 549.2 | 892.2 | 896.7 | 1305.4 | ----- |
| Beam B | 125.4 | 124.3 | 335.4 | 338.0 | 642.1 | 644.6 | 1060.2 | 1041.0 | 1565.8 | ----- |
| Beam C | 90.4 | 86.9 | 270.2 | 236.2 | 550.4 | 612.6 | 880.9 | 864.8 | 1279.7 | ----- |
| Beam D | 77.4 | 80.9 | 205.1 | 192.2 | 393.5 | 368.5 | 656.4 | 654.6 | 983.1 | 949.2 |
| Beam E | 94.5 | 94.9 | 247.0 | 247.2 | 460.2 | 475.8 | 747.0 | 758.9 | 1104.2 | 1088.0 |

Furthermore, the first group of the identified mode shapes for the five beams were compared and shown in Figures 6.20-6.24. The first two modes in the numerical analysis were rigid body modes and, for convenience, are not illustrated in the figures. The experimental modal parameters were estimated using the Quadrature Picking method as described later in section 7.2.4. The numerical and experimental modes overlaid well for the first two modes. The overlap became slightly less for the higher modes, suggesting that the test grid profoundly affected the higher modes.

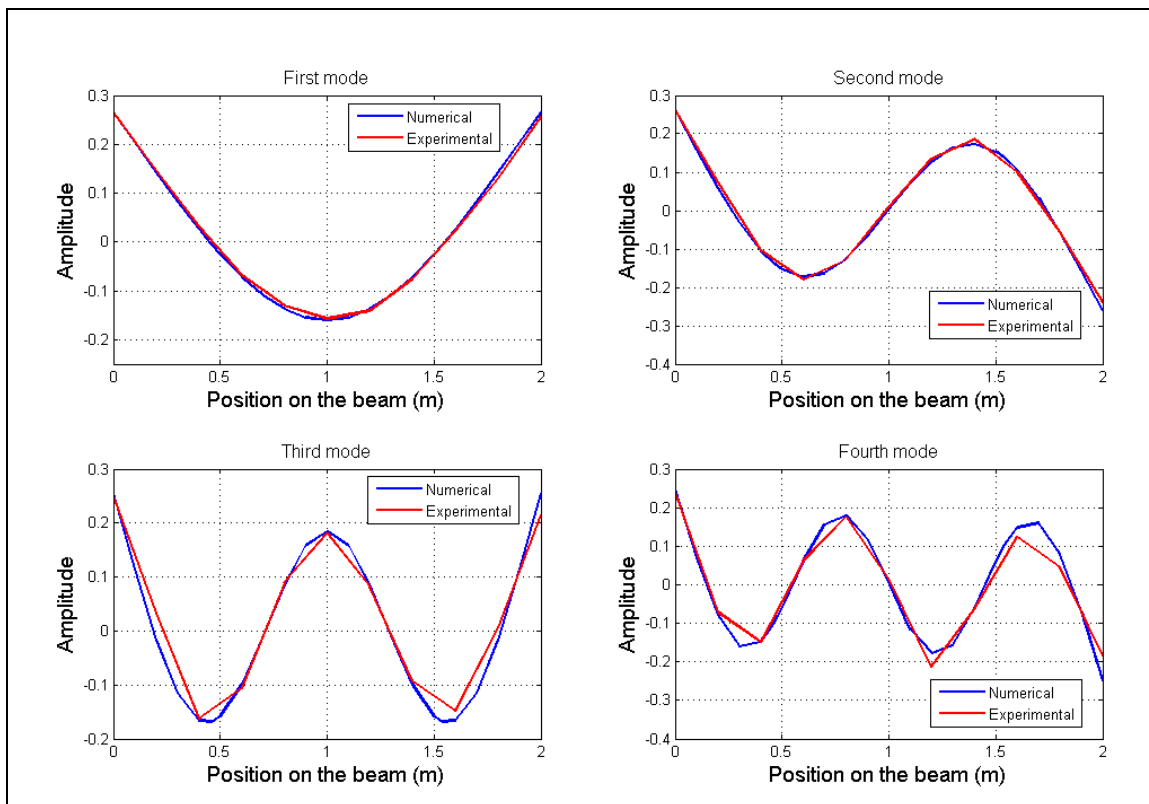


Figure 6.20: Beam A- numerical and experimental mode shapes (intact condition).

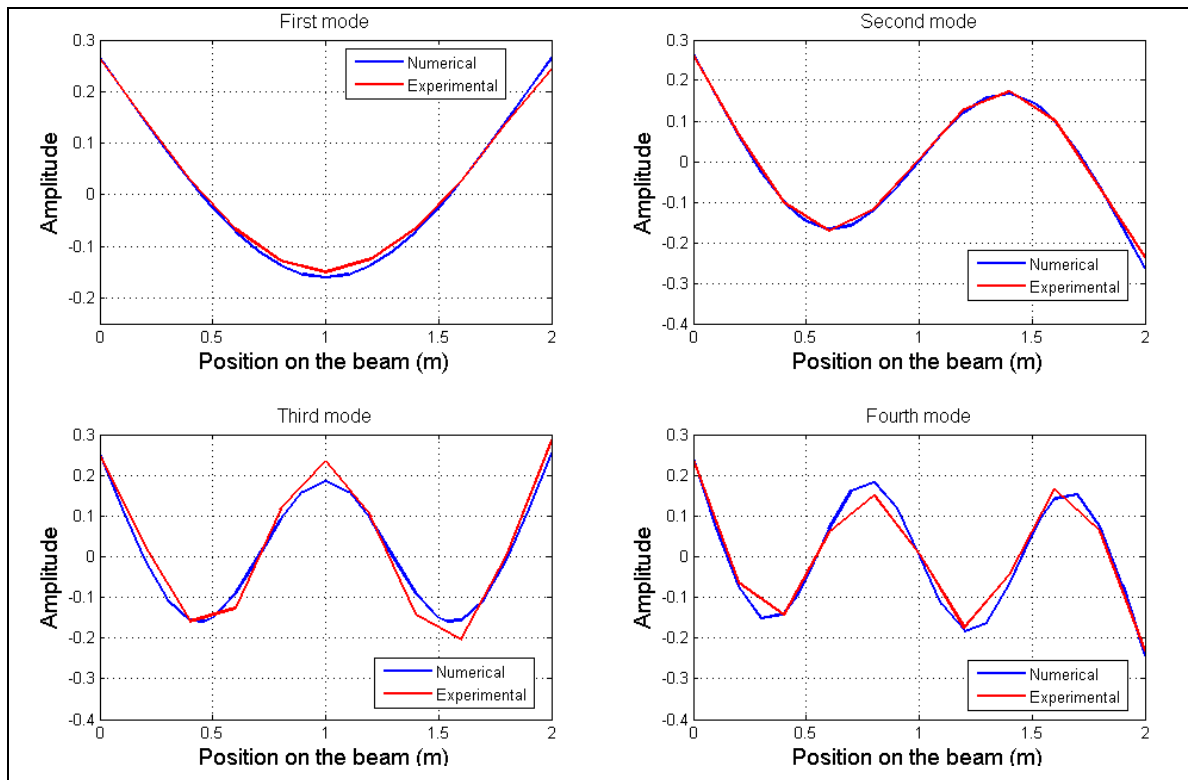


Figure 6.21: Beam B- numerical and experimental mode shapes (intact condition).

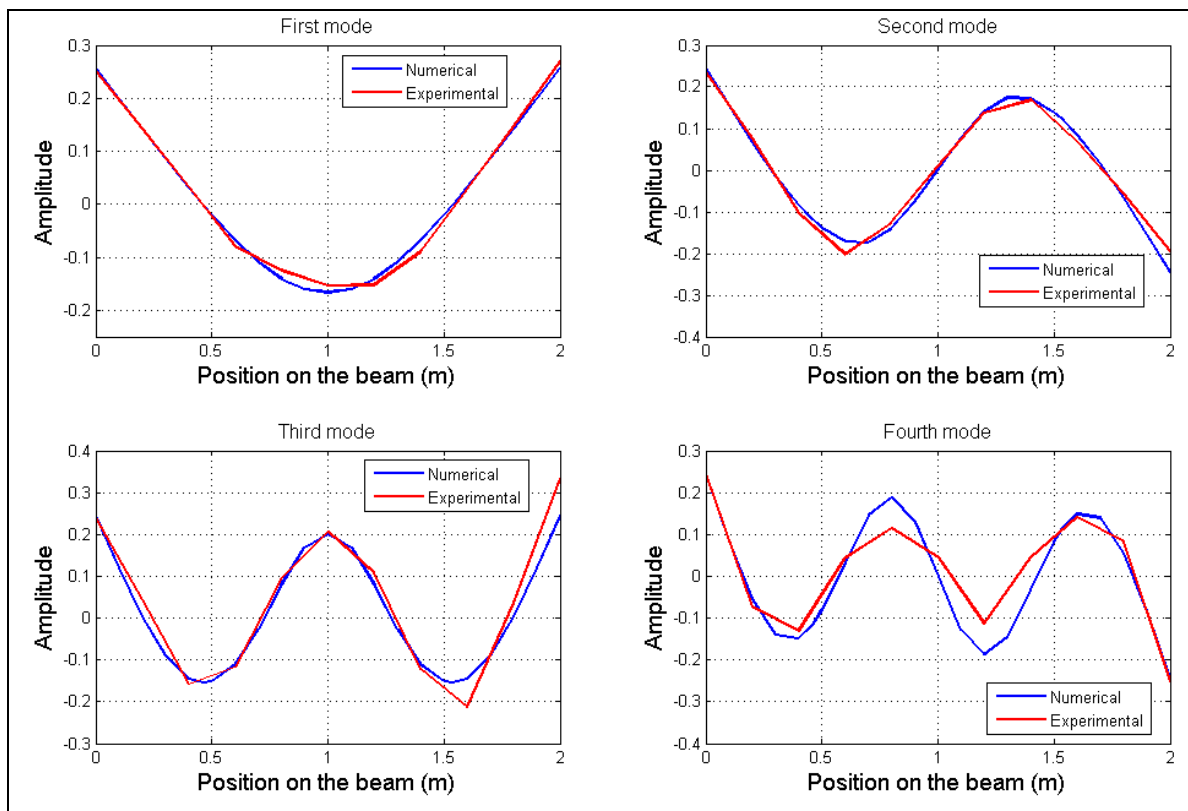


Figure 6.22: Beam C- numerical and experimental mode shapes (intact condition).

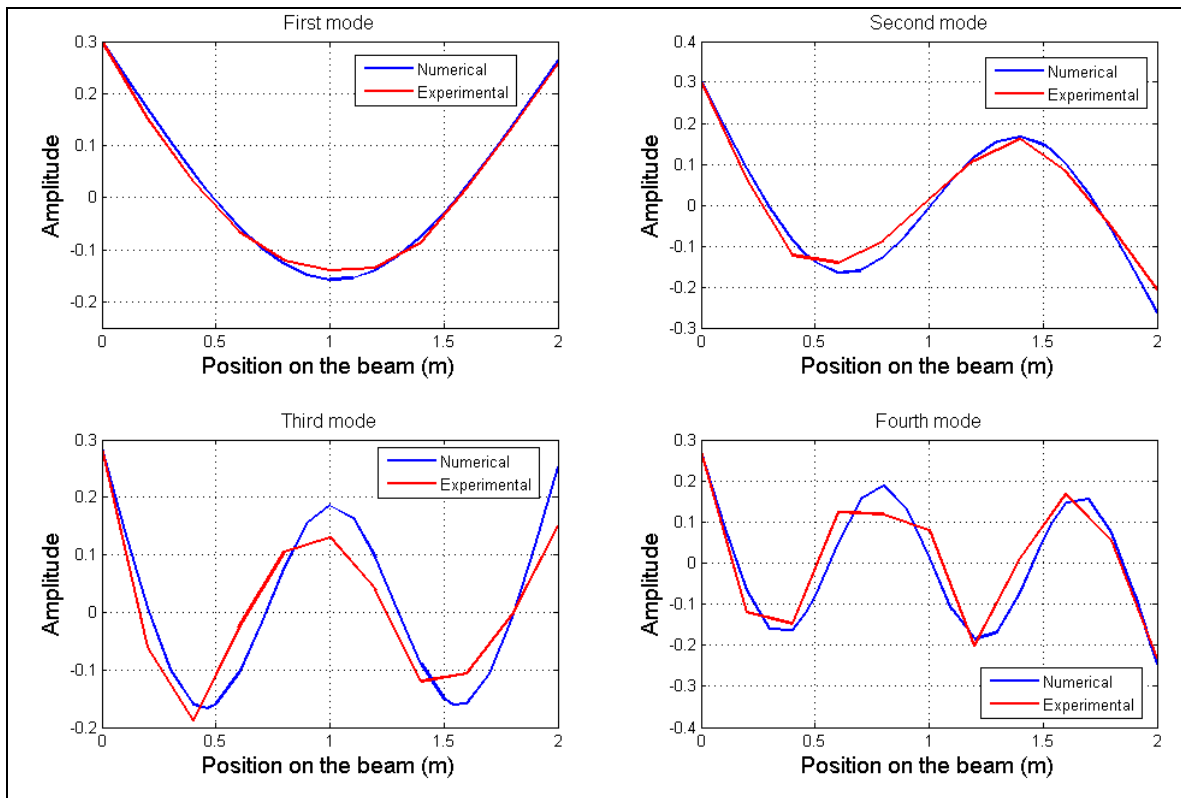


Figure 6.23: Beam D- numerical and experimental mode shapes (intact condition).

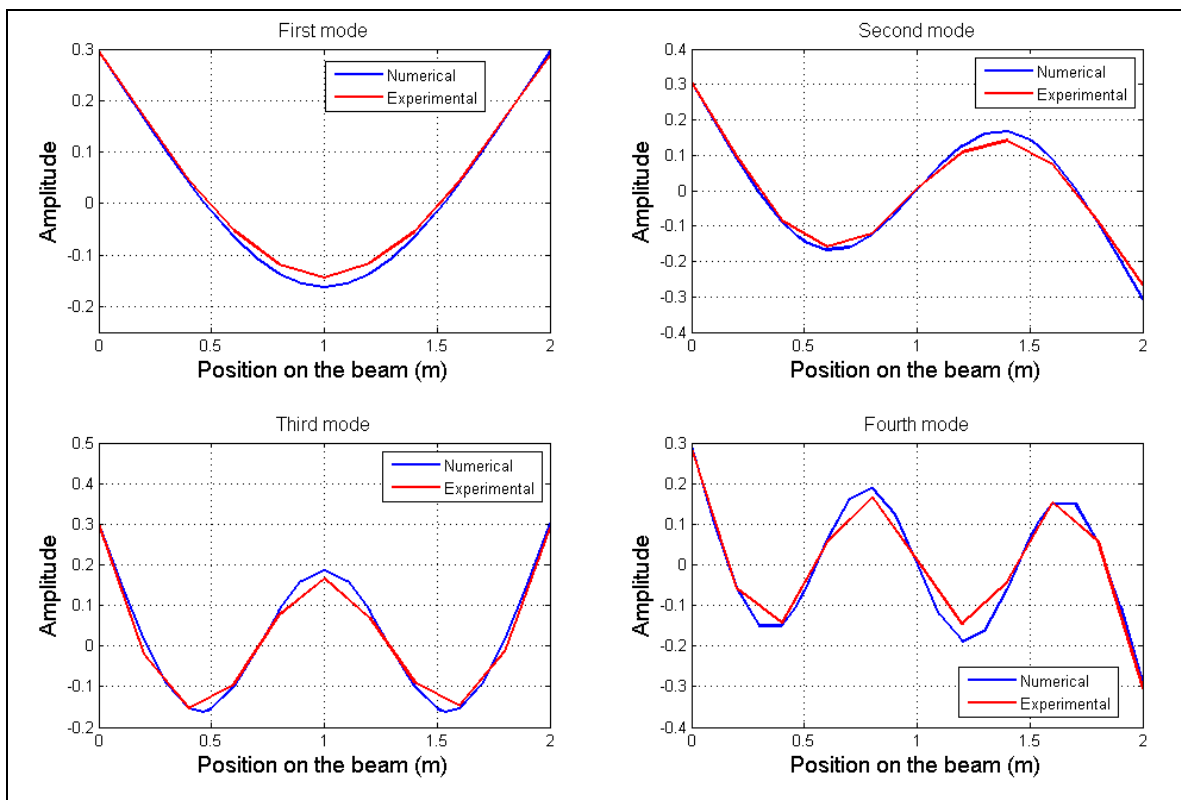


Figure 6.24: Beam E- numerical and experimental mode shapes (intact condition).

A further check to the accuracy of the experimental and numerical results was done by the means of overlaying the FRFs of both models, as shown in Figure 6.25. In this case, each FRF was estimated by averaging four cross power and auto power spectra generated from the time histories. The FFT was computed in each time using the associated time amplitude then; the set of spectrum estimates was averaged to form the final FRF measurement. The modulus of elasticity was corrected in order that the predicted natural frequencies agreed with the experimental ones. The shear deformation effect was neglected while computing the stiffness and mass matrix coefficients. The damping matrix was approximated as proportions of the stiffness matrix. The model shown predicted the measured baseline (intact) FRF with a high level of reliability. In Figure 6.25, the numerical FRF seemed to credibly fit the experimental FRF, even though the former had higher resonant frequency in the fourth mode. In conclusion, the results of this section summarised the development of the FE analytical model to better understand the vibration behaviour of each of the RC beams. The validated analytical model can further be used to regenerate measured and unmeasured modal parameters, and also to identify the perturbations that might arise from next steps.

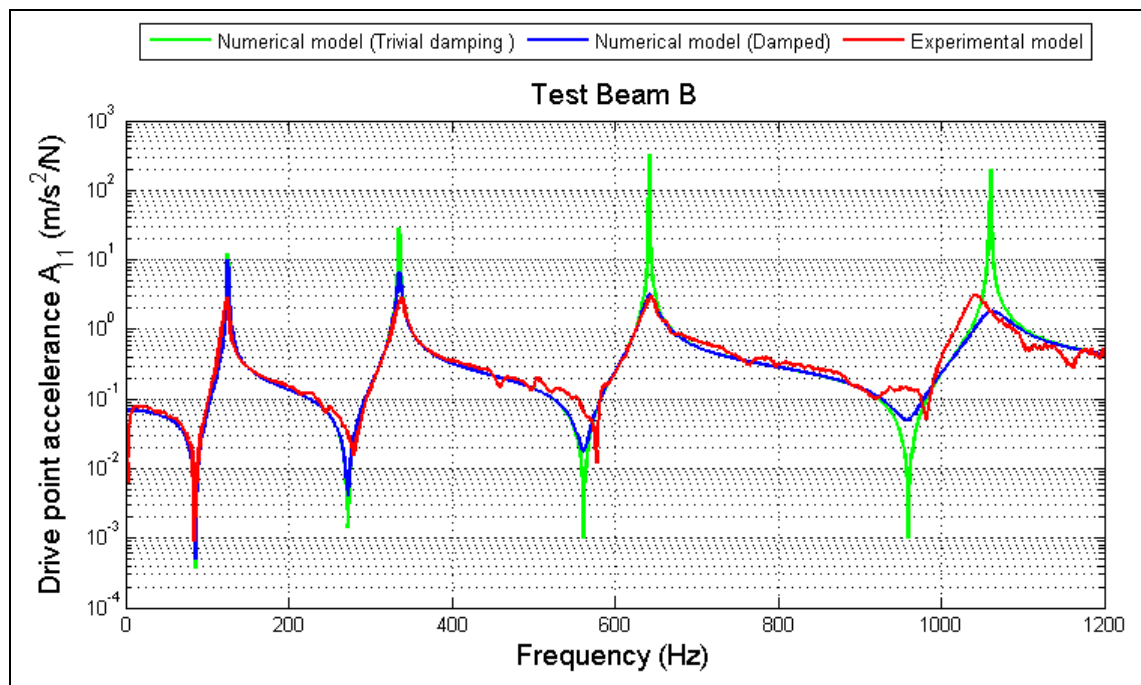


Figure 6.25: Beam B- FRF overlap check for effect of damping.

6.5.1 Effect of Damping on Predicted Data

In order to study the effect of damping on the response of the freely supported RC beams, some numerical examples were assessed for the proportional damping models. The damping matrix was calculated as directly proportion to the stiffness matrix with arbitrary proportion factors (a_0 and a_1) given in Equation 4.20 equal 0.0005% and 0%, respectively. A comparison between predicted FRFs using different damping factors and experimental measurement of beam B is shown in Figure 6.25. The plot of proportion damping factor showed how the damping effect expedites the decay of the FRF. In the meantime, damped FRF gave better overlay with the experimental results compared to the FRF of trivial damping effect. Including the effect of damping through the analytical model improved the overall behaviour, alleviated the sharp peaks and widened the response in the vicinity region of the resonance peaks and anti-resonance troughs, as shown in Figure 6.25. However, there are fundamental differences between the predicted and measured damping ratios. On the one hand, the measured modal damping ratios agreed with those predicted as they both indicated light damping characteristics to the tested beams, as was expected in RC beams. On the other hand, the measurements provided a completely disproportional behaviour for ratios from different modes.

As a parting comment, it would have been better to approximate the damping matrix for the beam model using the results of the modal damping ratios of the experiments. However, the current application was dictated by the limited truncated measured modes and difficulties of measuring the rotational DOFs experimentally.

6.5.2 Effect of Shear Deformation on Predicted Data

This section reports two possible solutions to model the RC beams, with or without the effect of transverse shear deformation. It also covers data visualisation of the effect of this property on FRF measurement for a case study of the free-free supported beam B.

In general, excluding the shear deformation effect may produce a considerable error to the analytical data; hence additional source of uncertainty in the measured data, where the accuracy is critical. To illustrate the significance of shear deformation on the

computed response of RC structures, the five RC beams in this work were investigated. Analyses were carried out assuming that the beam was freely supported, and for each case, FRFs were computed for two alternative models, Euler-Bernoulli beam model (where the effect of the shear is excluded) and Timoshenko model (where the effect of the shear is included). The influence of shear deformation on the natural frequencies for the intact state condition is summarised in Table 6.4. Also, comparisons for the effect of shear deformation on the FRFs from different beam models are shown in Figure 6.26.

It is evident from this figure that discarding the shear effect resulted in a remarkable increase in frequencies as the modes got higher. On contrary to the effect of the boundary conditions of a beam on the natural frequencies, the shear deformation tends to significantly affect the higher natural frequencies rather than the fundamental natural frequency. Results showed that the fundamental natural frequency was less sensitive to the effect of shear deformation. As the first mode shape of the case studies give a maximum deflection at midpoint; hence the effects of shear strain energy are distributed over the entire length of the beam. Though, the effect of shear strain energy is distributed over quarter of the beam length in the forth mode shape. In this case, the shear deformation has a considerable influence on the corresponding natural frequency.

In short, the observable fact is important as truncated sets of modal parameters are less sensitive to local damages. Other high order modal parameters are needed in order to provide better results for the benefit of damage detection methods (Shi et al., 2000).

Table 6.4: Comparison between numerical natural frequencies using Timoshenko (Timo) and Euler-Bernoulli (Euler) models alongside the experimental (Exp) results.

| Test Beam | Mode 1 | | | Mode 2 | | | Mode 3 | | | Mode 4 | | | Mode 5 | | |
|--------------|-------------|-------------|-------------|-------------|-------------|-------------|-------------|-------------|-------------|-------------|-------------|-------------|-------------|-------------|-------------|
| | Euler | Timo | Exp | Euler | Timo | Exp | Euler | Timo | Exp | Euler | Timo | Exp | Euler | Timo | Exp |
| | ω Hz | ω Hz | ω Hz | ω Hz | ω Hz | ω Hz | ω Hz | ω Hz | ω Hz | ω Hz | ω Hz | ω Hz | ω Hz | ω Hz | ω Hz |
| Beam A | 104.5 | 103.9 | 104.4 | 284.6 | 279.0 | 282.1 | 549.5 | 528.4 | 549.2 | 892.2 | 839.1 | 896.7 | 1305.4 | 1200.2 | ----- |
| Beam B | 125.4 | 124.6 | 124.3 | 335.4 | 328.7 | 338.0 | 642.1 | 616.5 | 644.6 | 1060.2 | 994.8 | 1041.0 | 1565.8 | 1437.5 | ----- |
| Beam C | 90.4 | 90.1 | 86.9 | 270.2 | 266.6 | 236.2 | 550.4 | 534.5 | 612.6 | 880.9 | 834.4 | 864.8 | 1279.7 | 1209.1 | ----- |
| Beam D | 77.4 | 77.2 | 80.9 | 205.1 | 203.1 | 192.2 | 393.5 | 386.6 | 368.5 | 656.4 | 636.6 | 654.6 | 983.1 | 941.6 | 949.2 |
| Beam E | 94.5 | 94.3 | 94.9 | 247.0 | 244.6 | 247.2 | 460.2 | 451.1 | 475.8 | 747.0 | 722.8 | 758.9 | 1104.2 | 1054.4 | 1088.0 |

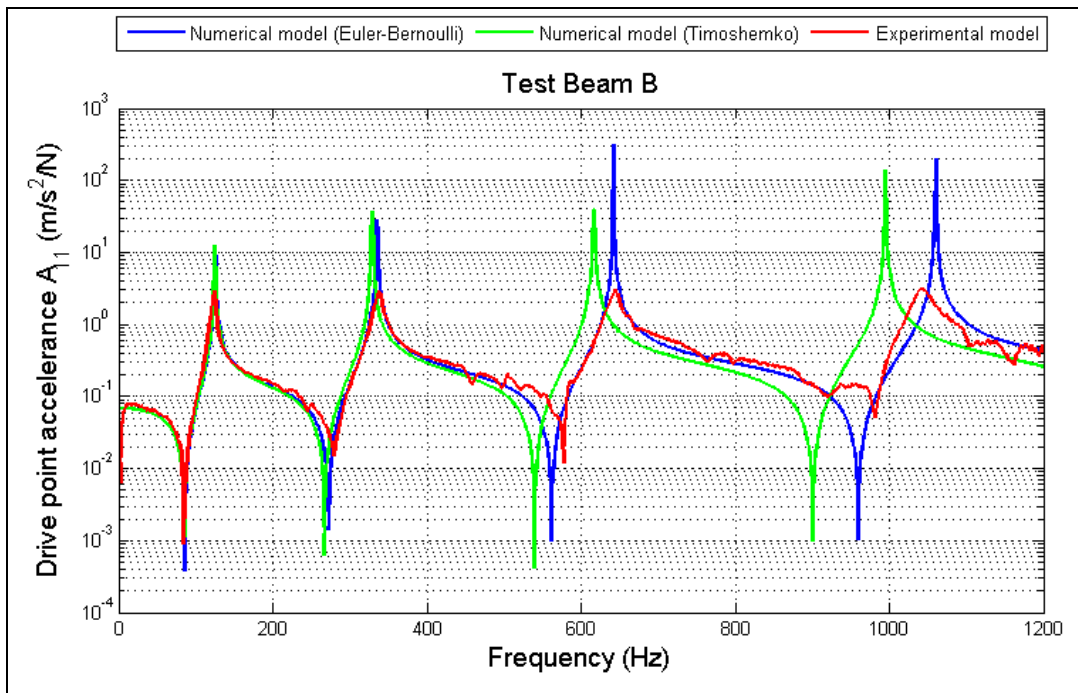


Figure 6.26: Beam B- FRF overlap check for effect of shear deformation.

6.5.3 Effect of Modulus of Elasticity on Predicted Data

The effect of using different moduli was studied in an effort to correct the analytical model of the intact state condition and make it with enough agreement compared to the experimental model. The dynamic (tangent) modulus of elasticity was found imperative to use in predicting closer resonance frequencies compared with the static (secant) modulus. In addition, its effect can influence regularly all modes of vibration as opposed to the shear deformation effect. However, the parameter was seen to be significant for the beams of higher compressive strength. Comparisons between resonance results using dynamic and static moduli are presented in Table 6.5. Results for beams D and E were given when the voids were exist in the analytical models. The resonances differed by up to approximately 8.5% when the two different moduli were examined. In addition, the shifts in the resonance frequencies of beam B as a result of using the two moduli are shown in Figure 6.27.

Table 6.5: Comparison between numerical natural frequencies based upon dynamic (E_d) and static (E_s) modulus of elasticity along with the experimental (Exp) results.

| Test Beam | Mode 1 | | | Mode 2 | | | Mode 3 | | | Mode 4 | | | Mode 5 | | |
|--------------|-------------|-------------|-------------|-------------|-------------|-------------|-------------|-------------|-------------|-------------|-------------|-------------|-------------|-------------|-------------|
| | E_d | E_s | Exp | E_d | E_s | Exp | E_d | E_s | Exp | E_d | E_s | Exp | E_d | E_s | Exp |
| | ω Hz | ω Hz | ω Hz | ω Hz | ω Hz | ω Hz | ω Hz | ω Hz | ω Hz | ω Hz | ω Hz | ω Hz | ω Hz | ω Hz | ω Hz |
| Beam A | 104.5 | 103.7 | 104.4 | 284.6 | 282.3 | 282.1 | 549.5 | 545.2 | 549.2 | 892.2 | 885.2 | 896.7 | 1305.4 | 1295.1 | ----- |
| Beam B | 125.4 | 112.9 | 124.3 | 335.4 | 302.0 | 338.0 | 642.1 | 578.2 | 644.6 | 1060.2 | 954.7 | 1041.0 | 1565.8 | 1410.0 | ----- |
| Beam C | 90.4 | 89.5 | 86.9 | 270.2 | 260.6 | 236.2 | 550.4 | 520.1 | 612.6 | 880.9 | 835.9 | 864.8 | 1279.7 | 1225.2 | ----- |
| Beam D | 77.4 | 70.7 | 80.9 | 205.1 | 187.2 | 192.2 | 393.5 | 359.3 | 368.5 | 656.4 | 599.2 | 654.6 | 983.1 | 897.4 | 949.2 |
| Beam E | 94.5 | 86.4 | 94.9 | 247.0 | 225.8 | 247.2 | 460.2 | 420.9 | 475.8 | 747.0 | 683.2 | 758.9 | 1104.2 | 1009.8 | 1088.0 |

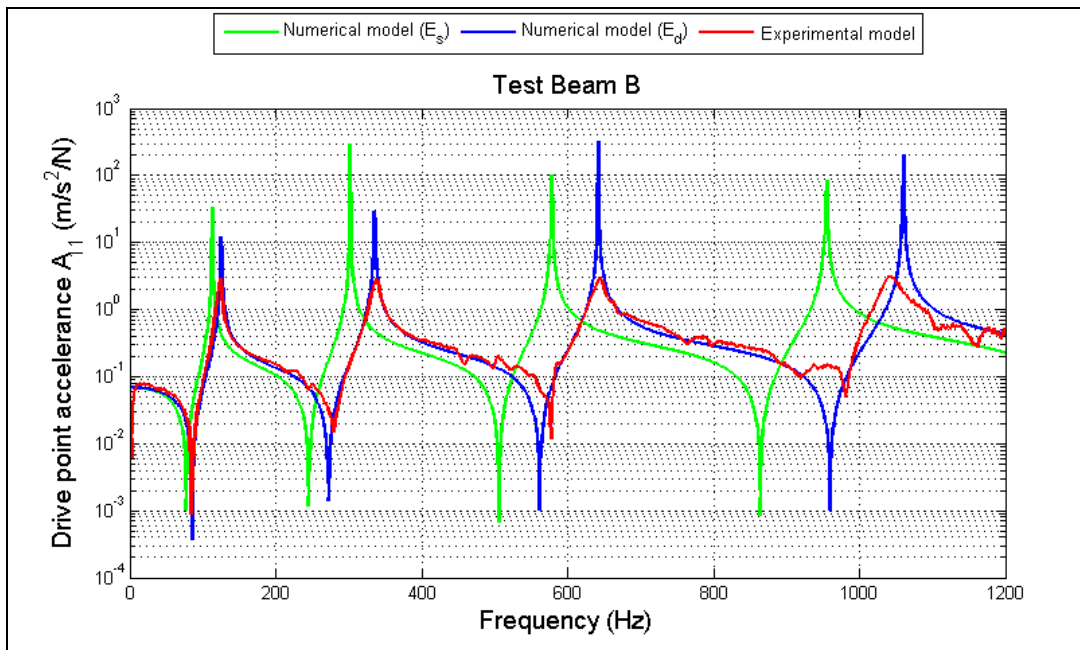


Figure 6.27: Beam B- FRF overlaps check for effect of modulus of elasticity.

6.6 Summary

This Chapter is divided into four main parts. The first part introduced the test beams with a thorough description to the specifications of each beam. The description extended to provide illustrated explanation to the scenarios of damage assigned to each individual state condition. In the second part, a pre-test FE model, which is a starting step in any modal testing analysis, was developed in accordance with estimating the range of first group of resonance frequencies and choosing the initial test grid so as to avoid the spatial aliasing.

A systematic EMA procedure including the four essential phases of the analysis process was applied in the third part of the Chapter reinforced with appropriate samples of results from each individual case. All necessary QA checks performed for a beam sample specified that there were no significant differences with what stipulated by the requirements set by the UK DTA. Therefore, rounds of measurements were carried out collecting great deal of signals with more credibility.

In order to update the preliminary analytical model, the fourth part was concerned with the discussion of several physical properties found critical to the correction process. A comprehensive comparison between predicted and measured data was presented using

resonances, mode shapes and FRF measurements. In the context of the effect of shear deformation, the variation in the resonances when the shear effect was included was as big as 9% in the fourth mode, but it was less than 1% in the first mode. Using the dynamic modulus of elasticity was also found critical to predict closer modal frequencies compared with the static modulus. The parameter was significant for the beams of high compressive strength and can affect almost equally all modes of vibration. The resonances differed by up to approximately 8.5% when the two different moduli were investigated. Finally, the effect of proportional damping was introduced as a constant ratio from the stiffness matrix. Damping effect in the analytical model manifested as lower and decaying amplitudes; and less sharp and wide peaks in the vicinity of the resonances and anti-resonances.

7. Damage Identification using Modal Parameters and their Formulations

7.1 Introduction

The characterisation of damage in RC elements subjected to cracking patterns using vibration data is reported challenging in the identified literature. Therefore, this Chapter endeavours to shine light on the shortcomings of dynamic methods when applied to RC beams simulated with various scenarios of defect. For this reason, five different RC beams were tested through the course of this project; three beams were loaded statically to failure in multiple successive load cycles and later rehabilitated and the rest were devised with cavities produced at the ends of each beam to model localised damage at zero stress area of flexural element. The beams were tested under a free-free support condition in order to remove the intervention of support rigidity dilemma using EMA.

A relevant post analysis methodology for surveys of EMA measurement of the predefined five RC beams was conducted in order to extract the basic modal parameters; namely, natural frequency, modal damping and mode shapes. The outcomes of the observed modal parameters and their correlations were presented and discussed during the course of this Chapter. Most importantly, the identified parameters along with the following more regularly used techniques were exploited to characterise the defect of each beam individually:

- Resonant frequencies.
- Modal damping values.
- Natural mode shapes and response mode shapes.
- Modal assurance and coordinate modal assurance criteria.
- Curvature mode shapes.
- Frequency response functions.
- Direct stiffness calculation method.

Therefore, in this sequence of events, the following subjects are appreciated in the Chapter:

1. The suitability of the methodology used to extract modal parameters from RPS density functions and FRFs.
2. The main features of each modal parameter or modal formula as a potential damage characterisation factor in relation to its suitability and extent to monitor the underlying structural changes.

In addition, an imperative practical note is that when the excitation forces cannot be measured, the conventional response parameters such as FRFs cannot be found. Thus, as a less effort process, the power spectral density (PSD) of response measurements caused by stationary noise rather than FRF can be used for structural damage identification purpose (Nauerz and Frizen, 2001). The mode shapes based on spectra of response measurements only were also computed herein, and their accuracy in quantifying the damage was questioned with their counterpart accurate mode shapes.

Finally, it is important to mention that the knowledge gained through detailed investigations conducted in this Chapter has been employed as a basis for development of new graphical damage localisation technique given at the end of this Chapter.

7.2 Post-test Analysis and Estimation of Modal Parameters

7.2.1 Overview

The post-test analysis phase is commonly carried out after field measurements are recorded and their quality is assured. In this stage, FRF measurements are analysed to determine the modal parameters of the tested structure. In this respect, various methods are available to perform a convenient analysis and obtain the mathematical model. The simplest modal post-test analysis method so-called peak-picking or peak-amplitude is normally used in conjunction with Single Degree Of Freedom (SDOF) systems to obtain the modal parameters. This method works effectively with structures whose FRFs show well-defined and sufficiently separated modes at resonance frequencies that the FRF data at the vicinity of a resonance frequency is treated as SDOF (Ewins, 2000; He and Fu, 2001). The method presumes that response measurements are controlled by resonant modes at their corresponding natural

frequency (Haritos and Owen, 2004). Other alternative methods are classified as Multi Degree Of Freedom (MDOF) modal analysis methods. These general global methods are used in particular cases where more detailed addressing is necessary for closely spaced coupled modes or for heavily damped structures whereby the resonance is not dominated by one mode only. Due to the observed characteristics of FRFs of this study, the appropriateness of peak-picking method is satisfactorily justified to use for modal parameters estimation.

7.2.2 Resonance Frequency Extraction

The easiest modal parameter to obtain reliably is the resonance frequency. A resonance frequency is recognised as the largest amplitude in the magnitude of the FRF, and the frequency corresponding to that peak represents the resonance frequency (ω) of the specific mode of vibration. The natural frequencies of each of the five RC beams in this work related to each artificial damage state are given in Table 7.1. The results were extracted for the first four global bending modes for the beams A, B and C, while they were extracted for the first five global bending modes for beams D and E. The outcomes showed that the natural frequencies were estimated with reasonable accuracy based only upon drive point measurement (H_{11}) associated with each damage state condition.

7.2.3 Damping Estimation

As the RC beams in this work are lightly damped structures, modal damping ratios were experimentally estimated from the width of the resonance peak.

The half-power bandwidth is widely common, simple and quick method and has been put into practice already (Wenzel, 2009). It is based on the fact that the width of the response amplitude of SDOF system is proportional to the damping ratio of the system. Viscous modal damping (ζ) is experimentally identified through the half-power points of a resonance magnitude for FRF, and can be written as (He and Fu, 2001):

$$\zeta = \frac{f_a - f_b}{2f_r} \quad (7.1)$$

Where:

$f_a - f_b$ is the width of the resonance curve at which the amplitude is $\frac{1}{\sqrt{2}}$ of the resonance amplitude

f_r is the resonance frequency

The estimated viscous modal damping ratios for the five beams from the EMA measurements are presented in Table 7.1. The listed results are summarised for the first identified bending modes, and related to each state condition.

Table 7.1: Comparison of identified frequencies and damping ratios for test beams.

| Beam A | | | | | | | | | |
|-----------|-------------|-----------|-------------|-----------|-------------|-----------|-------------|-----------|--|
| Load step | Mode 1 | | Mode 2 | | Mode 3 | | Mode 4 | | |
| | ω Hz | $\zeta\%$ | ω Hz | $\zeta\%$ | ω Hz | $\zeta\%$ | ω Hz | $\zeta\%$ | |
| Intact | 104.4 | 3.21 | 282.1 | 2.38 | 549.2 | 2.12 | 896.7 | 1.14 | |
| 3kN | 102.4 | 3.24 | 277.1 | 2.4 | 542.2 | 2.02 | 888.3 | 1.54 | |
| 6kN | 98.36 | 3.56 | 275.1 | 2.36 | 530.8 | 2.06 | 871.3 | 1.7 | |
| 10kN | 88.38 | 4.06 | 262.1 | 2.67 | 509.8 | 2.23 | 825.3 | 1.9 | |
| 13kN | 84.38 | 4.09 | 251.1 | 2.47 | 498.8 | 2.93 | 799.4 | 2.23 | |
| 16kN | 82.88 | 4.46 | 248.7 | 2.53 | 496.3 | 2.82 | 792.9 | 2.03 | |
| Repaired | 90.37 | 3.87 | 252.6 | 2.49 | 514.3 | 2.31 | 821.8 | 2.05 | |

| Beam B | | | | | | | | | |
|-----------|-------------|-----------|-------------|-----------|-------------|-----------|-------------|-----------|--|
| Load step | Mode 1 | | Mode 2 | | Mode 3 | | Mode 4 | | |
| | ω Hz | $\zeta\%$ | ω Hz | $\zeta\%$ | ω Hz | $\zeta\%$ | ω Hz | $\zeta\%$ | |
| Intact | 124.3 | 1.77 | 338 | 1.26 | 644.6 | 1.05 | 1041 | 0.83 | |
| 3kN | 122.8 | 1.71 | 336 | 1.21 | 640.9 | 1.02 | 1038 | 0.93 | |
| 6kN | 113.3 | 2.5 | 325 | 1.45 | 615.1 | 1.33 | 1007 | 1.2 | |
| 10kN | 94.4 | 4.15 | 298.6 | 2.18 | 571.7 | 1.76 | 913.7 | 1.97 | |
| 13kN | 88.9 | 4.34 | 284.1 | 2.85 | 557.2 | 2.36 | 890.7 | 2.2 | |
| 15.5kN | 86.4 | 4.3 | 274.1 | 2.47 | 550.7 | 2.25 | 869.3 | 2 | |
| Repaired | 98.4 | 3.57 | 284.6 | 2.06 | 583.2 | 2.01 | 924.7 | 1.74 | |

| Beam C | | | | | | | | | |
|-----------------|-------------|-----------|-------------|-----------|-------------|-----------|-------------|-----------|--|
| Load step | Mode 1 | | Mode 2 | | Mode 3 | | Mode 4 | | |
| | ω Hz | $\zeta\%$ | ω Hz | $\zeta\%$ | ω Hz | $\zeta\%$ | ω Hz | $\zeta\%$ | |
| Intact | 86.88 | 4.0 | 236.2 | 5.9 | 612.6 | 1.5 | 864.8 | 1.19 | |
| 10kN | 66.41 | 6.4 | 178.7 | 6.4 | 415.4 | 4.7 | 650.1 | 7.8 | |
| 14.5kN/modified | 57.92 | 4.7 | 156.8 | 3.11 | 355 | 3.1 | 581.2 | 3.95 | |

| Beam D | | | | | | | | | | |
|--------|-------------|-----------|-------------|-----------|-------------|-----------|-------------|-----------|-------------|-----------|
| Case | Mode 1 | | Mode 2 | | Mode 3 | | Mode 4 | | Mode 5 | |
| | ω Hz | $\zeta\%$ | ω Hz | $\zeta\%$ | ω Hz | $\zeta\%$ | ω Hz | $\zeta\%$ | ω Hz | $\zeta\%$ |
| Solid | 77.41 | --- | 205.1 | --- | 393.5 | --- | 656.4 | --- | 983.0 | --- |
| Voided | 80.9 | --- | 192.2 | --- | 368.5 | --- | 654.6 | --- | 949.2 | --- |

| Beam E | | | | | | | | | | |
|--------|-------------|-----------|-------------|-----------|-------------|-----------|-------------|-----------|-------------|-----------|
| Case | Mode 1 | | Mode 2 | | Mode 3 | | Mode 4 | | Mode 5 | |
| | ω Hz | $\zeta\%$ | ω Hz | $\zeta\%$ | ω Hz | $\zeta\%$ | ω Hz | $\zeta\%$ | ω Hz | $\zeta\%$ |
| Solid | 71.9 | 4.03 | 198.7 | 2.52 | 437.4 | 1.08 | 652.6 | 1.92 | 915.7 | 1.73 |
| Voided | 94.87 | 1.41 | 247.2 | 1.7 | 475.8 | 1.05 | 758.9 | 1.84 | 1088 | 0.7 |

7.2.4 Mode Shape Estimation

The easiest approach for obtaining the mode shapes of a structure is to use a technique referred to as Quadrature Picking. This technique is based upon the assumption that the coupling between the modes must be light (Gade et al., 2005). In practice, RC structures are often lightly damped systems where their damping is less than 10%. Therefore, the modes of vibration of such structures will be lightly coupled.

By exploiting the output response spectra only, the Relative Response Function (RRF) method is usefully used as a simplified procedure to unravel the mode shapes of a system. The method is able to determine the mode shapes to accuracy depends upon the number of grouped averages. This situation normally occurs in real-life application

when it is not possible to measure the excitation forces due to the difficulty caused by ambient excitation conditions (Haritos and Owen, 2004).

In the long-term automated monitoring, the estimation of the above-mentioned modal values can also be carried out without artificial excitation. Therefore, the time responses of each measurement point have to be analysed by using the Fast Fourier Transformation (FFT). Peaks of the Power Spectra Density (PSD) describe approximately the natural frequencies. Furthermore, the associated operational mode shapes need to be determined by simultaneous or successive measurements for various measurement points.

In practice, results of multiple successive measurements should be averaged, to eliminate noise interferences, exterior influences and other parts of the signal which are not dependent on the structural state. Averaged normalised PSD plots can be regarded as the signature of the structure. A change in the stiffness or mass of a structure should be indicated by changes in the pattern of the averaged PSD. By comparison with a reference state, it is possible to obtain qualitative information about the location and extent of structural changes (Wenzel, 2009).

In this simplified approach, the RRF can be defined as:

$$R_{jo}(\omega) = \frac{X_j(\omega)}{X_o(\omega)} \quad (7.2)$$

Where:

$X_j(\omega)$ and $X_o(\omega)$ represent the measured output (response) spectra at locations j and o (the reference point), respectively

Then, the relative response spectra $R(\omega)$ can be described as in the following equation:

$$R_{jo}(\omega) = \frac{\sum_{i=1}^n H_{ji}(\omega) F_i(\omega)}{\sum_{i=1}^n H_{oi}(\omega) F_i(\omega)} \quad (7.3)$$

Where:

i represents the force location on the grid

$H(\omega)$ represents the FRF

$F(\omega)$ represents the input excitation spectrum

The FRF for an undamped system in terms of the modal properties can be defined as (Haritos and Owen, 2004):

$$H_{jo}(\omega) = \sum_{r=1}^n \frac{\varphi_{jr} \varphi_{or}}{\omega_r^2 - \omega^2} \quad (7.4)$$

Where:

H_{jo} refers to the FRF at DOF (j) due to an exciting force at DOF (o)

φ_{jr} and φ_{or} represent the j^{th} and o^{th} elements of the mode shape vector for the r^{th} mode of vibration

ω_r is the eigenvalue of the r^{th} mode of vibration

Finally, substituting Equation 7.3 and 7.4 into Equation 7.2, the RRF, $R_{jo}(\omega)$, at the frequency (ω) of the related mode can approximately be written as:

$$R_{jo}(\omega_r) = \frac{X_j(\omega_r)}{X_o(\omega_r)} \cong \frac{\varphi_{jr}}{\varphi_{or}} \quad (7.5)$$

On the other hand, as an advanced use of the peak-picking method, mode shapes of a system can more sensibly be derived by including the excitation force where the modes are well separated and the damping is not very high (Maia and Silva, 1997). At the peaks of an FRF, the modal constant (A^r) of a damped system for a particular mode can be defined as (Ewins, 2000; Døssing, 1988):

$$|H| = \frac{A^r}{\omega_r^2 \eta_r} \quad (7.6)$$

Where:

η_r is the structural damping ratio of r^{th} mode of vibration

ω_r is the resonance frequency of r^{th} mode of vibration

A^r is the modal constant/residue of r^{th} mode of vibration

$|H|$ is the maximum amplitude of a receptance FRF

In order to present this method mathematically, the modal constant matrix, which extracted from one measured column of a receptance FRF matrix, is symbolically clarified by Equation 7.7:

$$[A]^r = q_r \{\psi\}_r \{\psi\}_r^T \quad (7.7)$$

Where:

q_r is the scaling constant in relation to r^{th} mode of vibration

$\{\psi\}_r$ is the r^{th} mode shape (Eigenvector)

After that, this matrix is disassembled into its equivalent actual mode shape coefficients, and can be expanded as in Equation 7.8:

$$\begin{bmatrix} A_{11}^1 & A_{11}^2 & \dots & A_{11}^r \\ A_{21}^1 & A_{21}^2 & \dots & A_{21}^r \\ \vdots & \vdots & \ddots & \vdots \\ A_{i1}^1 & A_{i1}^2 & \dots & A_{i1}^r \end{bmatrix} = q_r \begin{pmatrix} \psi_{1r} \\ \psi_{2r} \\ \dots \\ \psi_{ir} \end{pmatrix} \begin{pmatrix} \psi_{1r} \\ \psi_{2r} \\ \dots \\ \psi_{jr} \end{pmatrix}^T \quad (7.8)$$

Alternatively, for a general residue matrix the corresponding mode shape coefficients can be given as in Equation 7.9:

$$\begin{bmatrix} A_{11}^r & A_{12}^r & \dots & A_{1j}^r \\ A_{21}^r & A_{22}^r & \dots & A_{2j}^r \\ \vdots & \vdots & \ddots & \vdots \\ A_{i1}^r & A_{i2}^r & \dots & A_{ij}^r \end{bmatrix} = q_r \begin{bmatrix} \psi_{1r}\psi_{1r} & \psi_{1r}\psi_{2r} & \dots & \psi_{1r}\psi_{jr} \\ \psi_{21}\psi_{1r} & \psi_{22}\psi_{2r} & \dots & \psi_{2r}\psi_{jr} \\ \vdots & \vdots & \ddots & \vdots \\ \psi_{ir}\psi_{1r} & \psi_{ir}\psi_{2r} & \dots & \psi_{ir}\psi_{jr} \end{bmatrix} \quad (7.9)$$

Where:

i is the response DOF

j is the force excitation DOF

The scaling process is essential to preserve the relative motion between various points along the model and is important for utilising mode shape for further analyses such as

modelling, correlation, identification and prediction rather than for only visual representation (Avitabile, 2007). In this work, the scaling constant (q) is approximated to match the value of the numerical driving point residue for each mode that represents the largest ordinate of a mode shape and takes place at point (1) for all the five test beams.

In these modal surveys, the first identified mode shapes for the five beams were extracted using the techniques, RPS densities and FRFs. In each technique, the related mode shapes were computed, scaled, compared and correlated in an effort to reveal the best technique to give consistent results.

7.3 Damage Identification using Modal Parameters

7.3.1 Effect of Damage on Natural Frequencies

Principally, the presence of cracks in concrete beams reduces the stiffness; as a result, any reduction in stiffness is manifested as a decrease in the natural frequencies. Although it is fairly easy to detect the presence of damage in a structure from changes in the natural frequencies, it is difficult to determine the location of damage. This article attempts to evaluate the reliability of natural frequency measurements as a basic tool to monitor and classify the levels of damage and the effect of repair works for the five prescribed beams. The comparison of identified modal frequencies for different structural conditions is given in Table 7.1.

7.3.1.1 Natural Frequencies of Beam A

Beam A was artificially damaged so as to investigate the effects of increasing structural damage on modal parameters. Before starting the damage scenario and after each loading step different modal tests were conducted.

For the damage scenario, the beam was loaded by means of four-point static load, Figures 6.1 and 6.2. The loading was applied in five loading/unloading cycles with peak forces of 3, 6, 10, 13 and 16kN, respectively. The maximum load of the last loading cycle was decided to be corresponding to the analytical ultimate load with respect to flexural resistance of $P = 18\text{kN}$. Due to the significant flexural cracks emerged in the

beam; the loading process was stopped before the ultimate load is reached. After the last loading cycle, the beam had substantial distributed cracking over the central span. The first visually observed cracks occurred at a load of 10kN. At the end of each static load step, the beam surface was visually inspected to map out the crack distribution associated with that step. After the final load dynamic test, the beam was repaired as the defective zone strengthened by bonding external CFRP sheets type TORAYCA-FT 300B) of 500mm long and 90mm width.

The results of frequency deviation of each loading condition from the reference intact case for beam A are shown in Figure 7.1. As can be seen in this figure, the drop in natural frequencies for the first mode is quite significant compared to the drop in higher modes, which suggests that the first mode of vibration is more influenced by the crack pattern than higher modes. The variation of frequency appeared less significant for higher modes, which can be attributed to the fact that the mid span cracked area is close to the modal nodes of these modes. Close to the complete failure stage ($P=16\text{kN}$, $M=1.62\text{kNm}$), maximum drops of 20.6%, 11.8%, 9.6% and 11.6% were observed for the first four bending frequencies, respectively. A notable observation is drawn as thereabouts 6% drop in the first bending frequency (corresponding to 6kN load) was obtained, although the beams' sections were visually in a flawless condition. A maximum of 7.2% of frequency deviation was recovered for the first bending mode when the beam was repaired. However, the rate of recovery was slower for the higher modes because the modification likewise the deterioration affected heavily the first mode.

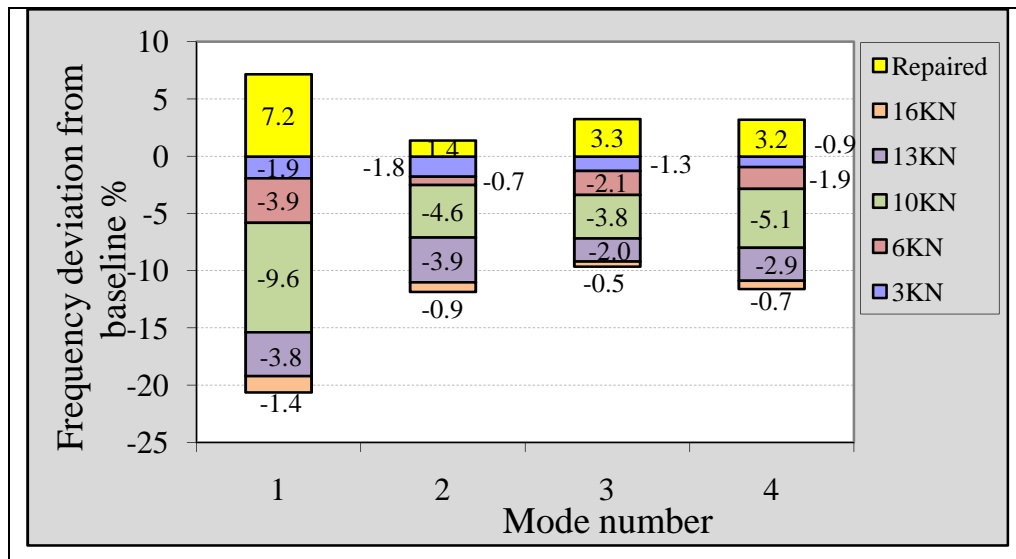


Figure 7.1: Deviation in resonances of beam A with different loading levels.

7.3.1.2 Natural Frequencies of Beam B

For the damage scenario, the beam B was loaded by means of four-point static load, Figures 6.1 and 6.2. Similar to beam A, the loading was also applied in five loading/unloading cycles with peak forces of 3, 6, 10, 13 and 15.5kN, respectively. The intended maximum load of the last loading cycle was corresponding to the theoretical ultimate load with respect to flexural resistance of $P = 18\text{kN}$. Due to the significant flexural cracks emerged in the beam; the loading process was stopped before the ultimate load is attended. Also as what happened in beam A, the first visible cracks took place at a load of 10kN, however unlike beam A, the number of cracks and their length increased substantially with the loading process. At the final stage of the damage scenario, many cracks with a typical length of 40–60 mm spread over more than half the central length of the beam (Figure 6.4). At the final static loading step, and just before the formation of plastic hinges, the process was stopped; the beam was dynamically tested and then repaired. To repair the damage, the defective zone was strengthened by bonding external CFRP sheets type TORAYCA-FT 300B) of 500mm long and 90mm width.

The modal frequencies of free-free beam B is decreased significantly with the progress of damage compared with beam A, as can be seen in Figure 7.2. Through the loading process the beam witnessed considerable number of cracks; therefore, it was manifested

as bigger drops in frequencies. When the beam's sections were visually in the uncracked state ($P=6\text{kN}$, $M=0.61\text{kNm}$), the first four frequencies decreased by 8.8%, 3.8%, 4.6%, and 3.3%, respectively compared to the initial intact state. The big differences in natural frequencies conclude that vibration-based methods are able to detect damage at its early stage, without any apparent visible change in the condition. At the final load step ($P=15.5\text{kN}$, $M=1.57\text{kNm}$), when the beam was severely damaged and formation of a plastic hinge was imminent, the first four natural frequencies decreased by 30.5%, 18.9%, 14.6% and 16.5, respectively, compared to the intact state. As the drop in natural frequencies of the severely damaged beam is quite big, vibration-based assessment methods could be recognisably utilised. When the damaged zone was repaired, the beam became noticeably stronger, and the properties were modified. The first four natural frequencies increased, respectively, by 9.7%, 3.1%, 5.0% and 5.3% compared to the undamaged stage. For both beams, beam A and beam B, and for all bending modes of interest the most important reduction in frequencies took place at the third loading cycle (10kN) when the damage became considerable and the cracks were visible.

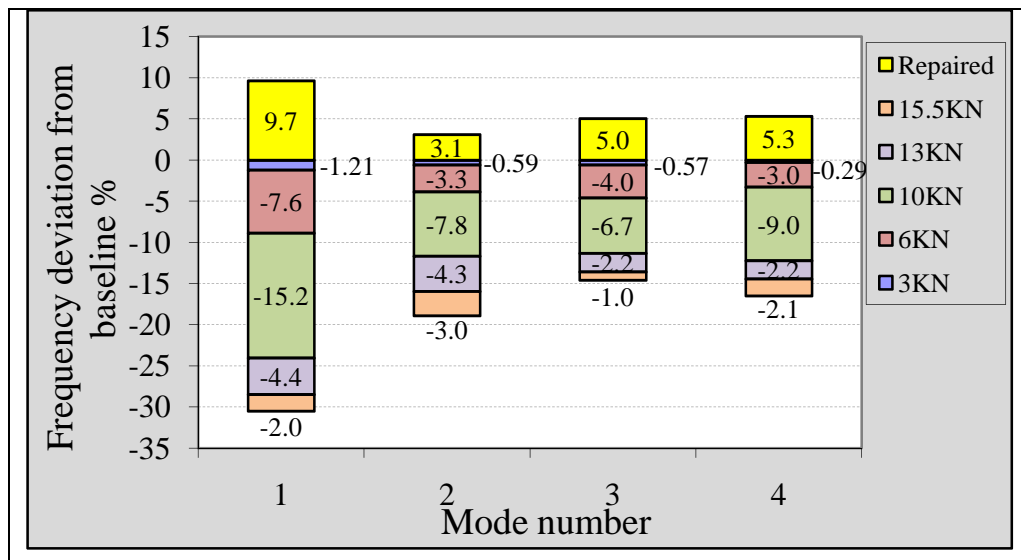


Figure 7.2: Deviation in resonances of beam B with different loading levels.

7.3.1.3 Natural Frequencies of Beam C

In this damage scenario, beam C was subjected to four-point static load. The loading was applied in two loading/unloading cycles with peak forces of 10 and 14.5kN, respectively. The maximum loads for the two loading cycles were far beyond the theoretical design ultimate load with respect to flexural failure of $P = 5.6\text{kN}$ (2.1kN.m). At the final stage of the damage scenario, many wide open cracks with a typical length of 60–80 mm spread over more than half the length of the beam. Also, the mid span compression zone of the beam was crumbled, Figure 6.7. The cracks went through the bottom face of the beam and displayed crack widths of 1-3 mm under full loading condition.

The investigation of the discrepancy of frequencies with escalation of damage for beam C is shown in Figure 7.3. In addition to the starting point condition, the effect of damage on the natural frequencies was limited to two loading conditions, where the beam was heavily loaded and severely cracked. As can be seen from Figure 7.3, the measured frequencies of the first four modes decreased continuously responding to the increasing damage. In contrast with the previous two case studies, damage location and size affected equally all the four bending modes as the loading pattern allowed cracking behaviour being out of the middle zone. Very close to the complete collapse stage caused by the beam self weight along with a static two point load of $P=14.5\text{kN}$, the first four natural frequencies decreased substantially by 33.3%, 33.6%, 42.1%, and 32.8%, respectively, compared to the initial intact state.

As the drop in natural frequencies of the severely damaged beam was quite big, vibration-based assessment methods could be perceptibly utilised as a safety warning tool for structures.

Interestingly, the deviations in natural frequencies caused by damage were large, measurable and higher than common changes generated by seasonal environmental changes, such as temperature. To conclude, approximately 30% deviation in resonance compared with the intact state resonance may be observed if the beam is imminent to complete breakage. As a parting comment, one can dwell to this conclusion and generalise a relationship between the damage and drop in natural frequencies as similar

results were repeatedly reported in research conducted on full-size RC girders (Mordini et al., 2007; Ren and De Roeck, 2002; Unger et al., 2006).

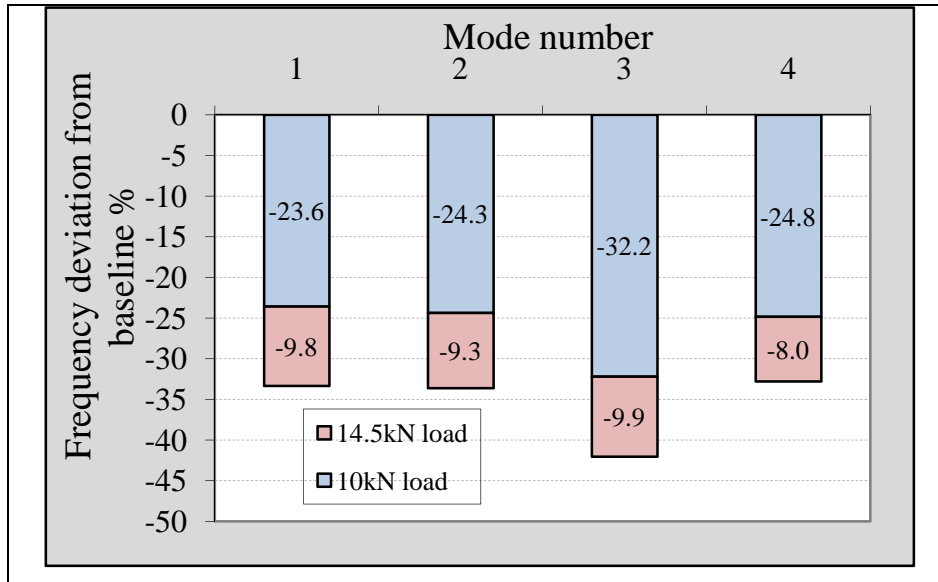


Figure 7.3: Deviation of frequency in beam C under different damage levels.

As a practical comparison with the effect of temperature variation on resonance frequency, the first resonance in the Z24 concrete bridge dropped only by 2.5% when the temperature changed between 0°C to 40°C, and the second natural frequency increased only by 2%. On the other hand, when the asphalt layer contributes significantly to the overall bridge stiffness at subzero temperature degrees, the first and second natural frequencies increased by 10% from the baseline frequency (Peeters et al., 2001). Moreover, about 10% seasonal variations in the frequencies of a three-span RC footbridge were frequently monitored by Askegaard and Mossing in each year of a three year period test (Sohn, 2007).

7.3.1.4 Natural Frequencies of Beam D

In beam D, the effect of artificially induced void of considerable size at one end of the beam was investigated in an effort to simulate practical non-symmetric defect. At one end of the beam, a cavity hole of (40 x 6 x 5)cm dimension was inserted. A comparison of natural frequencies for the first five bending modes gained for the solid beam as well as the end-hole beam can be seen in Figure 7.4. It is quite surprising that the natural

frequencies for both conditions of each specific mode were close. More specifically, the natural frequencies of the end-hole sample were slightly higher than frequencies of the solid sample, except for the second and third modes. The change was 6.9% for the first mode, but 2.4% and 0.4% for the fourth and fifth mode, respectively. The decreases for the second and third modes were 5.2% and 2.7%. Apparently, the effect of drop in mass for the defective beam on the natural frequencies was compensated by almost similar drop in stiffness. Unlike the previous damage cases (beams A, B and C) as the changes in frequency of similar trend for all modes, the unsymmetrical nature of this beam marked mutual trend in frequency change between modes. These results indicate that when a structure is inflicted with global damage such as voids, deviations in natural frequencies can be considered as quiet and modest parameters for structural condition assessment.

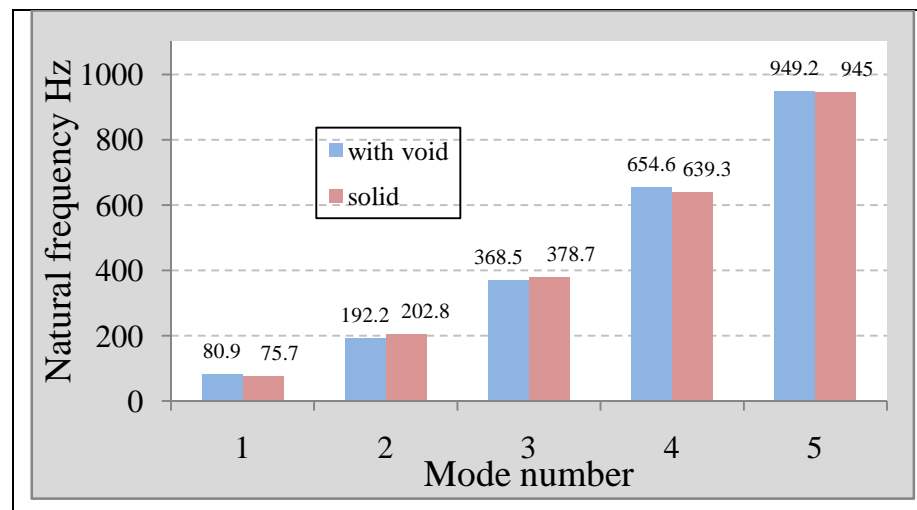


Figure 7.4: Comparison of frequencies in beam D.

7.3.1.5 Natural Frequencies of Beam E

The effect of two symmetrically induced voids of size (20 x 10 x 6)cm at the ends of flexural member was explored in beam E (Figure 6.8). A comparison of changes in frequencies between the solid and two-void beam is shown in Figure 7.5. In this case, the trend of change in frequencies was uniform as the two-void beam had higher frequencies compared with the solid beam for the first five modes of vibration. The variations of frequency of the defective sample from the solid baseline beam for the five modes were 32%, 24.4%, 8.6%, 16.3 and 18.8%, respectively. Obviously, the size and

location of these defects were big enough to be revealed through the changes in frequency. In addition, the substantial decrease in the mass of end elements contributed more to the frequency compared to the associated reverse action of stiffness loss. The global nature of modal frequency gives the advantage to detect these faults despite the fact that these holes were produced at minimum stress zone of the beam. In this context, frequency measurements and comparisons campaign indicate that natural frequency changes caused by the damage significantly higher than the expected changes produced by seasonal temperature changes that natural frequency can be used credibly as assessment parameter for the integrity of concrete structures.

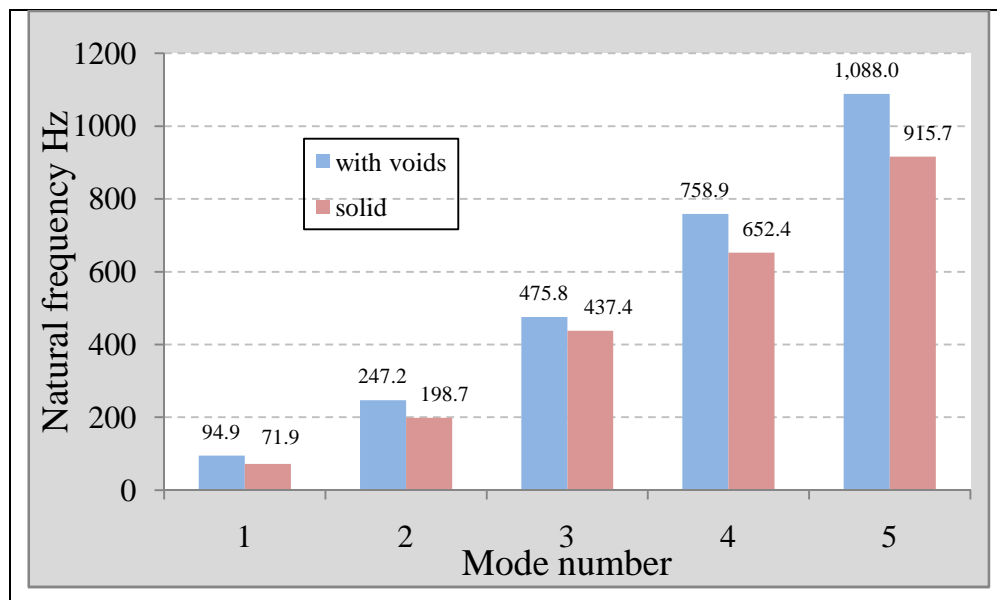


Figure 7.5: Comparison of frequencies in beam E.

7.3.2 Effect of Damage on Modal Damping

7.3.2.1 General

In general, the presence of cracks in structural elements often increases the amount of the energy dissipation. This manifests itself as controlled peak height and peak width of the FRF measurements. Damping measurement represents the only practical estimate of the dispersive energy in dynamic systems. In the context of damage and integrity identification, damping might be utilised as damage detection parameter, because it is sensitive to changes in stiffness of structural elements (Williams and Salawu, 1997). Modal damping ratios from the given five laboratory beams were experimentally

obtained for the original samples and after adding damage or defect to these samples. Although damping values are difficult to be checked and verified analytically, all reasons that could undermine the quality of estimate were overcome. Quality factors for damping ratio estimate such as resolution of spectral lines, quality of FRF measurements and suitability of testing model were ensured, which provides credibility to the results revealed in this investigation. However, damping estimation in unloaded free-free beam under dynamic testing could provide less damping than in the loaded simply supported beam because of the closing of open cracks. A comparison of the identified damping ratios for beams A, B, C, D and E is shown in Table 7.1. In addition, damping measurements as functions of increased damage and parameter to track the damage for each beam is individually discussed in the following subsections.

7.3.2.2 Modal Damping of Beam A

The normalised measured modal damping for beam A for the four bending modes are given in Figure 7.6. Although estimation of damping includes relatively high errors, quite consistent modal damping measurements were found through the course of this case. For the consecutive loading steps, changes in modal damping ratios were quite regular as they increased with the magnitude of load. High damping would suggest energy dissipation mechanism because of the presence of widely spread cracks. At the severely damaged beam stage ($P=16\text{kN}$), the modal damping increased by 39%, 6.3%, 33%, and 78.1% for the four modes of vibration respectively compared to the intact beam damping. In this case study, one unanticipated finding was the little damping ratios of the second mode, which can be accounted to the fact that modal damping of this mode was less likely influenced by damage. When the beam was repaired, damping ratio decreased by 19%, 1.7%, 24% for the first three bending modes, but it was increased by 1.9% for the fourth mode compared with the damping of severely damaged case. On the whole, this finding indicated an improvement in the strength of the repaired beam. Unusually and very limited, modal damping ratios of the second and third modes for 6kN load step, and third mode only for 3kN load step, were lower than damping ratios for the starting point (intact) beam condition. Trends similar to this were observed by other authors (Salawu and Williams, 1994). However, the rate of change of damping with the progressive damage appeared occasionally non-uniform because the

damping ratios were estimated assuming linear structure to non-linear FRFs. Non-similar repetitions of impact excitation in the direction, position and magnitude may also cause unexpected behaviour in damping measurements.

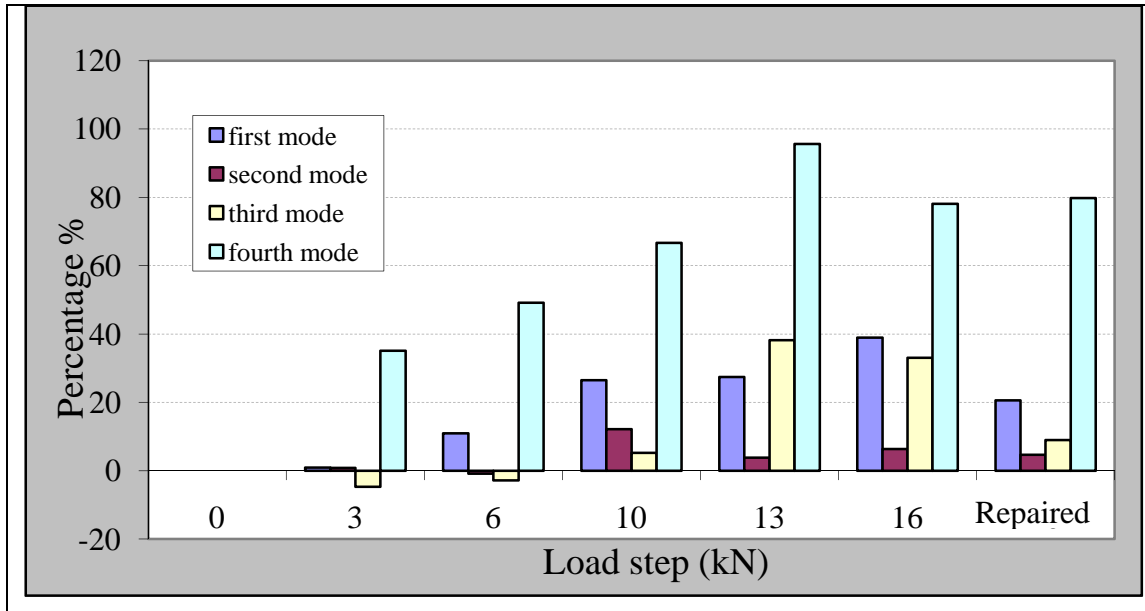


Figure 7.6: Deviation in damping ratios from the intact condition for beam A.

7.3.2.3 Modal Damping of Beam B

Even quite clearer than the case of beam A, this beam exhibited obvious increase in modal damping ratios with the progress of damage level. In Figure 7.7, the normalised measured damping ratios for the first four bending modes with evolution of damage are given in reference to the intact beam. At the severely damaged beam stage ($P=15.5\text{kN}$), the modal damping increased notably by 143%, 96%, 114%, and 141% for the four modes respectively compared to the intact beam damping. This indicates realistic situation of damage for beam B at the end of this load step, where the beam went through extensive cracked pattern. As was seen in natural frequency trends, modal damping of the first mode increased significantly responding to the increasing damage. Markedly, for the repaired beam, the first four damping ratios decreased by 40%, 33%, 23% and 31% from the severely damaged (15.5kN) load stage for the four modes, respectively. The effect of modification added to the repaired beam was sufficiently exposed. For this beam, damping ratios of the 13kN load step were oddly higher than the successive 15.5kN load step for the four modes. This is not uncommon phenomenon

as it was as well experienced by other researcher (Bayissa, 2007). This observation may be accounted to the model used to extract the damping ratios by which linear models are used to fit non-linear FRFs. Additionally, the variation in position, magnitude and direction of successive excitations are affected the consistency of FRF measurements.

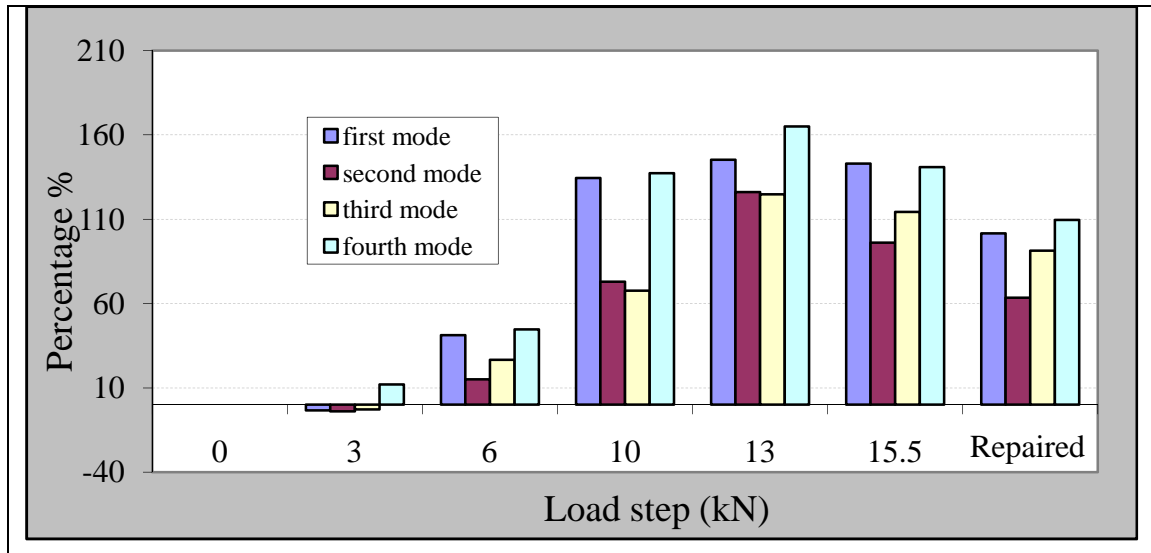


Figure 7.7: Deviation in damping ratios from the intact condition for beam B.

7.3.2.4 Modal Damping of Beam C

Results of the identified modal damping for flexural modes of beam C are given in Table 7.1. Subjecting beam C to a four-point static load of 10kN produced distributed cracked condition, and increased the identified damping ratios significantly, as shown in Figure 7.8. For this load step, the modal damping ratios were increased by 60%, 8%, 213% and 555% from the undamaged beam for the four modes, respectively. On the other hand, damping ratios were dropped as the beam loading condition was increased producing completely heavily distributed open cracks, Figure 7.8. The behaviour was also noted in beam B when the damping ratios dropped as the load was increased from 13kN to 15.5kN.

7.3.2.5 Modal Damping of Beam E

The damping ratios of the normal (solid) state and defective (two-void) state for beam E are given in Table 7.1. The measurements showed that modal damping of the solid beam is higher than damping of defective beam for all identified five modes. The highest difference was pronounced in the first mode. In general, the observation holds

satisfactorily with the theory seeing that the damping of each mode is $c = 2\xi\sqrt{km}$, and the loss of mass and stiffness manifested as low damping (c).

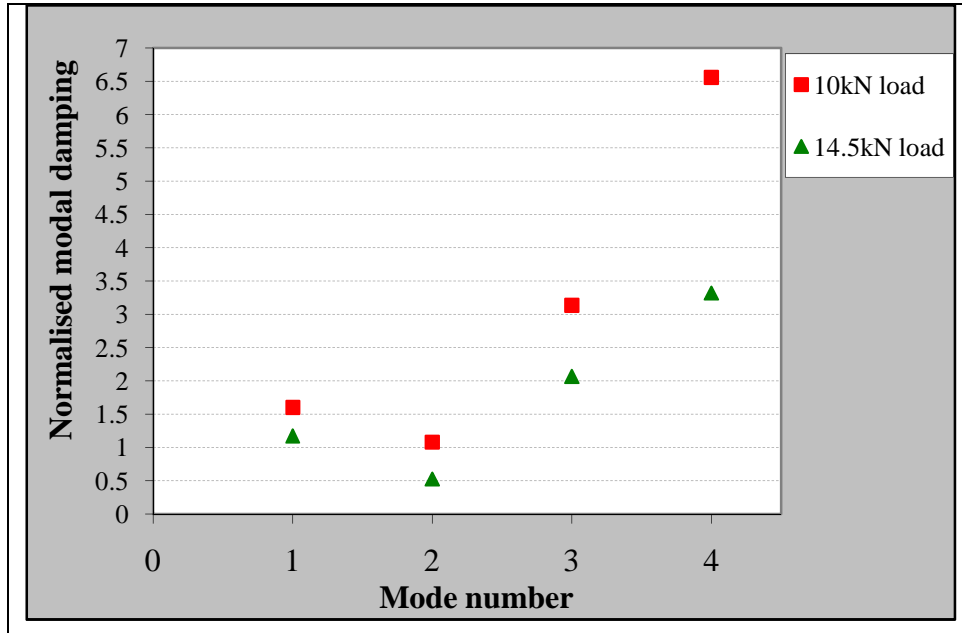


Figure 7.8: Normalised change in modal damping for beam C.

7.3.3 Effect of Damage on Frequency Response Functions

One of the direct and simplest methods to detect the existence of the nonlinearity of a concrete structure, prevailing as cracks, relies on the raw FRF measurements. It was noted that a clear difference between the shapes of a drive point FRF measurement for a beam in different damage stages could provide a useful estimation of the degree of damage. The distortion in the FRFs becomes greater when the level of damage is increased. The effect of damage development on the shape of drive point measurement for beams A, B and C is shown in Figure 7.9. As can be noted from the subplots of the figure, there are clear shifts in the resonance and anti-resonance with the progress of damage. The shift in resonance becomes higher in the higher modes. In addition, the amplitude of the spectrum for the severely damaged beam was less than for the lightly damaged beam. This is accounted for the released energy shown as higher levels of damping. Furthermore, in the cases of heavily loaded as well as the repaired beam, the beams tend to have less sharp resonance peaks compared to the intact and lightly loaded beam, suggesting again development of higher damping with the escalating damage. On the other hand, FRFs for the severely damaged beam show multiple secondary peaks,

which start to propagate, for higher frequencies. These local ripples appear as an evident of nonlinear characteristics developed in the beams due to the effect of cracks. The more cracks and separations the beam has, the more it will be prone to escalating nonlinearity. The ripples become of large amplitude in the frequency range over 600Hz as an evident of the increased damping with the increased frequency.

Furthermore, the hump-shape trends often correspond to the development of local modes (Owen, Pearson, 2004), and the peak splitting normally occurs as an evidence of lack of symmetry in the test beams. For the repaired beams, fewer secondary peaks as well as relatively clear anti-resonance troughs between each two adjacent resonances were recognised.

Finally, having looked closely at drive point measurements displayed in Figure 7.9, a consistent preliminary grouping for beam cases not distant in conditions was captured. The classification becomes visually obvious at higher modes since the large shift of frequencies allows better grouping for levels of very small differences.

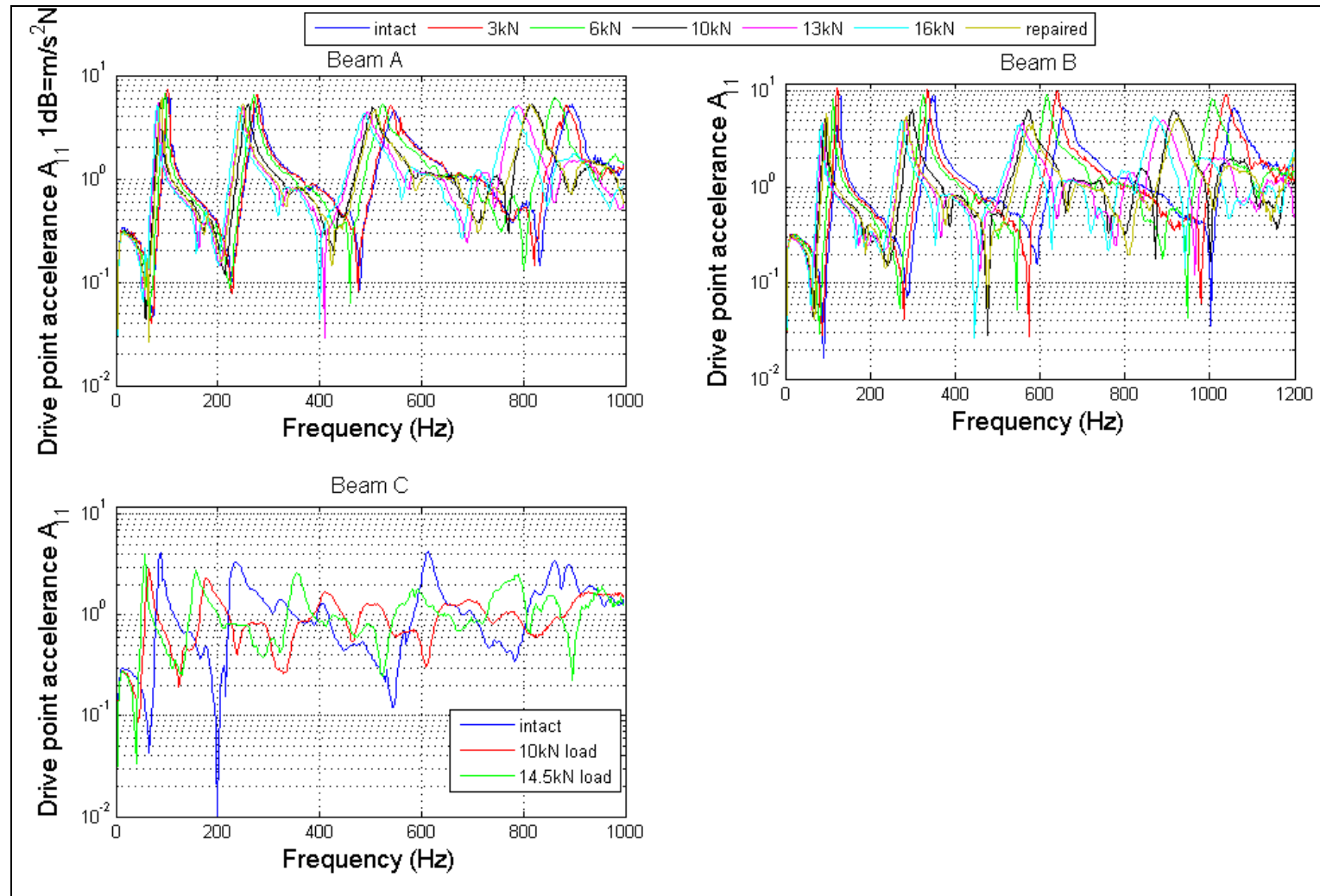


Figure 7.9: Drive point FRFs for beams A, B and C under different load levels.

7.3.4 Effect of Damage on Mode shapes

7.3.4.1 General

Throughout this work, the observed mode shapes of the five beams in this research and for all loading steps as well as for the initial healthy and repaired cases were thoroughly generated and verified with the numerical models whenever it was possible. Figures 7.10-7.14 display the overlaid bending mode shapes for the specified state conditions. In general, the observed measured mode shapes agreed very well with mode shapes of a freely supported beam. The agreement was satisfactory for both location of modal points and the symmetry or anti-symmetry of the respective mode shape. Additionally, the observed mode shapes using averaged FRF measurements based on roving accelerometers showed consistent visualisation compared with the identical mode shapes from roving hammer. This could be accounted to the difficulty of getting accurate location for the excitation force in each repetition. It is very likely that the input force shifts a definite distance in each shot. The effect of this situation is considerable on small size model, like the size of the beams adopted in this work. Additionally, the consistency, similarity or anti-similarity of higher modes is less likely to be computed reasonably compared with the lower modes. In relatively small-span samples, higher modes oscillate very frequently that a smoother mode shape requires finer measurement grid.

In particular, one distinguished observation through the visual evaluation of the different damage groups of the third and higher mode is slightly worse than for the first two modes, in perspective of symmetry and consistency. It also appeared, particularly for the first two modes, that the magnitude of the mode shape ordinates was lower than expected at points remote from the excitation location. It is possible that this was an unfortunate effect of the very low signal-to-noise ratio on the response channel caused by an inability to excite the beams properly using the hammer (Reynold et al.,1999). Providing a repetitive excitation is difficult because the inherent damping and increased damage damping tend to absorb the energy introduced by the impact force before it propagates to distant accelerometer locations (Atamturktur et al., 2009).

In the respective of damage identification, a change in the stiffness or mass of the structure should be indicated by changes in the pattern magnitude of mode shape graphs as a signature of the structure. By applying comparison with a reference state, it is possible to obtain qualitative information about the location and extent of structural changes (Wenzel, 2009). Meanwhile, the effect of the environmental influences is low on the mode shapes than their effect on frequencies (Wenzel, 2009).

7.3.4.2 Mode Shapes of Beams A, B and C

The first four overlaid flexural mode shapes for beams A, B and C are displayed in Figures 7.10, 7.11 and 7.12. The damage was well pronounced in the first and second modes compared to third and fourth modes. Additionally, the results discriminated clearly between different damage stages of the beam. Also, they showed the modified mode shape for the repaired beams. The damage induces small but poised changes to the mode shapes. The changes tend to increase with increasing damage level. The more cracks and flaws a beam is inflicted with, the more a mode shape magnitude will respond to escalating damage. However, the mode shapes of the first bending mode shape for beam A and beam B produced the most substantial changes in the magnitude of mid span where visual inspection did not reveal any cracks at early loading stages (3kN and 6kN). In addition, the changes of mode shape were not restricted at the damaged area of the beams, but were distributed over the entire length. The most significant changes were gained for the first mode shape of beam B and beam C (Figures 7.11 and 7.12). These observations contradict suggestions of other researchers (Owen et al., 2004; Yeung and Smith 2005) that mode shapes of different damage conditions may change a little, if the induced damage is widespread cracking in concrete beams. Nonetheless, similar findings to this research were found in investigation on prestressed concrete bridge girder done by Huth et al. (2005).

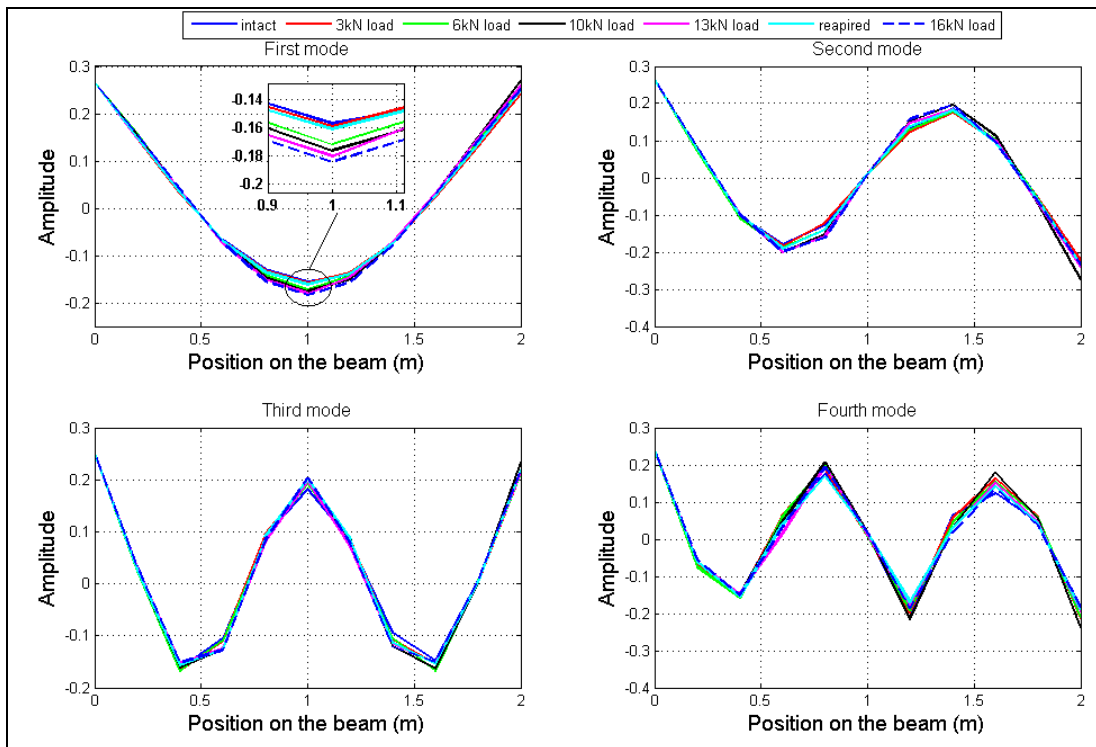


Figure 7.10: Experimental mode shapes for intact and damaged steps of beam A.

For beams A and B, in particular, the direction and pattern of changes tend to take a simple monotonic shape. The enlarge magnitude of the mode shape in the damaged area was observed in the four bending modes. Unexpectedly, in the same context, the mode shapes of beam C tended to decrease when the load changed from 10kN to 14.5kN. The changes were of small and unrealistic amplitude compared with the changes due to 10kN load, which suggests that the identified mode shape was corrupted by significant inaccuracies. In conclusion, for the last loading step of beam C, when the beam was brought to complete failure, the observed mode shapes cannot be relied on to justify the case of the beam, because they was prone to considerable errors.

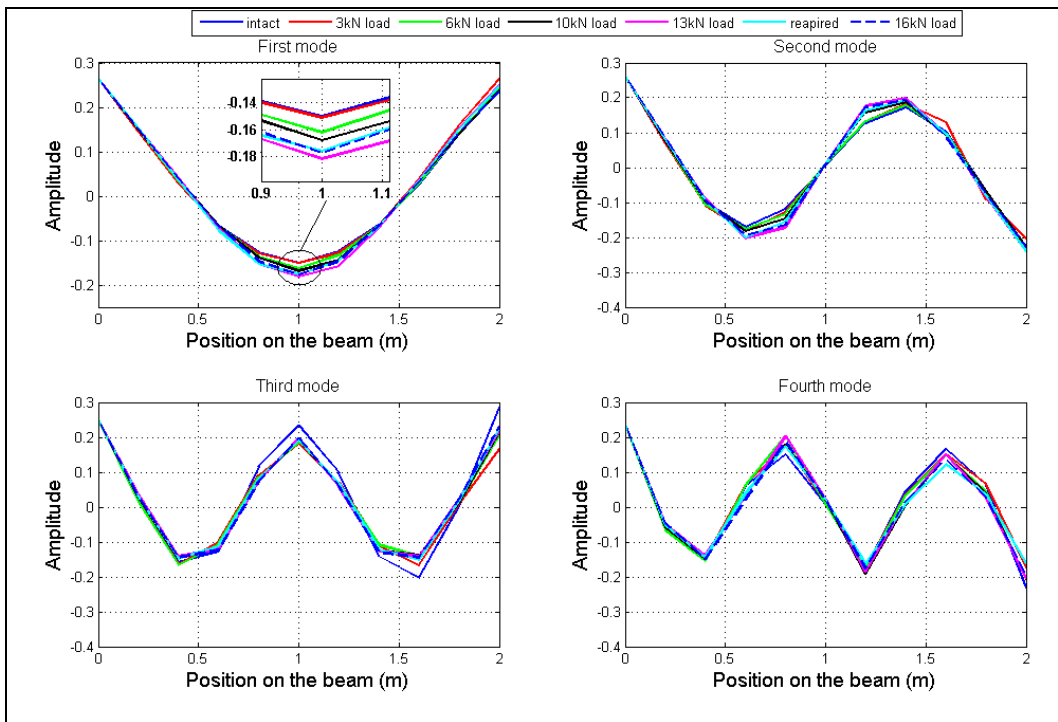


Figure 7.11: Experimental mode shapes for intact and damaged steps of beam B.

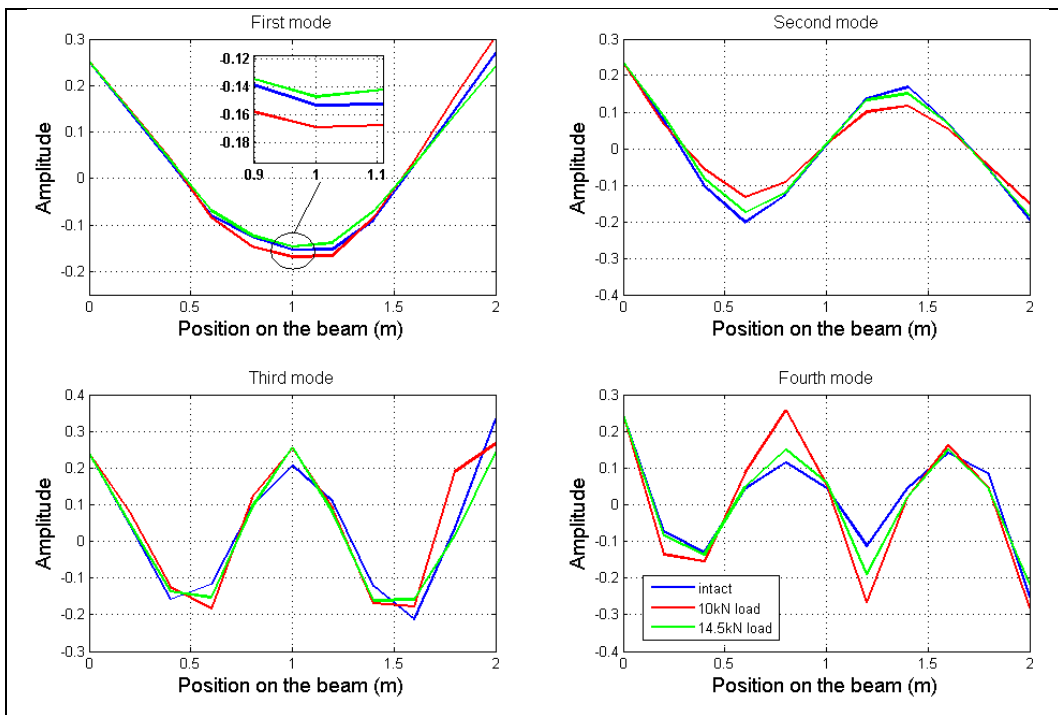


Figure 7.12: Experimental mode shapes for intact and damaged steps of beam C.

7.3.4.3 Mode Shapes of Beams D and E

One of the direct advantages of using mode shape for damage identification is benefited in this investigation through its ability to highlight the nature of damage, whether it is escalating uniform damage or unsymmetrical imperfection. In beams D and E, when the flaw was induced as interior holes inside the beams, the observed bending mode shapes performed very well. The changes of the mode shapes were not confined to the flaws area, but were spread across the entire span, Figures 7.13 and 7.14. The most substantial discrepancies appeared in the third mode and higher modes as the nature of reduced stiffness and mass of end-span voids affected strongly the higher modes. In brief, a comparison between results of mode shapes of the baseline healthy structure with identical modes from imperfect case can provide a possibility that any anomaly could be explained.

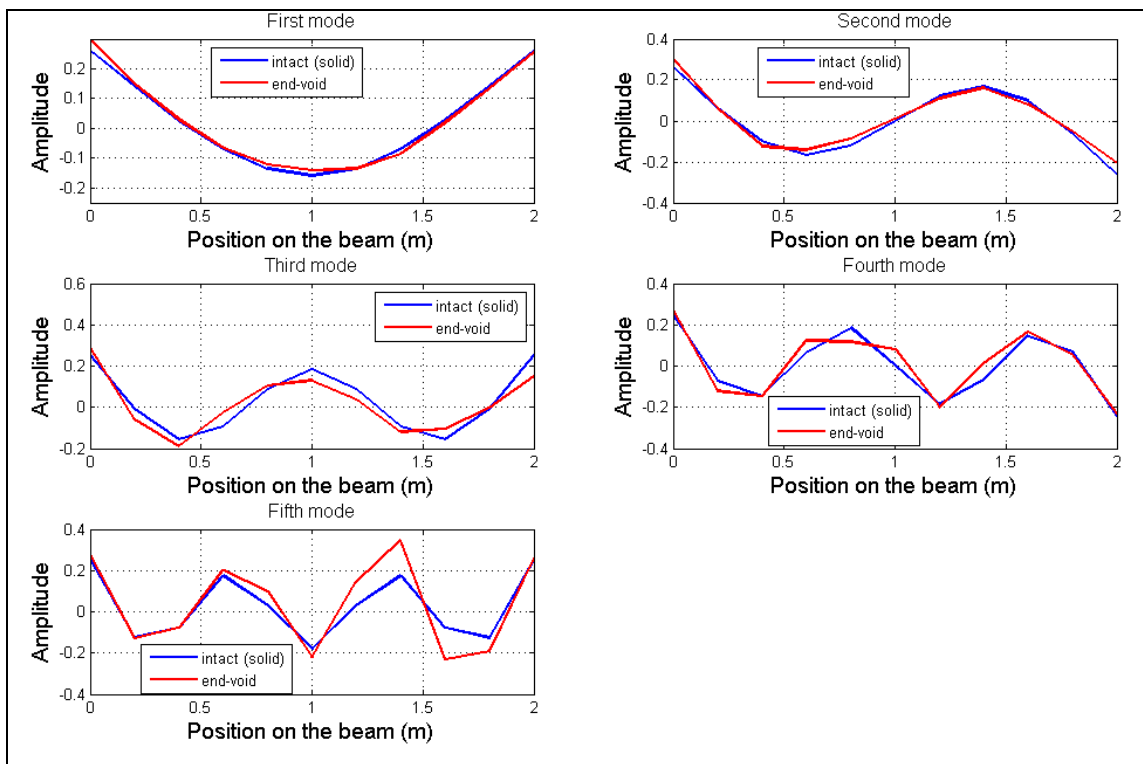


Figure 7.13: Comparison of the first five flexural mode shapes of beam D.

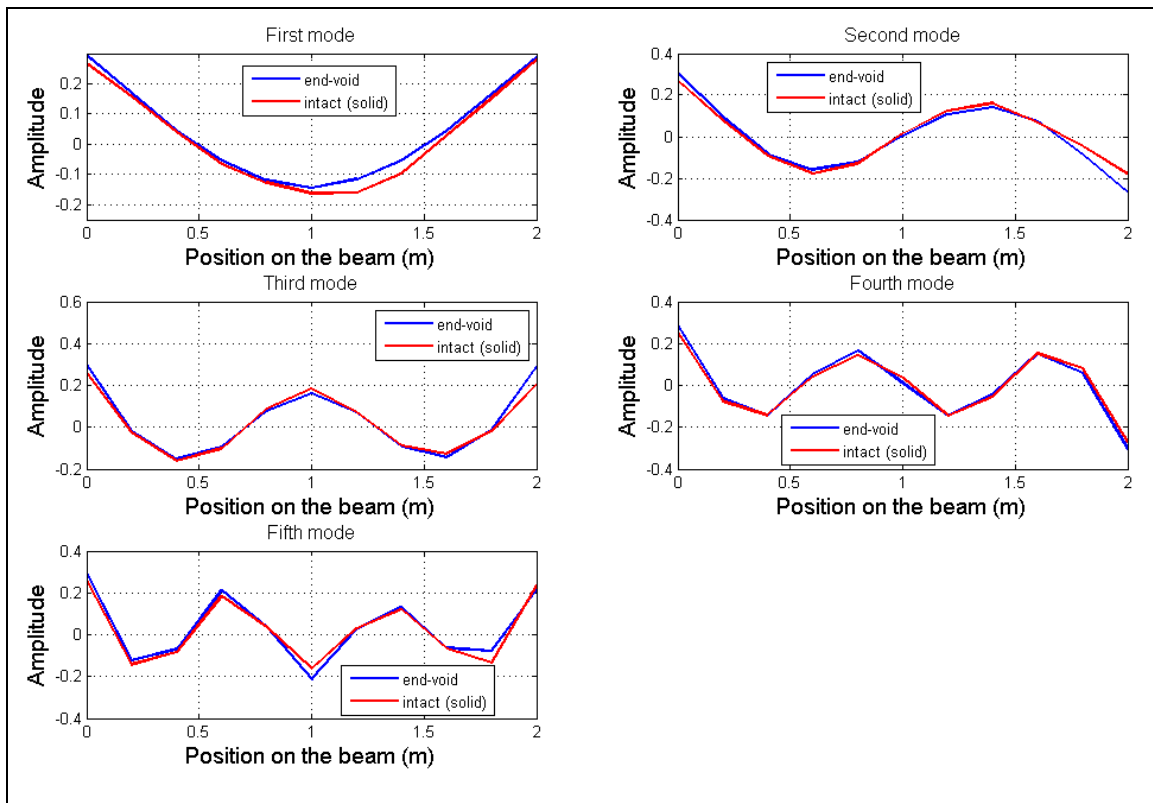


Figure 7.14: Comparison of the first five flexural mode shapes of beam E.

7.3.5 Effect of Damage on Modal Assurance Criterion

For the case study of multiple situations that has modal properties quite close of nature, degree of correlation between mode shapes using visual inspection becomes unreliable. Therefore, the suitable correlation procedure is to use values of Modal Assurance Criterion (MAC) and Coordinate Modal Assurance Criterion (COMAC). In particular, the natural mode shapes of undamaged case for each beam were compared with those for different damage conditions, using MAC. Table 7.2 shows elements of the main diagonal of the MAC matrix for the five RC beam samples. A MAC value of (1) implies no damage is present between (1) the intact and any damaged mode shape.

For beams A and B, MAC values for all damage ranges were greater than 0.96. In practice, this ensures that the two comparable modes are very well correlated. The relative little decrease in MAC values between two successive load steps was gradual. Also, the effect of repair work was observed as a slight increase in the values of MAC compared with MAC values of the last load step. In contrast, beam C and for the two load cases exhibits higher decrease in MAC values for the higher modes (third and

fourth modes) as the changes of natural frequencies were significant. More importantly, for the three beams, MAC values indicate the relative presence of damage in successive load steps, and manage, to some extent, to differentiate its extent as well as the impact of repair work.

For beam D, as an explicit non-symmetrical case, the drop in values of MAC became steeper compared to the rest beams, and for this drop was quite substantial in the third and higher modes.

Finally, the sensitivity of mode shapes, as measured by the MAC, depends very much on the nature of damage. If the damage is distributed, such as widespread cracks in RC element, the mode shape may change a little. Accordingly, MAC value is subjected to very small differences by damage because of its poor sensitivity to small changes of mode shapes. On the other hand, localised damage, such as the artificial void induced in beam D, results in larger reductions in MAC values. As a result, MAC values in RC beams could be used as a measure to identify the damage at its advanced stage, whereby relative changes up to 12% can be observed between the correlated modes (beam C).

7.3.6 Effect of Damage on Coordinate Modal Assurance Criterion

Equivalently, as a measure of location and the severity of damage, Table 7.3 shows COMAC values for the five tested beams. For beams A and B, COMAC values of all loading conditions were greater than 0.93 for all DOFs. In practice, this finding is driven by the fact that any differences obtained in COMAC calculations were averaged and spread over all mode shapes (Pandey et al., 1991). However, the small decrease in COMAC values for central span points, when the damage became severe, indicates greater damage at these points compared with the distant points. Steeper reduction in COMAC values were obtained for beams C and D suggesting that COMAC measures are more sensitive to the localised flaws compared with subtle gradual damage.

Table 7.2: Artificial damage influence on MAC values for the RC beams.

| MAC values with respect to intact reference case | | | | | | | |
|--|--------|-------|-------|--------|-------|-------|----------|
| Mode | Intact | 3kN | 6kN | 10kN | 13kN | 16kN | Repaired |
| Beam A | | | | | | | |
| 1 | 1 | 0.999 | 0.999 | 0.998 | 0.996 | 0.995 | 0.999 |
| 2 | 1 | 0.999 | 0.999 | 0.996 | 0.995 | 0.993 | 0.999 |
| 3 | 1 | 0.998 | 0.997 | 0.995 | 0.995 | 0.993 | 0.996 |
| 4 | 1 | 0.990 | 0.988 | 0.975 | 0.971 | 0.979 | 0.982 |
| Beam B | | | | | | | |
| 1 | 1 | 0.993 | 0.999 | 0.997 | 0.993 | 0.994 | 0.995 |
| 2 | 1 | 0.989 | 0.998 | 0.993 | 0.982 | 0.983 | 0.990 |
| 3 | 1 | 0.963 | 0.976 | 0.979 | 0.977 | 0.981 | 0.986 |
| 4 | 1 | 0.982 | 0.982 | 0.978 | 0.967 | 0.967 | 0.961 |
| Beam C | | | | | | | |
| Mode | Intact | 10kN | | 14.5kN | | | |
| 1 | 1 | 0.996 | | 0.996 | | | |
| 2 | 1 | 0.970 | | 0.995 | | | |
| 3 | 1 | 0.886 | | 0.947 | | | |
| 4 | 1 | 0.884 | | 0.950 | | | |
| Beam D | | | | Beam E | | | |
| | Solid | Voids | | Solid | Voids | | |
| 1 | 1 | 0.991 | | 1 | 0.980 | | |
| 2 | 1 | 0.970 | | 1 | 0.961 | | |
| 3 | 1 | 0.882 | | 1 | 0.972 | | |
| 4 | 1 | 0.910 | | 1 | 0.987 | | |
| 5 | 1 | 0.887 | | 1 | 0.967 | | |

Table 7.3: Artificial damage influence on COMAC values for the RC beams.

| COMAC values with respect to intact reference case | | | | | | | |
|--|--------|-------|-------|-------|-------|-------|----------|
| x (m) | Beam A | | | | | | |
| | Intact | 3kN | 6kN | 10kN | 13kN | 16kN | Repaired |
| 0 | 1 | 1.000 | 1.000 | 1.000 | 1.000 | 1.000 | 1.000 |
| 0.2 | 1 | 0.998 | 0.995 | 0.994 | 0.996 | 0.988 | 0.996 |
| 0.4 | 1 | 1.000 | 1.000 | 0.999 | 0.998 | 0.997 | 0.999 |
| 0.6 | 1 | 1.000 | 1.000 | 0.990 | 0.952 | 0.976 | 0.984 |
| 0.8 | 1 | 0.998 | 0.998 | 0.996 | 0.993 | 0.993 | 0.997 |
| 1.0 | 1 | 0.999 | 0.999 | 1.000 | 0.999 | 0.999 | 0.998 |
| 1.2 | 1 | 0.999 | 0.997 | 0.998 | 0.984 | 0.983 | 0.986 |
| 1.4 | 1 | 0.994 | 0.989 | 0.970 | 0.967 | 0.950 | 0.969 |
| 1.6 | 1 | 0.986 | 0.996 | 0.983 | 0.992 | 0.997 | 0.996 |
| 1.8 | 1 | 0.991 | 0.996 | 0.998 | 0.998 | 0.994 | 0.998 |
| 2.0 | 1 | 0.994 | 0.997 | 0.995 | 1.000 | 1.000 | 1.000 |

| Beam B | | | | | | | |
|--------|--------|-------|-------|-------|-------|-------|----------|
| x(m) | Intact | 3kN | 6kN | 10kN | 13kN | 16kN | Repaired |
| 0 | 1 | 1.000 | 1.000 | 1.000 | 1.000 | 1.000 | 1.000 |
| 0.2 | 1 | 0.996 | 0.995 | 0.997 | 0.982 | 0.981 | 0.992 |
| 0.4 | 1 | 1.000 | 1.000 | 0.996 | 0.994 | 0.993 | 0.997 |
| 0.6 | 1 | 0.985 | 0.991 | 0.984 | 0.973 | 0.966 | 0.975 |
| 0.8 | 1 | 0.982 | 0.961 | 0.959 | 0.942 | 0.947 | 0.964 |
| 1.0 | 1 | 0.984 | 0.978 | 0.975 | 0.965 | 0.972 | 0.966 |
| 1.2 | 1 | 0.988 | 0.983 | 0.970 | 0.954 | 0.957 | 0.966 |
| 1.4 | 1 | 0.983 | 0.981 | 0.964 | 0.966 | 0.978 | 0.963 |
| 1.6 | 1 | 0.970 | 0.982 | 0.978 | 0.978 | 0.991 | 0.989 |
| 1.8 | 1 | 0.993 | 0.986 | 0.976 | 0.933 | 0.935 | 0.958 |
| 2.0 | 1 | 0.973 | 0.982 | 0.988 | 0.985 | 0.993 | 0.976 |

| Beam C | | | | Beam D | | Beam E | |
|--------|--------|-------|--------|--------|-------|--------|-------|
| x(m) | Intact | 10kN | 14.5kN | Solid | Voids | Solid | Voids |
| 0 | 1 | 1.000 | 1.000 | 1 | 1 | 1 | 1.000 |
| 0.2 | 1 | 0.915 | 0.997 | 1 | 0.923 | 1 | 0.982 |
| 0.4 | 1 | 0.930 | 0.988 | 1 | 0.991 | 1 | 0.996 |
| 0.6 | 1 | 0.832 | 0.966 | 1 | 0.885 | 1 | 0.981 |
| 0.8 | 1 | 0.845 | 0.981 | 1 | 0.863 | 1 | 0.985 |
| 1.0 | 1 | 0.998 | 0.986 | 1 | 0.877 | 1 | 0.954 |
| 1.2 | 1 | 0.798 | 0.911 | 1 | 0.823 | 1 | 0.978 |
| 1.4 | 1 | 0.898 | 0.949 | 1 | 0.843 | 1 | 0.965 |
| 1.6 | 1 | 0.975 | 0.972 | 1 | 0.736 | 1 | 0.992 |
| 1.8 | 1 | 0.652 | 0.946 | 1 | 0.932 | 1 | 0.890 |
| 2.0 | 1 | 0.970 | 0.989 | 1 | 0.967 | 1 | 0.971 |

7.3.7 Effect of Damage on Curvature Mode Shapes

As an alternative to the use of mode shape, its derivative such as the curvature is also utilised as spatially distributed damage sensitive feature. Mode shape curvature is numerically calculated by differentiating the displacement mode shape vector twice to obtain an estimate of the curvature.

Mode shape curvature is proved to be more sensitive to small perturbations in the system than is the mode shape itself. In addition, for beam, beam-like and plate-like structures, changes in curvature can be related to changes in strain energy, which is shown to be a sensitive indicator of damage (Farrar et al., 2001a). In this study, the curvature mode shapes were investigated to find a better understanding about the distribution of damage as long as changes in displacement mode shapes were being found modest. The curvature of the continuous displacement mode shape (ψ'') was obtained using the central difference approximation, which can be written as:

$$\psi_i'' = \frac{\psi_{i+1} - 2\psi_i + \psi_{i-1}}{(\Delta x)^2} \quad (7.10)$$

Where:

Δx is the length of the element

ψ_i is the displacement mode shape at a specific position (i)

The calculated curvature of the measured first mode shape for each damage case is shown in Figure 7.15. Although the differences between curvature mode shapes appear clearer than in the displacement mode shape (Figures 7.10-7.14), the curvature mode shapes of beams A, B and C do not heavily react to the damage, particularly at the points of inflection. However, the symmetrical pattern of the damage nature for beams A, B and C were well pronounced. On the other hand, the signature of non-symmetrical defect in beams D and E emerged as distorted bulging curvature, as shown in Figure 7.15. Specifically, for beam D when a significant size hole was induced near one end of the beam, substantial deformed curvature mode shape was observed for the end-void beam, which was not the case when the displacement mode shape was drawn, Figure 7.13.

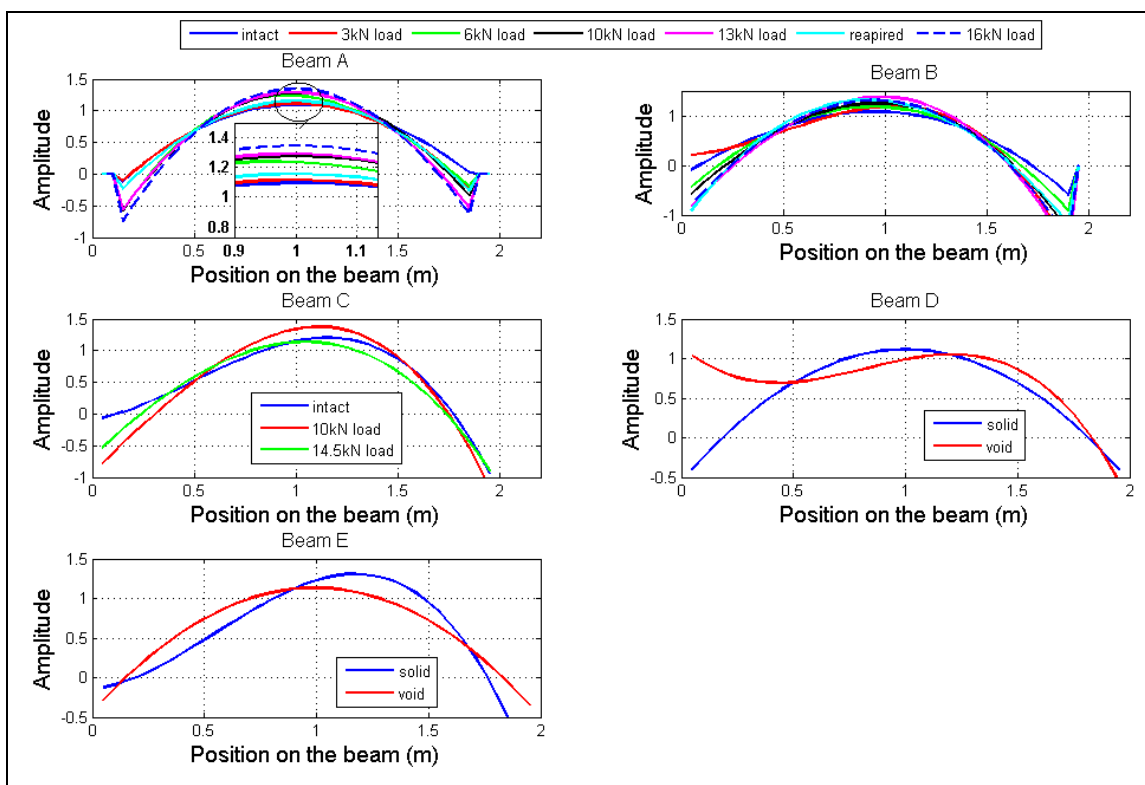


Figure 7.15: Comparison of curvature of the first bending mode for the five beams.

7.4 Damage Quantification using Moment-Curvature Relationship

7.4.1 Theoretical Background

The existence of damage in RC beams produces almost even reduction in the stiffness over a definite length. The reduction in the stiffness leads to a subsequent increase in the absolute magnitude of the curvature (κ), as shown in Figure 7.15. In Maeck and De Roeck (1999), a method designated Direct Stiffness Calculation (DSC) was postulated in an effort to locate and quantify damage using a curvature mode shape as replacement to deflection shape of ordinary static analysis. Accordingly, the method uses the same basic bending-curvature relationship of beam element that is applicable for small magnitude of deflection in each section, and can be defined mathematically as (Huth et al., 2005):

$$\kappa = \psi'' = \frac{d^2\psi}{dx^2} = \frac{M}{EI} \quad (7.11)$$

Where:

- κ is the curvature of the mode shape
- M is the bending moment at a section
- E is Young's modulus of elasticity of the material at the section
- I is the moment of inertia of that section

In the dynamics of structures, for free vibration analysis with neglected damping, the pseudo static inertia force system can be described as:

$$K\psi = \omega_r^2 m \psi \quad (7.12)$$

Here, the right-hand side of Equation 7.12 represents the modal inertia force for specific mode (r) acting on the beam of stiffness (K) in order to create a displacement vector (ψ).

For a continuous linear piecewise mode shape through the measurement points at location x_i , x_{i+1} , using the sign convention shown in Figure 7.16, the internal shear force and bending moment at section x_{i+1} (V_{i+1} , M_{i+1}) assuming that only the inertia

load is acting on the beam element, are given in Equations 7.13 and 7.14, respectively (Maeck and De Roeck, 1999).

$$V_{i+1} = V_i - \int_{x_i}^{x_{i+1}} \omega_r^2 \rho A \psi(x) dx \quad (7.13)$$

$$M_{i+1} = M_i + V_i(\Delta x) - \frac{1}{2} \int_{x_i}^{x_{i+1}} \omega_r^2 \rho A \psi(x) (\Delta x) dx \quad (7.14)$$

Where:

- ρ is the mass density of the element
- A is the cross-sectional area
- V is the shear force at the section
- M is the bending moment at the section

In fact, the bending moments and shear forces are considered as experimentally measured forces in this procedure, because the calculated inertia loads ($\omega_r^2 \rho A$) are based on the experimental natural frequency of the mode (ω_r). Additionally, the displacement vector (ψ_r) is also operated mode shape.

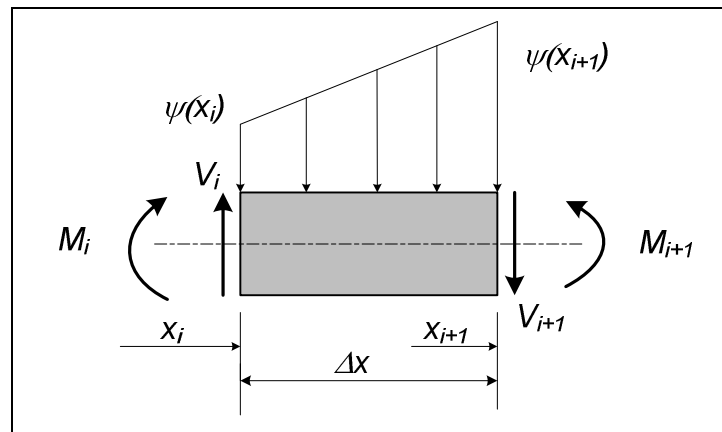


Figure 7.16: Internal pseudo static force system of a beam element.

7.4.2 Damage Quantification in Beam A

The distribution of the inertia shear forces and bending moments of the first mode for beam A at each damage state are shown in Figures 7.17 and 7.18, respectively. Slightly, less than perfect shear distribution was achieved. The slight lack of symmetry in the measured first mode shape caused trivial accumulated shifts in the shear and flexural moment distribution. Accordingly, the maximum bending moment values crept slightly from the mid span location, and the significant difference is notably at the end of the beam where it is not of interest.

Next, the approach was used to determine the unknown dynamic bending stiffness of the targeted damage ranges at each location. Additionally, only one measured displacement mode shape for each damage level will be sufficient to create a curvature mode shape; hence, to display inertia bending moment diagrams. The method considers two modal parameters to identify the distributed rigidity in an element, which are natural frequency and mode shape. Therefore, for exceptionally correlated mode shapes, rigidity changes are mainly dominated by changes of natural frequencies.

By using the calculated modal bending moment distribution found from Equation 7.14 along with the curvature corresponding to that mode, given by Equation 7.10, the dynamic bending stiffness (EI) can eventually be evaluated using Equation 7.11. From these computations, thriving insight on the location of spread damage followed by computation of its severity can be achieved.

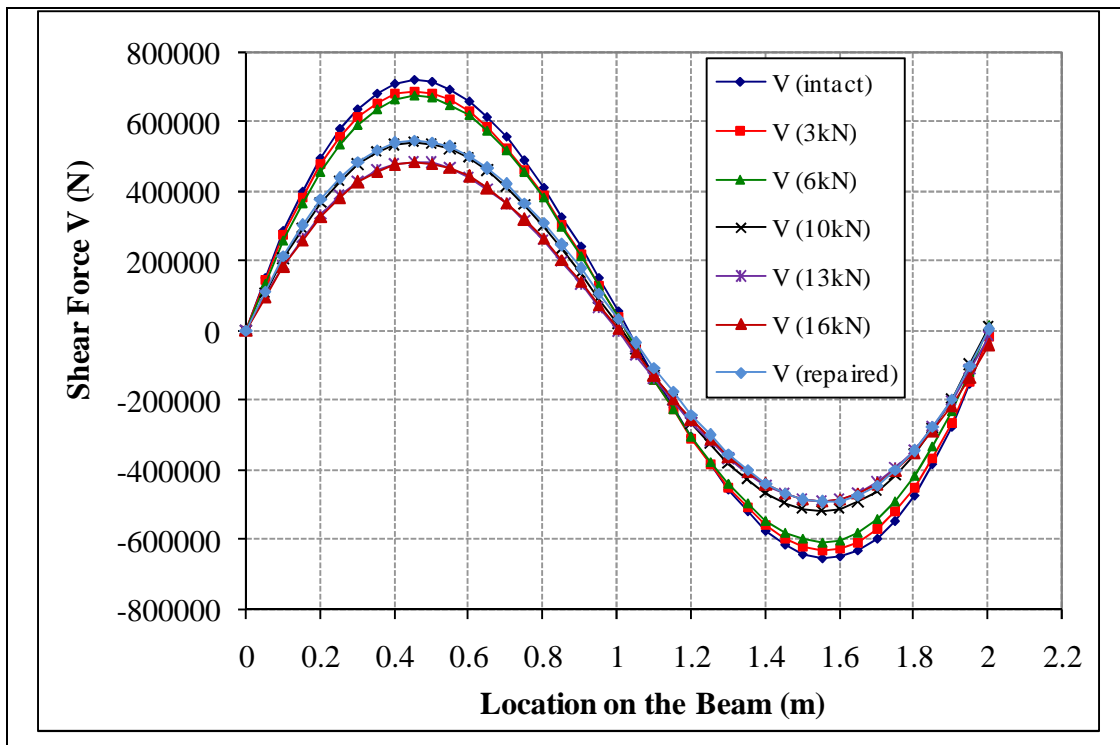


Figure 7.17: Inertia shear force distribution for beam A based on first mode.

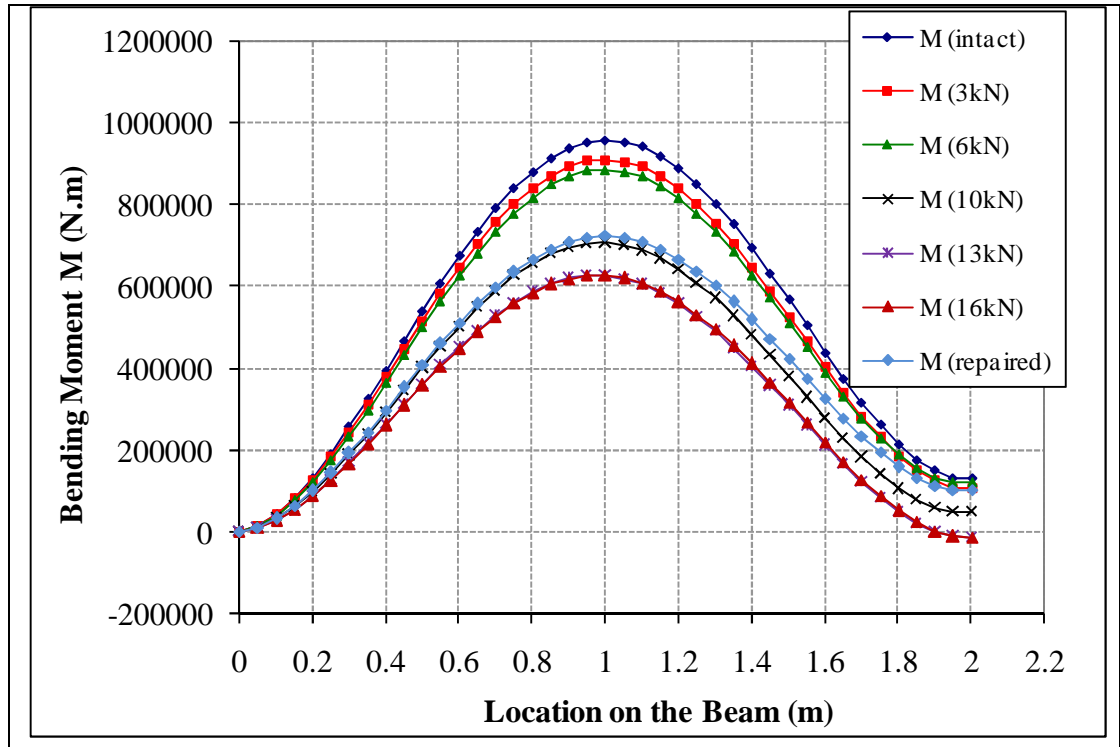


Figure 7.18: Inertia bending moment distribution for beam A based on first mode.

In the current investigation, the greatest damage located at mid span emerges out as reduction in flexural stiffness (EI) values compared to damage inflicted in less loading step. The drop of EI values imitates a typical realistic nature of related pattern damage. Furthermore, uniform decrease in EI values associated with each loading case as well as for repaired beam was obtained and obviously shown in Figure 7.19. However, the inflection points' effect corrupted the perfection of this methodology to completely reproduce the trend of stiffness decrease. Values of EI at end positions of the beam between 0.0 and 0.46m also between 1.54 and 2.0m of this relatively limited size model were substantially corrupted by existing of support and inflection points. Points of inflection, where the curvature changes from being concave to convex (or vice versa) result in a confusing interpretation. Moreover, support points which appear as zero curvature points often show larger changes of curvatures. The incoherent in curvature results at support and inflection points tends to appear as singularity in the bending formula, which manifests as big jumps in EI estimates.

For beam A, the successive reduction in flexural stiffness with the static load is given in Figure 7.19. The reduction was almost gradual and monotonic. A main notable observation is that the changes of dynamic stiffness were not limited to the damaged part of the beam, but extended beyond the loading points up to the supporting joints. As a proof of accuracy, the theoretical dynamic stiffness (EI) of the starting point (intact) beam is 0.843MN.m^2 , while the computed EI is 0.872MN.m^2 that the difference is about (3%) and is sensibly acceptable in RC testing practice. Interestingly, at the second load step ($P = 6\text{kN}$), the mid span EI dropped by thereabouts 17.96%, although no bending cracks were yet observed. However, at the final static load step ($P = 16\text{kN}$), close to the complete failure stage, the mid span EI reduced by 46.80% compared to EI of the intact beam. At this stage, wide and spread cracks at the mid span zone were observed. Moreover, the mid span EI of the repaired beam recovered by 34.6% compared to the severely damaged beam ($P = 16\text{kN}$).

The reduction factor of bending stiffness at mid span points is given in Table 7.4. The stiffness reduction factor (α) is set as the ratio of the difference in EI between any damage and intact stage to the EI of the intact stage, and given as:

$$a = \left| \frac{EI_{damaged} - EI_{intact}}{EI_{intact}} \right| \quad (7.15)$$

Theoretically, the values of reduction factor (a) vary between (0) and (1), with (1) for a complete failure stage and (0) for intact beam. Practically, for the current case study, a damage indicator of $a = 0.468$ indicates that the formation of a plastic hinge is quite imminent, when $P = 16\text{kN}$, as shown in Table 7.4. The drop of flexural stiffness is overestimated, when mode shapes based only on RPS density, and used to extract curvatures. As can be seen in Table 7.4, for 16kN load, the accumulated loss of bending stiffness based upon RPS is $D = 51.75\%$, while it is $a = 46.8\%$ when computations of curvature based upon FRFs.

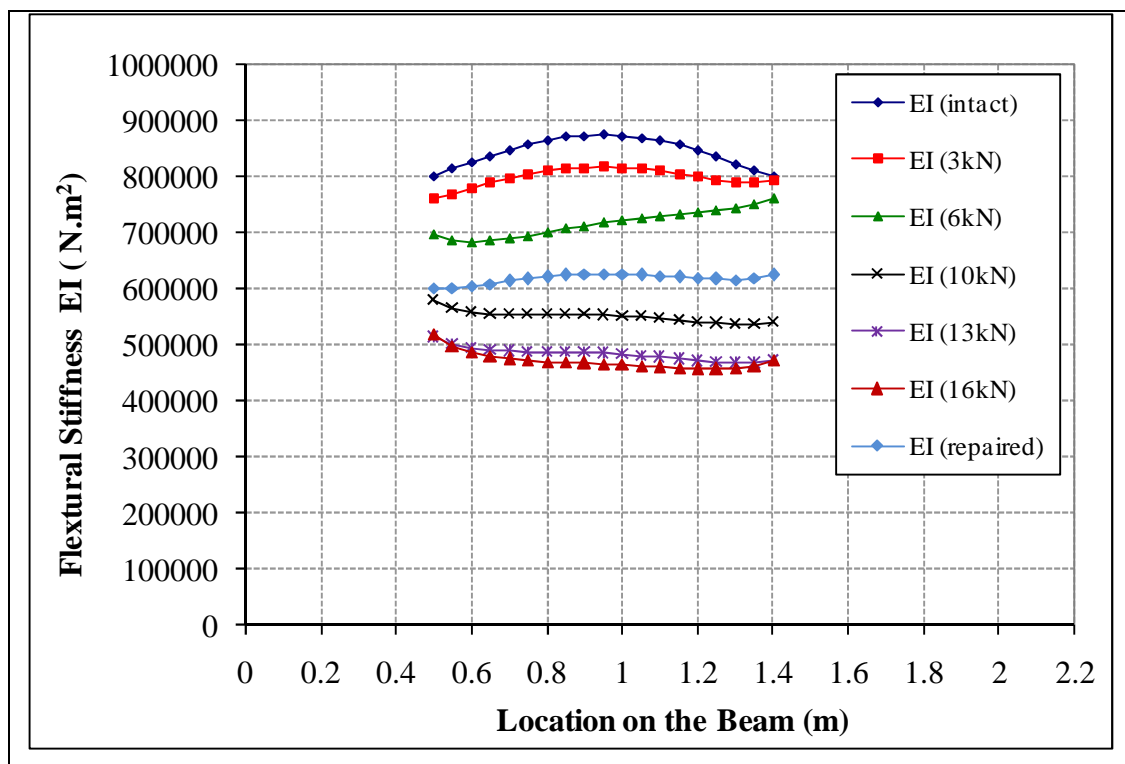


Figure 7.19: Flexural stiffness variation for beam A based on first mode.

Table 7.4: Successive mid span stiffness decrease of beam A based on the moment-curvature ratio.

| Load Step | Static BM kN.m | BM* MN.m | κ^\dagger 1/m | EI MN.m ² | a^\ddagger % | D ^{**} % |
|-----------|-------------------|-------------|----------------------|-------------------------|----------------|-------------------|
| Intact | 0 | 0.957 | 1.095 | 0.874 | 0 | 0 |
| 3kN load | 0.304 | 0.910 | 1.115 | 0.816 | 6.64 | 7.81 |
| 6kN load | 0.608 | 0.886 | 1.236 | 0.717 | 17.96 | 22.96 |
| 10kN load | 1.013 | 0.706 | 1.278 | 0.552 | 36.84 | 37.3 |
| 13kN load | 1.316 | 0.625 | 1.292 | 0.484 | 44.62 | 47.32 |
| 16kN load | 1.620 | 0.626 | 1.346 | 0.465 | 46.80 | 51.75 |
| Repaired | --- | 0.723 | 1.155 | 0.626 | 28.38 | 31.24 |

*BM = maximum mid span inertia bending moment.

$\dagger\kappa$ = curvature of first mode shape.

$\ddagger a$ = accumulated loss of bending stiffness.

**D = accumulated loss of bending stiffness based on RPS density function.

7.4.3 Damage Quantification in Beam B

The experimental distribution of dynamic bending stiffness (EI) with escalation of damage for beam B based on the first curvature mode shape is shown in Figure 7.20 for the entire length of the beam and in Figure 7.21 for the length between supporting points. As can be seen from Figure 7.20, the signature of the singularities due to the ill-conditioning of the computation aspect was evidently influential. On the other hand, at the central zone of the beam, the identified bending stiffness decreased significantly responding to the increasing damage, suggesting that damage location affected remarkably the high stress zone compared with the previous identical case study (beam A). At the final load step ($P = 15.5\text{kN}$), when the beam was heavily damaged, and formation of a plastic hinge was looming, reduction in EI of 58.1% ($a = 0.581$) was obtained compared with the healthy intact beam. Recognisably, the middle area of the beam at this stage was very fragile and went through extensive and intensive cracking condition. As the damaged zone is repaired, the beam became stronger, and the properties were modified. The damage factor (a) of the repaired beam was ($a=0.479$), where the bending stiffness (EI) improved notably by 24.4% from the severely damaged

level (15.5kN). Finally, in respect to beam B, dynamic bending stiffness associated with each damage state is logically determined by using related curvature along with the distributed bending moment. The situation of the beam at each condition is factually deduced by reduction of flexural stiffness.

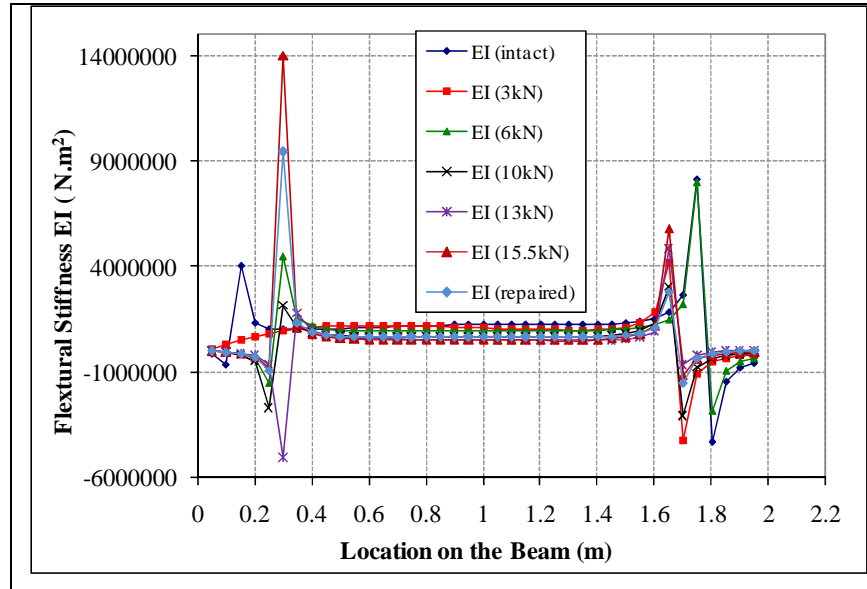


Figure 7.20: Flexural stiffness variation for the entire length of beam B based on first mode.

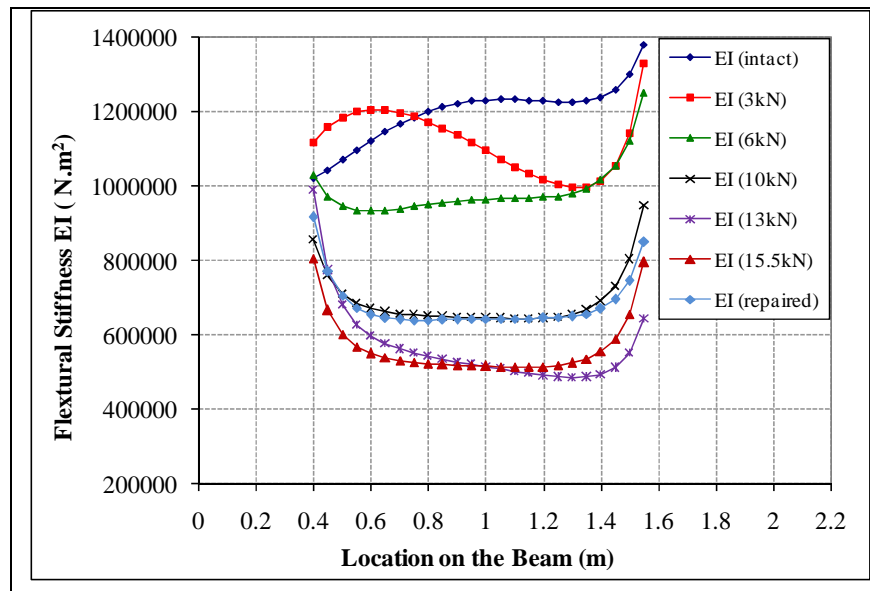


Figure 7.21: Flexural stiffness variation between support points for beam B based on first mode.

Table 7.5: Successive mid span stiffness decrease of beam B based on the moment-curvature ratio.

| Load Step | Static BM kN.m | BM* MN.m | κ^\dagger 1/m | EI MN.m ² | a [‡] % | D ^{**} % |
|-------------|-------------------|-------------|----------------------|-------------------------|------------------|-------------------|
| Intact | 0 | 1.328 | 1.079 | 1.231 | 0 | 0 |
| 3kN load | 0.304 | 1.280 | 1.170 | 1.094 | 11.13 | 18.3 |
| 6kN load | 0.608 | 1.137 | 1.180 | 0.964 | 21.69 | 40.36 |
| 10kN load | 1.013 | 0.806 | 1.249 | 0.645 | 47.60 | 64.4 |
| 13kN load | 1.316 | 0.709 | 1.378 | 0.515 | 58.16 | 73.2 |
| 15.5kN load | 1.569 | 0.677 | 1.312 | 0.516 | 58.08 | 73.9 |
| Repaired | --- | 0.846 | 1.317 | 0.642 | 47.85 | 54.6 |

*BM = maximum mid span inertia bending moment.

[†] κ = curvature of first mode shape.

[‡]a = accumulated decrease in bending stiffness.

**D = accumulated loss of bending stiffness based on RPS density function.

The drop in the flexural stiffness is overestimated when RPS density functions are only used to extract curvature mode shapes. As can be noted from Table 7.5, for 15.5kN load step, the accumulated loss of bending stiffness based upon mode shapes from RPS density function is $D = 73.9\%$, while it is $a = 58.1\%$ when computations of curvature based upon FRFs.

7.4.4 Damage Quantification in Beam C

Visual inspection of beam C reveals the weakness of this beam with the load cycles. At relatively advanced loading condition ($P = 10\text{kN}$, $M = 2.81\text{kNm}$), the beam displayed many cracks. Figure 7.22 shows the patterns in flexural stiffness of beam C along the entire zone between support points at different loading schemes based on first curvature mode shape. The calculation of modal curvatures is very sensitive to modal estimation errors. Therefore, the application of the DSC method should utilise the most reliable bending mode, which is the first mode shape. For the first time, in this case, the figure displays irregular and unexpected trend of bending stiffness changes despite the fact that the beam is in the intact condition before loading process starts. Evidently, the RC

beam is not perfectly linear, elastic and of non-homogeneous properties. At severely damaged load ($P = 10\text{kN}$), the beam continuously lost its bending stiffness for the central region. Therefore, almost constant drop in bending stiffness prevailed over all middle area points, which was approximately 50% compared with the intact case. Moreover, the reductions in flexure stiffness computed from this mode are presented in Table 7.6. The maximum reduction observed for the heavily damaged condition ($P = 14.5\text{kN}$) was 51.9%, while the percentage observed of the preceded condition ($P = 10\text{kN}$) was 48.8%. Locations at which the bending moment is low compared with the maximum bending moment were also discarded in the graphs because there were the inaccurate estimations of bending stiffness. This fact is due to numerical inaccuracies of the corresponding curvature at these locations (Huth et al., 2005).

After the last loading cycle, 52% loss in the bending stiffness was obtained at the central span, which concurs with the general damage evolution observed over the test.

Regarding the quantification of damage effects on bending stiffness, the DSC method indicates justifiable results. In agreement with the noted damage, the method identifies generally symmetrical and regular reduction in bending stiffness with increasing damage for the three prescribed samples. The maximum experimental rigidity of the healthy beam is close with respect to the analytical estimation.

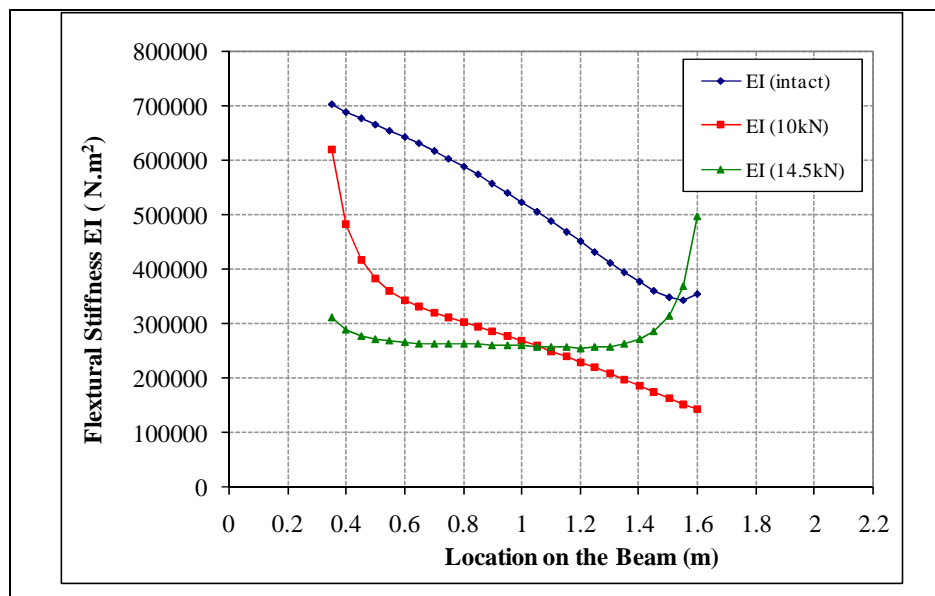


Figure 7.22: Flexural stiffness variation for beam C based on first mode.

Table 7.6: Successive mid span stiffness decrease of beam C based on the moment-curvature ratio.

| Load Step | Static BM kN.m | BM* MN.m | κ^\dagger 1/m | EI MN.m ² | a [‡] % |
|-------------|-------------------|-------------|----------------------|-------------------------|------------------|
| Intact | 0 | 0.622 | 1.150 | 0.541 | 0 |
| 10kN load | 2.813 | 0.371 | 1.340 | 0.277 | 48.80 |
| 14.5kN load | 4.078 | 0.295 | 1.135 | 0.260 | 51.94 |

*BM= maximum mid span inertia bending moment.

[†] κ = curvature of first mode shape.

[‡]a= accumulated loss in bending stiffness.

However, the spatial distribution of the stiffness loss in the mid span of beam C is not conclusive as the stiffness loss varies linearly. On the one hand, a major concern is that the method estimate significant stiffness loss in the central area of beam A and beam B which, by visual inspection, they did not display any obvious cracks. On the other hand, DSC results hold fairly dependable in the sense that the higher the damage evolved the higher the loss in stiffness. In addition, the observation of the structural changes is very well agreed with the results from the distribution and magnitude of induced damage.

7.5 Damage Identification using Curvature Difference Ratio

In fact, estimation of dynamic stiffness utilising the curvature along with the internal inertia forces experiences two difficulties. Firstly, a considerable computational effort must be paid to determine the inertia bending moments. Secondly, this procedure gives inconsistent results at low bending moment, supports and inflection points, which manifest as big jumps in EI, Figure 7.20. In order to overcome the drawbacks associated with application of this procedure, this study suggests eliminating these difficulties by normalising the difference in curvatures between two damage stages.

For a specific mode of vibration, the change in stiffness between two damage stages can be determined at any position on the beam using Equation 7.11. Consequently, for two different damage steps, a relative ratio of the difference in curvatures, designated Curvature Difference Ratio (CDR), can be established here to determine the

discrepancies of stiffness at any section over the beam, as a step forward. This non-dimensional expression is defined as:

$$\{CDR\}_r = \frac{\Delta \left\{ \frac{d^2\varphi}{dx^2} \right\}_{new\ case}}{\Delta \left\{ \frac{d^2\varphi}{dx^2} \right\}_{reference\ case}} \quad (7.16)$$

So that CDR for two damage steps and a specific mode (r) may now be expressed as:

$$\{CDR\}_r = \left| \frac{\varphi''_o - \varphi''_{new}}{\varphi''_o - \varphi''_{ref}} \right| \quad (7.17)$$

Where:

φ''_o is the curvature of the intact beam

φ''_{ref} is the curvature of the first damage step

φ''_{new} is the curvature of any subsequent mysterious damage step

Alternatively, in terms of the bending moment at a section (M) and the flexural stiffness (EI), CDR can be developed as:

$$\{CDR\}_r = \left| \frac{\frac{M}{EI_o} - \frac{M}{EI_{new}}}{\frac{M}{EI_o} - \frac{M}{EI_{ref}}} \right| \quad (7.18)$$

In RC beam and beam-like elements, the inertia bending moment for any two different damage steps at the same section are proved almost identical as the mode shapes did not change remarkably with the progress of damage. Therefore, by eliminating the parameter (M) from the numerator and denominator, CDR can be rewritten as:

$$\{CDR\}_r = \left| \frac{\frac{EI_{new} - EI_o}{EI_{new}}}{\frac{EI_{ref} - EI_o}{EI_{ref}}} \right| \quad (7.19)$$

In summary, Equation 7.19 can be used to obtain the numerical dynamic stiffness at a specific section based on the known reference stiffness value. The proposed technique relies on the fact that the difference between modal bending moments at a section for two different load steps is negligible.

The increase in the size of damage will result in uniform changes in curvature mode shape. This information can be exploited to locate the damage, follow its trend and estimate its extent. Apart from the inflection points, the last formula gives reliable and validated values for a drop in stiffness, particularly for continuous curvature discipline. In points of inflection, this estimate suffers from numerical inconsistency due to the occurrence of an ill-condition situation (zero division). To solve this problem, bending stiffness can be determined at the neighbourhood of zero curvature points. Otherwise, to get rid of the sharp jumps in the CDR curve at the positions of inflection points, it suffices to replace the actual curve by its second order polynomial best fit line. Distributions of CDR in beam B at different state conditions is shown in Figure 7.23. The parameter (CDR) revealed rationally the constant drop in flexural stiffness in the mid span zone with the progressive damage. In addition, the parameter hinted the linear distribution of flexural stiffness between the end and the support points.

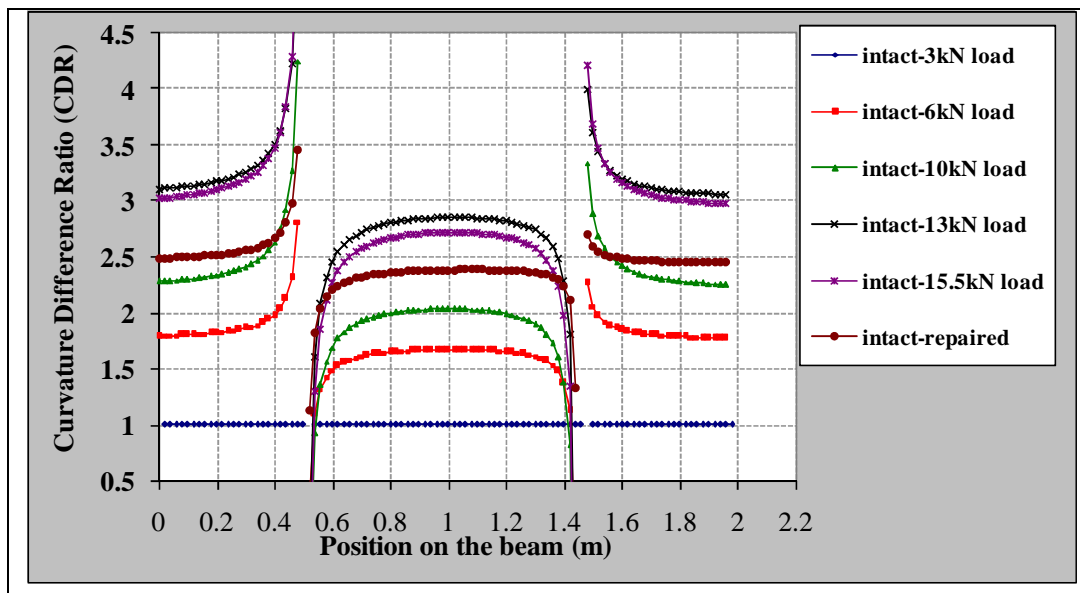


Figure 7.23: Curvature Difference Ratios for first curvature mode shape of beam B.

7.6 Summary

The experimental modal parameters as damage identification models have been shown computationally expensive, time consuming and require substantial inputs and considerable expertise. However, they have been proved successful for the condition monitoring of the present situation as well as structural changes in the course of induced progressive loads. It has been noted that a satisfactory location and quantification for structural changes (Level 2 and Level 3 of damage identification problem) can only be achieved reasonably through considering frequencies and mode shapes of a system in a proper analytical model.

In the context of FRF measurements, sound beam samples tend to display distinguished characterisations resulting in clear global resonances. On the other hand, frail samples show close, low and local resonances that are likely serious non-linear structural changes. The modal damping parameters are estimated by presuming a linear model in order to represent FRF measurements of non-linear structural behaviour. Therefore, the outcome is prone to certain degree of inconsistency, as it has been seen in the results of damping ratios from various beam samples.

The largest detected resonance changes of the RC beam state imminent to collapse was about 30% compared with the intact state condition. This drop was accompanying with maximum reduction in the flexural stiffness of 52%. The highest decrease was observed in the results of first mode of vibration, since the pattern of produced damage contributed mostly to this mode. The drop of flexural stiffness is overestimated, if mode shape measurements are based only upon RPS densities. Direct Stiffness Calculation (DSC) method can be used advantageously with beam and beam-like structures as damage quantification problem (level 3). Note that these conclusions are tenable because the process of monitoring was carried out in supervised environment, and the damage data was available.

Damage location characterisation, based upon mode shapes computation, holds fairly well for the damage area specifically for the first two modes, since the amplitude changes increased with the load in relation to the starting point condition. Moreover, the observed changes in first mode curvatures were even more localised for the position of

changes. The purpose-made cavities in beams D and E influenced the symmetry of the curvature mode shapes that the deviation and distortion were significant.

In conclusion, the extent of various damage identification techniques when applied to modal data representing different damage states from this work is summarised in Table 7.7.

Table 7.7: Summary of damage identification results tested on measurement from the five beams.

| Method | Input modal parameters | Detect damage | Locate damage | Quantify damage |
|-----------------------|---------------------------------|---------------|---------------|-----------------|
| Natural frequency | f_r | Yes | No | No |
| Modal damping ratio | ζ_r | Yes* | No | No |
| Mode shapes | Incomplete $\{\varphi\}_r$ | Yes | Yes | No |
| Curvature mode shapes | Incomplete $\{\varphi''\}_r$ | Yes | Yes | No |
| FRFs | One coefficient H_{ij} | Yes | No | No |
| MAC | Incomplete $\{\varphi\}_r$ | Yes* | No | No |
| COMAC | Incomplete $\{\varphi\}_r$ | Yes* | Yes** | No |
| DSC | Incomplete $f_r, \{\varphi\}_r$ | Yes | Yes | Yes |
| CDR | Incomplete $\{\varphi\}_r$ | Yes | Yes | No |

Yes* : inconsistent detection for some modes or some states;

Yes** : inconsistent localisation for some states

8. Implementation of Statistical Pattern Recognition Models to Vibration Data

8.1 Introduction

As a result of the limitations related to the inverse problem, and advantages gained from SPR procedures, with special focus on the current development of the monitoring technology relevant to deal with flooding real-time immense data, many researchers have described the structural damage identification as pattern recognition forward problem. A small amount of the given references exploit a statistical approach to quantifying the observed changes in these features, whilst the majority of the references found by the author and other researchers (Fugate et al., 2001; Sohn et al., 2000) propose many different methods for extracting damage-sensitive features from vibration response measurements.

The Chapter will deal with the problem of vibration-based damage detection process in the context of SPR. It will attempt to apply the SPR paradigm to the experimental raw signals collected through the course of this project.

Through the course of this Chapter, the measurements of the raw time signals and the frequency domain data from the five RC beams were employed with various ranges of conventional statistical models as well as with a new model in an effort to introduce a reliable timely diagnosis technique. As a consequence, the following main points are addressed:

- A good deal of this Chapter is assigned to introduce a new statistical methodology to classify damage according to its level. Both Response Power Spectral (RPS) densities and Frequency Response Functions (FRFs) collected from sensors deployed over the five beams were proved effective in separating the data. The method was tested and validated on data samples from the five test beams in this work.

- Other temporal features such as raw time-signals, statistical moments of the time signals, etc. were tested with the new approach in relation to its suitability and extent with different structural changes.
- The relative assets of different damage-sensitive parameters and its relevance in SPR models were examined and discussed.

8.2 Statistical Pattern Recognition Paradigm

In general, the process of SHM has been viewed as SPR problem by prominent researchers beginning from the early years of the last decade. As a replacement or supplement to the conventional model-based methods, a group of researchers of Los Alamos National Laboratory have established the new methodology in the following four-part paradigm for an effective damage diagnosis and prognosis process (Farrar et al., 2001a; Sohn et al., 2001):

- Operational evaluation.
- Data acquisition and data cleansing.
- Damage-sensitive feature extraction.
- Statistical model development.

First, the operational evaluation part includes a thorough investigation of the operational environment surrounding the data collection campaign, and its potential impact on the monitoring of the real condition of a structure. This part entails addressing two important questions regarding the upcoming SHM campaign, which are: the conditions, both operational and environmental, under which the structure to be monitored operates; and the limitations on acquiring data in the operational environment. Operational evaluation aims at assigning the monitoring outcomes to unique aspects of the system and unique features of the damage that is to be detected (Farrar et al., 2001a; Sohn et al., 2001).

Second, the data acquisition part of the SHM process entails issues related to the types of sensors to be used, the number of sensors, the positions where the sensors to be deployed and the data acquisition/storage/transmittal hardware (Farrar et al., 2001a). In addition, the nature of damage and related concerns must be considered to decide how

often the data should be acquired. Another consideration should be attributed to the normalisation of the collected data sets to mitigate the variability of the operating environment. This process can tacitly be implemented through normalising the responses by the corresponding inputs as in FRF computations (Farrar et al., 2001b).

It is evident that the above-mentioned two parts of the SPR paradigm are also basic parts in the damage identification when approached as a model-based problem. However, the third part in this programme, feature extraction, is the part that receives the greatest research efforts in the technical literature. Feature extraction is the process of suggesting damage-sensitive parameters, which derived from the measured vibration response that permits one to distinguish between the undamaged and damaged structure. The procedures of this part almost include implicit steps implementing some forms of data reduction. A compression of the data is useful and imperative, particularly if comparisons between numerous data sets over the real time monitoring of the structure are to be performed. Most importantly, vigorous data-reduction approaches must preserve sensitivity of the selected features to the structural changes of interest in the presence of environmental perturbations, because data may be captured over a lengthy period of time, and probably in an aggressive operational environment.

It is quite often that features extracted from vibration measurements are not sufficient to provide a complete diagnosis programme. Therefore, a corresponding essential fourth part, statistical model, should be devised for this purpose. This part of the SHM programme is that has received the least effort in the identified literature, although a development of such models enhances significantly the damage detection process. This part is concerned with the implementation of the algorithms that investigate the extracted features so as to define the damage state of the structure. Also, statistical model can answer question on the type of damage, when data sets from different damage types are available. In general, the algorithms in statistical model development belong to one of the following three groups (Farrar et al., 2001a):

1. Group Classification
2. Regression Analysis
3. Outlier Detection

The proper group is to be chosen depend on the available measurements and whether they cover both undamaged and damaged structural states.

The group classification type is that situates the features into particular (undamaged or damaged) subgroups. The second type is regression analysis, which signifies the process of correlating data features with particular types, locations or extents of damage. On the other hand, analysis of the outliers in the third type of the algorithm helps to indicate clear deviation in features of the investigated data compared with other sample, when data from a damaged structure is not specified for comparison purposes.

The main aspects of the postulated paradigm for SHM is summarised in the flow chart given in Figure 8.1.

After all, an efficient statistical model also should be able to establish a sound evaluation process in the respective of the possibility of false indications of damage. False indications of damage emerge into either one of the two types: (i) false-positive damage indication (indication of damage when none is present); and (ii) false-negative damage indications (no indication of damage when damage is present). Although the second category is usually very unfavourable to the damage detection procedure, and can have serious consequences on the safety, false-positive evaluations can also undermine confidence in the damage detection procedure (Farrar et al., 2001a).

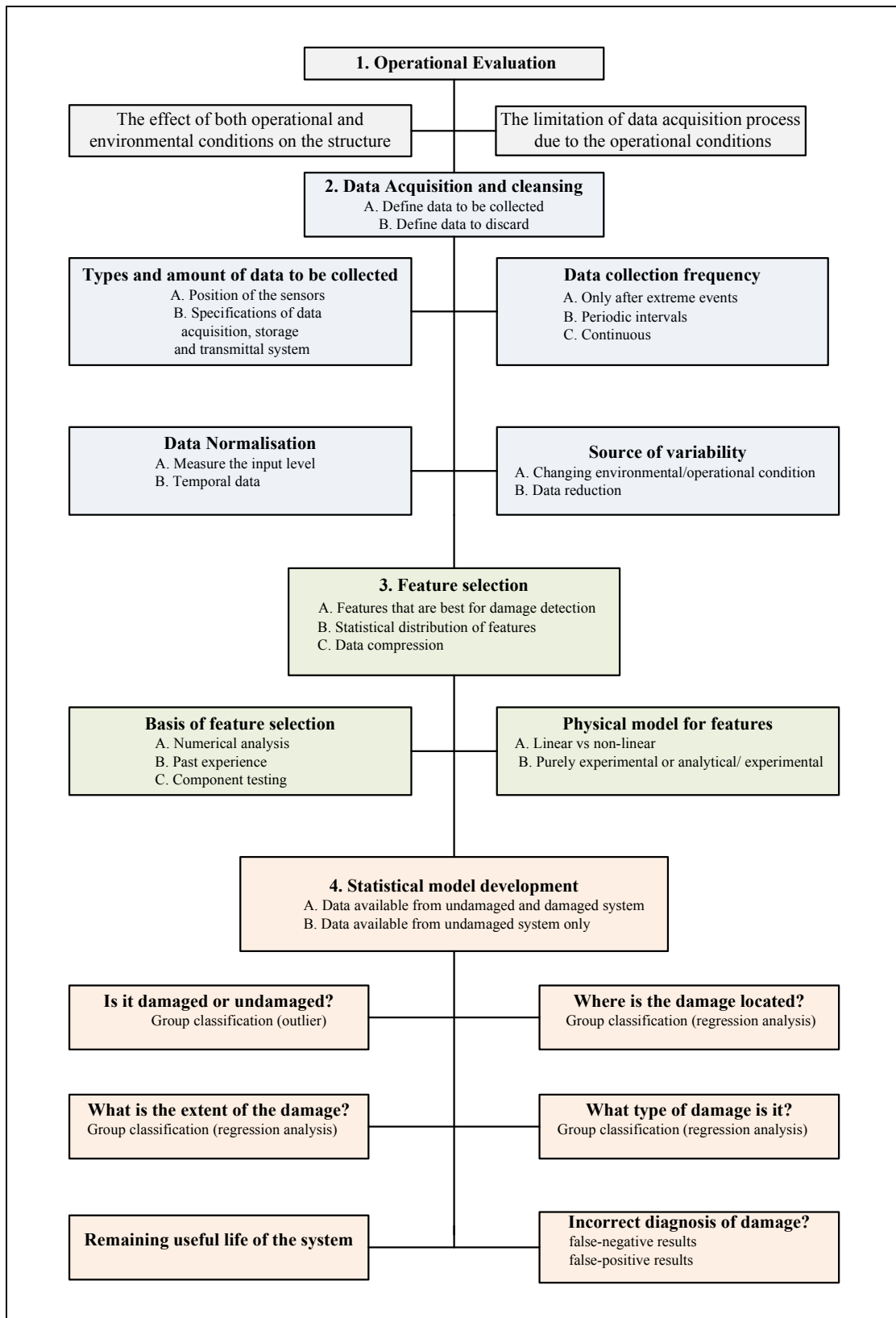


Figure 8.1: Flow chart for implementation of SHM programme (after Farrar et al., 2001a).

8.3 Data Analysis using Time Domain Records

8.3.1 The Raw Time Signals

The raw response time signals for the beams of this study subjected to different damage models were visualised so as to explore if they would offer any preliminary discrimination tool. As general samples, the response time histories at point (#1) and point (#6) of beam A due to excitation force at point (#1), for all structural conditions, are shown in Figure 8.2 and Figure 8.3, respectively. Also, the time histories of the response at point (#3) of beam B are plotted in Figure 8.4. The signals were captured using a four-channel data acquisition system with 4100 samples, taken at a rate of 8180 samples per second resulting in time period of 500.4ms. However, only 1000 data points were deliberately shown in the plots in order to get better visualisation, and because the signals oscillate very close to zero amplitude in the rest of data points. The main intuitive concern with response-time series collected with hammer is that the amplitude is hardly controlled to become consistent for all signals, even though the operator tries to make all impacts alike. The impact hammer has no control mechanism in general, and therefore has a difficulty to generate identical input forces. The amplitude is somewhat inconsistent as the input force is prone to human variability. Based on visual inspection, a few observations could be made from the response time histories (Figures 8.2-8.4): (1) all the signals are approximately similar in configuration and of regular unified oscillation and diminishing aspects; (2) the amplitude of one signal is virtually dissimilar to the amplitude of other signals, for the same measuring location, indicating the need for data normalisation; and (3) no substantial variation in the shape of signals can be accounted to the progress of damage for each position.

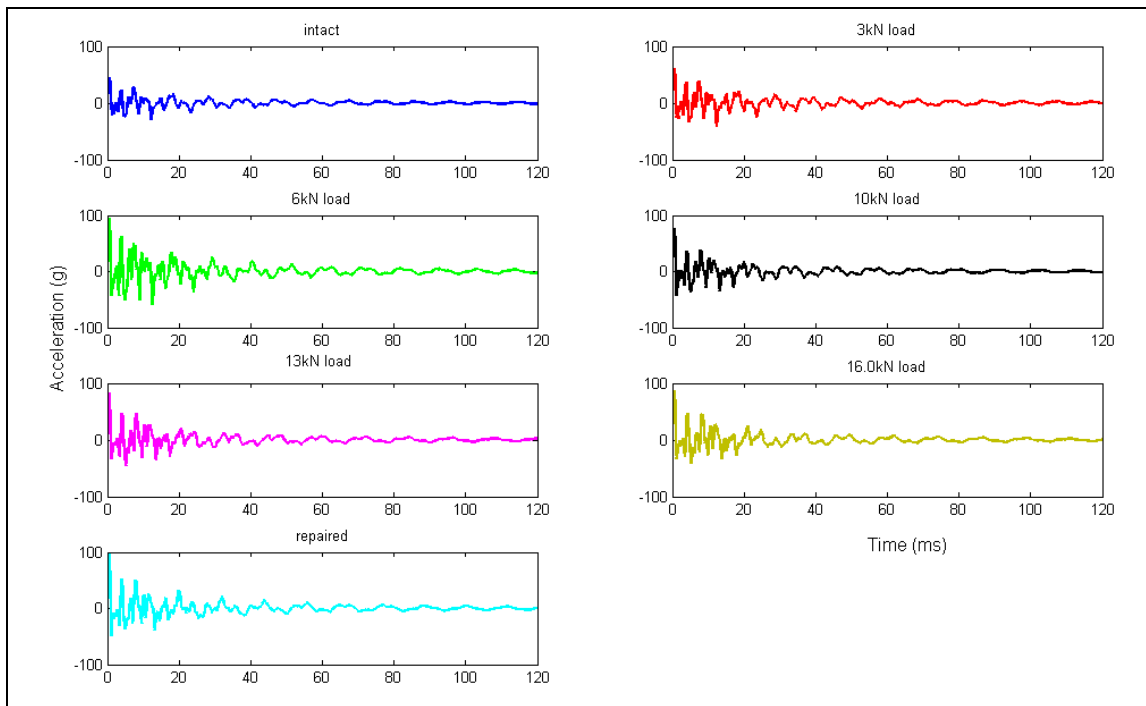


Figure 8.2: Raw response time signals of beam A at point #1, when force is at #1.

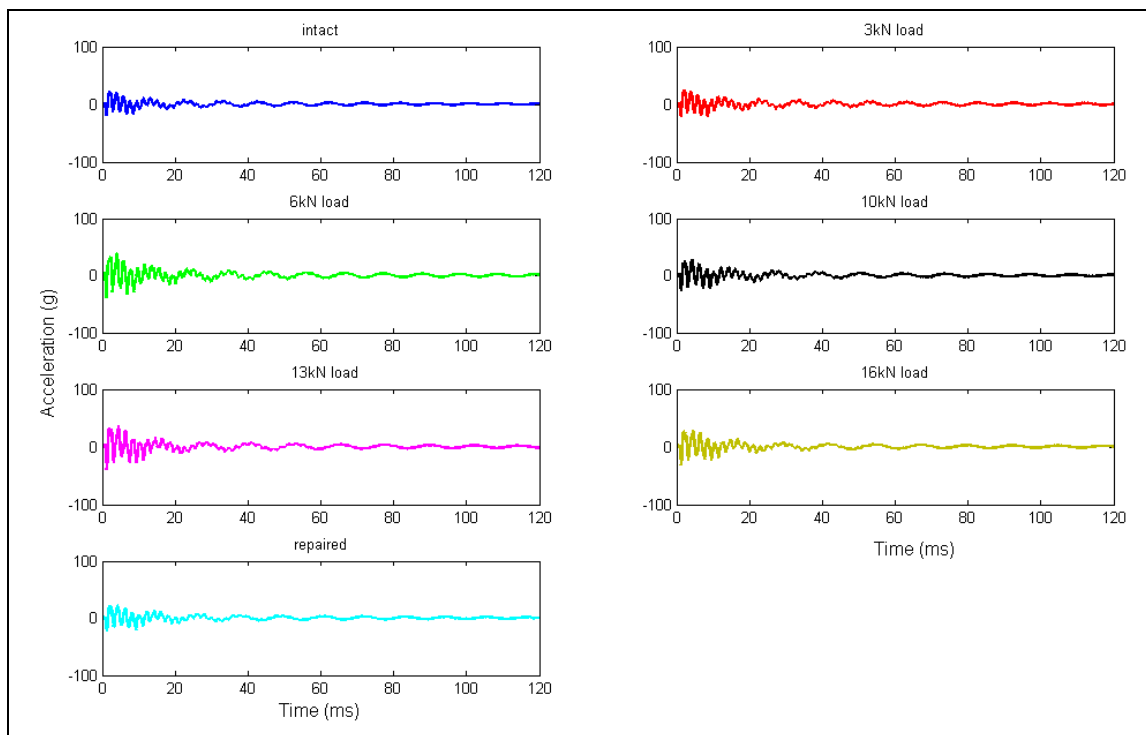


Figure 8.3: Raw response signals of beam A at point #6, when force is at #1.

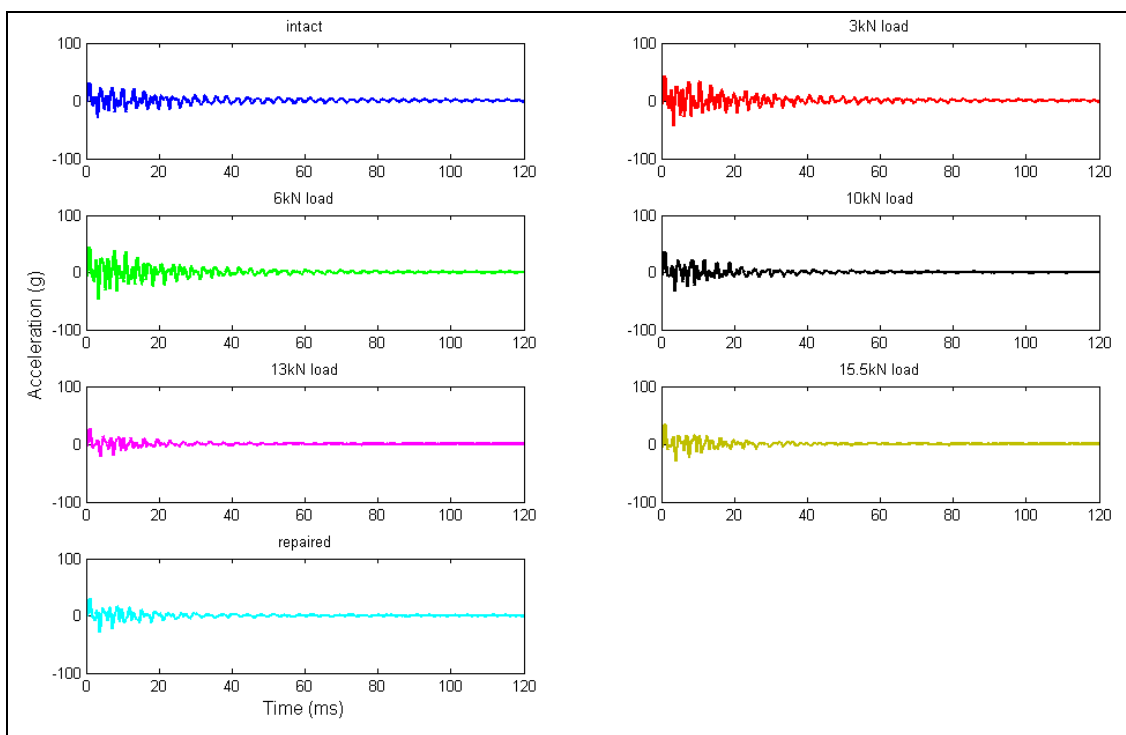


Figure 8.4: Raw response signals of beam B at point #3, when force is at #1.

8.3.2 Statistical Moments of Acceleration-time Histories

The response time signals generated in this project are random, and therefore, statistical procedures must be employed to define the characteristics of these signals as long as a mathematical valid model is impossible. In statistics, a random signal is considered stationary, when its moments do not change for different signals captured over time (Figueiredo et al., 2009). In this section, the first four statistical moments, namely mean, standard deviation, skewness and kurtosis are used so as to describe the implicit properties of the signals. Firstly, the moments are allocated to study the consistency of the ensemble time histories from same channel for each damage condition. Secondly, the deviation of the moments with damage state as a function of the sensor position is discussed. To this end, the first four statistical moments are to be evaluated as damage-sensitive features.

The measure of a random signal that represents the deviation from its centre is referred to as its mean. The first moment of a random variable of normal distribution is zero as the first moment of a symmetrical distribution around the mean is zero. The second

measure of the statistical moments is the variance (σ_x^2), which represents the scattering of the data from the mean, and is given as:

$$\sigma_x^2 = E(x - \bar{x})^2 \quad (8.1)$$

Where:

\bar{x} is the mean of a random variable x , and represents the central trend in the data sample

$E(x)$ is the mathematical expectation of the random variable x

σ_x^2 is the second statistical moment, and represents the dispersion from the mean

The square root of the variance is designated as the standard deviation (σ_x), and for a theoretical normal distribution is always (1).

The third statistical moment, skewness, is a measure of the lack of symmetry of the data around the sample mean and the skewness of a distribution (s) is described as:

$$s = \frac{E(x - \bar{x})^3}{\sigma_x^3} \quad (8.2)$$

If the skewness is negative, the data is skewed toward the negative direction of the mean. However, when the skewness is positive, the data has heavier tail to the positive direction of the mean.

The kurtosis is the fourth statistical moment, and gives an estimate to the amount of data located in the tails of the distribution. The kurtosis (k) of the distribution is defined as:

$$k = \frac{E(x - \bar{x})^4}{\sigma_x^4} \quad (8.3)$$

The kurtosis of a theoretical normal distribution is always (3). Distributions with kurtosis greater than 3 have more mass in the tails than a normal distribution, and distributions with kurtosis less than (3) have shorter tails than a normal distribution.

Skewness and kurtosis of values greater than (3) implies that normalisation of data is no longer useful (Figueiredo et al., 2009).

In order to get a general idea from the raw signals, prior to the centralisation or standardisation of the data sets, a global view of the first four statistical moments for the four raw time signals acquired at channel #1 of beam A corresponding to each beam condition is given in Figure 8.5. Furthermore, to study other position, where the sensor is closer to the damage zone, mid span position (node #6) was considered, and its four statistical moments were also plotted in Figure 8.6. The four plots of each figure display complete arbitrary distribution for all damage cases. For all condition cases, the results tend to vary arbitrarily for the same channel (either #1 or #6), although the signals are supposed to represent the same sensor location and same structural status. Based on this observation, it is quite clear that the arbitrariness in the signals is strong, and one selected time history from ensemble group of particular channel is not uniquely representing the associated beam condition. The observation underlines the unfeasibility of using the statistical moments of time histories purely as damage-sensitive features.

A close look at these figures further exposes important aspects regarding to the time histories. The sample standard deviation and skewness of one time signal are different from those of other signals, even though all the signals belong to same beam condition. Moreover, all signals have relatively large kurtosis values (greater than 10 for point #1 and slightly less than 10 for point #6) indicating that they all have rather long and heavy tails. This is accounted to the unusual operation conditions manifested as significant signal variation.

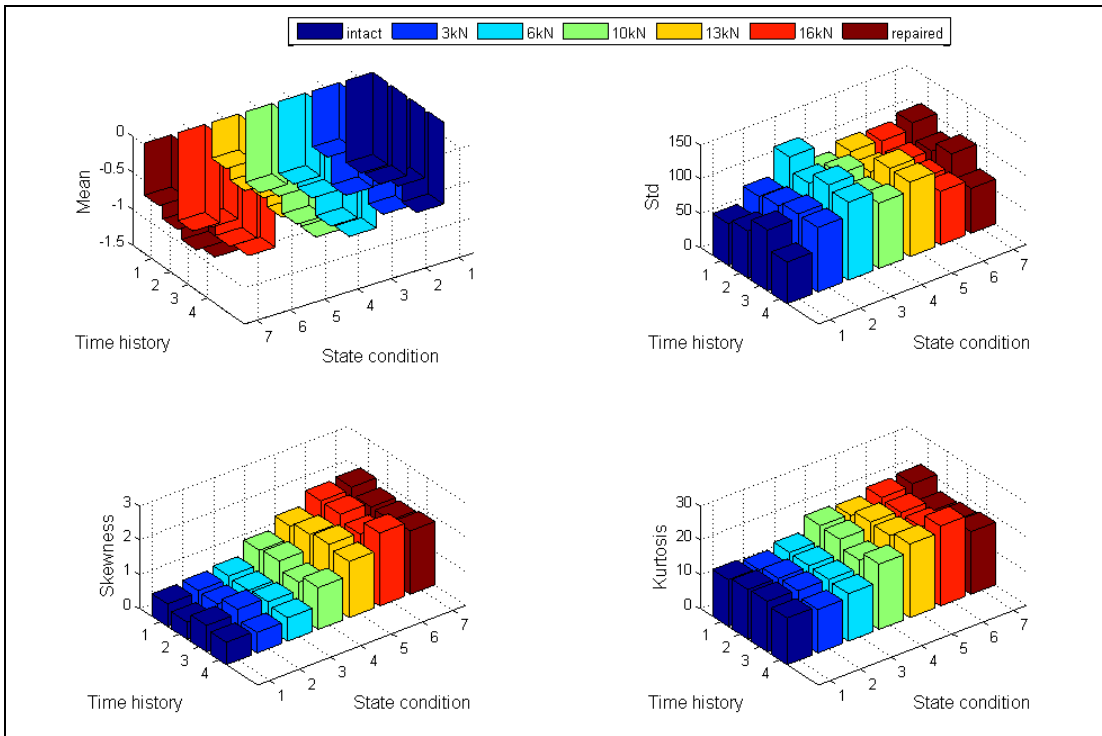


Figure 8.5: The first four statistic moments from position #1 (end span) of beam A.

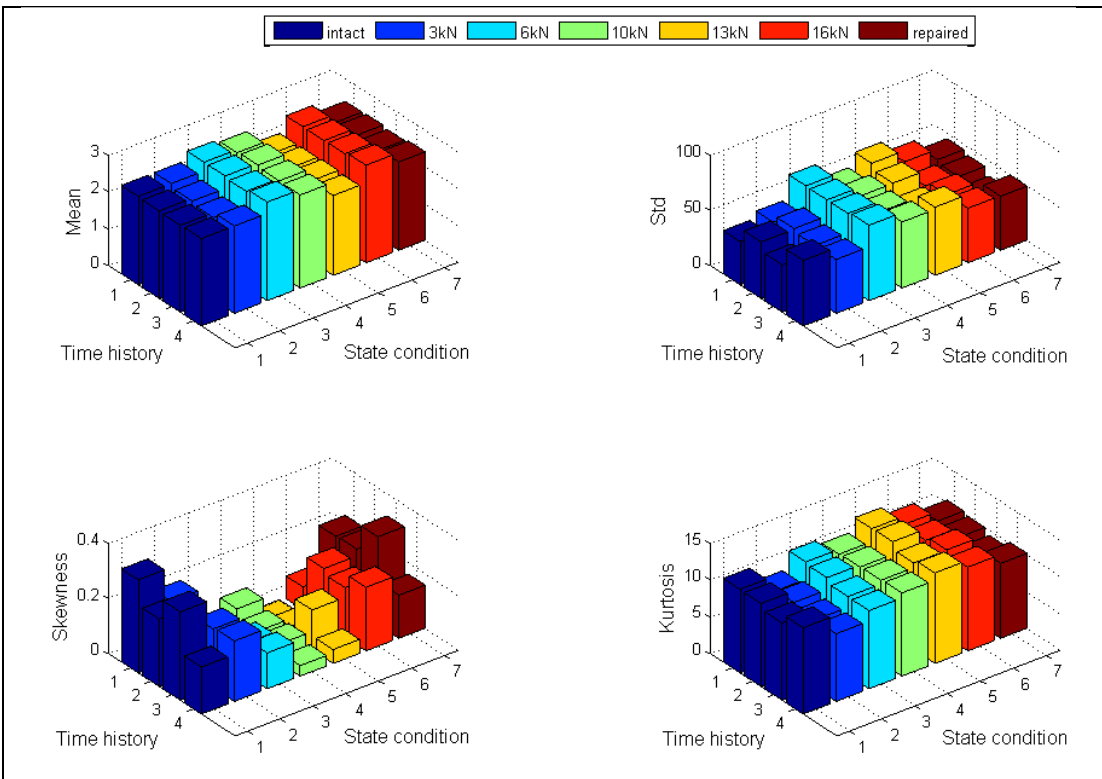


Figure 8.6: The first four statistic moments from channel #6 (mid span) of beam A.

Moreover, Figure 8.7 gives the first four statistical moments of one sample of time histories captured at the points along the entire beam locations (#1- #11) for each individual structural condition of beam A. The mean and standard deviation of the time histories do not give any clear understanding about the increased damage level coupled with the damaged conditions occur between (3kN - 16kN) load cycles. In addition, the skewness and kurtosis show greater changes for signals from channel (#2) compared with the rest (10) channels, which display almost constant skewness and kurtosis with the escalating defect for a particular channel. However, the spatial distribution of the four statistical moments is not conclusive neither for the location of damage nor for the extent of nonlinearities developed with the increased load. Therefore, it is worthy try to implement some form of data normalisation to alleviate the sharp differences in the signals occurred due to the operation variations.

It is desirable, in statistics, before embarking on subsequent computation that all data samples to be normalised, using the following equation:

$$x_s = \frac{x - \bar{x}}{\sigma_x} \quad (8.4)$$

Where:

x_s is the normalised data sample

\bar{x} is the mean of the data sample of n observations

σ_x is the standard deviation of the data sample x

As a result, the normalised sample given by x_s has a zero mean and a unit standard deviation. Figure 8.8 shows the moments for the same but normalised time histories used for presenting Figure 8.7.

It is noted from Figure 8.8 that the normalisation process for the captured signals does not mitigate the randomness, and does not enhance the consistency, but the process has yet changed the scale of each corresponding moment. From Figure 8.8, it is clear that for all damage states the skewness and kurtosis exhibits uniform behaviour, with an exception of 16kN load and repaired cases for skewness of channels #1 and #9.

Evidently, the normalisation of the data does not offer substantial improvement to the statistical moments because, in general, the skewness and kurtosis values are greater than (3).

It is of interest to note that the skewness has an opposite sign for the sensors on either side off the impact device, implying that the response from channel #7 and #9 has more values below the mean in its damaged condition. On the other hand, the response from channels such as #1, #2, #3, etc. has more values above the mean. In addition, the undamaged and damaged beams always show same kurtosis between (10-20) depending on the sensor location on the beam rather than the state condition. Theoretically, kurtosis of a value larger than (3) indicates that most of the variance is caused by non-frequent extreme deviations from the mean. Most importantly, for both skewness and kurtosis, the distributions are nearly uniform in data samples from all position points, for the undamaged and damaged states. In conclusion, statistical moments from acceleration-time histories do not present a sound classification means to neither the location nor the size of damage. To support this conclusion, the first four statistical moments for beam B are likewise drawn in Figure 8.9. The results of beam B provide as same as the previous observations of beam A. The bottom line is that statistical moments are more sensitive to the location of the sensor where the signals have been captured rather than to the level damage of the beam.

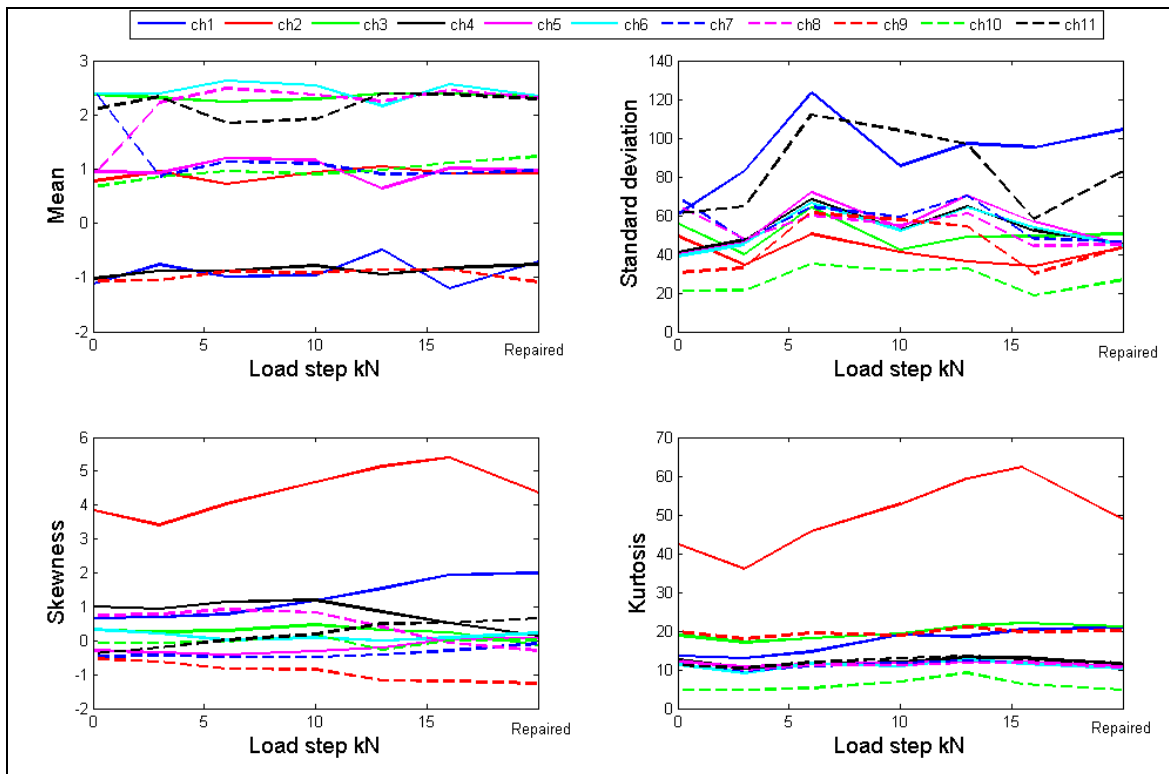


Figure 8.7: First four statistical moments of beam A (raw time histories).

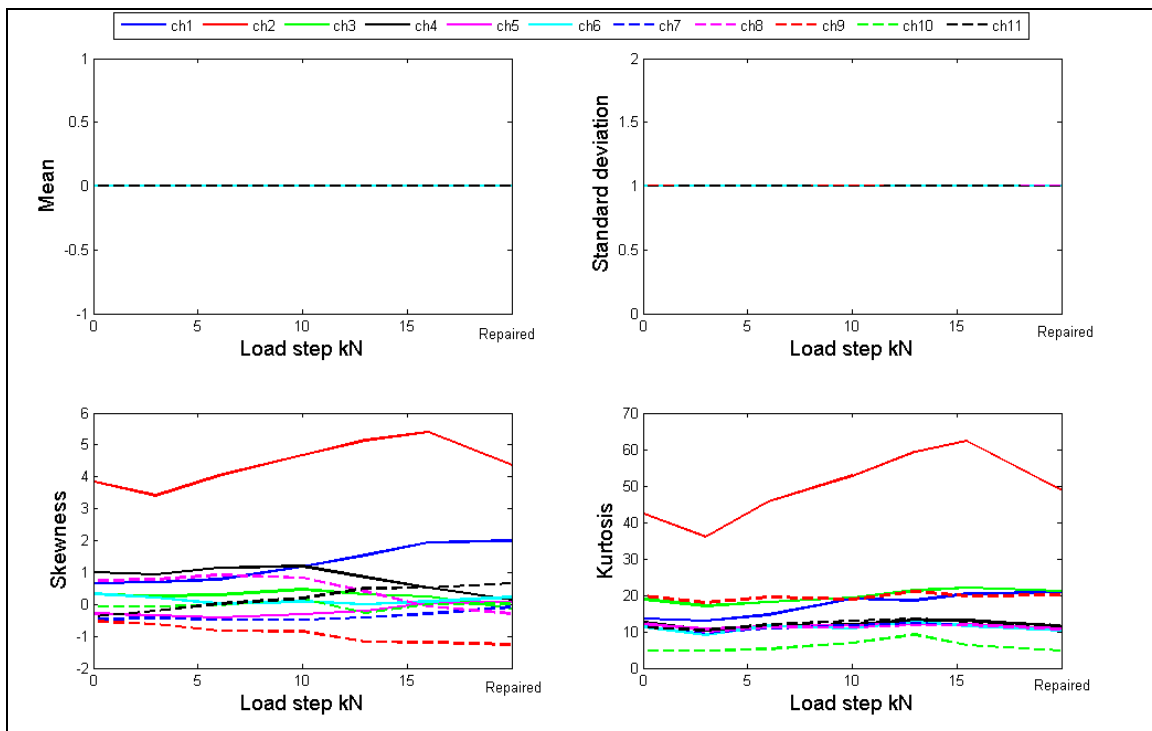


Figure 8.8: First four statistical moments of beam A (normalised data).

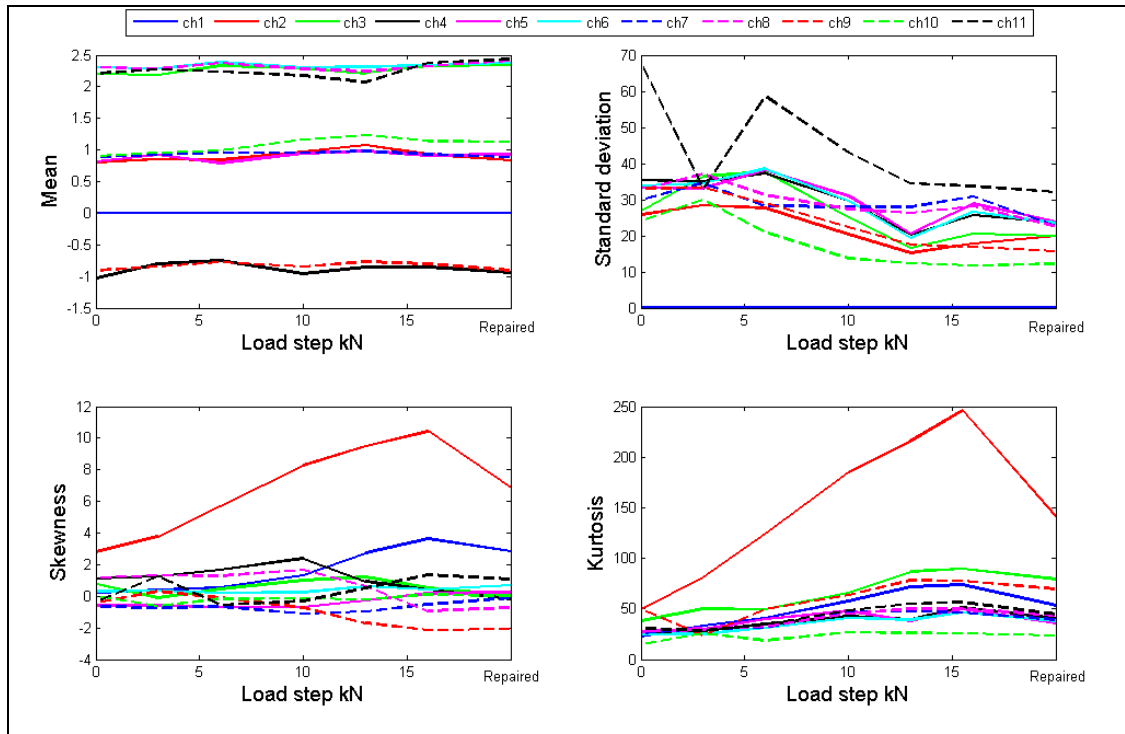


Figure 8.9: First four statistical moments of beam B (raw time histories).

8.3.3 Probability Density Functions

In the damage identification context, another tool to identify an unobservable underlying distribution in the time history is to obtain its probability density function (PDF) using the most eminent probability distribution, namely the normal or Gaussian distribution. In statistics, the normal distribution is often employed as an initial description of real-value random variables that have a bell-shaped around a mean value. The PDF is the probability that the variable has the value x . The histogram density estimator and the kernel density estimator are two techniques used to estimate an underlying PDF of a random variable. The general Gaussian distribution function is the most important because of its fixed behaviour about the mean and standard deviation, and can be given as:

$$p(x) = \frac{1}{\sigma\sqrt{2\pi}} e^{\left\{-\frac{1}{2}\left(\frac{x-\bar{x}}{\sigma}\right)^2\right\}} \quad (8.5)$$

Where:

\bar{x} is the mean or expectation (location of the peak)

σ^2 is the variance of the observations

The simplest case of the normal distribution with $\bar{x} = 0$ and $\sigma^2 = 1$ is called the standard normal distribution or the unit normal distribution, and takes the following form:

$$p(x) = \frac{1}{\sqrt{2\pi}} e^{-\frac{1}{2}(x)^2} \quad (8.6)$$

The normal distribution is very simple to implement mathematically, because a large number of observations resulting from a particular process can be derived in explicit form. In signal identification respective, the observational error in an experiment is usually assumed to follow a normal distribution, and the propagation of uncertainty is computed using this assumption.

In Figure 8.10 the PDFs of all state conditions for beam A derived from acceleration-time histories captured at channel #1 and channel #2 follow typically the normal distribution form. Even though beam A is severely damaged in 16kN loading step, the PDF converges from a normal distribution shape. The median values (the peaks) of the PDFs are positioned near zero value in the horizontal axis (the mean value of each normalised PDF is zero.) From this Figure, it is concluded that there exists a noticeable difference between PDFs of the signal from the baseline condition and the rest of the signals that represent the unhealthy conditions. Furthermore, the PDF of signals from unhealthy beam seem closer to each other compared with the PDF from the normal condition. The negative and positive skewness, found from statistical moment for this signal and other signals, are insignificant and do not appear clear in these probability distribution functions. However, more non-frequent values in the tails of damaged states than the other normal state as indicated by its large value of kurtosis. Again, unfortunately this is not a sound conclusion as the observation rather changed when deal with signals from other position. PDFs for signals at point #2 for all state conditions of beam A display inconsistent behaviour for time histories collected from different trials at same or different positions, PDFs do not provide sound discrimination for these signals as well.

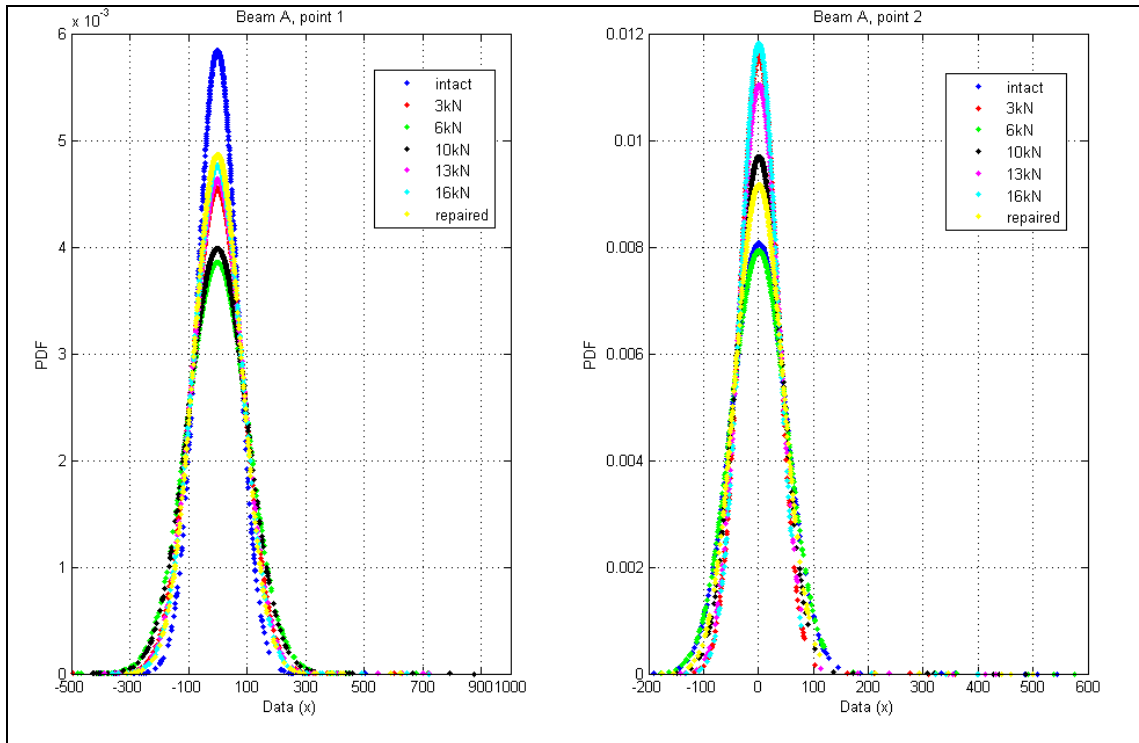


Figure 8.10: PDFs using time histories from point #1 and point #2 of beam A.

8.3.4 Normal Probability Plots

In order to get clearer graphical representation than the PDF, normal probability plots are used to evaluate whether or not random measurements from a normal distribution offer useful visualisation. In this procedure, the data is plotted against a theoretical normal distribution in such a way that the points should form an approximate straight line. Departures from this straight line indicate departures from normality. The normal probability plot is drawn between the ordered response values (to change the order to become between 0-1) on the y-axis and normal order statistic medians (the data records of acceleration or voltage are ordered to find the median order on the x-axis). Accordingly, the y-axis values are represented by the following formula:

$$Probability(x_i) = \left\{ \begin{array}{ll} 1 - 0.5 \frac{1}{n} & \text{for } i = 1 \\ 0.5 \frac{1}{n} & \text{for } i = n \\ \frac{i - 0.3175}{n + 0.365} & \text{for } i = 1, 2, \dots, n - 1 \end{array} \right\} \quad (8.7)$$

That is, the observations are plotted as a function of the corresponding normal order statistic medians. Another way to think about this is that the sample values are plotted

against what is expected to see if it is strictly coherent with a process of a normal distribution.

The further the points vary from the straight line, the greater the indication of departures from normality. If the data are normal, the plot will be linear. Otherwise, distribution types will introduce curvature in the plot (Figueiredo et al., 2009; The Mathworks, 2008).

Figure 8.11 and Figure 8.12 present normal probability plots of the acceleration time histories from various state levels of beam A at points #1 and #2, respectively. The PDFs of the same cases are displayed and discussed previously in Figures 8.10. The solid red line joins the 25th and 75th percentiles in the data, and the y-axis values are probabilities from zero to one, but the scale is not linear, versus the accelerations data points in voltage values in the horizontal axis. The distance between tick marks on the y-axis matches the distance between the quantiles (the points that are taken at regular intervals) normal distribution. The quantiles are close together near the median (probability = 0.5) and divert out symmetrically as data values move away from the median.

The plots clearly show that data from the baseline condition (intact) and the following damaged cases (3kN, 6kN, 10kN and 16kN load) are non-normally distributed. Note that in this case the impact hammer does not have a feedback control mechanism and as such has difficulty in reproducing an accurate Gaussian input. This difficulty manifests itself in the tails of the distribution where insignificant deviations from the normal condition can be perceived. However, the states with the nonlinearities (3kN-16kN loads) show that an assumption of normality is not justified, as shown by the significant curvature in the tails of the normal probability plots. From the normal probability plots, it is noticeable that the abnormality in distribution of the time histories was conceived for both normal and damaged cases. One of the limitations with this explanation is that even though the non-normality appeared more substantial in the damaged cases compared with the intact condition, the level of damage was not conclusively discriminated in this tool.

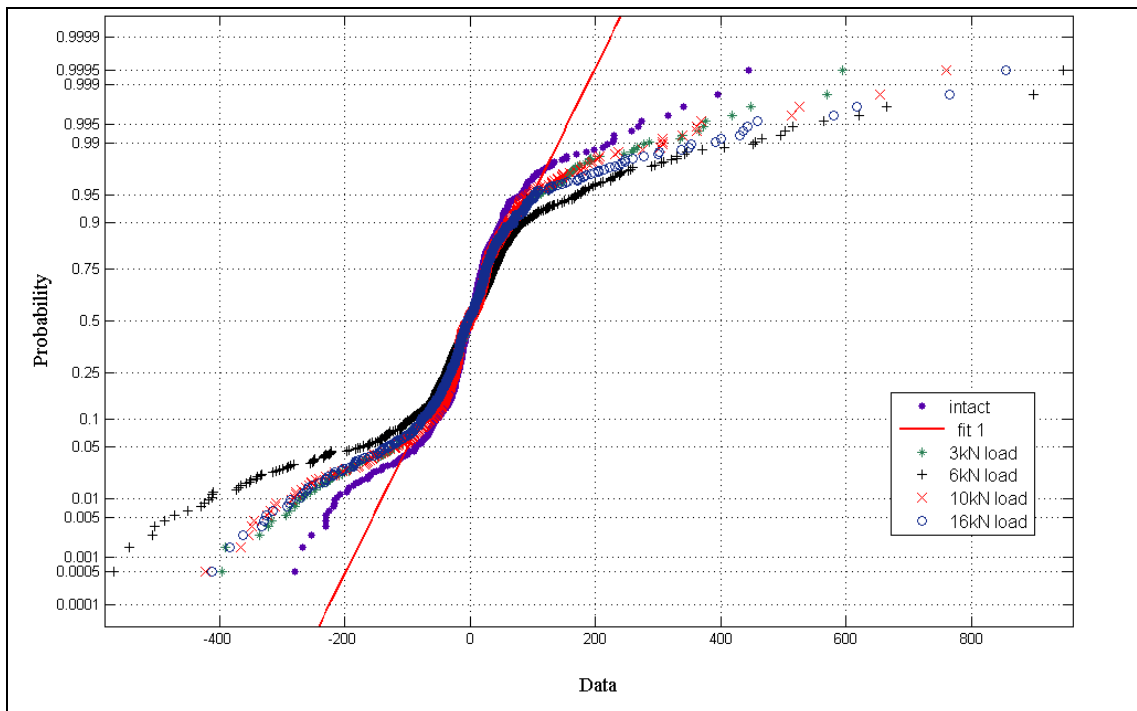


Figure 8.11: Normal probability plots of time signals from channel #1 of beam A.

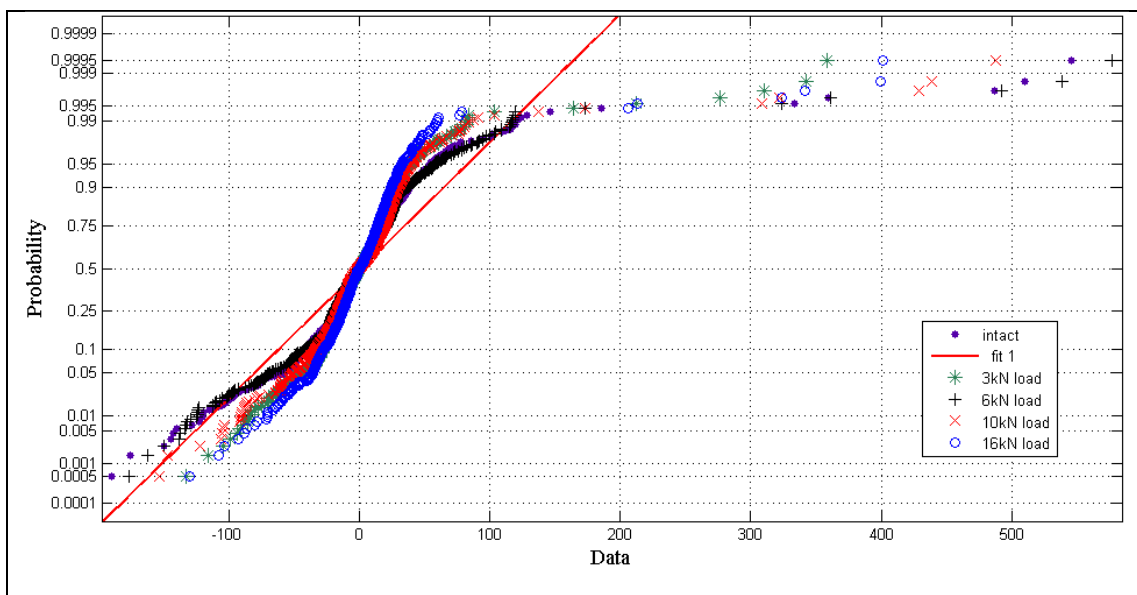


Figure 8.12: Normal probability plots of time signals from channel #2 of beam A.

8.3.5 Correlation Coefficients of Raw Time-histories

In order to determine useful damage-sensitive feature, an effort has been made to use the correlation coefficient between time histories to discriminate signals come from different positions and various system conditions.

The correlation is a statistical technique used in signal processing for analysing the relationship between two or more signals from different events. The general idea of using the correlation coefficients for comparison between signals is that signals from same structural state are much correlated, whereas the correlation will decrease for signals from different states (Trendafilova, 2011). The quantity (r), known as linear correlation coefficient, represents the strength and the direction of a linear relationship between two signals. The estimation of autocorrelation coefficient for a signal of (n) dimension denoted by (x) with itself gives the autocorrelation of that signal, and can be defined as:

$$r_{xx} = \frac{1}{n-1} \frac{\sum_{i=1}^n (x_i - \bar{x})(x_i - \bar{x})}{\sigma_x \sigma_x} \quad (8.8)$$

Where:

\bar{x} is the mean of the corresponding time history signal

σ_x is the standard deviation of the signal

In addition, the estimation of the correlation coefficient between two different signals signified by (x) and (y) of same dimension (n) is likewise given by:

$$r_{xy} = \frac{1}{n-1} \frac{\sum_{i=1}^n (x_i - \bar{x})(y_i - \bar{y})}{\sigma_x \sigma_y} \quad (8.9)$$

The correlation coefficient (r) from this process is such that $-1 < r < 1$, and denotes the linearity strength between the random variables (x) and (y). A correlation coefficient of (+1) indicates a complete positive correlation generally described as perfect, whereas a coefficient of (-1) is generally describes a perfect anti-correlation. In a weak correlation between the random variable events, the coefficient is close to (0).

Before embarking on the correlation coefficient (r) as a damage-sensitive feature, it was used efficiently, in this research, to proof the strong correlation between the output time-signals captured at the same channel, but from different excitation attempts.

In the context of damage identification, this section is assigned to scrutinise the possibility of using correlation coefficients as damage-sensitive features to identify the presence, size and location of damage among the sensors. For this purpose, a standardised correlation matrix with elements described by Equations 8.8 and 8.9 was calculated for each system condition. In this case, the variables were represented by one time history from each sensor (#1 to #11), and for each structural status. Since the accelerometers were mounted at (11) different positions, and for each position the beam was subjected to seven different conditions, each correlation matrix $[\Sigma]$, for any sensor location has a dimension of (7×7) . The time histories of two beam case studies, beams A and B, were taken as samples to investigate the prospect of the correlation coefficient as a damage-sensitive feature. Two correlation aspects for each case study were addressed; the correlation between signals from same damage level, but different locations; and the correlation between signals from same location, but various structural conditions. Figure 8.13 displays the results from the two aspects for beam A. Equally; Figure 8.14 displays the results of beam B. The figures provide two remarkable characteristics. First, the correlation coefficients based upon the time histories from specific location were able to discriminate objectively the damaged from undamaged states, especially discriminate between the successive damage levels. This observation was absolutely conclusive for signals from the (11) different locations over beam A. However, the results were rather non-conclusive for channels #2 and #3 for beam B, where the correlation was quite strong, but negative at 3kN load step (Figure 8.14). Second, the correlation coefficients were found incoherent in locating the damage among the sensors, because the coefficients follow non-systematic pattern that can be related to the location of the area that afflicted severely by damage. The bottom line is that the correlation data from different conditions for every particular position seems sufficient to produce patterns, which manage to identify the damage. Nevertheless, the data is not successful to generate the same useful pattern to locate the damage.

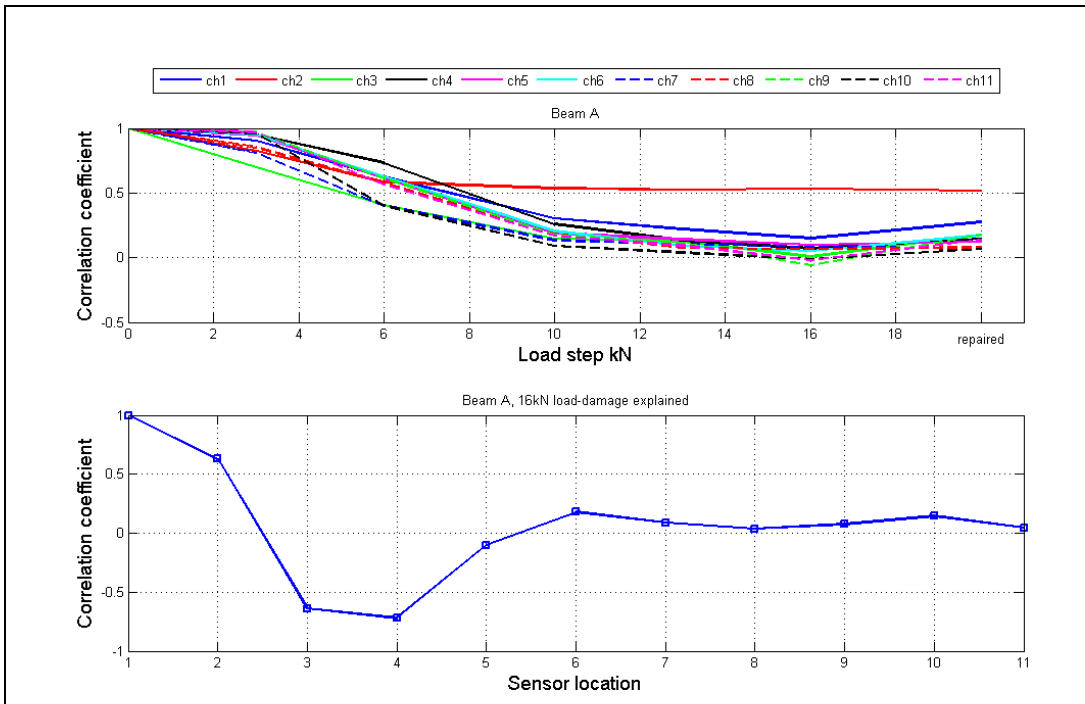


Figure 8.13: Correlation coefficients from beam A for different states and locations.

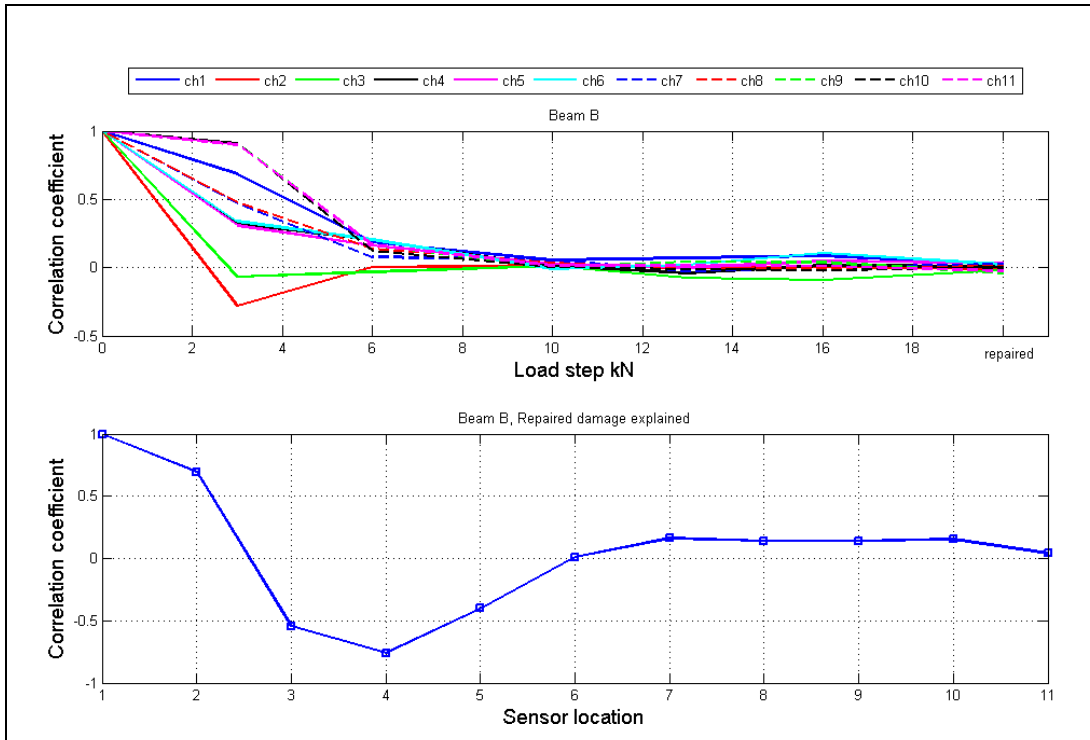


Figure 8.14: Correlation coefficients from beam B for different states and locations.

8.3.6 Application of Principal Component Analysis on Various Data Sets

8.3.6.1 PCA of Statistical Moments

In order to investigate the performance of the PCA explained in theory in section 5.5.1.1, the study will embark on using the first four statistical moments as damage sensitive features in a transformed space explained by PCA. The moment data for (44) time histories from each of the seven structural conditions of beam A were used in the PCA. For each structural condition, the statistical computations provide (44 x 4) dimensional feature-vectors. In the level of the seven status of the beam, the concatenation of the (44) feature-vectors result in a matrix of (7 x 176) dimension. The (7) rows represent (7) different state conditions, whereas (176) columns represent (4) static moments for (44) signals from each condition. The covariance matrix of the feature-vectors was decomposed, and the projections onto the first two PCs then plotted in Figure (8.15). From this presentation, it is noticeable that the features corresponding to the (7) structural conditions representative by the four static moments were indivisible in the two-dimensional projection. The (44) time histories came from (11) measuring positions along the beam did not uniquely and explicitly segregate the records of each particular state condition. Apparently, the statistic moment data of each beam case was not sensitive to the level of damage. Meanwhile, the data was sensitive to the location of the sensor capturing the time histories as can be seen from Figures (8.7-8.9). The illustration was assumed to give same outcome by projecting the first PC onto the third, fourth, fifth, etc., because all the remaining PCs have negligible residual variance as displayed in Figure 8.16(a).

The visualisation of the data failed to separate the data into their original subgroups because the first PC explained 95% of the variance, Figure 8.16(a). In an effort to quantify the damage through the variance in the first PC, the highest variance corresponding to each structural condition for beam A was computed and individually drawn in Figure 8.16(b). Although the intact and moderately damaged cases tended to exhibit higher variance in first PC compared with the severely damaged cases, the deviation in variance was rather insignificant.

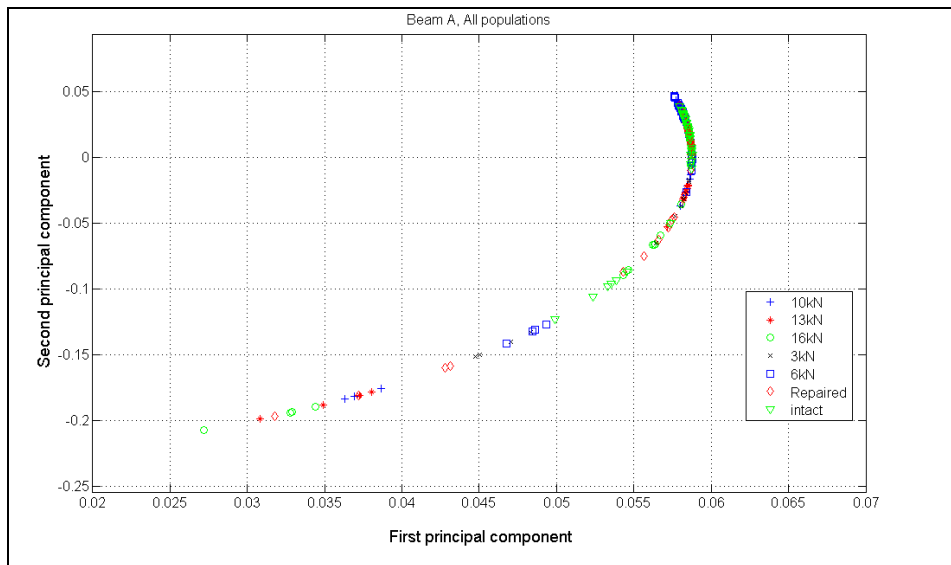


Figure 8.15: Statistical moments of time histories of beam A projected on the first two PCs.

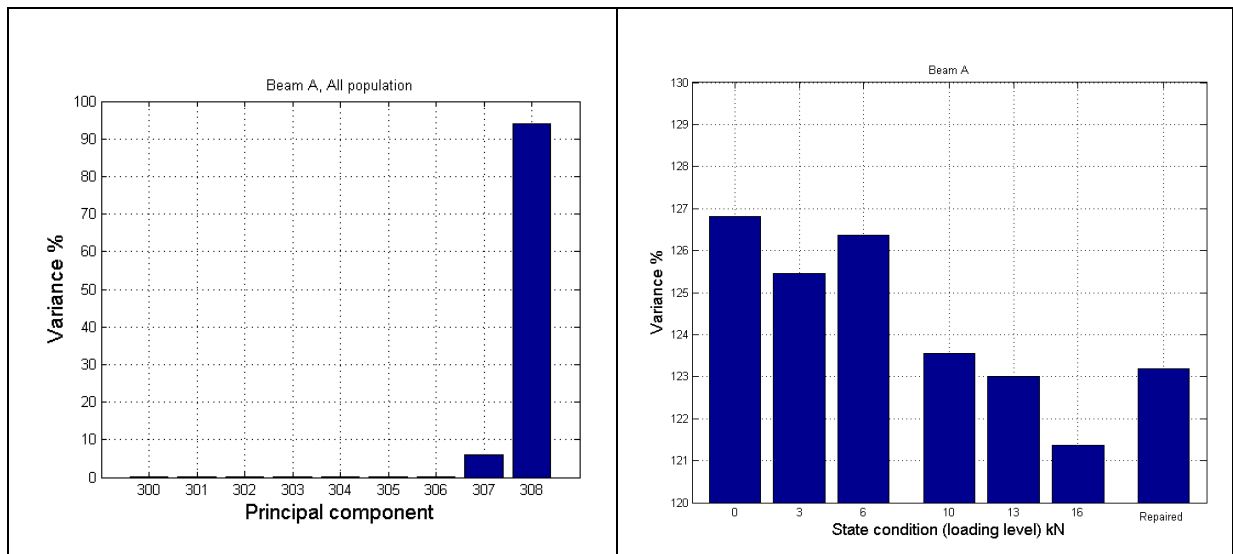


Figure 8.16(a): Percentage variance given by each PC of beam A; (b): Variance values given by the first PC of each state for beam A.

8.3.6.2 Principal Component Analysis on Response Time-histories

Moreover, as an effort to exemplify graphically the performance of PCA on the raw time histories collected at all sensors from different state conditions, PCA was carried out on data samples from beams A and B. The data samples for analysis were mobilised as follow. Firstly, four samples of the raw output time signals were captured at each

sensor position. Secondly, the data acquisition process was repeated for (11) measuring positions along each beam to cover its whole length. For each state condition, this process results into (44) time signals with length of (4096) points. Thirdly, the measurement survey was recurred for the same beam samples for (7) rounds to include all condition events. The (44) feature-vectors from each beam condition were assembled in a unique data matrix of (308 x 4096) dimensional space. Before embarking on using PCA, the time signals were normalised using the mean and standard deviation of each feature vector, as given in Equation 8.4. The corresponding covariance matrix was further obtained and decomposed by doing PCA on (308) features (time signals), as given in Equation 8.11. The first two PCs (308 and 307) for the data from either beam sample (beam A or beam B) account for nearly 37% and 30% of the total variation, respectively. Therefore, a two-dimensional graph with respect to these two PCs gives insufficient approximation to the relative positions of the observations in seven-dimensional space. An illustration of the (308) feature-vectors representing the (7) situations of beams A and B, with respect to the first two PCs is shown in Figure 8.17. The amounts of variance in the original data samples carried by the (20) strongest PCs for beams A and B are also given in Figure 8.18.

The graphical interpretation reveals two striking observations. Firstly, the plots expose a little loose clustering structure in the data for the two case studies. Although it is looser in beam B for the features from the intact and 3kN load cases, the clustering structure is more pronounced in the rest cases (10kN-repaired). The main feature of Figure 8.17(a) is that observations from similar beam condition are mostly close to each other in long cloud, but Figure 8.17(b) reveals random distribution for the features of the intact beam and barely damaged beam. Meantime, a distinct structure for data from severely damaged and repaired situations is recognised. Secondly, as the data sets represent many variables in the main data, it is evidence from the variance percentage of each PC (Figure 8.18) that these variables do not lie close to the two-dimensional plane explained by the first two PCs. Therefore, the two-dimensional (or even q-dimensional) graphical illustration is unable to digest the inherent randomness of the main sets of data. Also, the arbitrary distribution of clusters undermines the effort to use PCA to examine the consistency of a new data set with other sets from normal cases (Sohn et

al., 2001). These conclusions are only defensible because the damage information is available and well-controlled.

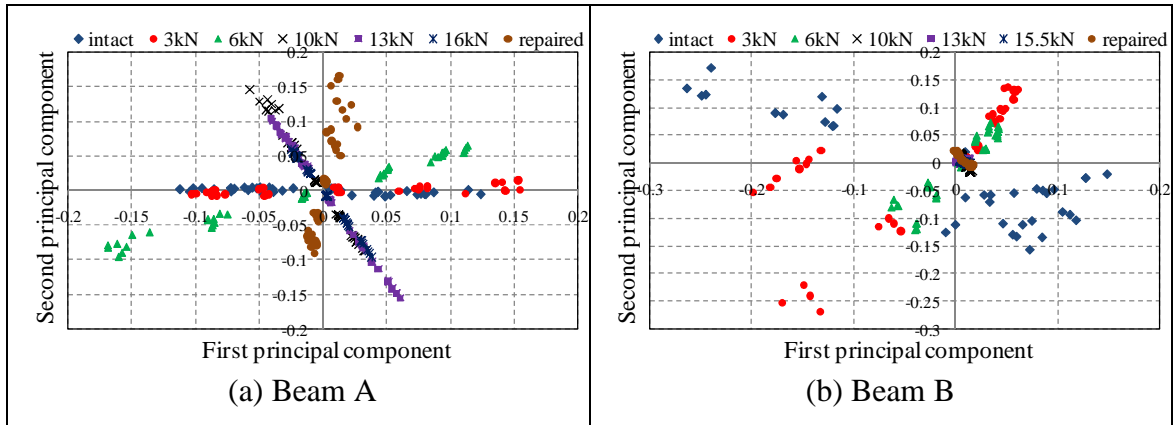


Figure 8.17: Condition discriminant using response time signals with respect to the first two PCs.

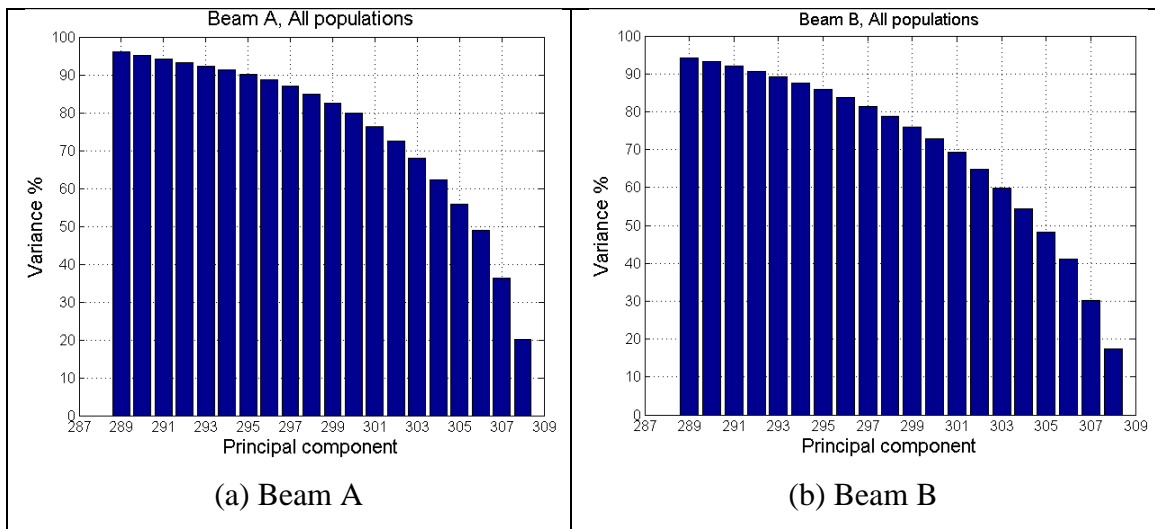


Figure 8.18: Cumulated percentage variance using output time signals.

8.4 Frequency Domain Analysis

Having examined the PCA method on data samples from response time histories and statistical moments of these signals, the separation process of real-beam condition features was rather ambiguous and far from straight interpretation. Therefore, two basic reformations are considered to enhance the performance of the PR scheme that gives more realistic interpretation to the results. First, temporal data as damage-sensitive

feature is dropped and will be replaced by data samples from frequency domain. Second, a new modification on the PR scheme as represented by the PCA tool is postulated.

The following subsections are devoted to investigate the validation of data sets from frequency domain as damage-sensitive features. Specifically, the investigation focuses barely on response spectra as well as FRFs computed from time signals of different state conditions and captured at various locations. Of course, the investigation drops out the extracted modal parameters (resonance frequencies, modal damping ratios and mode shapes) as they were discussed elaborately as damage sensitive parameters in Chapter six of this thesis.

8.4.1 Power Spectra of Response Time Histories

As an essential step in any modal testing analysis, the raw response time signals are transformed into the frequency domain using Fast Fourier Transformation (FFT). Without conducting any normalisation to the time signals, FFT is carried out in order to produce a convenient visualisation to the data in the frequency domain. It is worth mentioning that the sampling parameters selected to digitise the response-acceleration analogue signals are entirely captured the signal in the recording time period ($T=500\text{ms}$). Therefore, this characteristic immunises the necessity for applying any window function to the time signals (Avitabile, 2007). Samples of auto-power response spectra (raw, not averaged) from acceleration time histories of different state conditions and for two different locations of beam A are shown in Figures 8.19 and 8.20. It is obvious from these graphs that the results after 1200Hz are neglected, and only data in the frequency range (0-1200Hz) is presented. Although the Nyquist frequency corresponding to the sampling rate of this study is (4096Hz; $\Delta t = 0.1222\text{ms}$) higher frequencies are impossible to excite using the current toughest hammer tip.

Apart from the resonance deviation developed with progress of damage, it was difficult to deduce any visual variation between spectra of various conditions. Another anticipated difference between spectra collected at different locations from the beam was evidence from these two Figures. The first four resonance frequencies appeared clearly in the spectrum observed at point #1 (end point), but only the odd resonances

appeared when the response was captured at point #6 (mid span). Therefore, the shape of the spectra was quite significant from measuring position to other, even though the spectra belonged to the same testing condition. Additionally, the amplitude distinction diverged between attempts, which accounted for the discrepancy of force magnitude applied per each trial (as explained in subsection 8.3.1).

As a preparation effort for the discriminant analysis using PCA, the feature-vectors matrix was assembled by using the amplitude of response spectra with frequency range 0-1200Hz, which corresponded to (600) samples in frequency resolution ($\Delta f = 2\text{Hz}$), and related to the (11) sensors set on the beams. Response spectra related to the (11) sensor positions were estimated (4) times for each intact, each level of damage as well as repaired conditions in addition to extra spectrum for each state from the averaging process resulting in total of 55-7 feature- vectors each of (600) point length.

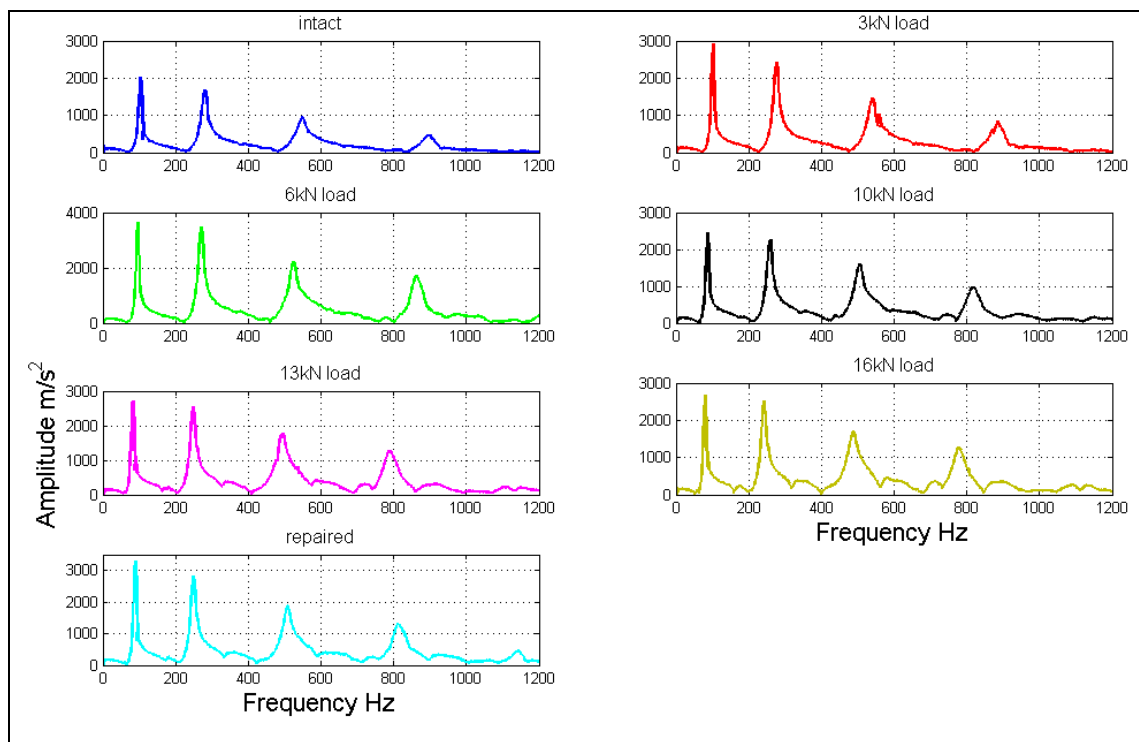


Figure 8.19: The RPS of beam A at position #1 (end point).

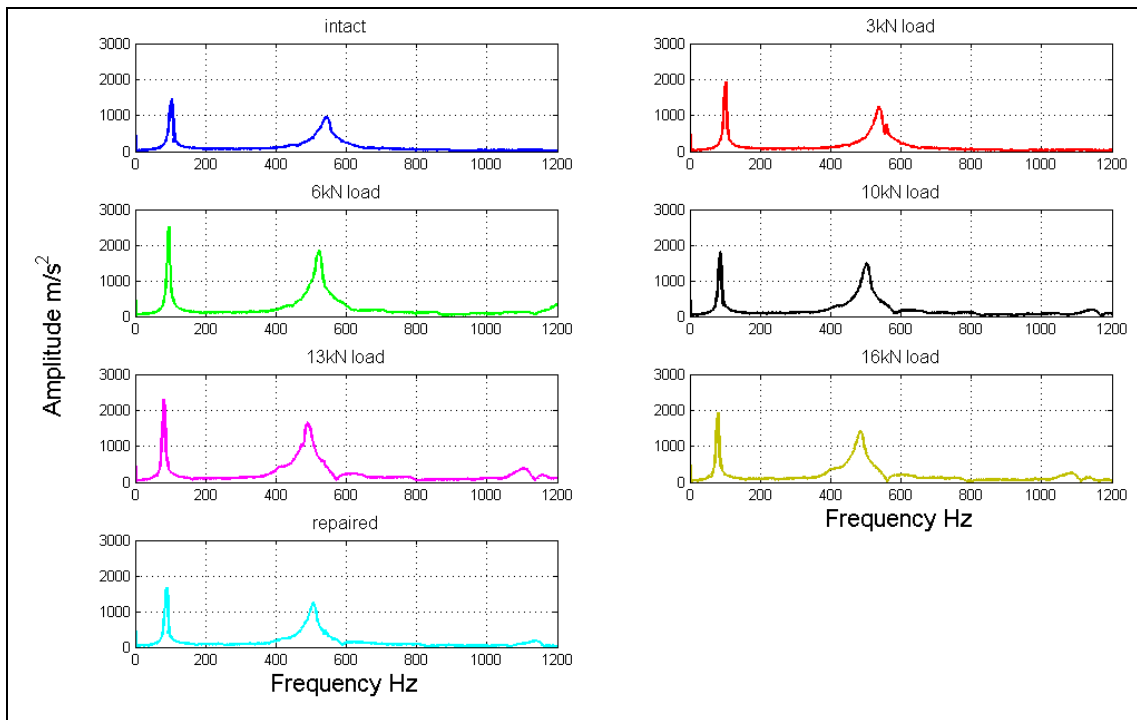


Figure 8.20: The RPS of beam A at position #6 (mid span).

8.4.2 Frequency Response Functions

Once the time data is sampled, the raw time signals of the input force and output accelerations are transformed into the frequency domain using the FFT. The non-averaged auto-power input and output spectra alongside with the cross-power spectrum between the output and input signals are utilised to obtain the important FRF measurements. In fact, the FRFs are carried out to normalise the measured response by the measured input. As a result this normalisation method eliminates the effect of the input from the parameter estimation procedure, wherever the system is linear (Farrar et al., 2001b). Samples of the FRFs obtained at point (#4) from a range of conditions for beam B are given in Figure 8.21.

In the respective of employing FRFs as damage-sensitive features, individual spectra from input and output locations are used to operate the non-averaged populations of FRFs. This procedure is necessary in the context of applying SPR techniques for two major points; to increase the training data sets used to define each condition, and to explore the efficiency of the proposed technique in the presence of data noise and singularities. FRFs related to the (11) sensor positions were estimated (4) times for the

intact, each level of damage as well as repaired conditions resulting in total of (44×7) feature vectors. Relatively similar to the previous response spectra, feature-vectors matrix was populated by using the amplitude of FRFs with frequency components for the range (0-1200Hz), which corresponds to (600) samples in frequency resolution ($\Delta f = 2\text{Hz}$), and related to the (11) sensors set on the beam.

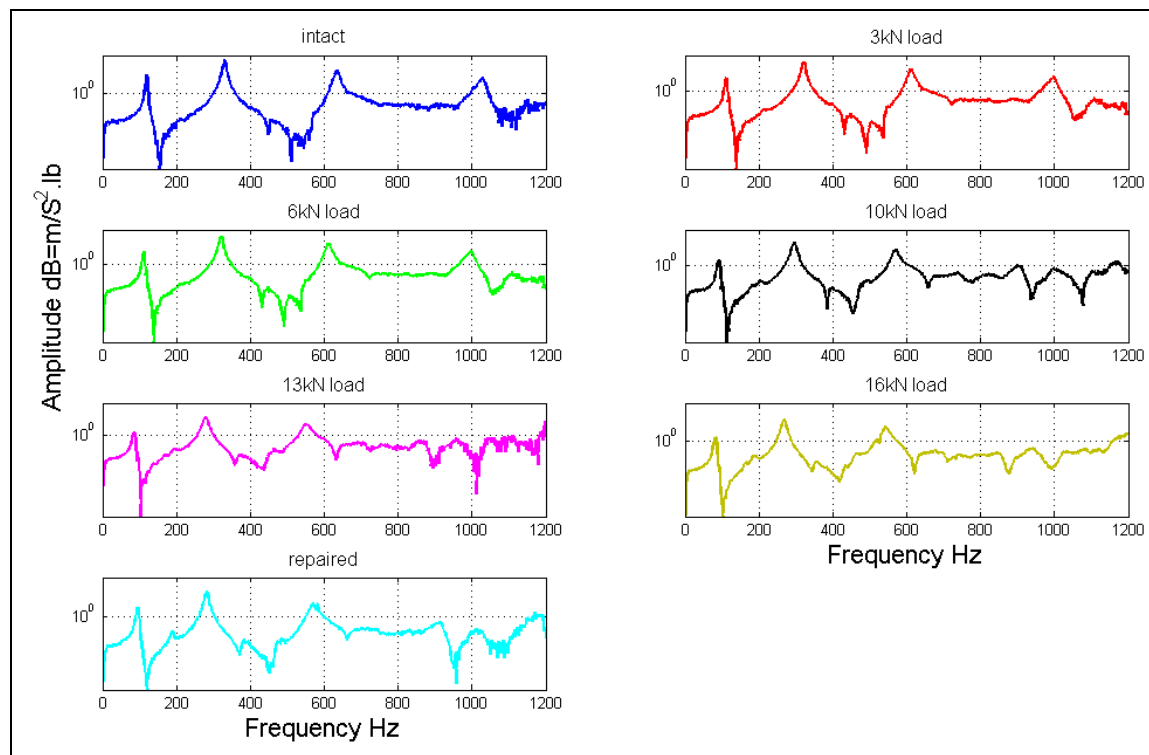


Figure 8.21: The FRFs of beam B at position #4.

8.4.3 Principal Component Analysis on Data Sets from FRFs

With a view to assess the performance of the PCA as damage classification tool, FRF data sets as damage-sensitive features were examined in this subsection. On the one side, FRF as a damage-sensitive feature entails further computational effort compared with the time histories data. On the other side, FRFs explain the relationship between the inputs and the responses; therefore they completely describe the structural dynamic properties (Figueiredo et al., 2009; Maia and Silva, 1997).

The training data sets tested by the PCA were collected for the identification of damage in the five RC beams of this project. Consequently, the sets for the analysis and graphical illustration were aggregated as in the following steps:

- The training-set matrix ($n \times p$) of FRFs was piled from all structural conditions corresponding to the beam case study. For beam A and beam B, the state conditions were divided in (7) groups, intact, five different damage levels and repaired beam. For beam C, however, the state conditions were three, intact and two severely damaged cases. Finally, for beams D and E, the conditions were two, the solid beam and beam with void(s).
- The rows (n) of the training feature matrix represent the frequency data points (600). The columns (p) represent the features related to the beam and their number varies according to the particular beam case study.
- For beams A and B, the number of feature vectors (p) was (44×7) resulting in data from all channels with four repetitions for each sensor. In beam C, the number of the feature vectors was (55×3) with five repetitions for the (11) measurement points for the three cases. Finally, in beams D and E, (p) was (44×2).
- The global training matrix was normalised using Equation 8.4, and the corresponding covariance matrix $[\Sigma]$ was obtained from Equation 5.1.
- The covariance matrix of each beam case study was transformed to the uncorrelated feature space conducted by the SVD, and the first two PCs were plotted, accordingly. Each feature vector in the $[\Sigma]$ arose as a dot in the first two PCs plot.

Figure (8.22) shows the first two PCs of all the five beams analysed for this task. Based on the graphs of this figure, the following concluding remarks can be drawn:

- The most interesting finding is that two clouds of data are visually distinct for almost each of the five beams. This reasonable separation done by the first two PCs features the damage condition of a beam and carried out in an unsupervised mode. In particular, for beam A and likewise beam B, one cloud contains all data from (intact, 3kN and 6kN load steps), but the second cloud contains data points from the further damage, namely 10kN, 13kN, 16kN and repaired states. Furthermore, plot of beam C displays the same two clouds, one for the intact condition and the second for the severely damaged two cases (10kN, 14.5kN

load steps). In Beam D and beam E finally, the data feature of the solid beam is perfectly segregated from the data of the beam with void(s).

- The visual discrimination holds fairly well between data from intact and lightly damaged and data from severely damaged conditions. However, this discriminant analysis does not tend to further dissect every main cloud of data into its original subgroups. There are signs of local congregation of data from closer levels of loading can be recognised when each cloud is scrutinised carefully. Providentially, features of the same type of underlying damage condition arise close to each other, when visualised by the first two PCs.
- The two-dimensional graphical representations display nearly 60% of the total variation in the data based on FRFs (see Table 8.1) compared with approximately 30% when data samples were piled from the raw time histories.
- The significance of this analysis is that is performed in unsupervised learning mode without a need to mention the label of each feature, as well as no necessity to build the feature vectors with specific unique order. The investigation reveals that the bigger the training matrix is, the clearer the separation between data from various features. These findings are profoundly tenable because they are accomplished on FRFs from identified condition source.

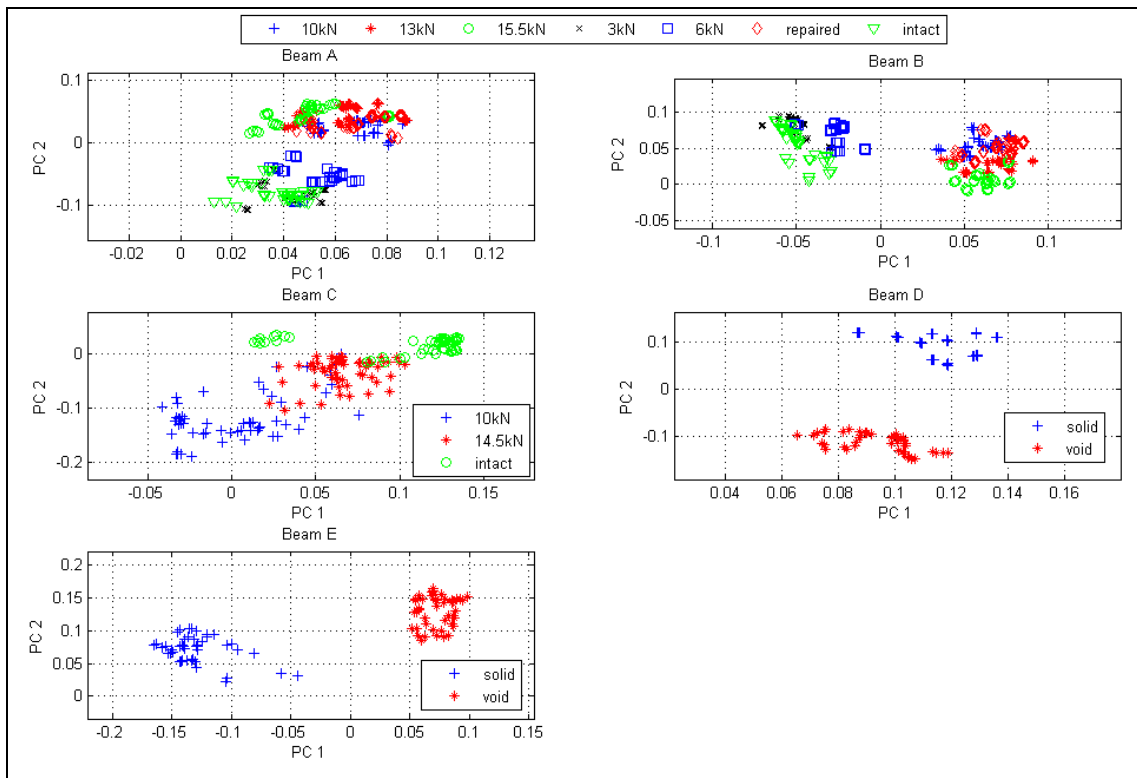


Figure 8.22: First and second PCs based on data sets of FRFs, all five beams.

Table 8.1: Cumulative percentage of total variation carried by the first 10 PCs, based on data sets from FRFs.

| Beam Sample | PC1 | PC2 | PC3 | PC4 | PC5 | PC6 | PC7 | PC8 | PC9 | PC10 |
|-------------|------|------|------|------|------|------|------|------|------|------|
| Beam A | 35.7 | 61.7 | 69.7 | 76.9 | 81.8 | 85.0 | 87.3 | 89.4 | 91.0 | 92.5 |
| Beam B | 36.4 | 54.9 | 67.4 | 74.0 | 78.6 | 82.8 | 85.3 | 87.7 | 89.3 | 90.0 |
| Beam C | 41.7 | 59.1 | 70.0 | 74.5 | 78.1 | 80.9 | 83.1 | 85.3 | 87.2 | 88.7 |
| Beam D | 70.2 | 80.4 | 85.5 | 89.9 | 92.8 | 95.0 | 96.2 | 97.1 | 97.8 | 98.2 |
| Beam E | 37.9 | 64.4 | 78.0 | 82.1 | 85.5 | 88.6 | 90.7 | 92.2 | 93.5 | 94.5 |

8.4.4 Principal Component Analysis on Data Sets from RPS

Quite similar to the investigation carried out in subsection (8.4.3); this subsection is allocated to assess the performance of the PCA as damage classification tool, on data sets from RPS density. By using the response PSD, as damage sensitive features, two

main advantages are satisfied; there is less calculation effort in processing the spectra compared with FRFs, and it is more practical in the real-life structural assessment to use the response measurements due to the ambient excitation, where it is difficult to record the excitations.

The training data sets for this survey are collected in the same manner, which is done on the FRFs survey. The classification study was implemented on data samples from three RC beams of this project (Beams A, B and C). For each event, the training matrix ($n \times p$) of the response spectra corresponding to each beam was concatenated from all conditions related to the beam case study. Figure (8.23) displays the first two PCs of the three beams analysed in this subsection. By removing the effect of the input excitation from the damage-sensitive feature, the classification clouds of the feature data appeared more articulate compared with the clouds of the previous subsection analysis. Visual demonstration of all three graphs showed two subgroups of populations separated reasonably in the direction of the first PC according to the level of damage in that beam. The two-dimensional representations of PCs accounted for 68%, 63% and 67% of the total variation in the data of beams A, B and C, respectively, Table 8.2.

In conclusion, the PCA method when applied at data samples from frequency domain presents a powerful qualitative unsupervised classification means to isolate the features into two main groups based on the level of damage. The more feature vectors for different state conditions are ready and persistent, the sounder the isolation process will be.

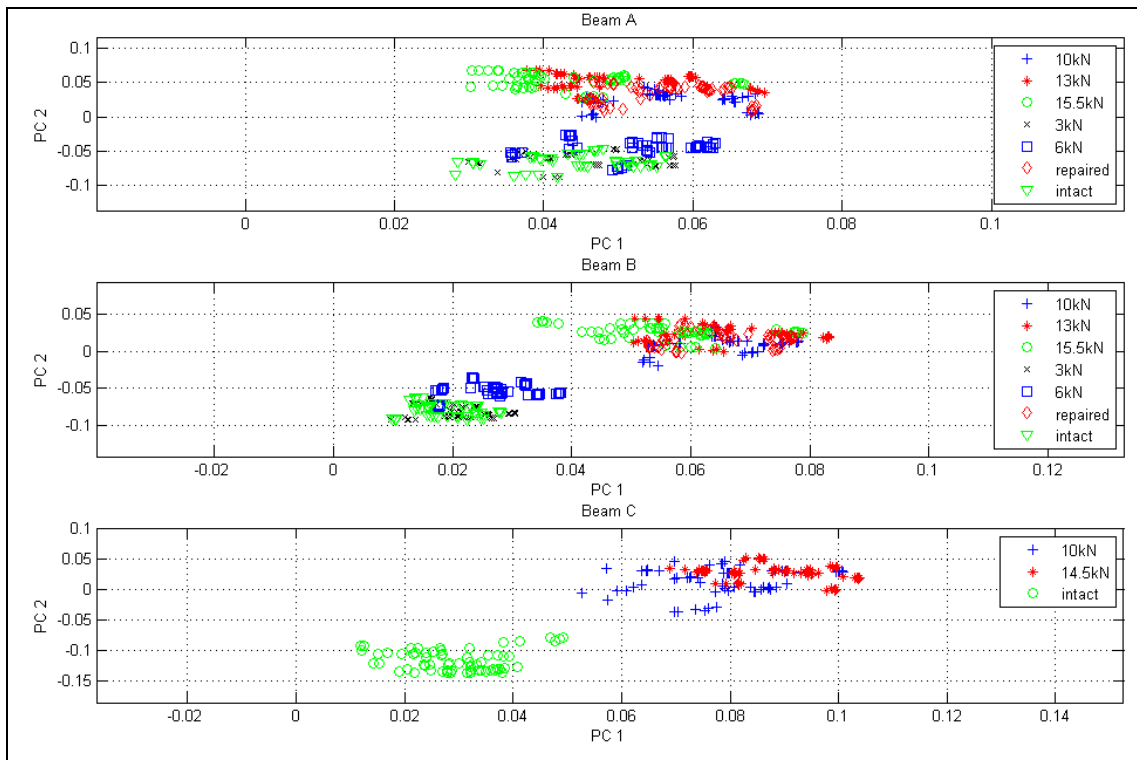


Figure 8.23: First and second PCs based on data sets of RPS, beams A, B and C.

Table 8.2: Cumulative percentage of total variation carried by the first 10 PCs, based on data sets from RPS densities.

| Beam Sample | PC1 | PC2 | PC3 | PC4 | PC5 | PC6 | PC7 | PC8 | PC9 | PC10 |
|-------------|------|------|------|------|------|------|------|------|------|------|
| Beam A | 43.9 | 68.2 | 75.2 | 79.8 | 83.9 | 87.4 | 89.7 | 91.7 | 93.5 | 94.6 |
| Beam B | 39.7 | 62.8 | 72.9 | 77.8 | 82.5 | 86.0 | 88.4 | 90.1 | 91.5 | 92.7 |
| Beam C | 42.4 | 67.4 | 74.4 | 79.8 | 83.8 | 87.1 | 89.5 | 91.4 | 93.2 | 94.5 |

8.5 Karhunen-Loève Transformation

8.5.1 Two-stage PCA-KLT on Data Sets from FRFs

For comparison purpose, same data sets used in PCA (subsections 8.4.3 and 8.4.4) were utilised as well in the proposed classification methodology (explained in details in sections 5.5.1.2 and 5.5.1.3). After the new transformation is carried out, the variance hold by the first 10 PCs from the new transformation scheme is given in Table 8.3. It

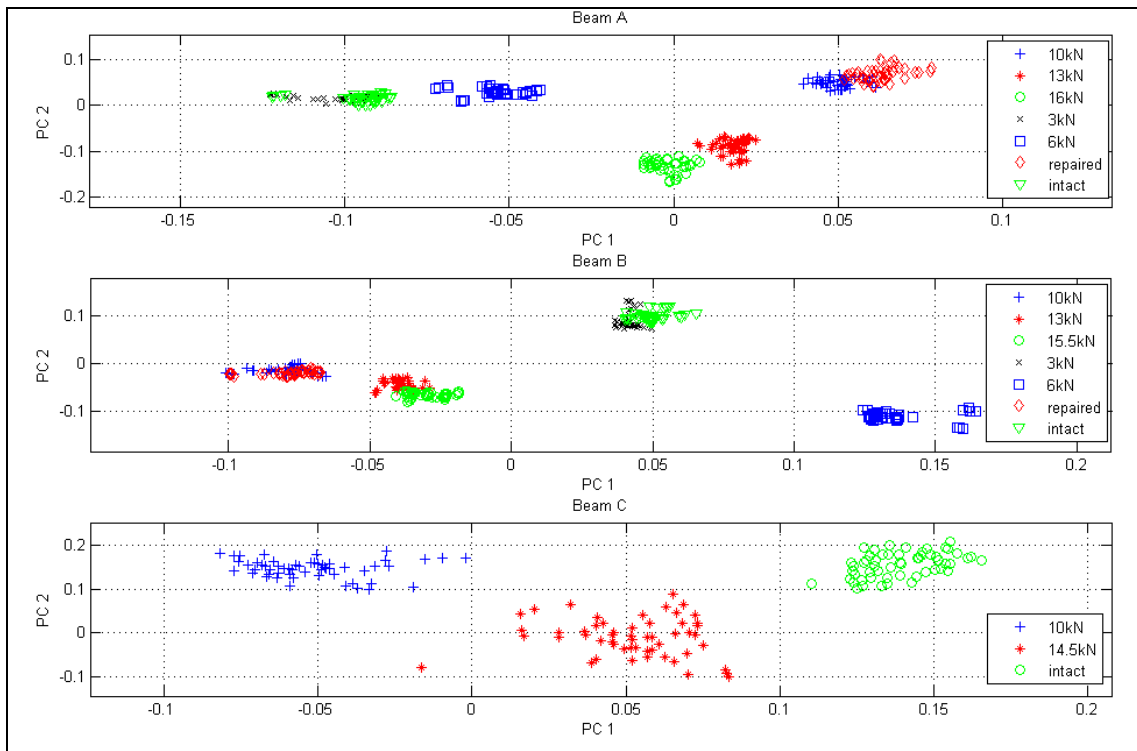


Figure 8.24: First and second PCs of PCA-KLT based on data from FRFs.

8.5.2 Two stage PCA-KLT on Data Sets from Response Power Spectra

In the context of using RPS densities as damage-sensitive feature, Figure 8.25 displays the first two component plots based upon the proposed transformation method, and on data from RPS density. In this context, the first two PCs hold 93%, 78% and 100% of the total variance. This suggests that data from RPS density is more convenient to be represented by first two PCs than data from FRFs, (Table 8.4). The first two components from the new transformed space of RPS as damage-sensitive feature provide better approximation for the data; hence, the visualisation defines the groups objectively. For beams A and B, the graphical illustration recognises four distinctive groups, related to the seven cases, suggesting that data from (intact, 3kN), 6kN, (10kN, repaired) and (13kN, 16kN) are separate four subgroups. Most importantly in the classification context, separation process always situates the data from intact and barely damaged groups away side from data of severely damaged beams. Also, this is the case in beam C, where three groups are clearly isolated in the meantime the data per each group is less dispersive compared with the groups in Figure 8.24.

The bottom line is that RPS densities provide more eloquent and practical damage-sensitive feature compared with their counterpart FRFs. Meanwhile, the proposed transformation methodology outperforms PCA method as a statistical model for both classification and outlier detection.

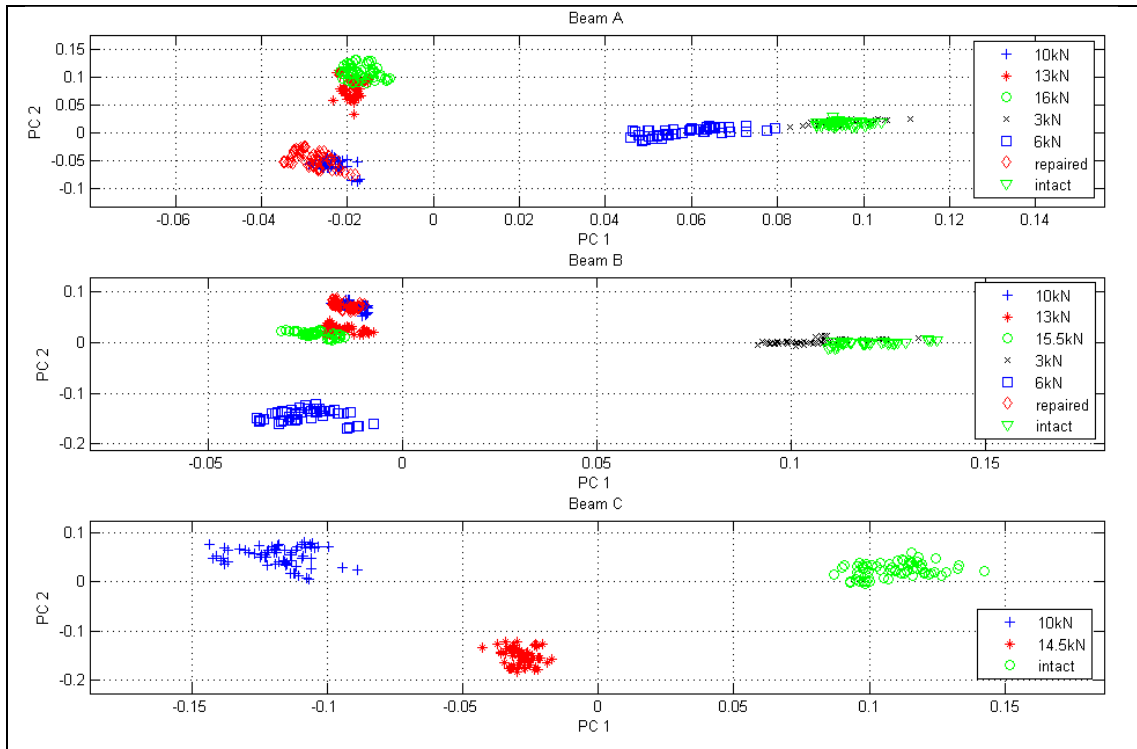


Figure 8.25: First and second PCs of PCA-KLT based on data from RPS.

Table 8.4: Cumulative percentage of total variation carried by the first 10 KL-PCs, based on data sets from RPS.

| Beam Sample | PC1 | PC2 | PC3 | PC4 | PC5 | PC6 | PC7 | PC8 | PC9 | PC10 |
|-------------|------|------|------|------|------|-----|-----|-----|-----|------|
| Beam A | 76.7 | 92.6 | 97.8 | 99.6 | 100 | 100 | 100 | 100 | 100 | 100 |
| Beam B | 40.4 | 77.6 | 94.4 | 97.7 | 98.9 | 100 | 100 | 100 | 100 | 100 |
| Beam C | 75.1 | 100 | 100 | 100 | 100 | 100 | 100 | 100 | 100 | 100 |

8.6 Performance of Novelty Detection Approach on Data from FRFs

The statistical classification applied and verified successfully in section 8.5 was simply a qualitative means of classification of features from various structural states. Therefore,

there is a need to set threshold values for the basic baseline measurements that can be evaluated if statistically significant changes have occurred in a new set of measurements. Novelty detection approaches are typically exploited for this purpose. The novelty detection is the lowest level of damage characterisation, and simply examines whether or not a new data set is quantitatively consistent with data related to the previously observed normal states (Sohn et al., 2001). The main idea in this subject is to discern quantitatively between undamaged and damaged structures.

One of the direct and easiest ways to accomplish that is by comparing the amount of the difference between discrete spectral distances from several FRFs. The symmetrised adaptation of the Itakura-Saito discrete spectral distance designated as COSH distance presents an inclusive estimate of the difference between two discrete spectral envelopes (Trendafilova, 2001). The discrete adaptation of the COSH spectral distance is given by:

$$COSH(H, \bar{H}) = \frac{1}{2n} \sum_{i=1}^n \frac{H(\omega_i)}{\bar{H}(\omega_i)} - \log \frac{H(\omega_i)}{\bar{H}(\omega_i)} + \frac{\bar{H}(\omega_i)}{H(\omega_i)} - \log \frac{\bar{H}(\omega_i)}{H(\omega_i)} - 2 \quad (8.10)$$

Where:

n is the frequency points

$H(\omega)$ is the transfer function from specific record of the baseline state condition

$\bar{H}(\omega)$ is the identical transfer function for the same record, but from the suspected new condition

Nevertheless, Haritos and Owen (2004) consider $\bar{H}(\omega)$ as the mean of observations from both undamaged and damaged situations.

Ideally, for two spectra from same DOF of the same condition, COSH distance is very close to zero. In contrast, the higher the damage is in the structure, the bigger the COSH measure will be; consequently, COSH distance will diverge from zero.

The summation of the COSH distances over all the DOFs (C) along the whole structure offers a global measure for the differences between spectra from the baseline condition and suspicious case. This measure can be expressed as (Trendafilova, 2001):

$$\bar{C}(H, \bar{H}) = \frac{\sum_{j=1}^m C(H, \bar{H})}{m} \quad (8.11)$$

Where:

m is the total number of DOFs, also with recorded averages for each particular FRF

Figure 8.26 shows the results of COSH distance for beams A and B. In these two cases, the distances were obtained by comparing (44) spectral envelopes for each underlying damage case with (44) spectra from the intact condition, as a reference data. The (44) spectra were collected from 11 positions over the beam with (4) repetitions for each specific position. The number of data points (n) considered in estimating the error between spectra from two different cases is (500) points, cover frequency range of a transfer function of (1000Hz). The comparison reveals increases in the distance with the progress of deterioration. However, it is factual that the increase is not uniform for all records of DOFs for a particular status because this depends upon the length of the envelope under consideration.

Most importantly, the damage level is reasonably quantified through the mean of COSH distance over the DOFs, Equation 8.11. The results of mean COSH distance from beams A and B are shown in Figure 8.27. The higher the damage is introduced, the greater is the mean of COSH distance. The degree of damage is consistently arranged according to its significance. Also, the impact of the strengthening work added to the beams was obviously distinguished by this quantity. It is noticeable that the increase in the summation of all spectral distances with respect to the progressive damage. This suggests the practical use of this quantity to trigger the concern on unusual case, when the value crosses the threshold set for normal condition.

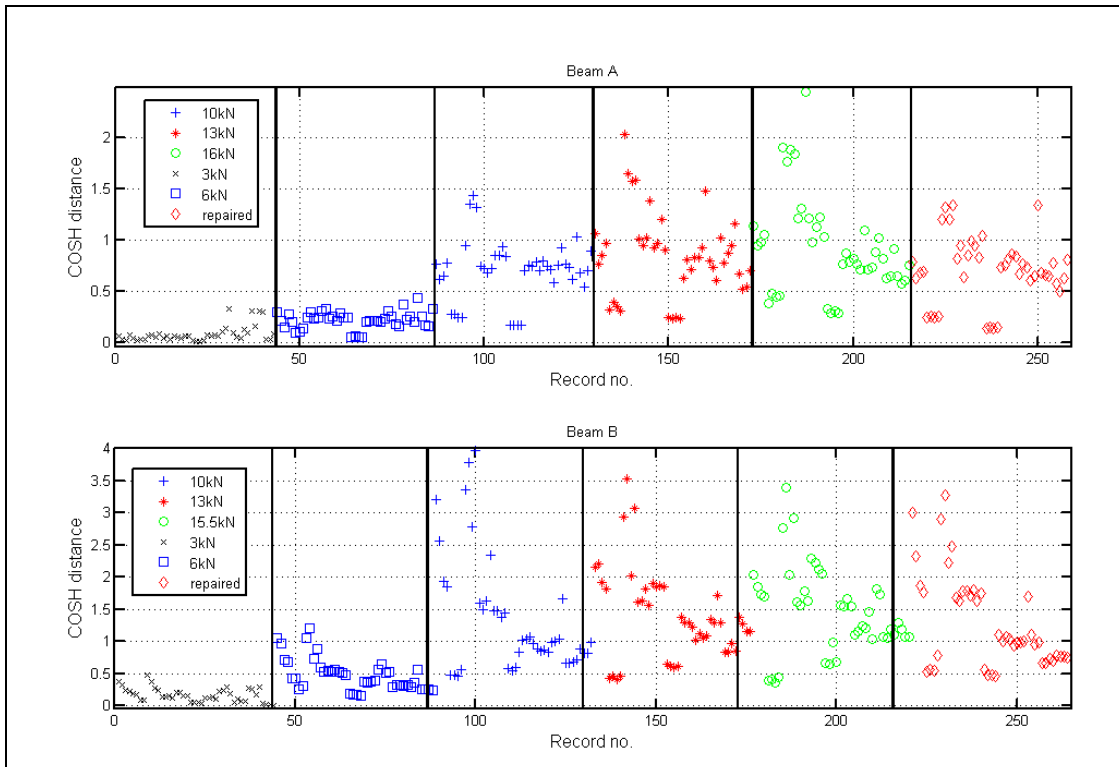


Figure 8.26: Variation of COSH distance with record number.

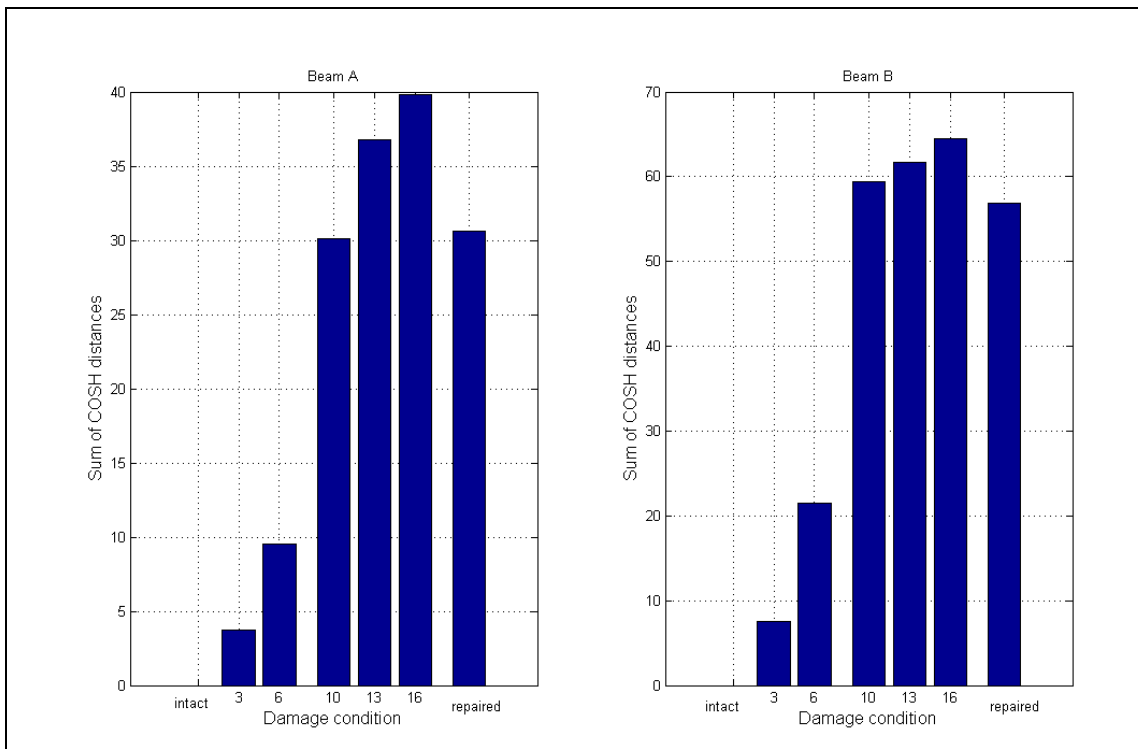


Figure 8.27: Summation of COSH distance over all DOFs with respect to the states.

8.7 Discussion and Summary

This Chapter is dedicated to identify the damage in the five RC beams by using only time domain and frequency domain vibration data. Meantime, only Statistical Pattern Recognition (SPR) models have been tested through the course of this Chapter.

The Chapter begins with the validity of using measurements from time or frequency domain as damage-sensitive features. Although locating and quantifying damage is vital in predicting the remaining life-time of a structure, these steps must be preceded by a complete description for the structural changes. Classification step has been added to the structure of damage identification paradigm in order to give information for the type of damage. This step is necessary for higher levels of identification using pattern recognition, where examples of data related to each structural condition class should be made (Worden and Dulieu-Barton, 2004). An authentic classification routine will offer a qualitative means of grouping data sets come from different types and features of structural changes.

In the context of damage sensitive features, the raw time histories, statistical moments (mean, standard deviation, skewness and kurtosis), FRFs and RPS were tested in this Chapter. In the meantime, PDFs, normal probability plots, PCA method, supervised KLT method, correlation coefficients and spectral distance measure COSH were applied at the previous damage features as suggested statistical models.

In the current investigation, the statistic moments of the raw time histories are proved more sensitive to the location of the sensor rather than to the level damage of the structure. In addition, PDFs for time signals from all state conditions of beam A display incompatible behaviour for time histories collected from different trials at same or different positions. That is, PDFs do not provide sound discrimination means between signals from various structural conditions. Furthermore, the abnormality in distribution of the time histories is seen by the normal probability plots for both normal and damaged cases. The non-normality seems more significant in the damaged cases

compared with the intact condition. The level of damage size is not discriminated conclusively by the normal probability plots.

Results of correlation coefficient data of time histories from different conditions for every particular position are found sufficient to produce patterns, which manage to identify the damage, but the data is not enough to generate the same useful pattern to locate the damage.

The PCA method when applied to frequency domain data from the five RC beams succeeds to separate qualitatively feature vectors from various damage levels into only two main groups. In general, the graphical representation of the first two PCs tends to distinguish between undamaged structural states and damaged states without further dissection for the subordinate data included in each main group. Therefore, PCA indicates the incapacity to provide more than two groups. Conversely, the proposed PCA-KLT methodology performs better than PCA method as a classification model. The first couple of PCs account higher percentage of the total variation, and no significant loss in the information is experienced. As a result, the visualisation of the first two components discriminates qualitatively between the subgroups from different conditions. The method is tested successfully on experimental measurements of FRFs and RPS from five RC beams. The results of classification model after using RPS as damage vectors provide more distinctive visualisation compared with their comparable FRFs. This finding should be of practical interest considered the complexity of input forces measurement caused by ambient excitation.

In the outlier detection context, COSH distance and results of the mean COSH distance are proved effective in detecting the damage quantifiably, when a threshold value set to the normal condition is crossed by presumably damaged condition. The grade of damage is coherently ordered by the mean of COSH measurements according to its significance.

Finally, Table 8.5 summarises the results obtained when various statistical damage diagnosis systems are applied to data sets corresponding to the damage state conditions of this work.

Table 8.5: Summary of statistical-based identification methods tested on measurement from the five beams

| Method | Input data sets | Detect damage | Classify damage | Locate damage | Quantify damage |
|------------------------------|---------------------|---------------|-----------------|---------------|-----------------|
| Statistical moments | Raw time signals | No | No | No | No |
| PDF | Raw time signals | Yes* | No | No | No |
| Normal probability plots | Raw time signals | Yes* | No | No | No |
| PCA | Statistical moments | No | No | No | No |
| PCA | Raw time signals | No | No | No | No |
| PCA (variance of each state) | Raw time signals | Yes | No | No | No |
| PCA | FRFs | Yes | Yes** | No | No |
| PCA | RPS | Yes | Yes** | No | No |
| PCA-KLT | FRFs | Yes | Yes | No | No |
| PCA-KLT | RPS | Yes | Yes | No | No |
| COSH distance | FRFs | Yes | No | No | No |

Yes* : inconsistent detection of time signals from various damage states;

Yes** : classification is less detailed

9. Conclusions and Recommendations for Future Research

9.1 Conclusions

1. A number of systematic tests of Experimental Modal Analysis (EMA) are implemented on five laboratory-scale Reinforced Concrete (RC) beams. The tests are conducted using impact hammer as an excitation source. The five RC beams are modelled with different damage status, repaired and tested under freely supported condition. The damage is simulated as increasing levels of flexural cracks and purpose-made concealed voids. The testing programme provides successfully modal parameters that are well-correlated with the analytical results. Between the two measurement alternatives (roving hammer and roving accelerometer), the latter procedure gives more consistent results.
2. Modal parameters estimation and their use to identify the damage are shown time consuming, computationally expensive and require considerable expertise. Nevertheless, they are effective for locating and quantifying the damage (level 2 and level 3 of the damage identification problem). Quantitative results are only obtained and proved sensible using combination of resonant frequencies and mode shapes in the Direct Stiffness Calculation (DSC) method.
3. The measured resonant frequencies are found sensitive to the damage in its early stage. For 3kN load state condition (when the beam theoretically is still in the uncracked state), the maximum observed change in first natural frequency is about 2%. The measured frequencies of the first mode decreased significantly responding to the increasing damage, suggesting that damage location affected remarkably the high stress zone of the first mode. However, the variation of frequency became less significant for higher modes. The largest detected change in resonance frequency of a RC beam imminent to collapse is approximately 30% compared to the intact condition. This change is associated with maximum reduction in flexural stiffness of approximately 52%.

4. The effect of strength improvement carried out using single external CFRP layer is detected by the natural frequencies and mode shapes. The maximum noted change in the resonant frequency when the RC beam strengthened is 20% compared to the intact beam, while the change in the resonant frequency is 30% for the beam imminent to failure. The accumulated decrease in flexural stiffness of the repaired beam is about 30% and 48% for beams A and B, respectively. The mid span bending stiffness of the repaired beam increased by 40% and 17% for beams A and B, respectively compared to the severely damaged beam. Sensible coherent between results of modal frequencies, modal shapes and modal curvatures with each damage state condition is noticed.
5. The direct comparison between mode shapes shows better understanding about the location of anomalies. Pronounced differences are obtained by comparing the amplitude changes in mode shapes of the beam prior to and after damage and after rehabilitation works are introduced. Damage location task (Level 2) can be acknowledged only if sufficient number of measurement points is deployed in relation with the size of the tested structure.
6. By considering the practical limitations facing mode shape measurements, curvatures tend to display spurious noisy features. By this means, it is inevitable to use interpolation procedures in conjunction with fitting polynomials so as to produce consistent and smooth curvatures. Although processing the mode shapes and their curvatures of a system sounds lengthy and tedious routine, it is supposed to give a comprehensive knowledge on the condition.
7. Damping measurements collected before and after damage indicate that important increase in damping is quite common. Imperative changes in damping ratios with the progress of structural changes are found. The damping values often increased with the escalating cracking distribution. However, the rate of change in damping with the progressive damage is non-uniform for the three samples tested under incremental loads (beams A, B and C). Damping values deviated satisfactorily between different damage steps, but they did not constitute a sound criterion for all

test samples. This observation may be accounted to the model used to extract the damping ratios by which linear models were used to fit non-linear FRF measurements. When the defect is presented in term of concentrated voids (beam E), the change in modal ratio is more explicable. Of all modal parameters, modal damping is used only to detect damage and proved to be the least reliable as damage detection parameter.

8. Different Statistical Pattern Recognition (SPR) models are applied to temporal and spectral data from the five RC beams. Results of the correlation coefficients of the time histories from different damage conditions are found successful in producing pattern for the severity of damage. Data obtained from all 11 sensor locations gives consistent interpretation to the level of damage. Nonetheless, the data is proved unsuccessful in providing useful pattern for location of damage.
9. The principal component analysis (PCA) method succeeds to separate feature vectors qualitatively into two major groups when applied to frequency domain data from the five RC beams. The graphical representation of the first two components tends to separate the undamaged condition data (intact, slightly damaged) from damaged (moderately damaged, severely damaged and repaired) conditions without further discrimination between the subgroups.
10. The most important contribution of this research is the established method for a reliable classification, which is vital step in higher levels of the structural identification. The proposed PCA-KLT methodology outperforms PCA method as an advanced statistical classification model. The first two principal components from PCA-KLT model account for higher percentage of the total variance of data sets compared with the PCA method alone. Therefore, the visualisation of the first two components discriminates qualitatively between the subgroups of each major state condition group. The same data that classified into two major groups by using PCA method is further dissected into five distinctive subgroups by using the suggested PCA-KLT method.

11. The proposed PCA-KLT is tested efficiently on experimental data of frequency domain from FRFs and RPS densities for all the five beams. The method is very quick, computationally simple and no a priori information about data sets is necessary. The verification of the success of this classification model is substantially tenable because the observed clusters come from well-controlled and known state conditions. The results of classification model using RPS as damage-sensitive features provided more expressive visualisation compared with their counterpart FRFs. This success is of practical benefit considering the difficulty of measuring the forces caused by ambient excitation. However, neither the PCA method nor its suggested rival (PCA-KTL) is likely to work satisfactorily with feature-sensitive samples from time domain.

12. The work investigates several physical properties found critical to the correction process of the preliminary analytical model. A comprehensive comparison between predicted and measured data is presented using resonances, mode shapes and FRF measurements. In the context of the effect of shear deformation, the variation in resonances when the shear effect included is as big as 9% for the fourth mode, but it is less than 1% for the first mode. Using the dynamic modulus of elasticity is also found critical to predict closer modal frequencies compared with static modulus. This parameter is significant for the beams of high compressive strength and can affect almost equally all modes of vibration. The resonances differed by up to approximately 8.5% when the two different moduli are investigated. Finally, the effect of proportion damping is introduced as a constant ratio of the stiffness matrix. Damping effect on the analytical model manifested as lower and decaying amplitudes; and less sharp and wide peaks in the vicinity of the resonances and anti-resonances.

9.2 Recommendations for Future Research

- The classifier of this research is found decisive of identifying the structural changes in all cases and of labelling individual classes associated to different structural states. However, due to the limited resources existing in this work, only five RC beams were modelled with some practical damage scenarios. In order to increase

confidence in the drawn conclusions, the programme and expertise of this research can be utilised and applied to full-scale structures that represent real-life case studies.

- The damage of the beams in this study was presented as different flexural cracking levels and concentrated purpose-made voids that represent common defects in concrete members. The robustness of the classifier can further be tested on more recurrent defects in large-scale structures. For instance, problems in bridges, such as support settlement, support losing, corrosion and boundary support changes are additional practical defects to be investigated. Also, the programme can be extended to learn the influence of different strengthening, retrofitting and bracing works.
- In damage identification discipline, a fundamental attribute is the technique should be able to detect the onset of damage and distinguish it from a change in the operational or environmental conditions. It is recommended that more research should be undertaken to enable the suggested method to deal with structures which alter their normal operational conditions over time. The application of state conditions in concrete structures may be extended to cover aspects such as variations of temperature and changing in position and magnitude of additional moving masses.
- In SHM, the autoregressive (AR) family models are used to fit the time histories so as to extract damage-sensitive features based on two approaches: using the AR parameters; and using the residual errors. It is recommended to examine the proposed method on the damage-sensitive features from AR analysis. Nair et al. (2006) suggested a new damage-sensitive feature to locate the damage in the ASCE four-storey frame benchmark model. Additionally, Chung et al. (2008) presented an AR analysis algorithm on using vibration-based data for damage detection, localisation and quantification. A positive employment of these AR damage-sensitive features with the current classifier will be valid to incorporate the classifier along with several prominent algorithms in order to create a multifold statistical-based damage identification algorithm.

- The linear analytical model presented in this thesis on the intact beams can be developed in nonlinear mode in order to apply to progressively cracked beams. The experimental data collected through this research can be used to predict RC beam with multiple cracks to use for damage diagnosis and prognosis. The cracks can be simulated by a model that accounts for crack formation, propagation and closure. The beam model can be investigated under impact excitations, for various damage levels. The changes in resonant frequencies and mode shapes with increasing loads can be correlated with the measurements of this study.

Appendix A: Stiffness and Mass Matrices of the Beam Element

In this appendix, the stiffness and mass matrices for the beam element used in this thesis is briefly presented.

In the beam analysis, the main internal forces are bending moments and shear forces. For this reason, the displacement in beams subjected to bending moment and shear force (Δ) can be calculated, in most cases, by the virtual work given as (Ghali et al., 2009):

$$\Delta = \int \frac{Mm}{EI} dx + \int \frac{Vv}{GA_r} dx \quad (\text{A.1})$$

Where:

- M is the external bending moment at the section
- V is the external shear force at the section
- m is the bending moment at the section due to a virtual unit load
- v is the shear force at the section due to a virtual unit load
- E is the modulus of elasticity
- I is the second moment of the cross-sectional area
- G is the shear modulus of elasticity
- A_r is the effective (reduced) shear area

In practice, the cross-section of a slender beam often makes shear force contribution to deflection small and can be neglected. However, this is not necessarily the case in vibration analysis. The vibration parameters are found to be highly influenced by the effect of shear deformation, as validated in the current study. Therefore, the effect of shear deformation is considered in the analytical modal models.

The stiffness matrix of a beam element with shear deformation $[K]_e$ can be written as (Ghali et al., 2009):

$$[K]_e = \begin{bmatrix} \frac{12EI}{(1+\alpha)L^3} & \frac{6EI}{(1+\alpha)L^2} & -\frac{12EI}{(1+\alpha)L^3} & \frac{6EI}{(1+\alpha)L^2} \\ & \frac{(4+\alpha)EI}{(1+\alpha)L} & \frac{6EI}{(1+\alpha)L^2} & \frac{(2-\alpha)EI}{(1+\alpha)L} \\ & & \frac{12EI}{(1+\alpha)L^3} & \frac{6EI}{(1+\alpha)L^2} \\ & \text{Symmetrical} & & \frac{(4+\alpha)EI}{(1+\alpha)L} \end{bmatrix} \quad (A.2)$$

Where:

$$\alpha = \frac{12EI}{L^2GA_r}$$

L is the beam element length

For a rectangular section, the effective shear area can be taken as $A_r = A/1.2$. For beams where the effect of shear deformation is not to be accounted, the coefficient (α) should be set to zero. Shear deflection effect is often significant in the lateral deflection of short beams. The shear effect decreases as the slenderness ratio reduces.

Using the shape functions which satisfy the Timoshenko beam equation for transverse displacements and applying the principle of virtual work for an elastic system, the consistent mass matrix for a beam element $[M]_e$ with the effect of shear strains can be written as (Przemieniecki, 1985):

$$\begin{aligned}
 [M]_e &= \frac{mL}{840} \begin{bmatrix} 312 + 588\alpha + 280\alpha^2 & (44 + 77\alpha + 35\alpha^2)L & 108 + 252\alpha + 175\alpha^2 & -(26 + 63\alpha + 35\alpha^2)L \\ & (8 + 14\alpha + 7\alpha^2)L^2 & (26 + 63\alpha + 35\alpha^2)L & -(6 + 14\alpha + 7\alpha^2)L^2 \\ & & 312 + 588\alpha + 280\alpha^2 & -(44 + 77\alpha + 35\alpha^2)L \\ & & & (8 + 14\alpha + 7\alpha^2)L^2 \end{bmatrix} \\
 &+ mL \left(\frac{r}{L}\right)^2 \begin{bmatrix} \frac{6}{5} & & & \\ & \left(\frac{1}{10} + \frac{1}{2}\alpha\right)L & & \\ & \left(\frac{12}{5} + \frac{1}{6}\alpha + \frac{1}{3}\alpha^2\right)L^2 & & \\ & & -\frac{6}{5} & \left(\frac{1}{10} + \frac{1}{2}\alpha\right)L \\ & & \left(-\frac{1}{10} + \frac{1}{2}\alpha\right)L & \left(-\frac{1}{30} + \frac{1}{6}\alpha + \frac{1}{6}\alpha^2\right)L^2 \\ & & & \frac{6}{5} & \left(-\frac{1}{10} + \frac{1}{2}\alpha\right)L \\ & & & & \left(\frac{12}{5} + \frac{1}{6}\alpha + \frac{1}{3}\alpha^2\right)L^2 \end{bmatrix} \quad (A.3)
 \end{aligned}$$

Where:

m is the mass per unit length of the beam element

r is the radius of gyration of the cross section

Appendix B: Sampling and Quantisation of Continuous Time Signals

In fact, one of the fundamental steps in signal processing analysis is to convert the original analogue signals into digital signals. In this step, an analogue signal is converted at equal time steps (Δt) over a specific time period (T). The resulting series of discrete points are used to objectively replace the original continuous time signal, as shown in Figure B.1. The original signal might be poorly converted into digital signal if the sample rate is too slow. Conversely, an adequate digital representation can be achieved when the sample rate is sufficiently fast, Figure B.1. In general, continuous signals must be sampled at a rate of at least twice as fast as the highest frequency to rationally describe the time data. However, sampling should be of 10 to 20 times the highest frequency when it is intended to describe the time characteristics of a structure (Avitabile, 2007).

Sampling rate of an analogue-digital convertor (ADC) is specified as maximum as that is possible. Each sample point is spaced Δt seconds apart, which must be sufficient so that the entire event is captured. The maximum observable frequency is inversely proportional to the time step (Δt) chosen. In order to extract valid frequency information, digitisation of the analogue signal must occur at a certain rate. Shannon's sampling theorem states that the sampling rate must be at least twice the desired frequency to be measured, as given below (Maia and Silve, 1997):

$$f_s = 2 f_{max} \quad (B.1)$$

Where:

f_{max} is the Nyquist frequency (working frequency)

f_s is the sampling or digitising frequency

In the meantime, for a time record of T seconds, the resolution of lines for the observed frequency spectrum (Δf) can be obtained as:

$$\Delta f = \frac{1}{T} \quad (B.2)$$

For the above-mentioned two critical properties, the sampling parameters can be summarised as:

$$f_{max} = \frac{1}{2 \Delta t}$$

$$T = N \Delta t \quad (B.3)$$

Where:

N is the number of discrete sampling values, which is fixed and commonly taken as a power of 2 to be 512, 1024, 2048, 4096, etc.

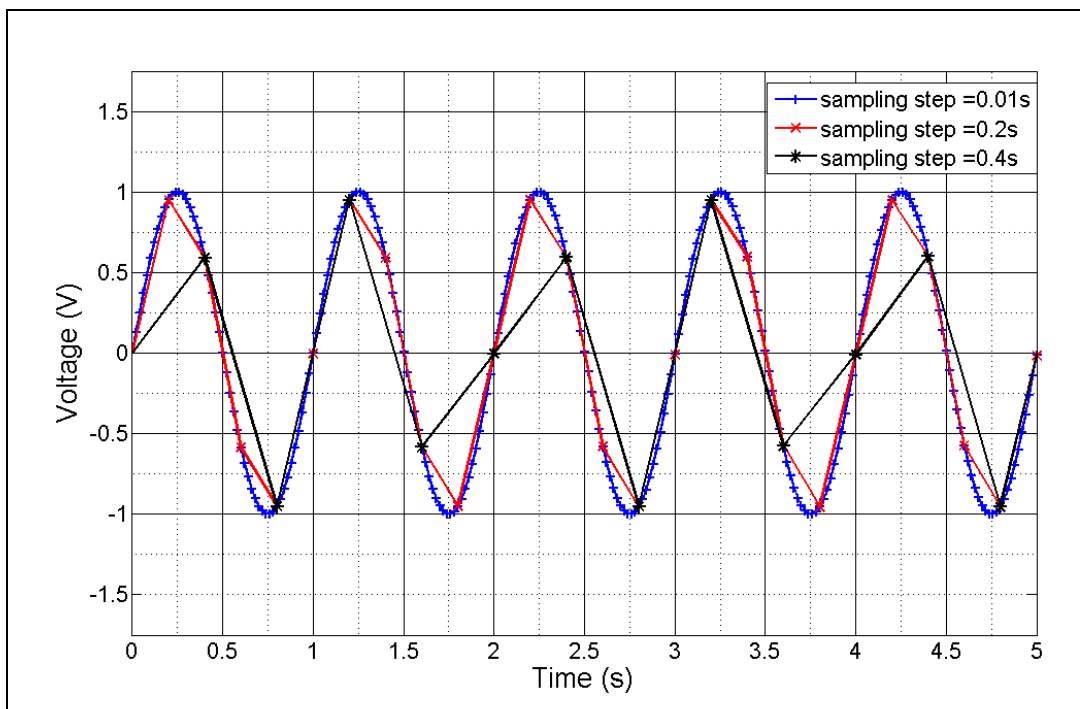


Figure B.1: Sampling of analogue signal using various sampling rates.

Aside from the horizontal sampling, the process of describing the amplitude of a digital signal is referred to as quantisation. In this process, the sampled signal is rounded up to the nearest discrete output value. In order to digitise the amplitude of the signal precisely, the higher bits the ADC holds, the better a signal is represented. Figure B.2 exemplifies two exaggerated ADC with different quantisation levels (n) designated as number of bits (number of bits in a converter has 2^n count levels).

Some of the major concerns lie in the sampling and quantisation errors that could potentially move slowly into the digitised approximation. Whereas sampling rate controls the resolution in the time and frequency representation, quantisation is related with the accuracy of vertical resolution of the captured signal. Nevertheless, both sampling and quantisation can cause some errors in the measured data but are not nearly as significant as the worst of all the signal processing errors (Avitabile, 2001).

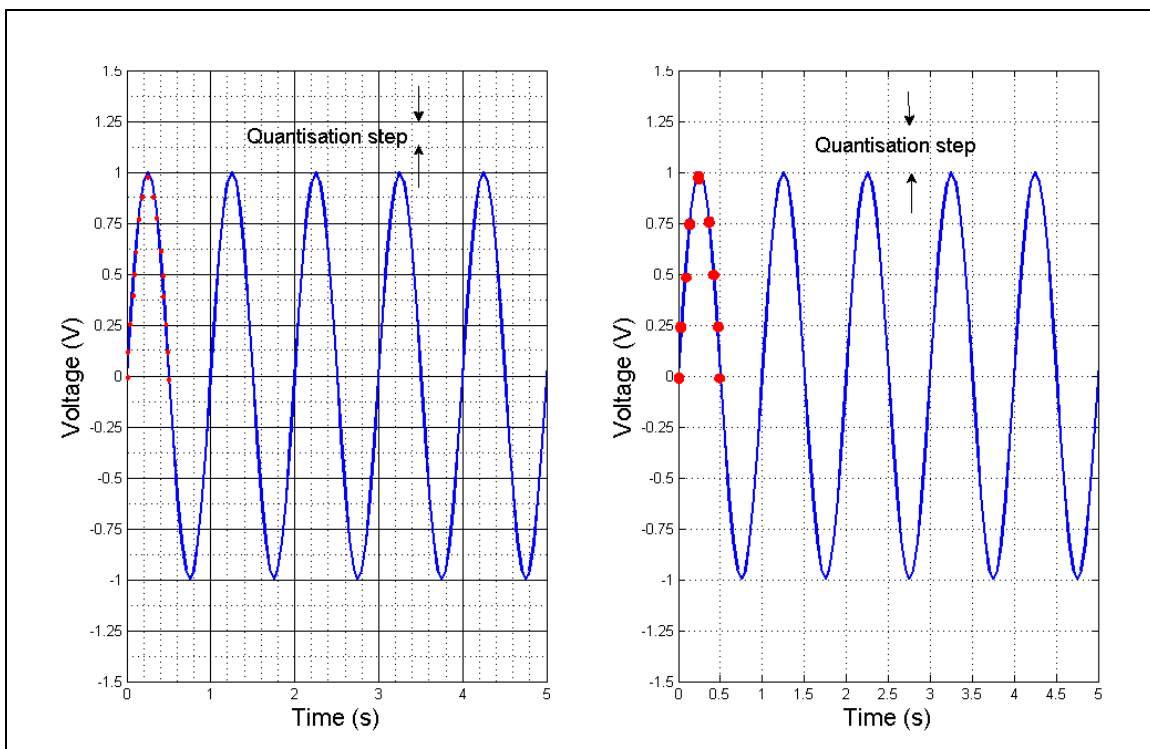


Figure B.2: Quantisation of analogue signal using different vertical resolutions.

References

ABEELE KOEN VAN DEN and DE VISSCHER JOËLLE (2000). Damage Assessment in Reinforced Concrete using Spectral and Temporal Nonlinear Vibration Techniques. *Cement and Concrete Research*, 30, pp. 1453-1464.

AGILENT TECHNOLOGIES (2000). The Fundamentals of Modal Testing. Application Note 243-3, USA.

ATAMTURKTUR S, PAVIC A, REYNOLDS P and BOOTHBY T (2009). Full-Scale Modal Testing of Vaulted Gothic Churches: Lessons Learned. *Dynamic Testing of Civil Engineering Structures Series, Experimental Techniques*, Society for Experimental Mechanics, Issue: July/August, pp. 65-74.

AVITABILE P (2001). Experimental Modal Analysis: A Simple Non-Mathematical Presentation, *Sound and vibration magazine*, January, pp. 1-11.

AVITABILE P (2007). *Modal Space: Back to Basics*. Society for Experimental Mechanics & Blackwell Publishing.

BAKIR P, REYNDERS and DE ROECK G (2007). Sensitivity-Based Finite Element Model Updating Using Constrained Optimization with a Trust Region Algorithm. *Journal of Sound and Vibration*, 305, pp. 211-225.

BAKIR P, REYNDERS and DE ROECK G (2008). An Improved Finite Element Model Updating Method by the Global Optimization Technique ‘Coupled Local Minimisers’. *Journal of Computers and Structures*, 86, pp. 1339-1352.

BALAGEAS D, FRITZEN CP and GEMES A (2006). *Structural Health Monitoring*. ISTE Ltd, London, UK.

BAXTER M (2003). *Statistics in Archaeology*. Hodder Arnold, London.

BAYISSA W (2007). *Damage Identification and Condition Assessment of Civil Engineering Structures through Response Measurements*. Doctoral Dissertation, Department of Civil and Environment Engineering, University of Melbourne, Melbourne.

BISHOP CM (2006). *Pattern Recognition and Machine Learning*. Springer Science + Business Media, Spring Street, New York, USA.

BRITISH STANDARDS (1986). *Testing concrete: Guide to the Use of Non-Destructive Methods of Test for Hardened Concrete*. BS 1881, part 2, BSI, London.

BROWNJOHN JM (2007). Structural Health Monitoring of Civil Infrastructure. *Philosophy Transactions of Royal Society*, Vol.365, pp. 589-622.

CARDEN EP and FANNING P (2004). Vibration Based Condition Monitoring: A Review. *Journal of Structural Health Monitoring*, 3(4), pp. 355-377.

CARDEN P and BROWNJOHN J (2008). ARMA Modelled Time-Series Classification For Structural Health Monitoring of Civil Infrastructure. *Mechanical Systems and Signal Processing*, 22, pp. 295-314.

CASAS JR (2006). Bridge management: Actual and Future Trends. *Proceedings of the International Conference on Bridge Maintenance, Safety, Management, Life-Cycle Performance and Cost, IABMAS, Porto, Portugal*. Editors: Cruz PJ, Frangopol DM and Neves LC, Taylor and Frances, London.

CATBAS F, BROWN D and EMIN AKTAN A (2006). Use of Modal Flexibility for Damage Detection and Condition Assessment: Case Studies and Demonstrations on Large Structures. *Journal of Structural Engineering, ASCE*, Vol. 132, No. 11, pp. 1699-1712.

CATBAS FN, CAICEDO JM and DYKE SJ (2006). Development of a Benchmark Problem for Bridge Health Monitoring. *Proceedings of the International Conference on Bridge Maintenance, Safety, Management, Life-Cycle Performance and Cost, IABMAS, Porto, Portugal*. Editors: Cruz PJ, Frangopol DM and Neves LC, Taylor and Frances, London.

CATBAS N, GUL M and BURKETT JL (2008). Conceptual Damage-Sensitive Features for Structural Health Monitoring: Laboratory and Field Demonstrations. *Mechanical Systems and Signal Processing*, 22, pp.1650-1669.

CAWLEY P and ADAMS RD (1979). The Location of Defects in Structures from Measurements of Natural Frequencies. *Journal of Strain Analysis*, Vol. 14, No.2, pp. 49-57.

CHEUNG A, CABRERA C, SARABANDI P, NAIR KK, KIREMIDJIAN A and WENZEL H (2008). The Application of Statistical Pattern Recognition Methods for Damage Detection to Field Data. *Journal of Smart Materials and Structures*, Vol. 17, pp. 1-12.

CLOUGH RW and PENZIEN J (2003). *Dynamics of Structures*. Third edition, Computers & Structures Inc., USA.

CORNWELL PJ, DOEBLING SW and FARRAR CR (1999). Application of the Strain Energy Damage Detection Method to Plate-Like Structures. *Journal of Sound and Vibration*, Vol. 224, No. 2, pp. 359-374.

DAE KUN KWON, TRACY KIJEWski-CORREA, AHSAN KAREEM and AHMAD ABDELRAZAQ (2011). SmartSync Framework in Structural Health Monitoring. *Proceedings of the 35th International Symposium on Bridge and Structural Engineering, jointly organised by IABSE-IASS*, London, UK.

DEVIJVER PA and KITTLER J (1982). *Pattern Recognition: A Statistical Approach*. Prentice Hall International, Inc., London.

DOEBLING S, FARRAR C and PRIME M (1998). A Summary Review of Vibration-Based Damage Identification Methods. *The Shock and Vibration Digest*, 30(2), pp. 91-105.

DOEBLING SW, FARRAR CR, PRIME MB and SHEVITZ DW (1996). *Damage Identification and Health Monitoring of Structural and Mechanical Systems from Changes in Their Vibration Characteristics: A Literature Review*. Technical Report LA-13070-MS, Los Alamos National Laboratory, Los Alamos, NM, USA.

DØSSING O (1988). *Structural Testing, Part II: Modal Analysis and Simulation*. Brüel & Kjær, Denmark.

DUDA RO, HART PE and STORK (2001). *Pattern Classification*, Second edition. John Wiley & Sons, New York.

ETTOUNEY MM and ALAMPALLI S (2012). *Infrastructure Health in Civil Engineering, Application and Management*. Volume II, CRC Press, Taylor and Francis Group, London.

EWINS DJ (2000). *Modal Testing: Theory, Practice and Application*, Second edition, Research Studies Press Ltd., Baldock, Hertfordshire, England.

FARRAR C and DUFFEY T (1999). Vibration Based Damage Detection in Rotating Machinery and Comparison to Civil Engineering Applications. *Proceedings of the 3rd International Conference on Damage Assessment of Structures, DAMAS'99*, Dublin, Ireland.

FARRAR CR and JAUREGUI DA (1998). Comparative Study of Damage Identification Algorithms Applied to a Bridge: I. Experiment. *Journal of Smart Material Structures*, Issue 7, pp. 704-719.

FARRAR C and WORDEN K (2007). An Introduction to Structural Health Monitoring. *Philosophy Transactions of Royal Society*, Vol.365, pp. 303-315.

FARRAR C, DOEBLING S and NIX D (2001a). Vibration-Based Structural Damage Identification. *Philosophy Transactions Royal Society*, Vol. 359, pp. 131-149.

FARRAR CR, CORNWELL PJ, DOEBLING SW and PRIME MB (2000). *Structural Health Monitoring Studies of the Alamosa Canyon and I-40 Bridges*. Los Alamos National Laboratory Report: LA-13635-MS, Los Alamos, New Mexico.

FARRAR CR, SOHN H and WORDEN K (2001b). *Data Normalization: A Key for Structural Health Monitoring*. Los Alamos National Laboratory Report: LA-UR-01-4212, Los Alamos, New Mexico.

FIGUEIREDO E, PARK G, FIGUERIRAS J, FARRAR C and WORDEN K (2009). *Structural Health Monitoring Algorithm Comprises Using Standard Data Sets*. Report LA-14393, Los Alamos National Laboratory, Los Alamos, New Mexico.

FRISWELL MI and PENNY JET (1997). Is Damage Location using Vibration Measurements Practical? Structural Damage Assessment using Advanced Signal Processing Procedures, *Proceedings of the 2nd International Conference on Damage Assessment of Structures, DAMAS'97*, Sheffield, UK, pp. 351-362.

FRISWELL MI (2007). Damage Identification using Inverse Methods. *Philosophy Transactions of Royal Society*, Vol.365, pp. 393-410.

FUGATE ML, SOHN H and FARRAR CR (2001). Vibration-Based Damage Detection using Statistical Process Control. *Mechanical Systems and Signal Processing*, 15(4), pp. 707-721.

GADE S, HERLUFSEN H and KONSTANTIN-HANSEN H (2005). *How to Determine the Modal Parameters of Simple Structures*. Application Note 3560, Brüel & Kjær, Denmark.

GASSMAN S and TAWHED W (2004). Non-destructive Assessment of Damage in Concrete Bridge Decks. *Journal of Performance of Constructed Facilities, ASCE*, Vol. 18, No.4, pp. 220-231.

GHALI A, NEVILLE AM and BROWN TG (2009). *Structural Analysis: A Unified Classical Matrix Approach*. Sixth edition, Taylor & Francis, New York, USA.

HARITOS N and OWEN J (2004). The Use of Vibration Data for Damage Detection in Bridges: A Comparison of System Identification and Pattern Recognition Approaches. *Journal of Structural Health Monitoring*, Vol. 3(2), pp. 141-163.

HE J and FU ZHI-FANG (2001). *Modal Analysis*. Butterworth-Heinemann, Oxford, England.

HEARN G and TESTA R (1991). Modal Analysis for Damage Detection in Structures. *Journal of Structural Engineering, ASCE*, Vol. 117, No. 10, pp. 3042-3063.

HM TREASURY (2010). *Infrastructure UK, Infrastructure Cost Review*. Technical Report prepared by HM Treasury.

HUNT V (2000). *Non-destructive Evaluation and Health Monitoring of Highway Bridges*. Doctoral Dissertation, Department of Electrical and Computer Engineering and Computer Science, University of Cincinnati, Cincinnati.

HUTH O, FELTRIN G, MAECK J, KILIC N and MOTAVALLI M (2005). Damage Identification Using Modal Data: Experiences on a Prestressed Concrete Bridge. *Journal of Structural Engineering, ASCE*, Vol. 131, No 12, pp. 1898-1910.

HWANG H and KIM C (2004). Damage Detection in Structures using a Few Frequency Response Measurements. *Journal of Sound and Vibration*, Vol.270, No. 1, pp. 1-14.

IRAQI PLANNING MINISTER (2009). [Online] Available at: <http://www.meanfn.com> [Accessed on 1st July 2009].

JAISHI B and REN WEI-XIN (2005). Structural Finite Element Model Updating Using Ambient Vibration Test Results. *Journal of Structural Engineering, ASCE*, Vol. 131, No. 4, pp. 617-628.

JAISHI B and REN WEI-XIN (2007). Finite Element Model Updating Based on Eigenvalue and Strain Energy Residuals Using Multi-Objective Optimisation Technique. *Mechanical Systems and Signal Processing*, Vol. 21, pp. 2295–2317.

JOLLIFFE IT (2002). *Principal Component Analysis*. Second edition, Springer, Verlag, New York Inc.

KATO M and SHIMADA S (1986). Vibration of PC Bridge during Failure Process. *Journal of Structural Engineering, ASCE*, Vol. 112, No. 7, pp. 1692-1703.

KIM J and STUBBS N (2003). Non-destructive Crack Detection Algorithm for Full-Scale Bridges. *Journal of Structural Engineering, ASCE*, Vol.129, No.10, pp. 1358-1366.

LANÇON H, CAMP G, CARREAUD P and PIOT S (2011). SCANSITES 3D[®]: The Method to Fingerprint The Health of Cooling Towers. *Proceedings of the 35th International Symposium on Bridge and Structural Engineering, jointly organised by IABSE-IASS, London, UK.*

- LEVIN R and LIEVEN I (1998). Dynamic Finite Element Model Updating using Neural Networks. *Journal of Sound and Vibration*, Vol. 210, No. 5, pp. 593-607.
- LIFSHITZ JM and ROTEM A (1969). Determination of Reinforcement Unbonding of Composites by Vibration Techniques. *Journal of Composite Materials*, Vol.3, Part 3, pp. 412-423.
- LYDON FD and BALENDRAN RV (1986). Some Observations on Elastic Properties of Plain Concrete. *Cement and Concrete Research*, Vol.16, No.3, pp. 314-324.
- LYNCH J (2007). An Overview of Wireless Structural Health Monitoring for Civil Structures. *Philosophy Transactions of Royal Society*, Vol.365, No 1851, pp. 345-372.
- MAECK J and DE ROECK G (1999). Dynamic Bending and Torsional Stiffness Derivation from Modal Curvatures and Torsion Rates. *Journal of Sound and Vibration*, Vol. 225, No. 1, pp. 153-170.
- MAIA NMM, SILVA JMM, HE J, LIEVEN NAJ, LIN RM, SKINGLE GW, TO W-M and URGUEIRA APV (1997). *Theoretical and Experimental Modal Analysis*. Editors: Maia and Silva, UK: Research Studies Press Ltd., Taunton, Somerset, England.
- MALLAT S (1999). *A Wavelet Tour of Signal Processing*. Second edition. Academic Press.
- MAZUREK DF and DEWOLF JT (1990). Experimental Study of Bridge Monitoring Technique. *Journal of Structural Engineering, ASCE*, Vol.116, No. 9, pp. 2532-2549.
- McConnell K and VAROTO P (2008). *Vibration Testing: Theory and Practice*. John Wiley & Sons, Inc., USA.
- MESSINA A, WILLIAMS EJ and CONTURSI T (1998). Structural Damage Detection by a Sensitivity and Statistical-Based Method. *Journal of Sound and Vibration*, Vol. 216, No. 5, pp. 791-808.
- MORDINI A, SAVOV K and WENZEL H (2007). The Finite Element Model Updating: A Powerful Tool for Structural Health Monitoring. *Structural Engineering International*, 17(4), pp. 352-358.

MOTTERSHEAD JE and FRISWELL MI (1993). Model Updating in Structural Dynamic: A Survey. *Journal of Sound and Vibration*, Vol. 167, No.2, pp.347-375.

NAIR KK and KIREMIDJIAN AS (2007). Time Series Based Structural Damage Detection Algorithm Using Gaussian Mixtures Modelling. *ASME Journal of Dynamic Systems, Measurement and Control*, 291, pp. 285-293.

NAIR KK, KIREMIDJIAN AS and LAW KH (2006). Time Series-Based Damage Detection and Localization Algorithm with Application to the ASCE Benchmark Structure. *Journal of Sound and Vibration*, 291, pp. 349-368.

NAUERZ A and FRIZEN CP (2001). Model Based Damage Identification using Output Spectral Densities. *ASME Journal of Dynamic Systems, Measurement, and Control*, 123, pp. 691-698.

NEVILLE AM (1995). *Properties of Concrete*. Longman Group Limited, Essex, England.

OWEN J and PEARSONR S (2004). The Use of Dynamic Data for the Structural Health Monitoring of Bridges. *Proceedings of First FIG International Symposium on Engineering Surveys for Construction Works and Structural Engineering*, Nottingham, United Kingdom.

OWEN JS, PEARSON SR, TAN CM and CHOO BS (2004). *Classification of Damaged and Modified Beams with Vibration Signatures*. Transportation Research Record 1814, Paper No. O2-2504, pp. 135-144.

PANDEY A and BISWAS M (1994). Damage Detection in Structures using Changes in Flexibility. *Journal of Sound and Vibration*, Vol. 169, No 1, pp. 3-17.

PANDEY A, BISWAS M and SAMMAN M (1991). Damage Detection from Changing in Curvature Mode Shapes. *Journal of Sound and Vibration*, Vol. 145, No.2, pp. 321-332.

PAVIC A, PIMENTEL R and WALDRON P (1997). Instrumented Sledge Hammer Impact Excitation: Worked Examples. *Proceedings of the 16th International Modal Analysis Conference (IMAC)*, Santa Barbara, CA, pp. 929-935.

PAZ M (1991). *Structural Dynamics: Theory and Computation*. Third edition, Van Nostrand Reinhold, New York, USA.

PEETERS B, MAECK J and DE ROECK G (2001). Vibration-Based Damage Detection in Civil Engineering: Excitation Sources and Temperature Effects. *Journal of smart materials and structures*, Vol. 10, pp. 518-527.

PRZEMIENECKI JS (1985). *Theory of Matrix Analysis*. Dover Publications.

REN W X and DE ROECK G (2002). Structural Damage Identification using Modal Data, II: Test Verification. *Journal of Structural Engineering, ASCE*, Vol. 128 No.1, pp. 96-104.

Report Card for America's Infrastructure (2009). American Society of Civil Engineers, ASCE, [Online]. Available at: <http://www.infrastructurereportcard.org> [Accessed on 1st July 2009].

REYNOLDS P (2000). *The Effects of Raised Access Flooring on the Vibrational Performance of Long-Span Concrete Floors*. A thesis submitted for the Degree of Doctor of Philosophy in Engineering, University of Sheffield, Department of Civil and Structural Engineering, Sheffield, UK.

REYNOLDS P and PAVIC A (2000). Quality Assurance Procedure for the Modal Testing of Building Floor Structures. *Structural Testing Series: Part 8, Experimental Techniques*, pp. 36-41.

REYNOLDS P, PAVIC A and WALDRON P (1999). Dynamic FE Modelling of a Multi-Storey Car Park Verified by Modal Testing. *Proceedings of the 17th International Modal Analysis Conference IMAC*, Kissimmee, FL, USA, pp. 7-13.

RUOTOLO R and SURACE C (1997). Damage Detection Using Singular Value Decomposition. *Structural Damage Assessment using Advanced Signal Processing*

Procedures, *Proceedings of the 2nd International Conference on Damage Assessment of Structures, DAMAS'97, University of Sheffield, Sheffield, UK*, pp. 87-96.

RYTTER A and KIRKEGAARD P (1997). Vibration Based Inspection Using Neural Networks. Structural Damage Assessment using Advanced Signal Processing Procedures, *Proceedings of the 2nd International Conference on Damage Assessment of Structures, DAMAS'97, University of Sheffield, Sheffield, UK*, pp. 97-108.

SALAWU OS and WILLIAMS C (1994). Damage Location using Vibration Mode Shapes, *Proceeding of the 12th International Modal Analysis Conference*, Bethel, Conn, USA, pp. 933-939.

SAMMAN M and BISWAS M (1994). Vibration Testing for Non-destructive Evaluation of Bridges. I-Theory. *Journal of Structural Engineering, ASCE*, Vol. 120, No.1, pp. 269-289.

SHI Z, LAW S and ZHANG L (2000). Damage Location by directly using Incomplete Mode Shapes. *Journal of Engineering Mechanics, ASCE*, Vol. 126, No. 6, pp. 656-660.

SOHN H, CZARNECKI JA and FARRAR CR (2000). Structural Health Monitoring Using Statistical Process Control. *Journal of Structural Engineering, ASCE*, Vol. 126, No. 11, pp.1356-1363.

SOHN H and FARRAR CR (2001). Damage Diagnosis using Time Series Analysis of Vibration Signals. *Journal of Smart Material and Structures*, Vol. 10, pp. 446-451.

SOHN H (2007). Effects of Environment and Operational Variability on Structural Health Monitoring. *Philosophy Transactions of Royal Society*, Vol.365, pp. 539-560.

SOHN H, FARRAR C, HUNTER H and WORDEN K (2001). *Applying the LANL Statistical Pattern Recognition Paradigm for Structural Health Monitoring to Data from a Surface-Effect Fast Patrol Boat*. Technical Report LA-13761-MS, Los Alamos National Laboratory, Los Alamos, NM, USA.

SOHN H, FARRAR CR, HEMEZ FM, SHUNK DD, STINEMATES DW, NADLER BR and CZARNECKI JJ (2004). *A Review of Structural Health Monitoring Literature:*

1996–2001. Technical Report LA-13976-MS, Los Alamos National Laboratory, Los Alamos, NM, USA.

STASZEWSKI J and ROBERTSON A (2007). Time-Frequency and Time-Scale Analyses for Structural Health Monitoring. *Philosophy Transactions of Royal Society*, Vol.365, pp. 449-477.

STASZEWSKI W (2000). Identification of Non-Linear Systems Using Multi-Scale Ridges and Skeletons of the Wavelet Transform. *Journal of Sound and Vibration*, 214(4), pp. 639-658.

STUBBS N, KIM J-T and FARRAR CR (1995). Field Verification of a Non-Destructive Damage Localization and Severity Estimation Algorithm. *Proceedings of the 13th International Modal Analysis conference*, Vol. 1, Nashville, TN, USA, pp. 210-218.

SUN Z and CHANG CC (2002). Structural Damage Assessment Based on Wavelet Packet Transform. *Journal of Structural Engineering, ASCE*, 128(10), pp. 1354-1361.

SUNG-PIL CHANG (2006). *Application of the Structural Health Monitoring System to the Long-Span Cable-Supported Bridges*. In Bridge Maintenance, Safety, Management, Life-Cycle Performance and Cost. Editors: Cruz PJ, Frangopol DM and Neves LC, Taylor and Frances, London.

TEUGHEL A and DE ROECK G (2004). Structural Damage Identification of the Highway Bridge Z24 by FE Model Updating. *Journal of Sound and Vibration*, Vol. 278, pp. 589-610.

The Mathworks Inc., Matlab version R2008a (2008). Statistics Toolbox Help, Natick, MA, USA.

TRENDAFILOVA I (2001). Pattern Recognition Methods for Damage Diagnosis in Structures from Vibration Measurements. *Key Engineering Materials*, Vols. 204-205, pp. 85-94.

- TRENDAFILOVA I (2011). A Method for Vibration-Based Structural Interrogation and Health Monitoring Based on Signal Cross-Correlation. *Proceedings of the 9th International Conference on Damage Assessment of Structures, DAMAS 2011, Journal of Physics: Conference Series*, Vol. 305.
- UNGER J, TEUGHEL A and DE ROECK G (2006). System Identification and Damage Detection of a Prestressed Concrete Beam. *Journal of Structural Engineering, ASCE*, Vol. 132, No.11, pp. 1691-1698.
- VANDIVER JK (1977). Detection of Structural Failure on Fixed Platform by Measurement of Dynamic Response. *Journal of Petroleum Technology*, March, pp. 305-310.
- VANIK MW, BECK JL and AU SK (2000). Bayesian Probabilistic Approach to Structural Health Monitoring. *Journal of Engineering Mechanics, ASCE*, Vol.126, No. 7, pp. 738-745.
- WANG X, SWANSON J, HELMICKI A and HUNT V (2007). Development of Dynamic-Response-Based Objective Function for Finite-Element Modelling of Bridges. *Journal of Bridge Engineering, ASCE*, Vol.12, No.5, pp. 552-559.
- WEBB A (2002). *Statistical Pattern Recognition*. Second edition, John Wiley & Sons, Ltd., West Sussex, United Kingdom.
- WENZEL H (2009). *Health Monitoring of Bridges*. John Wiley & Sons Ltd., West Sussex, United Kingdom.
- WILLIAMS C and SALAWU OS (1997). Damping as a Damage Indication Parameter. *Proceedings of the 15th International Modal Analysis Conference IMAC*, Volume 2, Orlando, FL, USA, pp. 1531-1536.
- WORDEN K and DULIEU-BARTON JM (2004). An Overview of Intelligent Fault Detection in Systems and Structures. *Journal of Structural Health Monitoring*, Vol. 3(1), pp. 085-098.

WORDEN K, FARRAR C, MANSON G and PARK G (2007). The Fundamental Axioms of Structural Health Monitoring. *Philosophy Transactions of Royal Society*, Vol.463, pp. 1639-1664.

WORDEN K, MANSON G and FIELLER NRJ (2000). Damage Detection Using Outlier Analysis. *Journal of Sound and Vibration*, Vol. 229, No. 3, pp. 647-667.

WU D and LAW S (2004). Damage Localization in Plate Structures from Uniform Load Surface Curvature. *Journal of Sound and Vibration*, 276, pp. 227–244.

YEUNG WT and SMITH JW (2005). Damage Detection in Bridges using Neural Networks for Pattern Recognition of Vibration Signatures. *Journal of Engineering Structures*, Vol.27, pp. 685-698.

ZANG C and MREGUN M (2001). Structural Damage Detection using Artificial Neural Networks and Measured FRF Data Reduced via Principal Component Projection. *Journal of Sound and Vibration*, 242(5), pp. 813- 827.

ZÁRATE BA and CAICEDO JM (2008). Finite Element Model Updating: Multiple Alternatives. *Journal of Engineering Structures*, Vol. 30, pp. 3724–3730.

ZHANG Z and AKTAN AE (1995). The Damage Indices for the Constructed Facilities. *Proceedings of the 13th International Modal Analysis Conference*, Vol. 2, Nashville, TN, USA, pp. 1520–1529.

ZHENGSHENG L, SWANSON J, HELMICKI A and HUNT V (2005). Modal Contribution Coefficients in Bridge Condition Evaluation. *Journal of Bridge Engineering*, ASCE, Vol.10, No.2, pp.169-178.